Understanding the role of electrolytes solvation structure for electrochemical energy storage applications

Nicolas Dubouis

Sorbonne Université

Ecole doctorale 397 - Physique et Chimie des Matériaux

Chimie du Solide et Energie, Collège de France, UMR 8260

Understanding the role of electrolytes solvation structure for electrochemical energy storage applications

By Nicolas Dubouis

Ph.D. thesis of Physics and Chemistry of Materials

Supervised by Alexis Grimaud

Presented and defended publicly on June 1st, 2021

In front of the Jury:

Prof. Hubert Girault	Professor, LEPA EPFL, Sion	Referee
Prof. María Escudero Escribano	Associate Professor, University of Copenhagen	Referee
Prof. Marc Koper	Professor, University of Leiden	Examiner
Prof. Marie-Laure Bocquet	Senior Researcher, Ecole normale supérieure, Paris	Examiner
Dr. Alexis Grimaud	Research Scientist, Chimie du Solide et Energie, Paris	Ph.D. director
Prof. Jean-Marie Tarascon	Professor, Chimie du Solide et Energie, Paris	Invited member
Prof. Mathieu Salanne	Professor, PHENIX, Paris	Invited member

Sorbonne Université

Ecole doctorale 397 - Physique et Chimie des Matériaux

Chimie du Solide et Energie, Collège de France, UMR 8260

Impact de la structure de solvatation des électrolytes pour le stockage électrochimique de l'énergie

Par Nicolas Dubouis

Thèse de doctorat de Physique et Chimie des Matériaux

Dirigée par Alexis Grimaud

Présentée et soutenue publiquement le 1er Juin 2021

Devant un jury composé de :

Prof. Hubert Girault	Professeur, LEPA EPFL, Sion	Rapporteur
Prof. María Escudero Escribano	Professeure associée, Université de Copenhague	Rapporteuse
Prof. Marc Koper	Professeur, Université de Leiden	Examinateur
Prof. Marie-Laure Bocquet	Directrice de Recherche, Ecole normale supérieure, Paris	Examinatrice
Dr. Alexis Grimaud	Chargé de Recherche, Chimie du Solide et Energie, Paris	Directeur
Prof. Jean-Marie Tarascon	Professeur, Chimie du Solide et Energie, Paris	Membre invité
Prof. Mathieu Salanne	Professeur, PHENIX, Paris	Membre invité

Acknowledgements

More than four years ago, I crossed for the first time the door of the Chimie du Solide et de l'Energie laboratory, in Collège de France and discussed very openly with Jean-Marie Tarascon, and Alexis Grimaud and they gave me the opportunity to work in this prestigious, international and challenging environment for my Master thesis and then for a 4 years Ph.D thesis that is ending now.

I am immeasurably grateful to Alexis, my Ph.D. supervisor. His dedication for science and for his students were very inspiring. I gratefully acknowledge him for leaving me enough freedom to explore a large variety of topics during my stay in the lab. This was truly enriching. Finally, I would like to thank him for spending so much time at working on papers, talks, etc. and giving insightful advices, from a scientific point and view, and beyond.

For sure, the journey would have been very different without the presence of Jean-Marie in the lab. He has been very challenging, and his feedback on the studies presented in this thesis were insightful. He is also very open minded, and humble and I really enjoyed discussing openly science and others with him. He is also thanked for synthetizing some of the materials that were used in during my thesis. The great team he has built and leads at the Chimie du Solide et de l'Energie laboratory reflects his passion and dedication for science.

About the team, I had the great opportunity to meet so many talented, enthusiastic and friendly colleagues during my stay in the laboratory. I am grateful to Chunzhen Yang, who welcomed me in the catalysis/electrochemistry team composed notably from Iban, Wei, Yan, Rona, Linjie, Damien. I thank all of them for fruitful discussions about electrochemistry. Outside of the electrocatalysis team, I would like to particularly acknowledge Gwen, Pierre, Paul, Vanessa, Sujoy, Thomas, Léa, Ivette, Fanny, Romain, Valentin, Sathyia, Benjamin, Antonella and all the other members of the lab for ensuring a good scientific and friendly atmosphere during these years.

The work of this thesis also reflects the possibility offered to the students from this lab to collaborate together. Especially, Pierre Lemaire is acknowledged for his help with EQCM and SEM measurements. Special thanks to Florencia Marchini for her contribution on solid-state testing for the VX_3 study. Ivette Aguilar and Valentier Meunier contributed to ICP-MS

measurements. Gwenaelle Rousse is acknowledged for helping with diffraction measurements. Also, many thanks to Amandine Brige, who worked for two months with me on the aqueous biphasic systems. Finally, the last chapter of this thesis is the fruit of a great collaboration with Thomas Marchandier who brought me to the solid-state chemistry universe. I truly enjoyed our various discussions. This work would not have been possible without the support of Jessica Duvoisin, who was super-efficient at managing all the administrative aspects.

During this Ph.D., I also had the great opportunity to work with many scientists from various fields. First, I would like to thank Mathieu Salanne and Alessandra Serva who taught me so much on molecular dynamics simulations. Benjamin Rotenberg, Chanbum Park, Matej Kanduč, Joachim Dzubiella, Roxanne Berthin, Guillaume Jeanmairet and Arthur France-Lanord are also acknowledged for their contributions on molecular dynamics simulations. Elodie Salager, Michaël Deschamps and Benjamin Porcheron helped me to set up and realized some of the NMR measurements presented in this manuscript. François Fauth is acknowledged for helping us with the synchrotron XRD measurements in Alba. Maxim Avdeev is acknowledged for performing neutron diffraction experiments. Finally, Antonella Iadecolla is gratefully acknowledged for performing the *operando* XAS measurements at Soleil.

The Ecole normale supérieure is acknowledged for the financial support for this thesis. Frederic Lemaître and François Ribot are acknowledged for attending the Comité de Suivi de Thèse.

Finally, I would like to thank Prof. Hubert Girault and Prof. María Escudero Escribano for accepting to review this thesis and to be part of the Ph.D. committee. I also acknowledge Prof. Mark Koper and Prof. Marie-Laure Bocquet for agreeing to be part of the jury.

Contents

Acknowledgements **4**

Context and Manuscript Outline **9**

General context 9

Outline of the thesis 11

Chapter I - Electrochemical transformation of water into hydrogen: from fundamental to applications. **15**

I.1. Producing hydrogen from water and electricity 15

Electrocatalytic water-splitting 15

Dominant technologies for water electrolyzers 17

I.2 Slowing down the water splitting kinetics: toward high-voltage aqueous batteries? 20

I.3 Historical and emerging strategies to understand and tune the hydrogen evolution reaction kinetics 23

The hydrogen binding energy descriptor and its limits 29

Interfacial interactions: how to rationalize them? 31

Interfacial reorganization: role of the solvent 35

I.4 Conclusions of the chapter 38

Chapter II - Confinement of water into an inert organic matrix to tune the water reactivity **39**

II.1 Motivations 39

II.2 Influence of the proton source: H_2O vs. $HClO_4$ 42

II.4 Free water vs. coordinating water 43

II.5 Water as a solvent: H-bonds vs. water-cations interactions 50

II.6 Nanostructuration of water at electrochemical interfaces 58

II.7 Conclusions of the chapter 65

Chapter III - From *water-in-salt* electrolytes to aqueous biphasic systems **71**

III.1 Motivations 71

III.2 Reactivity of water in superconcentrated electrolytes 74

Evaluation of the impact from the salt concentration on the electrochemical reactivity of aqueous superconcentrated electrolytes 74

Growth of a passivating layer on the electrodes upon water reduction and LiOH formation 77

III.3 Immiscibility of aqueous superconcentrated electrolytes 85

Formation of aqueous biphasic systems 85
Geometrical descriptors for the formation of ABSs 92
Probing the influence of the anion size from simple density measurements 95
Probing the influence of the anion hydrophobicity using gas phase DFT calculations 98
Probing the solvated anions geometry using ab initio molecular dynamics simulations 100
Can ABSs be used for electrochemical applications? 102
III.4 Conclusion of the chapter 106

Chapter IV - Reversible intercalation in vanadium halides enabled by the use of superconcentrated electrolytes 109

IV.1 Motivations 109
IV.2 Synthesis and characterization 111
IV.3 Electrochemical activity of VX_3 in various electrolytes 112
IV.4 Determination of the mechanism for the phase transformation upon cycling 114
IV.5 Rationale for the decreased solubility of halides in superconcentrated electrolytes 119
IV.6 Conclusions of the chapter 125

General conclusion and perspectives 127

List of abbreviations 133

Supplementary data and methods 135

Chapter II - 135
Supplementary Data 135
Methods 142
General procedures 142
Electrochemical measurements 142
Liquid Nuclear-magnetic resonance characterization 143
Small-angle X-Ray Scattering 143
^{1}H and ^{7}Li self-diffusion coefficient measurements by NMR 144
Molecular dynamic simulations for bulk electrolytes 144
Molecular dynamic simulations at constant applied voltage 146
Chapter III - 147
Methods 147

Materials....147
Electrochemical measurements....148
Electrodes characterization....151
Electrolytes Characterization....152
Phase Diagram Construction....154
Molecular simulations....154
Chapter IV -....157
Supplementary Data....157
Methods....161
Synthesis....161
Electrochemical measurements....161
Materials characterization....162
X-Ray Absorption Spectroscopy....163
Solubility measurements....164
UV-vis characterization....164
References 165
Résumé en Français de la Thèse....184

Context and Manuscript Outline

General context

Driven by the population growth and the appetite for automation, the worldwide energy consumption has been tremendously growing since the 19th century and the beginning of the industrial era. Despite the recent sanitary crises that has largely affected the worldwide economic and political situation, recent forecasts still predict an increase of the global energy demand of around 10% by 2030, compared to pre-crises level, primarily driven by the economic and population growth in Asia and Africa.[1] In parallel, the world is facing an increase in greenhouse gases (GHG) atmospheric concentrations that are for a large part emitted when primary energies are converted (CO_2 emissions from combustion reactions). Such high concentrations are inevitably leading to a global increase of the temperature at the surface of the Earth. To satisfy this appetite for energy while limiting the GHG emissions, there is a strong need to decrease the carbon intensity of our energy supply.

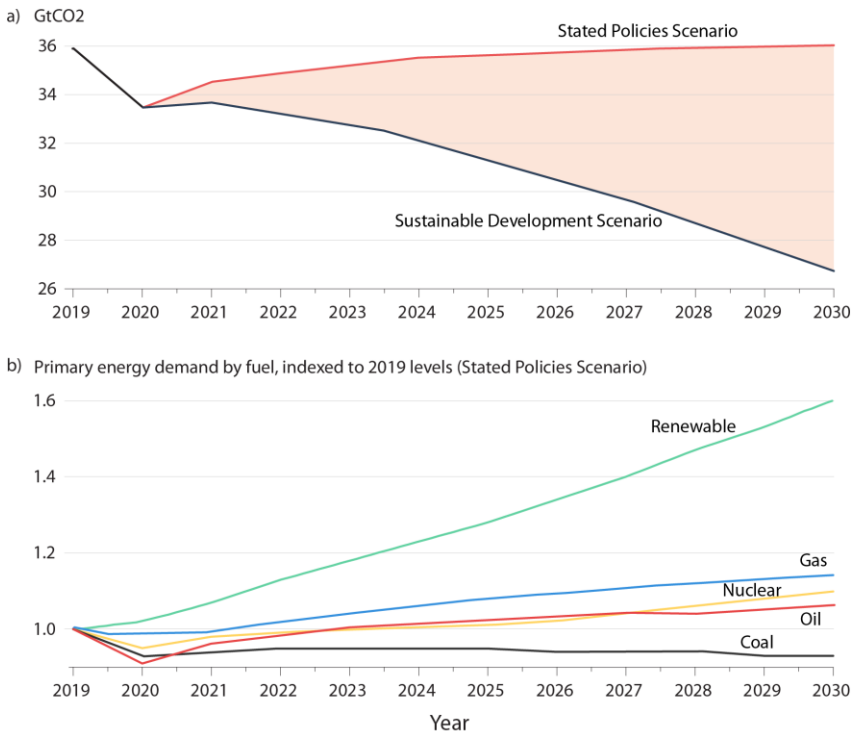

Introduction Figure 1. a) Forecast of the worldwide CO_2 emissions (in giga ton per year) for the next 10 years and **b)** forecast of the production for the different primary energy sources indexed to their levels in 2019 for the next 10 years within the stated policy scenario framework. Data are taken from ref. 1.

As shown in **Introduction Figure 1**, the mitigation of the global GHG emissions can only arise from a substantial modification of the primary energy sources share in the global production. Especially, even in the stated policies scenario (that is restricted to the application of already adopted policies and does not take future improvements into accounts), renewable energy sources installed capacities are expected to grow by more than 1.5 times within the next decade.

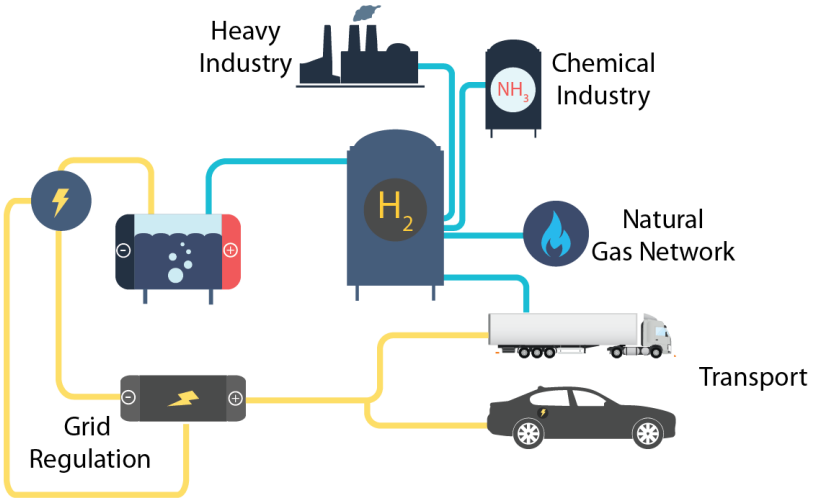

Introduction Figure 2. Various applications for electrochemical energy storage devices. Yellow lines represent electricity flows, while blue lines account for hydrogen flows.

To implement those drastic changes in our energy supply, the development of efficient electrical energy storage solutions is crucial. Indeed, because renewable energy sources (wind and solar) are intermittent, the electrical grids need to be buffered to ensure a proper regulation of their operating frequencies. Moreover, since the transportation sector is accountable for around 25% of the GHG emissions,[2] its electrification is one of the top priority to limit anthropologic GHG emissions and it will require the massive deployment of cheap and efficient energy storage devices. Some of the most advanced energy storage technology rely on the transformation of electricity into chemical energy. For instance, electrolyzers are used to convert water and electricity into "green hydrogen" that can be used as it as chemical reagent, or even converted back to electricity within fuel-cells. Also, rechargeable (or secondary) batteries store and release electrical energy on demand, through reversible electrochemical reactions.

Each of these devices may match various applications. For instance, because batteries exhibit good reversibility, they are envisioned for grid frequency regulation applications. Also,

thanks to their high volumetric energy density (> 1 kWh/L), they are widely used to power zero-emission personal cars. Even if the transformation of hydrogen into electricity inside a fuel-cell is also envisioned to power heavy-duty transportations (trucks or boats), hydrogen is above all attractive because it finds direct industrial applications. For instance it can substitute for carbon as a reducing agent for steel and aluminum industries, be used as a reactant the chemical industry (e.g. ammonia production), or even be injected in the natural gas network to lower heating systems carbon intensity.[3]

Interestingly, water electrolyzers and batteries share a common structure: they both encompass two electrodes and an electrolyte. The electrodes are made from conductive materials to which electric charges are brought by an external circuit, while the electrolyte is often the mixture of solvent(s) and supporting salt(s) that ensures the electroneutrality by assuring the shuttle of ionic species between the electrodes. For both systems, the choice of the electrodes materials tremendously governs their performances. Thus, materials with large energy and high power densities have been designed for battery applications, while materials exhibiting good catalytic properties and long-term stability have been engineered for electrolyzers. Nevertheless, these high performances materials are in contact with electrolytes, and the nature of the electrode-electrolyte interface may limit their performances. Hence, it appears crucial to better understand the nature of those electrochemical interfaces in order to unlock cheaper, more efficient and more sustainable electrochemical energy storage devices.

Outline of the thesis

This thesis aims to contribute to the development of electrochemical energy storage devices, by providing a better understanding of the role of the electrolyte, and especially of the solvent, in electrolyzer and battery devices. Electrochemical measurements, molecular dynamics simulations, liquids physical and chemical properties characterization techniques as well as spectroscopies were employed to this purpose. Material characterization techniques (diffraction and spectroscopies) completed the panel of experimental techniques.

The first chapter introduces this thesis by looking at the hydrogen evolution reaction (HER). After recalling the historical developments of water splitting, it discusses the implications of the HER kinetics and thermodynamics for electrolyzers and aqueous batteries. Then, it focuses on the

quest for finding physical descriptors to describe HER kinetics, emphasizing recent developments that highlighted the importance of understanding how the water structure at electrochemical interfaces may alter its reactivity.

The second chapter describes results regarding a chemical strategy employed to glimpse a molecular picture of water electrochemical reactivity. Briefly, it consists in "confining" water in an organic solvent to finely tune its short-range and long-range environments and monitor how they alter its reactivity upon reductive conditions. The combined use of molecular dynamics simulations and spectroscopies shines a light on how the water structure in electrolytes can be tuned just by varying by the water concentration and/or the supporting salt nature and/or concentration. Electrochemical measurements prove that the modification of the water short and long-range environment drastically alters the water reactivity, and a water "structure-reactivity" correlation is drawn.

The third chapter is dedicated to the study of superconcentrated aqueous electrolytes, also called water-in-salt electrolytes. They exhibit a large electrochemical window (>3V) and are promising for the development of high-voltage aqueous batteries. First, their electrochemical reactivity is assessed on model electrodes, and rationalized thanks to the fundamental framework developed in the first chapter. The formation of aqueous biphasic systems is assessed for different lithium salts, and the physics that drives the formation of such intriguing systems is explored thanks to the analysis of the physico-chemical properties of these liquids coupled with molecular modeling. Criteria based on the size and shape of the anions emerged from these investigations to be used as descriptors for the formation of aqueous biphasic systems. The use of aqueous biphasic systems for electrochemical applications is discussed.

The last chapter extends the framework of this thesis to organic electrolytes. It proposes to electrochemically intercalate lithium cations into materials that are reputed soluble in most of electrolytes commonly used in Li-ion batteries (LIBs). Inspired by the physics that drives the formation of aqueous biphasic systems, the use of organic superconcentrated electrolytes is proposed to tackle this solubility issues. Li batteries using those electrolytes are assembled, and the formation of new lithiated vanadium halide phases is demonstrated using diffraction techniques.

Solubility measurements demonstrate that superconcentrated electrolytes thermodynamically suppress the transition metal dissolution.

Altogether, this manuscript highlights that mastering the solvent structure at the electrode/electrolyte interface is a key to innovate in the electrochemical energy storage sector. Also, it suggests that the developments of *à façon* electrolytes may help to trigger the development of new materials that would serve for energy applications and beyond.

Chapter I - Electrochemical transformation of water into hydrogen: from fundamental to applications[a]

I.1. Producing hydrogen from water and electricity

Electrocatalytic water-splitting

The transformation of water into molecular hydrogen has been extensively studied since the 16th century, even though the hydrogen was only properly categorized as an element by the French chemist Lavoisier in 1784.[4] Until this date, hydrogen is known as the product of the reaction between a metal, acting as a reducing agent, with acidic water as escribed by the following chemical equation:

$$n\mathrm{H}^+ + \mathrm{M} = \mathrm{M}^{n+} + \frac{n}{2}\mathrm{H}_2 \qquad \text{(I-1)}$$

In 1789, two Dutch and German scientists highlighted for the first time the feasibility of using an external electric field to transform water into molecular hydrogen ("*air inflammable"*) and molecular oxygen ("*air vital*").[5] A year later, the German chemist J.W. Ritter took profit of the discovery of the voltaic pile and assembled the first water electrolysis apparatus, that allows to recover separately the two gas evolved at the anode and the cathode.[6] At each electrode, electrons meet protons or water molecules to evolve the two gases according to the following electrochemical equations:

$$2\mathrm{H}^+ + 2\mathrm{e}^- = \mathrm{H}_2 \text{ hydrogen evolution in an acidic electrolyte} \qquad \text{(I-2)}$$

$$2\mathrm{H}_2\mathrm{O} + 2\mathrm{e}^- = \mathrm{H}_2 + 2\mathrm{OH}^- \text{ hydrogen evolution in an alkaline electrolyte} \qquad \text{(I-3)}$$

$$\mathrm{H}_2\mathrm{O} = \frac{1}{2}\mathrm{O}_2 + 2\mathrm{e}^- + 2\mathrm{H}^+ \text{ oxygen evolution in an acidic electrolyte} \qquad \text{(I-4)}$$

$$2\mathrm{OH}^- = \frac{1}{2}\mathrm{O}_2 + 2\mathrm{e}^- + \mathrm{H}_2\mathrm{O} \text{ oxygen evolution in an alkaline electrolyte} \qquad \text{(I-5)}$$

[a] Part of this chapter is based on the following paper that I co-authored: N. Dubouis and A. Grimaud, The hydrogen evolution reaction: from material to interfacial descriptors, *Chem. Sci.*, **2019**,10, 9165-9181

These discoveries were rapidly followed by the engineering of applied systems using hydrogen (fuel cells, internal combustion engines, balloons, etc.) and by the development of fundamental tools to describe the physico-chemical properties of electrolysis (Avogadro's gas law, Faraday's laws, manometers, etc.).

Since then, the HER has been extensively studied from a fundamental point of view. One of the motivation behind this broad interest from the scientific community is that the HER is a prototypical electrochemical reaction. Indeed, it can be measured in simple aqueous electrolytes (water is both the solvent and the reactant), and no side reactions can be expected since the metallic electrodes are held at reductive potentials, unlike for the oxygen evolution reaction (OER), for which metals tend to oxidize and dissolve.

As early observed by electrochemists such as Bockris, the kinetics for the HER are highly dependent on the nature of the electrode material.[7] For instance, in acidic media, the value of the Tafel slope (which measures how much overpotential should be added to increase the current density) for the HER ranges from ~ 30 mV/decade when measured on platinum (Pt) up to 120 mV/decade when measured on mercury (Hg).[8] Measuring such different values led to the conclusions that the HER is an electrocatalyzed reaction, for which the mechanism depends on the nature of the electrode material. Simply speaking, the electrode acts as a heterogeneous catalyst by creating a reaction intermediate in the reaction pathway, minimizing the Gibbs free energy of activation ($\Delta_r G^{\ddagger}$), as illustrated in the **Figure I-1**.

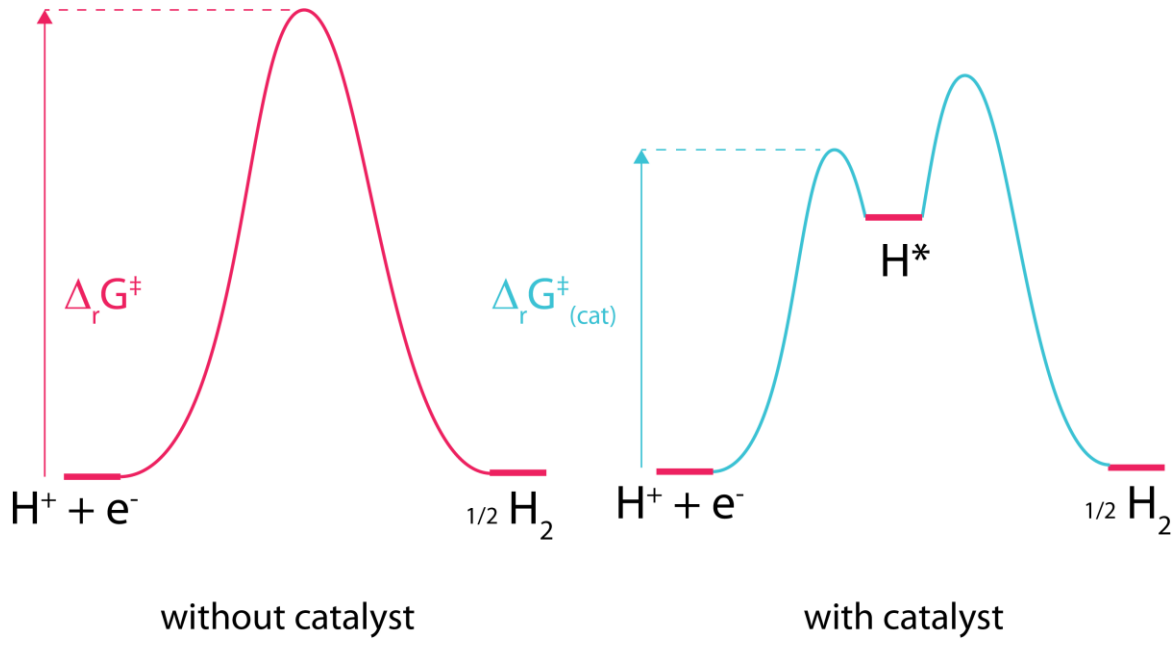

Figure I-1. Illustration of the reduction for the microscopic activation energy in presence of an electrocatalyst.

The fact that the HER is an electrocatalyzed reaction finds also its importance regarding the practical production of hydrogen from water and electricity. Indeed, the choice of the catalyst will directly set up the HER kinetics, and thus the power capacity and the electrical efficiency of the electrolyzer, *i.e.* the device embarking the catalysts and other components required for the reaction to occur at an industrial scale. These two parameters are intimately correlated to the price of the green hydrogen. Indeed, a higher electrical efficiency means lower operating costs while a higher power capacity lowers the capital expenditures. Thus, despite the cost of the catalyst represents only few percent of the one of the total electrolyzer, its performances will directly affect the green hydrogen price.[9,10] Therefore, it is prime of interest to understand how the catalysts work in the electrolyzers environments.

Dominant technologies for water electrolyzers

The mass production of hydrogen using water splitting requires the assembly of efficient, cheap and long lifetime electrolyzers. One of the main challenges that exists for designing a practical electrolyzer is the stability of the system in presence of an aqueous electrolyte. Such stability criteria exclude the use of strong acidic electrolytes for the assembly of MW-scale electrolyzers. Indeed, while suitable HER catalysts can be found in acidic conditions, only scarce

and expensive compounds such as ruthenium (Ru) or iridium (Ir) oxides are suitable for the OER in acidic conditions.[11–14] Moreover, the practical stability of the materials used for the electrolyte and gas flow management is even a larger concern. Thus, the first generation of commercial electrolyzers was designed based on two electrodes made from abundant metal, namely nickel (Ni),[15] separated by a diaphragm that prevents gas crossover and short-circuit, all being immersed in a strong alkaline electrolyte (typically 40w% KOH solution) forming a so-called alkaline electrolyzers, as schematized in **Figure I-2**. Even if alkaline electrolysis is the most mature technology, with a low capital cost and good electrical efficiencies of ~63-70%, it suffers from several drawbacks such as a relatively poor purity (<99%) for the gas produced, a low output pressure (1-30 bars) and more importantly from the need of recycling the highly corrosive KOH electrolyte.[3,10]

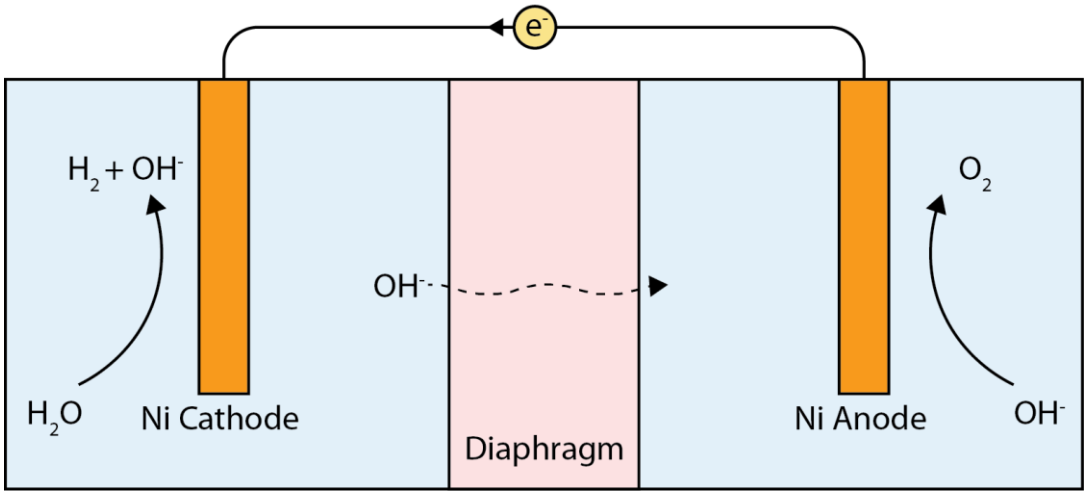

Figure I-2. Schematic representation of an alkaline electrolyzer.

In order to overcome those shortcomings relative to the alkaline technology, polymer electrolyte membrane water electrolyzers were developed. The most common technology is using a proton exchange membrane (such as Nafion), on which OER (resp. HER) catalysts such as RuO_2 or IrO_2 (resp. Pt/C, Pt) are directly coated forming a so-called membrane electrode assembly (MEA). Ultrapure water (liquid or vapor), is feeding the MEA through bipolar plates equipped with gas flow channels, that are connected to the external circuit by stainless-steel current collectors as described in **Figure I-3**.[10,16] The mechanism at play is similar to acidic water splitting: the oxidation of water into O_2 generates protons that can shuttle across the proton exchange membrane to the

negative catalyst to be reduced into H_2. Polymer electrolyzers outperform alkaline ones since they do not need an aggressive electrolyte, they exhibit high output pressures (up to 200 bars with a compressor), can produce high purity grade hydrogen (> 99.999%) and are highly flexible regarding their load.[3,10] However, scalabilities issues are at play. Indeed, even if HER catalysts could eventually be replaced by earth-abundant sulfides, or nitrides for instance,[9,17] no abundant OER catalysts operating in acidic conditions are known today. Thus, a system operating with the same catalysts as in alkaline electrolyte and based on a MEA architecture is highly desirable and can be obtained by replacing the proton exchange membrane by an anion exchange membrane that allows the transfer of hydrogen anions generated by the HER to the OER catalyst. Even if not as mature as alkaline electrolyzers or proton exchange membrane electrolyzers, anion exchange membrane electrolyzers are currently at the beginning of their commercialization[10] and may help to the deployment of H_2 production at a TW scale.

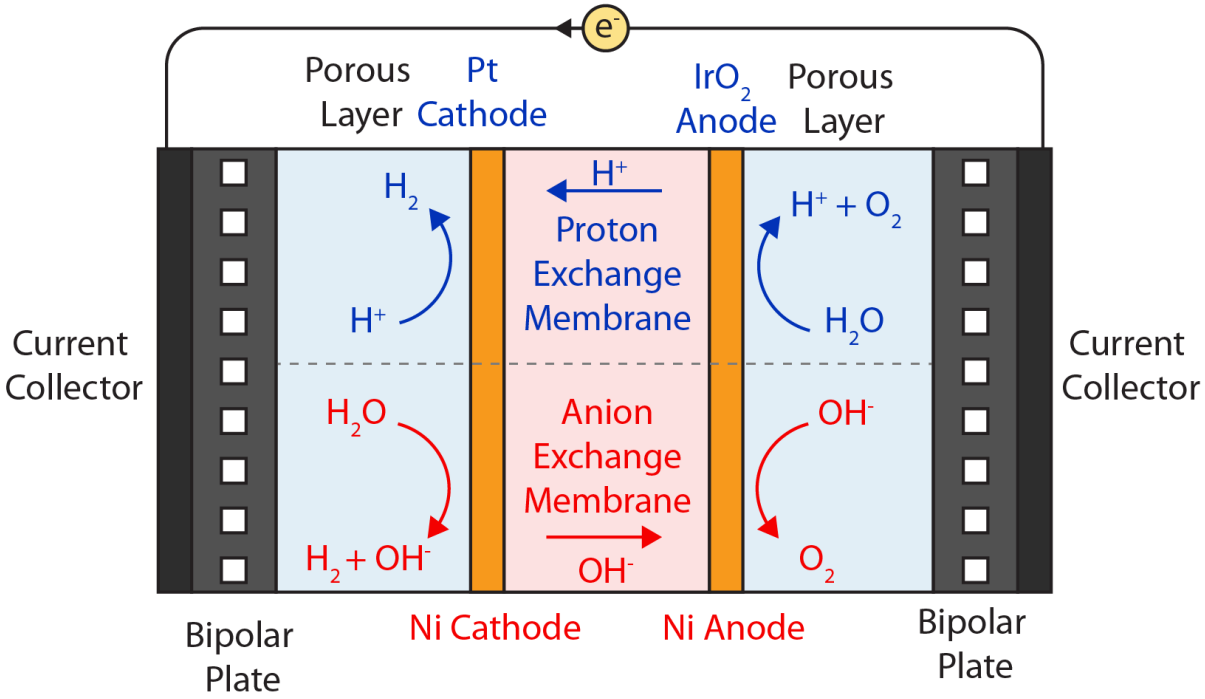

Figure I-3. Schematic representation of a polymer electrolyte membrane electrolyzer based either on a proton exchange membrane (blue) or on an anion exchange membrane (red) technology. Captions in black are similar for both systems.

Finally, it is worth mentioning that while the technologies previously listed operate at relatively low temperature (~ 20 – 100°C); high-temperature electrolyzer technologies are slowly

brought to the market. For instance, solid oxide electrolyzer cells operate at ~650-1000°C and use doped zirconia as a solid electrolyte and fuel-cell electrodes, the operation at higher temperature maximizing the electrical efficiency (> 75%). Moreover, these systems could be attractive for reversible applications such as grid frequency regulation since they can operate in a fuel-cell mode, but with relatively poor efficiencies.[3] However, they also suffer from their short stack lifetime and high capital cost.[3]

A massive adoption of the hydrogen economy should lead to a drastic price decrease for the production and installation of electrolyzers thanks to scalability and learning by doing effects. Combined with a drop of the electricity prices resulting from the connection of renewable power plants to the grid, the production cost of green hydrogen could meet the 2 $/kg target at a short horizon, in certain geographic locations.[3]

However, as mentioned earlier in the thesis, hydrogen suffers from intrinsic drawbacks that prevents its widespread for personal transportation and to power small electronic devices. For these applications, rechargeable batteries are more competitive. While the kinetics for the HER and OER set up the performances for water electrolyzers, they also start to be recognized as an issue to tackle for the development of greener high-voltage secondary batteries based aqueous electrolytes.

I.2 Slowing down the water splitting kinetics: toward high-voltage aqueous batteries?

The conversion of chemical energy into electricity was discovered by Volta at the same period as the electrochemical water-splitting. Since then, many other primary (non-rechargeable) and secondary (rechargeable) battery technologies were invented. Batteries are made by assembling two electrodes, having different redox potentials, with an electrolyte. For instance, the voltaic cell was obtained by stacking discs of copper and zinc, separated by paper fibers, these components being soaked into a brine solution. During the discharge of the battery, the positive electrode (or the cathode) is reduced and the negative one (the anode) is oxidized while the electrolyte ensures the local electrical neutrality. While the molar mass of the electrode materials, and the number of charge they can accumulate/give, governs the battery "capacity" (expressed in Ah g^{-1}), the "energy density" (in Wh kg^{-1}) will be the product of this capacity with the working voltage. Most of the commercial batteries that are still used today (lead-acid, nickel-cadmium,

nickel-iron, nickel-metal hydride) were developed in the 19th and 20th century and all share the use of a water-based electrolytes. Hence, practically speaking, all these technologies operate at voltage under 2.0 V to limit the electrolyte degradation and are limited to energy densities below 100 Wh kg^{-1} as shown in **Figure I-4**.

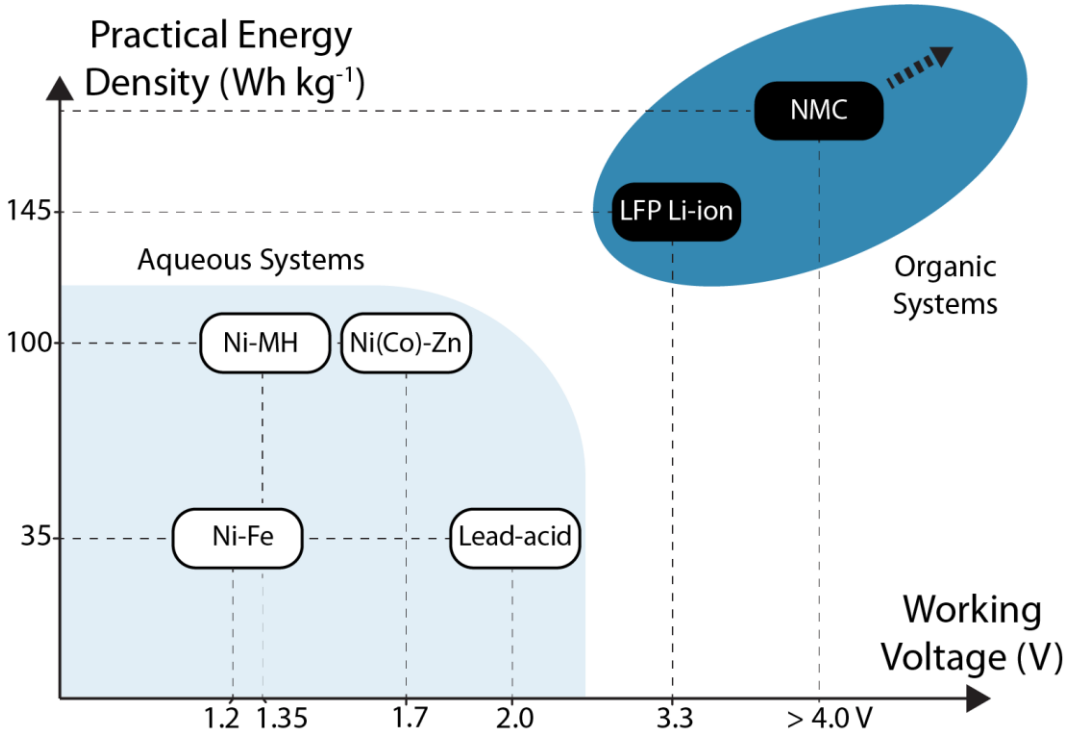

Figure I-4. Practical energy density and working voltage of the main aqueous (light blue) and non-aqueous (dark blue) commercial secondary batteries technologies. Values are given for the entire device, and are taken from ref. 18.

The recent boom of the battery technology was allowed by the discovery of the intercalation chemistry, directly implemented into the so-called Li-ion battery technology. LIBs were invented in the late 80's, and are based on a "rocking-chair" technology: the cathode and the anode are materials that can reversibly intercalate Li^+ cations and the electrolyte is a matrix containing a lithium salt that ensures the flow of alkali cations between the electrodes. The potential at which the reversible intercalation/deintercalation operates is directly correlated with the electronic structure of the electrode material. Today, the negative electrode is made of carbon-graphite, while the positive electrodes are often picked up from transition metal oxides (e.g. $LiCoO_2$) or polyanionic compounds (e.g. $LiFePO_4$). Because graphite can intercalate lithium at very low potentials (0.1 V vs. Li^+/Li *i.e.* – 2.9 V vs. the standard hydrogen electrode (SHE)) and positive

electrodes at relatively high potentials (> 3 V vs. Li^+/Li *i.e.* > 0.0 V vs. SHE, or more than 4.0 V vs. Li^+/Li (1 V vs. SHE)) for the most advanced technologies (such as nickel manganese cobalt oxides, so called NMC, cathodes), one could assemble high operating voltage and high gravimetric energy density devices.

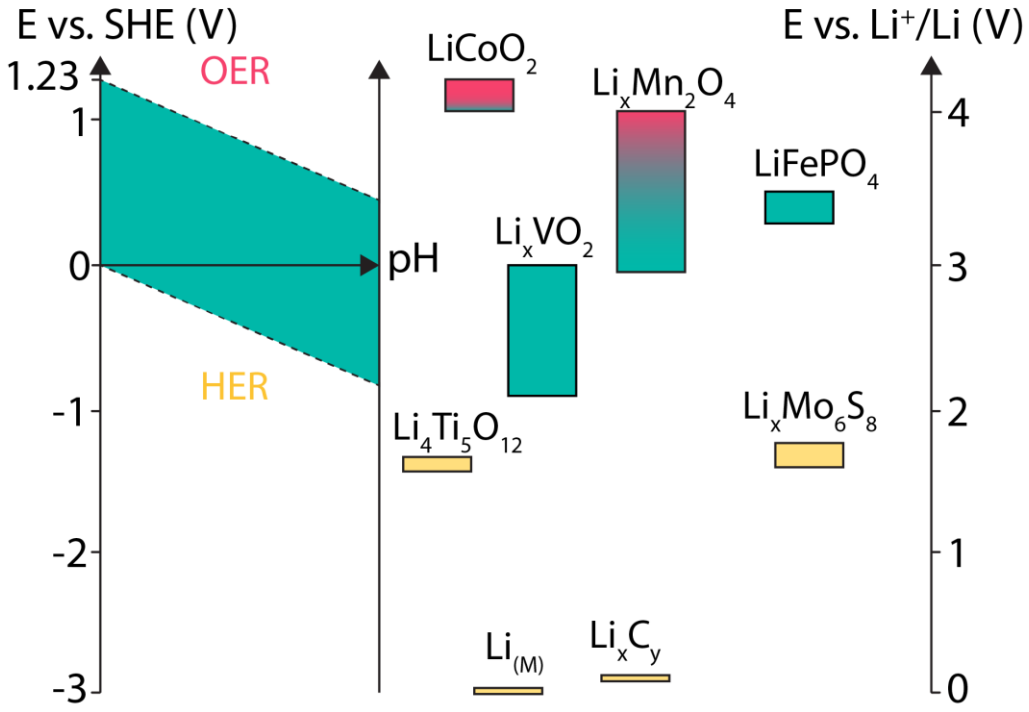

Figure I-5. Operating potentials for materials used in Li-ion (or Li-metal) batteries compared to the water Pourbaix diagram. When a material can operate in an aqueous electrolyte, the color is green. If the operating potential is too low it is colored in yellow and too high in red. Data are taken from ref. **19**.

Nevertheless, even though aqueous electrolytes are safe (less flammability and toxicity), sustainable, cheap and easy to manufacture (no dry room are needed in the factories), and exhibit great conductivities,[18,19] they have a narrow electrochemical stability window. Thus, plenty of intercalation materials would not be stable when soaked in aqueous electrolytes. Indeed, if the intercalation potential of a material is too low (resp. high) relatively to the Pourbaix diagram for water (as shown in **Figure I-5**), the material would deintercalate (resp. intercalate) by reacting with water through the following redox reaction: $LiA + H_2O = A + Li^+ + OH^- + \frac{1}{2}H_2$ (resp. $A + Li^+ + 2\,H_2O = \frac{1}{2}O_2 + LiA + H_3O^+$) (A being the host material) preventing the battery to

operate. Thus, blend of organic solvents (carbonates) were originally preferred to assemble high-voltage LIBs since they exhibit wider electrochemical stability windows. Nevertheless, few examples of aqueous LIBs were developed. For instance, the first rechargeable aqueous LIB, which was engineered by Dahn and coworkers 1994 using $LiMn_2O_4$ as positive electrode and VO_2 as negative electrode and concentrated $LiNO_3$-based or LiOH-based electrolytes with a 1.5 V operating voltage and a about 50 Wh kg^{-1}.[20,21] Despite such low metrics that preclude rechargeable aqueous LIBs from competing with their organic counterparts, these prototypes confirm the feasibility for a "rocking-chair" electrochemistry in aqueous electrolytes. Thus, it appears crucial to develop strategies in order to tackle this redox stability issue between the intercalation materials and aqueous electrolytes and combine all the advantages from the Li-ion chemistry (high voltage, coulombic efficiency and reversibility) and of water-based electrolytes.

If the thermodynamic stability window of water cannot be easily tuned, because the associated reactions are electrocatalyzed, as discussed above, the kinetics for the HER and OER are strongly dependent on the experimental conditions. Thus, one could take advantage of this effect and select intercalation materials that are bad catalysts for water splitting. Looking at **Figure I-5**, it clearly appears that the intercalation compounds usually employed as positive electrode would have their potential close to the OER one (especially at low pH), while negative electrodes such as $Li_{(Metal)}$ or graphite operate at very negative potentials compared to the HER potential, whatever the pH. Thus, to improve the energy density of aqueous LIBs, one should focus on the kinetics of the HER on negative electrode materials. A prototypical example illustrating this challenge is MoS_2. Indeed despite its intercalation potential being not so far from the water stability region (~1.5V vs. Li^+/Li),[22] the 1T-Li_xMoS_2 phase obtained upon lithiation has been found as one of the best transition-metal based catalysts for the HER,[23] which prevents its use as a negative electrode in an aqueous LIB. The MoS_2 example definitely demonstrates the existence of synergies in the development of more performant water electrolyzers and rechargeable aqueous LIBs.

I.3 Historical and emerging strategies to understand and tune the hydrogen evolution reaction kinetics

Earlier in this chapter, we have clearly highlighted that finely assessing how efficient or not a material will be for the water reduction is one of the key challenge in order to build more efficient

electrolyzers or aqueous batteries. In this section, we will review how different physical parameters were identified and proposed as good "descriptors" for the HER kinetics.

The heterogeneous HER comprises two concerted proton-electron transfers that were identified to occur in two successive elementary steps.[8] The reductive adsorption of hydrogen atoms onto the electrode surface was ascribed as the first step for the electrocatalytic HER and named the Volmer step: $H^+ + e^- = H^*$. Then, the as formed reaction intermediate (H*) can either chemically recombine with another H* to evolve molecular H_2 ($2H^* = H_2$, Tafel step) or undergo an electrochemical recombination ($H^* + H^+ + e^- = H_2$, Heyrovsky step).[8] The mechanism at play is highly dependent on the experimental conditions (*i.e.* electrode material and electrolyte) and can be approached by combing microkinetics modeling and Tafel analysis.[24]

Importantly, a good catalyst should exhibit high exchange current density and a low Tafel slope values. Platinum meets those two criteria, and is widely recognized as the state of the art electrocatalyst for the HER. Also, the HER is found to be highly reversible on Pt, which means that the kinetics for the hydrogen oxidation reaction (HOR) are fast. Even if Pt is quite scarce (worldwide annual production ~ 180 tons,[9] unequally distributed[25]) and expensive (~ 35 000 $/kg in February 2021), it is one of the catalyst that is used in industrial electrolyzers because it exhibits very fast kinetics for the HER. Because Pt is a reversible for the HER/HOR, it is also massively employed as a fuel cell catalyst.

From a more fundamental point of view, the fast kinetics and the good reversibility for the HER and HOR on Pt are also useful to define and assemble a reversible hydrogen electrode (RHE) by bubbling H_2 into an electrolyte which can be used as a reference electrode. Using this reference electrode, the overpotential for the HER (η_{HER}) can simply be defined by the difference between the applied potential and this reference electrode. The RHE potential, which is pH dependent, can be directly derived from the Nernst equation:

$$E_{RHE} = E_{SHE} - \frac{RT}{F}pH \qquad \text{(I-6)}$$

where E_{SHE} is the potential for the standard hydrogen electrode, an ideal electrode that adopts the potential of a platinum electrode in an ideal solution that contains 1 M H^+, with an activity

coefficient of 1, and under a 1 bar H_2 atmosphere with a fugacity of 1, R the universal gas constant, T the temperature and F the Faraday constant.

Owing to its outstanding electrocatalytic activity, most of studies are therefore focusing on the HER mechanism on the surface of Pt in acidic media. A typical cyclic voltammogram (CV) recorded for polycrystalline platinum ($Pt_{(pc)}$) electrode in acidic media is shown in **Figure I-6**.

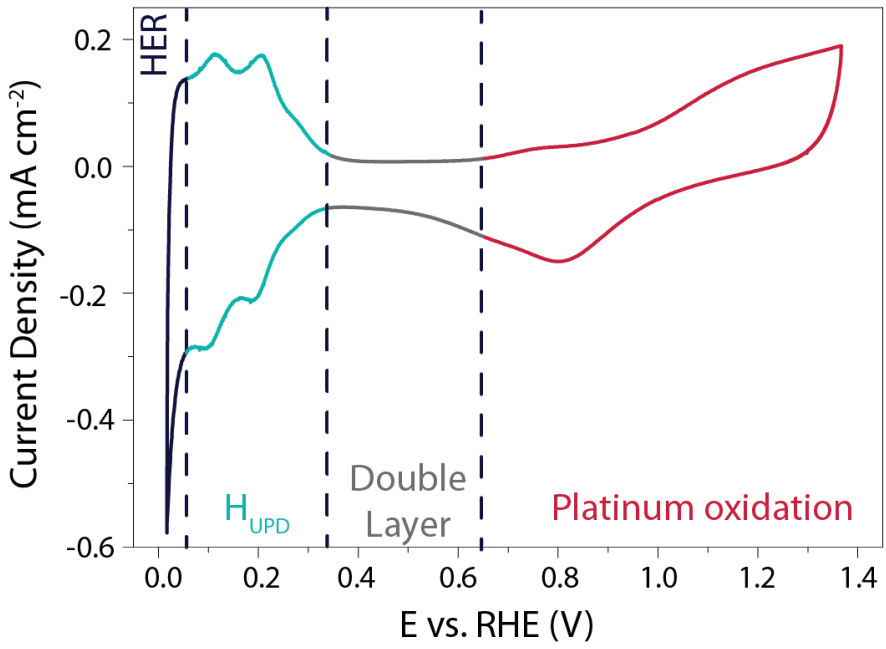

Figure I-6. Cyclic voltammogram recorded on a $Pt_{(pc)}$ electrode at 50 mV s^{-1} in a 0.5 M H_2SO_4 solution degassed with argon.

This typical CV exhibits 4 regions. At high potentials (> 0.65 V vs. RHE), the Pt surface is oxidized/reduced with the subsequent formation of Pt-OH and/or Pt-oxide that can be concomitant with the specific adsorption of anions on the surface of the platinum. The second region at potentials comprised between 0.35V and 0.65 V vs. RHE is referred to as the "double layer region" as no faradic process occurs. At potentials comprised between 0.05 V and 0.35 V vs. RHE, the third region was usually ascribed as the hydrogen underpotential deposition (H_{UPD}) region and is characterized by the discharge of protons on the Pt surface following the reaction: $Pt^* + H^+ + e^- = Pt - H_{UPD}$, where Pt* denotes a free site on the Pt surface. Nevertheless, recent studies highlight that the mechanisms at play in this potential region may be more complex, and involve the transfer of water molecules and hydroxide ions as well.[26–28] Finally, at more negative potentials,

H_2 is evolved in the HER region. Interestingly, one should note that two types of adsorbed hydrogen atoms exists on Pt, H_{UPD} and H*, but the latter is only formed at potential more negative than in the UPD region, and is the reaction intermediate for the HER.[29,30]

Three main features can be observed in the H_{UPD} region: one broad envelope, a couple of redox peaks at ~0.20 V vs. RHE followed by a third peak at ~0.10 V vs. RHE. While these phenomena were already described by comparing CVs recorded on single-crystal surfaces in the 60's and tentatively assigned to the hydrogen UPD on different facets of platinum,[31] this assignment was confirmed in the 80's owing to the development by Clavilier of new methods for preparing high-quality surface single crystals.[32] Hence, the large envelope is related to the H_{UPD} on Pt(111) facets, while the peaks at ~0.10 V vs. RHE and ~0.20 V vs. RHE are related to H_{UPD} on the Pt(110) and the Pt(100) sites, respectively. It should be noted that the UPD of hydrogen is not unique to platinum and is known to occur on other metallic surfaces.[33] Due to the ultra-fast kinetics of the HER on platinum electrodes, the Faradic current is often limited by the mass-transport of H_2 generated during the HER, even when a rotating-disk electrode (RDE) apparatus is employed.[34,35] This limitation hinders a proper fitting with microkinetics models[24] and has thus prevented the community from achieving a fine understanding of the HER mechanisms in acidic conditions. Despite this limitation, by measuring the HER and HOR currents in the micropolarization zone (small potential window across the RHE) at low temperature, Marković *et al.* were able to discriminate different activations energy for the HER on different Pt-single crystals facets, with activation energy ranging from 9.5 kJ mol^{-1} for the Pt(110) to 18 kJ mol^{-1} for the Pt(111).[34]

While the growth of high quality single crystals has been tremendous for the understanding of the HER on Pt, the development of computational methods has also brought a deeper understanding for the HER/HOR. For instance, combining molecular dynamics (MD) with density-functional theory (DFT), the HOR was predicted to follow a Heyrovsky-Volmer mechanism on Pt(111).[36] Furthermore, these calculations also confirmed the presence of two types of hydrogen atoms adsorbed on the Pt(111) surface. The first one is directly absorbed from the H_2 molecule on the bridge sites of the Pt slab and is found not to be reactive, thus its tentative assignment to the H_{UPD}. The second one, adsorbed on the top of the Pt(111) slab corresponds to a proton in solution being reductively adsorbed on the femtosecond time scale on the electrode surface. While theoretical insights help the understanding of the mechanism at a very short timescale, they must

be confronted to experimental results to assess their probity. Toward that goal, femto spectro-electrochemical techniques were recently used to correlate the activation energies measured by Marković *et al.*[34] with the rate of electron transfer along the Pt-H_{UPD} bond, showing that this transfer occurs at the femtosecond time scale.[37] Doing so, the interfacial solvent reorganization which is taking place at a greater timescale prior to any electron transfer was also shown to be critical for the H_{UPD} formation kinetics.[37]

While fundamental investigations on platinum model single-crystal electrodes started in the 80's with Clavilier pioneering work,[38] numerous other polycrystalline electrodes were historically investigated aiming to correlate kinetic parameters with physical properties of these different metals. Hence, inspired by the pioneering work from Conway and Bockris,[39] the exchange current densities for numerous *sp* metals and transition metals were measured by Trasatti.[40] From this investigation, a linear relationship between the exchange current density of the HER on metallic surfaces and their work-function was shown, which was ascribed to a different orientation of water molecules at the surface of the electrode depending on the nature of the metal. However, this classification does not provide insights on the intermediates for the HER. Thus, comparing the hydrogen binding energy (HBE) on the metal with the exchange current density, a typical Volcano shape was later found (**Figure I-7 a**), suggesting that the Sabatier principle can apply to the HER. Indeed, an ideal catalyst for the HER should bind hydrogen strongly enough to adsorb protons from the electrolyte (Volmer step). However, if the binding is too strong, it slows down the desorption of H* necessary to evolve H_2 (either through Heyrovsky or Tafel step), thus limiting the HER kinetics. Inspired by these experimental works, Nørskov *et al.* computed by DFT the free energy of formation (ΔG_{H*}) of the H* intermediate on several metal surfaces and obtained a similar Volcano shape (**Figure I-7 b**), confirming the HBE to be a good physical descriptor for the HER.[41]

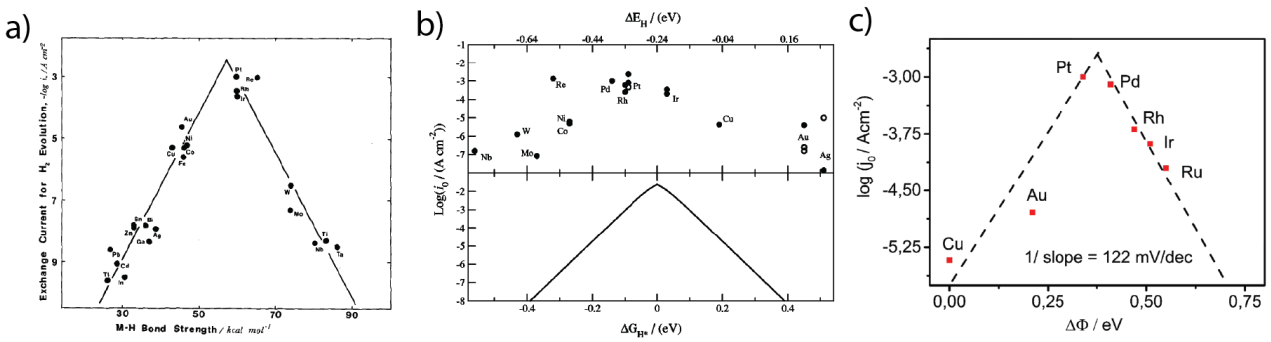

Figure I-7. Dependence on the exchange current density for the HER on the **a)** measured metal-hydrogen bond strength (reproduced from ref. 40), **b)** calculated metal hydrogen binding energy (reproduced from ref. 41) and **c)** difference of work-function measured between an hydrogenated and a wetted surface with no hydrogen (reproduced from ref. 42).

Nevertheless, as mentioned by Trasatti, one of the challenges pertaining to this approach is the reliability in measuring physical properties of pure metals, omitting the presence of the electrolyte and adsorbed species, alike in the work of Trasatti, or even of a passivation layer (e.g. Mo or W are covered by an oxide layer while platinum is covered by the H_{UPD}). In light of these limitations and thanks to recent advances in ultra-high vacuum (UHV) techniques, the work-function of realistic surfaces was recently reinvestigated by Zeradjanin *et al.* as a physical descriptor for the HER including the role of adsorbed water.[42] Considering that the free energy of activation ΔG^* for proton adsorption is a combination of 1) the work to transfer a proton from the Outer-Helmholtz plane (OHP) to the Inner-Helmholtz Plane (IHP), 2) the proton desolvation and the energy resulting from the difference of potential between the metal and the IHP and 3) the energy to transfer electrons from the metal (at its Fermi level) to the IHP, it was thus qualitatively predicted that the proton adsorption energy becomes more endergonic (weaker E(M-H)) when the electrode (with an interfacial water layer) work function is increased.[42] As a direct consequence, increasing the work function should decrease the rate constant of the electrochemical reaction usually described within the framework of the transition-state theory (TST) as: $k = \kappa_{el}\Gamma_n \upsilon_n e^{-(\frac{\Delta G^*}{RT})}$ where κ_{el} is the electronic transmission coefficient ($0 \leq \kappa_{el} \leq 1$) which traduces the tunneling-probability of the electron increasing with the electrode-reactant coupling, Γ_n is the nuclear tunneling factor ($\Gamma_n \geq 1$) which corrects the rate expression taking into account molecules/ions that react without entirely surmounting the classical electrochemical free energy barrier, υ_n is the nuclear frequency factor which represents the frequency at which the reacting species approach the transition state thanks to solvent and bond coordinates motions and ΔG^* is the

activation free energy.[42] However, as deduced from this expression, increasing the work function not only affects the activation free energy but also results in an increase of the pre-exponential constant (greater reactant-electrode coupling resulting in larger values of both κ_{el} and Γ_n), which is often omitted. Thus, a more precise Volcano plot is obtained when plotting the exchange current density versus the difference of work functions of hydrogenated and non-hydrogenated metals in the presence of an interfacial water layer (**Figure I-7 c**).

Interestingly, despite it presents some approximations, the HBE theory remains largely used by the catalysis community since it can easily guide for the discovery of new catalysts. For instance, it was used to explain the great performances of new cheap catalysts, such as MoS_2 for the HER,[43,44] and helped to clarify the nature of active sites which led to the design of new chalcogenide compounds enriched in active sites.[23]

Hence, the HER in acidic conditions is now relatively well understood. Nevertheless, when increasing the pH of the electrolyte from acidic to alkaline conditions, the HER and HOR performances of numerous catalysts were reported to dramatically decrease. This is prime of interest for industrial applications. Indeed, we should recall that since no cheap and earth-abundant OER catalyst operating in acidic conditions exist, technologies allowing operating the HER in alkaline conditions would be highly desirable (including anion exchange membrane water electrolyzers). Thus, understanding the physical parameters that slow down the HER kinetics in alkaline conditions may help to boost the efficiency of alkaline-based electrolyzer technologies. For instance, platinum is known to undergo a decrease from 2 to 3 orders in magnitude for the HER exchange current density from pH = 0 to pH = 13.[45,46] This pH effect thus renders the use of the HBE theory to find a simple activity descriptor based on a sole materials' property difficult.

The hydrogen binding energy descriptor and its limits

Inspired by the seminal work on the HBE,[40,41] Shen *et al.* recently correlated the HER activities of several monometallic surfaces in 0.1 M KOH solutions with computed HBE.[47] Similarly to the results obtained by Nørskov in acidic media,[41] they could exhibit that the HER activity of the selected metals follows a volcano trend in alkaline media, with Pt being the most efficient catalyst. Following this finding, the authors subsequently focused on the behavior of

Pt(pc)[48] and found a pH-dependence for the H_{UPD} potentials on (110) and (111) facets. Using the relation $\Delta H_{HBE} = -FE_{peak}$, where ΔH_{HBE} is the difference of HBE between two surfaces and E_{peak} the potential of the redox peak, the experimentally determined H_{HBE} were then compared with the HER overpotential at fixed current density. Doing so, a linear decrease of the HER activity with the experimentally determined HBE was found (**Figure I-8 a** and **b**). This methodology was then tentatively generalized for different carbon supported platinoid metals[49] and while a similar trend was found (decrease of the activity while the HBE increases in absolute value), the initial findings were tempered when observing that the HBE values evaluated by electrochemistry in alkaline electrolyte are far from those measured with UHV techniques for Pt(pc). This realization brought to the conclusion that the orientation of adsorbed water should be taken into account.[49]

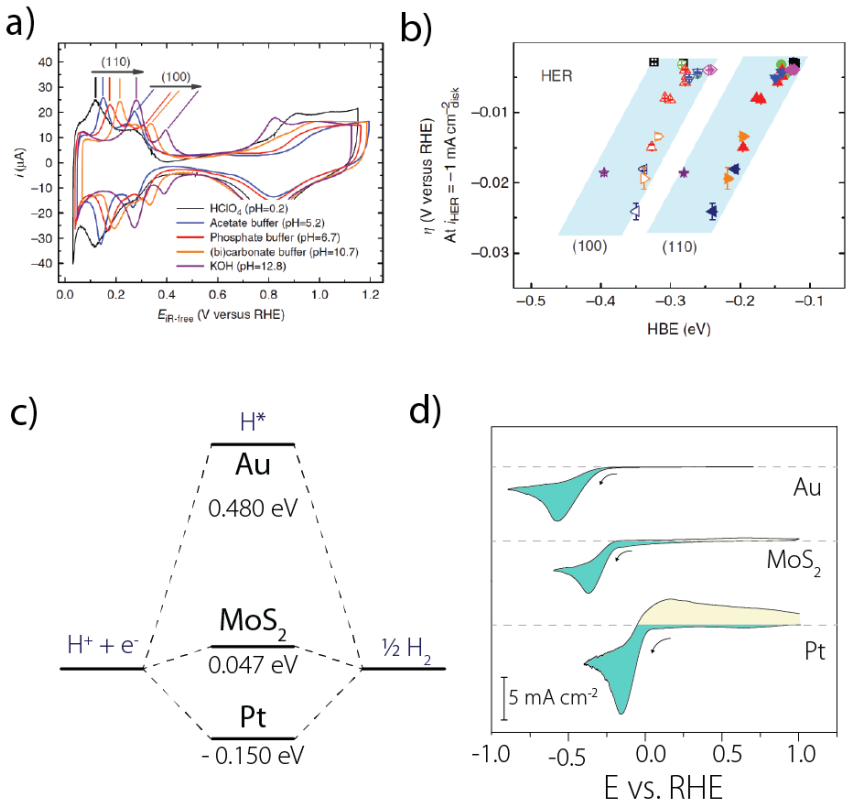

Figure I-8. a) CV recorded at different pH on a polycrystalline platinum electrode from which are extracted the hydrogen binding energy. **b)** Overpotential for the HER at -1 mA cm^{-2} on a polycrystalline platinum electrode in different buffered electrolyte, plotted versus the HBE obtained from electrochemical measurements (reproduced with permission from ref. 48). **c)** Calculated free energy diagram for the HER at pH = 0 and no overpotential for Pt, MoS_2 and Au surfaces (data are from ref. 44) and **d)** cyclic-voltammogram at pH = 2 (H_2SO_4 18 mM +K_2SO_4 82 mM) on Pt, amorphous MoS_2 and Au electrodes with a scan rate of 50 mV s^{-1} with oxidation currents in yellow and reduction current in blue, dashed lines indicating the $j_{=0}$ axis.

While attractive, some concerns have been recently raised about the HBE theory.[27] Indeed, as the H^+/H_2 couple is found to be reversible on Pt surface for instance,[34] all the HER elementary steps are reversible and the HOR intermediates are certainly identical.[45] Therefore, the HBE should control the HER and the HOR in a similar fashion. However, exploring other materials with relatively good HER performances and a small HBE value such as MoS_2[43,50] (**Figure I-8 c**), the observation is made that MoS_2 poorly catalyzes the HOR (**Figure I-8 d**). Hence, this absence of reversibility on a low-HBE material suggests that the energy and the nature of the intermediates for the HOR and HER reactions are not identical, thus preventing the use of HBE as a sole descriptor. Furthermore, as previously mentioned, the HBE measurement by either UHV or electrochemical measurements (H_{UPD}) involves hydrogen atoms that are likely to be different from those involved as reactive intermediates in the HER. One obvious manifestation of this difference is that while the H_{UPD} deposition potential on Pt(111) follows a Nernstian behavior with pH (60 mV per unit) and so the HBE determined from electrochemical measurements is not expected to change with pH, the HER activity drastically decreases by 2-3 orders of magnitude changing from pH = 0 to pH = 13 for the same surface.[46] Finally, the effect of buffer solution should also be investigated when performing measurements at intermediate pH values, as it can also alter the proton transfer kinetics.[51]

At this point, we have discussed how the identification of reaction intermediates on single-crystal model electrodes has triggered the quest for finding universal descriptors for the HER activity. While the HBE has emerged as a good candidate, this theory cannot totally predict how the electrode-electrolyte interfacial structure influences the performances of a given surface. Indeed, puzzled by the severe loss of activity of Pt when used in neutral or alkaline conditions, the electrocatalysis community recently investigated questions previously overlooked: what is the rate determining step for HER in alkaline conditions? What is the proton donor? What is the role of spectator species? How the catalyst surface is modified?

Interfacial interactions: how to rationalize them?

Unlike in acidic media, the Tafel slope measured for Pt electrodes in alkaline solutions is around 120 mV per decade, indicating that the Volmer or the Heyrovsky step is the rds.[24] Nevertheless, one of the main differences between alkaline and acidic HER is that the proton

concentration is drastically diminished, so that the Volmer and Heyrovsky steps are likely to include a water-dissociation step (*i.e.* the cleavage of an O—H bond) [46,52] as detailed below:

$$H_2O + e^- = H^* + OH^- \text{ (Volmer)} \quad \text{(I-7)}$$

$$H^* + H_2O + e^- = H_2 + OH^- \text{ (Heyrovksy)} \quad \text{(I-8)}$$

Moreover, observation was made that the HER kinetics over Pt(111) in alkaline conditions are drastically enhanced by the presence of oxophilic groups, such a Pt-islands (defects) and $Ni(OH)_2$ on the catalyst surface (**Figure I-9 a**),[46] which could be explained as originating from an easier H_2O dissociation. Following this observation, it was confirmed that the HER activity for Pt(111) decorated by different 3*d* transition metal hydroxides $M(OH)_2$ follows the Brønsted-Evans-Polanyi principle and the oxophilic groups affinity with OH_{ads} should be neither too strong (surface poisoning) nor too weak (no binding) to promote the HER kinetics.[53]

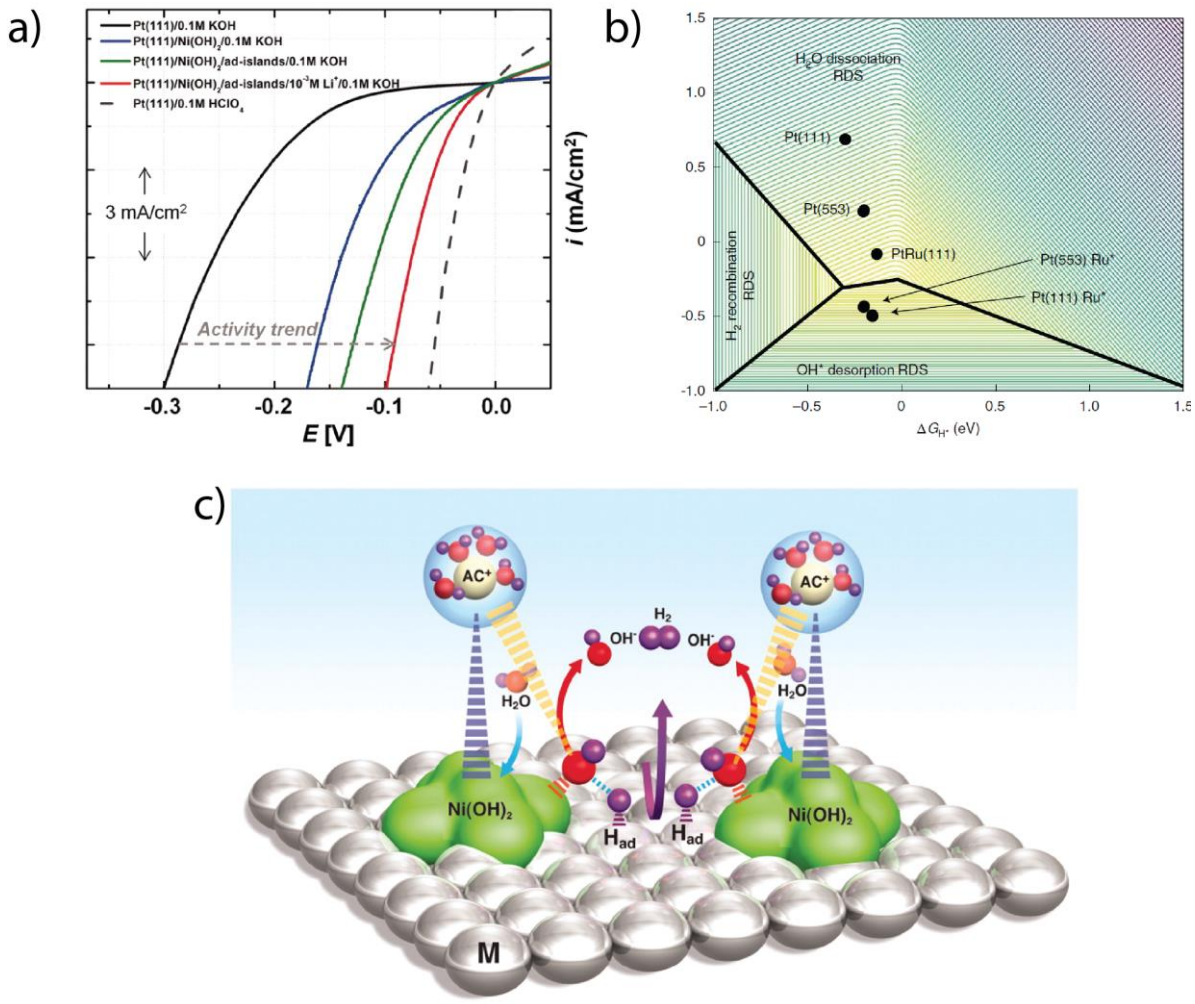

Figure I-9. a) HER activity in alkaline solutions measured on Pt(111) single crystal electrode, customized with different oxophilic groups. **b)** 3D Volcano plot showing the evolution of the exchange current density from low (blue) to large (yellow) values depending on the hydrogen and hydroxide binding energies (reproduced from ref. 54). **c)** Bi-functional mechanism responsible for the enhanced activity when groups that promote water dissociation are present on the Pt(111) surface (reproduced from ref. 46).

Thus, in alkaline electrolytes, the cleavage of water O—H bond and the transport of OH^- from the catalyst surface to the bulk of the electrolyte are likely to be part of the limiting step for this so-called bi-functional mechanism. Similar conclusion was recently made for copper electrodes for which a larger HER activity was measured with more oxophilic surface created by applying a mechanical or electrochemical surface treatment.[55] Overall, switching from H_3O^+ to H_2O as proton donor could simply hamper the Volmer step,[56–58] explaining the difference in activity between acidic and alkaline conditions. This assumption is well supported by the fact that the activation energy for water auto-ionization (around 75 kJ mol^{-1} at 300K[52,59]) is larger when compared to the one for HER in alkaline electrolytes (around 30-45 kJ mol^{-1} for Pt catalysts[45,52]),

as recently discussed using DFT calculations.[60] Alike for the HBE, recent studies however interrogate the importance of the surface oxophilicity and of the bi-functional mechanism on the HER kinetics.[49,61,62] Indeed, comparing the HER activity for Pt/C, PtNi/C and PtNi/C treated in acid to remove Ni from the surface of the nanoparticles revealed that while the presence of nickel increases the HER kinetics in alkaline media when compared to Pt/C,[61] removing it from the surface does not hinder the HER and HOR kinetics for PtNi/C. Thus, the role of the 3*d* metal was rather assigned to a modification of the HBE. Additionally, it was demonstrated that in unbuffered solutions, the two reduction events previously attributed to a different kinetics for the H_3O^+ and the H_2O reduction[56] may simply arise from the modification of the surface pH with the applied potential.[63] More recently, it was proposed that a "3D-Volcano plot" comparing the catalyst activity with the HBE and also the hydroxide binding energy could accurately reflects those limitations related to the water dissociation step for the alkaline HER (**Figure I-9 b**).[54] Even more revealing than the surface decoration of Pt with $M(OH)_2$, the addition of Li^+ cations in the electrolyte was found to be beneficial for the HER in the presence of surface oxophilic groups (**Figure I-9 a**).[46] This effect was initially rationalized by the Li^+ anchoring to the $M(OH)_2$ moieties promoting the water-dissociation through non-covalent interactions (**Figure I-9 c**).[46]

While most of the researches carried out recently have been focusing on the role of the cationic species at the solid/liquid interface, the seminal work conducted by Trasatti more than 50 years ago suggested than the water orientation at the interface could be responsible for the discrepancies in activity over different metallic surfaces.[40] Pitfalls exist for experimentally assessing such sensitive effects and the accuracy of theoretical calculations suffers as well from the high computational cost of including explicit solvent molecules.[64] However, while it was shown by UHV and DFT calculation than interfacial water does not drastically affect the H_{UPD} energetics,[65,66] it is expected to largely influence the alkali cations and hydroxides adsorption.[66] Therefore, investigating the water structure (orientation, chemical environment) and dynamics (lifetime in the IHP, structure reorganization along charge transfer) at the electrode-electrolyte interfaces will be key to unravel the mechanisms by which interfacial interactions impact the HER activity.

Interfacial reorganization: role of the solvent

Only few experimental characterizations of the water structure at the electrode-electrolyte interface during the HER have been carried out, the main reason being the ambivalent role of water as solvent and active molecule so that reactive water molecules are often masked by their environment. Consequently, indirect measurements such as laser-jump measurements[67] or *in-situ* spectroscopies[68] are so far used to gain insights on the water interfacial structure.

For instance, the use of laser-jump experiments revealed that the $Ni(OH)_2$ addition on Pt(111) lowers its potential of zero free charge (pzfc)[69–71] which eventually reduces the interfacial electric field at the HER operating potential, and soften the double-layer to facilitate the OH^- and H^+ transport.[69–71] Similarly, this can explain the sluggish activity of Pt(111) in alkaline electrolyte as its pzfc remains unchanged with the pH while the operating potential (referred vs. the SHE) for the HER is much more negative, which rigidifies the double-layer and hampers the charged reactants/products transport (**Figure I-10 a**).[69,72] Nevertheless, such explanation goes against the initial observations made by Trasatti[40,73] and more recently by Zeradjanin *et al*.[42] who noticed an increase of the HER activity with the catalyst work-function as well as found a positive linear correlation between the work-function value and the catalyst potential of zero charge (pzc), resulting in a poor activity for low pzc materials (**Figure I-10 b**).

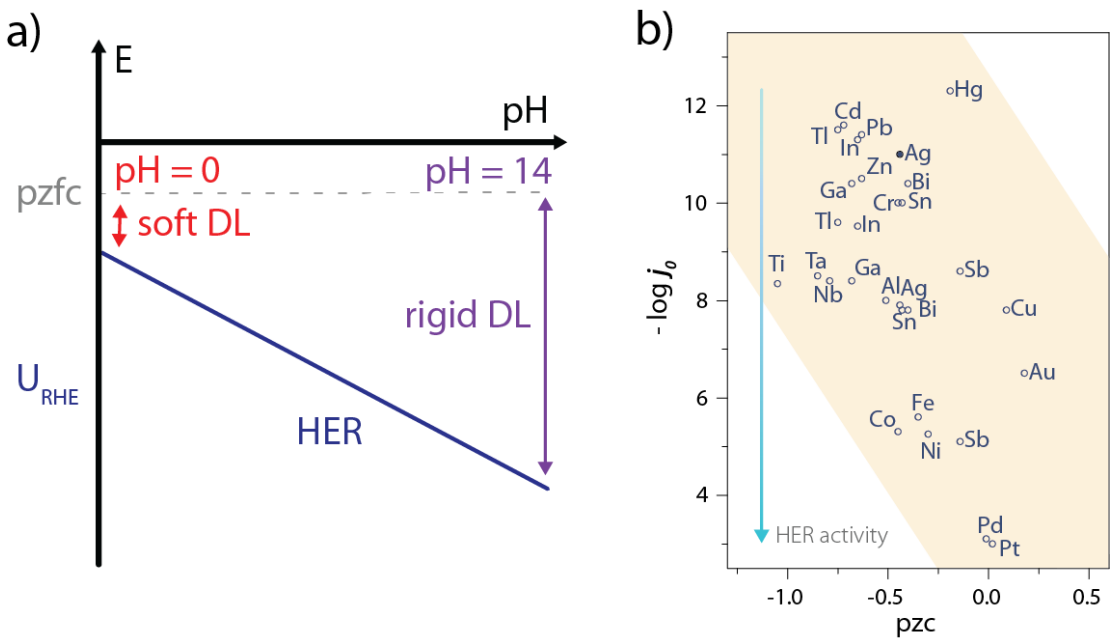

Figure I-10 a) Effect of the pH and pzfc on the double-layer rigidity during the HER. **b)** Plot of HER exchange current density in function of the potential of zero charge for several metallic electrodes (pzc are taken from ref. [73] and exchange current densities from [40])

While the pzfc model should properly work for surfaces having similar properties (*i.e.* similar active sites), a more precise picture of the influence of the pzc of a given surface on the proton-transfer kinetics must also consider eventual modifications of the pre-exponential factor of the kinetic constant which can reflect a modification of the proton/electron tunneling or the H^+ concentration at the interface, among numerous parameters.[42,72] Other models considering the double-layer ordering were thus developed to explain this pH-dependent activity. Hence, it was suggested that the activation energy for proton adsorption is mainly driven by a loss of entropy while protons are transferred from the bulk of the electrolyte to the OHP, loss which increases with the pH.[74] This entropy lost is compensated by the enthalpic term with a delay, so that the variation in the Gibbs free energy remains null, satisfying the equilibrium conditions.[74] Such a proposition relies on the assumption that the liquid water structure between the OHP and the electrode is not affected by pH variations,[74] which should be discussed in light of the study discussed above on the influence of interfacial water structure on the HER activity (pzfc theory).[69] Furthermore, it is worth highlighting some computational efforts attempting to explicitly model the electrode-electrolyte interface. For instance, seminal work on the water dissociation on a Pd surface by Filhol *et al.* proposed that at least three distinct water layers at the electrochemical interface are required for

the H_2O reductive (resp. oxidative) dissociation: a layer with protons (resp. hydroxide) donors, a layer to accept the generated hydroxide (resp. protons) by H-bonding and a layer to diffuse the as generated species in solution.[75] Moreover, thanks to recent advances in DFT calculations, a reduced charge of +0.7 e for protons located in the OHP at the Pt(111)-H_2O interface was found, which was explained by a charge transfer between the electrode and the interfacial solvent molecules. Interestingly, a bulk behavior (protons exhibiting a unit charge) was found for protons located in the third layer of water. These differences in charge highlights the importance of understanding the electrode-electrolyte interface at the molecular scale to precisely assess the charge transfer energetics. Finally, we should recall that all these models share the same assumption: water self-ionization is in a fast equilibrium and H_3O^+ should be considered as the reactant at every pH. However, since the H_2O self-ionization activation energy exceeds by a factor of ~2 the one measured for the HER on Pt,[60] the validity of this hypothesis has to be demonstrated.

Naively speaking, considering all the parameters reviewed above, the properties for an ideal HER catalyst should be to possess an active site that can bind H and OH neither too strongly, neither too weakly (HBE/OHBE theory). Regarding its pzc, it should be high enough to enhance the pre-exponential factor of the rate constant (more protons at the interface and more coupled to the electrode), but low enough to minimize the double-layer rigidity and facilitates charge transport through the double layer. A fine tuning of these properties could be achieved by a phase engineering of the electrode surface, bearing in mind that the electrolyte itself can play a major role, especially in alkaline media. Taking into account the surface properties, non-reactive species such as Lewis acids can help tuning the intermediates energies by for instance promoting the H_2O self-ionization and reduce the overall HER activation energy. Nevertheless, these effects have mostly been overlooked till recently, the reason being the relative lack of experimental and theoretical studies that could draw a molecular understanding of the catalyst-electrolyte structure.

As previously discussed, the nature of the double-layer has a tremendous influence on the faradic processes encountered at the electrode-electrolyte interface.[76,77] However, due to its narrow thickness (~30 nm in diluted aqueous electrolytes),[78] its precise characterization is challenging. In order to overtake this difficulty, new tools were recently developed to investigate the physical properties of the aqueous double layer. For instance, advanced *in-situ* spectroscopies such as ambient-pressure X-ray photoelectron spectroscopy (APXS),[78] surface X-ray scattering,[79] total

electron yield (TEY XAS)[68] or even Raman SHINERS[80] were used to better glimpse the water structure and environment at electrochemical interfaces. However, such advanced spectroscopies are most of the time coupled with *ab-initio* molecular simulations. Also, information on the dynamics of water molecules at the electrode-electrolyte interface could be glanced by classical MD simulations which is preferred to *ab-initio* methods since larger systems (thousands of molecules vs. few dozens for *ab-initio* simulations) can be studied.[81–83]

I.4 Conclusions of the chapter

The understanding of the physical parameters that governs the HER has been identified as a key to unlock more efficient electrical energy storage devices, such as aqueous LIBs and water electrolyzers. Historically, the role of the HBE on the surface of a given catalyst was proposed as a descriptor for the HER, and led to the discovery of new promising materials such as transition metal phosphides or sulfides. However, experimentally assessing the reaction enthalpy and entropy formation for H_{UPD} on Pt, let alone for the initial proton discharge Volmer step, remains challenging.[52] Furthermore, realization was recently made that the HBE theory may not be sufficient to explain the pH-dependence for the HER and the slow kinetics measured in alkaline aqueous electrolytes. Thus, since the introduction of a new "bi-functional" mechanism in which non-covalent interactions play a critical role on the HER kinetics, novel studies focusing on the effect of non-covalent interactions, adsorbed species, etc. on model electrodes were carried out. These studies as well as the emergence of high-resolution *operando* spectroscopies or laser-based techniques combined with theoretical/computational studies made possible an in-depth understanding of the water structure at the electrode-electrolyte interface, and demonstrated the influence of the double-layer structure and rigidity on surface adsorption properties. However, a direct correlation with water reactivity is yet to be reached.

In addition to these *operando* and theoretical studies, developing simple chemical strategies can be designed to gain deeper understandings at the molecular level could reveal useful. For that, decoupling all the different interactions at the interface (water-catalyst, water-water, ions-water and ions-catalyst) is critical. While challenging in aqueous solutions, the difficulty to decouple these interactions could be alleviated by studying the HER in "non-usual" conditions such as in aprotic solvents or confined structure, as we will discuss in the next chapter.

Chapter II - Confinement of water into an inert organic matrix to tune the water reactivity[b]

II.1 Motivations

As discussed in the introductive **Chapter I -**, the HER kinetics intimately depends from the nature of the electrolyte. Especially, the HER exhibits sluggish kinetics in alkaline electrolytes, which is susceptible to hamper the efficiency of anion exchange membrane water electrolyzers. Moreover, it is now well established that non-covalent interactions taking place in the double-layer may drastically alter the HER kinetics, similarly to what was described by Frumkin[84] who revealed that adsorbed spectator species may alter electrochemical reaction rates. Even if numerous models were proposed (such as: bifunctional mechanism, HBE, pzfc), our comprehension of how the non-bonding interactions in the electrolyte impacts the HER kinetics at the molecular scale remains in its infancy.

Especially, the following key points remains partly unanswered. First, the nature of the reactant for the HER in alkaline media is unclear. Indeed, while the Volmer step (reductive adsorption of an hydrogen atom on the surface) is well accepted as the rate determining step (on Pt at least), question remains as whether the water dissociation step is in a fast equilibrium[85] or if the water dissociation step is the rate determining step for the Volmer step.[46] Moreover, while it has been shown that alkaline cations may boost the HER kinetics in alkaline media thanks to non-bonding interactions, for instance by introducing Li^+ cations into the electrolyte, their role is not yet fully understood. Finally, theoretical studies have shown the importance of the hydrogen bond network in the vicinity of the electrode to transport HER reactant and products, but it could not be experimentally imaged.

Realizing the importance of water structuration at the electrochemical interface on the electrocatalytic activity of metals,[86] new strategies based on constraining H_2O molecules environment can be envisioned to tune and understand the HER kinetics independently on the

[b] This chapter is based on the two articles that I co-authored: **(1)** Dubouis, N.; Serva, A.; Salager, E.; Deschamps, M.; Salanne, M.; Grimaud, A. The Fate of Water at the Electrochemical Interfaces: Electrochemical Behavior of Free Water Versus Coordinating Water. *J. Phys. Chem. Lett.* **2018**, 9 (23), 6683–6688 and **(2)** Dubouis, N.; Serva, A.; Berthin, R.; Jeanmairet, G.; Porcheron, B.; Salager, E.; Salanne, M.; Grimaud, A. Tuning Water Reduction through Controlled Nanoconfinement within an Organic Liquid Matrix. *Nature Catalysis* **2020**, 3 (8), 656–663.

nature of the electrocatalyst. We decided to develop a strategy to constrain the environment of H_2O molecules by using non-reactive chemical matrices such as organic solvents or ionic liquids (ILs). Such chemical strategy was not widely explored and only few studies focused on the HER activity and the effect of the water structure in aprotic media such as ionic liquids (ILs) or organic electrolytes. However, doing so, different protons donors can be used and the concentration of ions and water modulated to constraint the water-electrolytes interactions.

Among the few studies carried out in ILs, most of them were focusing on the impact of moisture contamination on the cathodic stability of these ILs,[87–89] with the aim to generate H_2 through H_2O reduction with low-cost catalysts[90,91] or to construct a hydrogen-based reference electrode for ILs.[92] Interestingly, following this strategy, it was found that electrochemical interfaces are enriched in water upon polarization, following the hydrophilicity of the ions in solution (more water molecules at the positive electrode as ILs anions are more hydrophilic).[88] Furthermore, alike for aqueous electrolytes, the redox couple H^+/H_2 was found to be reversible on a Pt electrode in bis(trifluoromethanesulfonyl)amide (TFSI) based ILs.[92] However, in these conditions, the Volmer step was identified as the rate determining step which differs from the step usually found to be rate determining in acidic aqueous electrolytes.[92] Similarly, using H_2O as proton donor, the activity of non-precious low carbon steel electrodes was found to outweigh the one for Pt in BF4-based ILs.[91] Altogether, these observations confirm the strong dependence of the proton donor structure on the HER mechanism and activity and certainly open further experimental explorations.

In contrast with ILs, a deeper understanding on the HER mechanism was developed in organic electrolytes. From a practical point of view, the influence of traces of water in organic electrolytes for LIBs electrochemistry has been a subject of interest since their commercialization in the 90s', its presence being detrimental for the stability of the electrode materials and of the electrolytes and degrades the cycling performances of the system owing to its influence on the formation and the nature of the solid electrolyte interphase (SEI).[93–99] It has also been employed as an additive for new chemistry intercalation batteries based on divalent cations.[100]

More importantly, the hydrogen electrocatalysis has also been studied in aprotic electrolytes. Pioneering works in the 70's already suggested that tuning the proton environment in

acetonitrile/water mixtures could drastically impacts its electrochemical reactivity.[101] More recently, works from Ledezma-Yanez and Koper revealed that the HOR on Pt and Au is tremendously impacted by the water environment in similar solvent mixtures.[102,103] Also, it was highlighted that even in absence of "protons" (*i.e.* acids), water molecules can themselves be reduced on Pt in water-acetonitrile mixtures with a reduction potential depending on the nature of the supporting salt.[104] Inspired by these seminal studies, we decided to establish a clear methodology that would allow us to modify the proton/water environment molecules. To do so, we decided to use acetonitrile (ACN) as a solvent, since it was previously demonstrated to be stable upon cathodic polarization and mixes well with water and supporting salts.[102–104] Then, we can vary the nature of the proton source (strong acid or water) and focus on the water reduction itself. As shown in **Figure II-1**, this strategy allows us to study separately the water-water and water cations interactions and reveal useful to understand how non-bonding interactions may influence the HER kinetics.

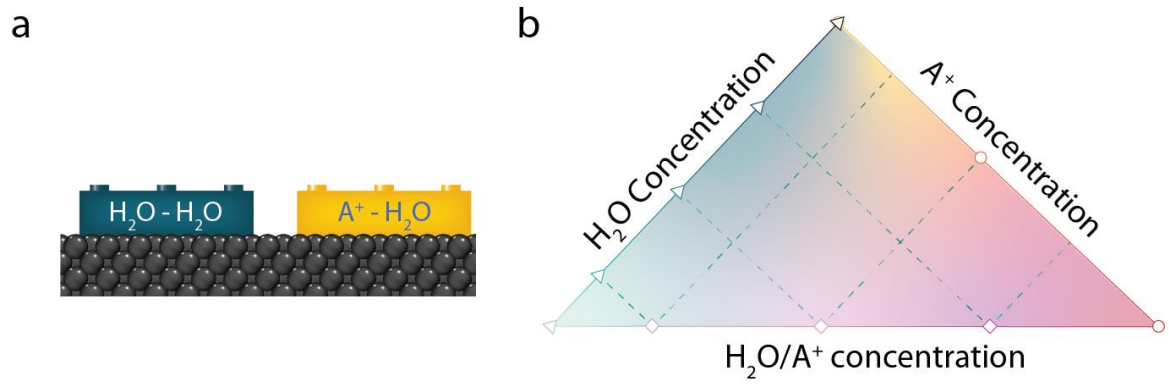

Figure II-1. Chemical strategy to select long- and short-range interactions. a) Building blocks representing the interactions between water-water (blue) or cation-water (yellow) molecules that are studied and b) visual representation of the 3 series of systems that can be studied by playing on the water or supporting salt concentration.

II.2 Influence of the proton source: H_2O vs. $HClO_4$

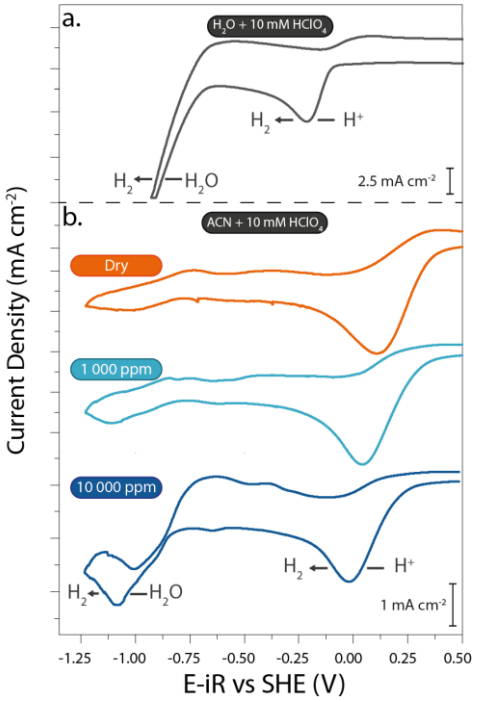

Figure II-2. Cyclic voltammograms recorded at 50 mV s^{-1} on a polycrystalline platinum electrode in electrolytes containing 10 mM $HClO_4$ and 90 mM $LiClO_4$ **a)** in water (black) and **b)** in acetonitrile based electrolytes with different water concentrations (dry = orange, 1 000 ppm = light blue, 10 000 ppm of water added = dark blue). Potentials were measured vs. an organic Ag^+/Ag electrode (see material and methods), are compensated for the ohmic drop (E-iR) and reported versus the Standard Hydrogen Electrode (SHE).

As mentioned earlier in this manuscript, the origin of the large decrease for the HER kinetics onto Pt observed when the electrolytes changes from acidic to alkaline is a puzzling question for the electrocatalysis community. This can be evidenced by the presence of two reduction events (a peak at "high" potentials and a wave at lower potentials) when cyclic voltammograms are measured in mild acidic electrolytes on a Pt electrode (**Figure II-2 a**). As the potential is decreased, protons are slowly consumed (reduction peak) and the interfacial pH goes alkaline, which finally leads to a reduction wave at highly negative overpotential. To further explore the existence of two reduction mechanisms (H^+ in acidic electrolytes and H_2O in alkaline electrolytes), we decided to investigate the reactivity of a "strong acid" ($HClO_4$) in ACN electrolytes (**Figure II-2 b**). In dry ACN with 10 mM $HClO_4$, a first peak is observed at around 0 V vs. SHE, similarly to what is measured in water with 10 mM $HClO_4$ (**Figure II-2 a**). This first peak therefore involves the reduction of protons from $HClO_4$ (pKa ~ 1.5 in acetonitrile[102]). By

slowly adding H_2O into ACN, a second reduction event is seen starting at a more negative potential at around -0.75 V vs. SHE. This second event, that occurs at a similar potential than what is measured in water-based electrolyte, is associated with the reduction of water molecules and is characterized by a greater overpotential as a result of the energy penalty required to break O—H bonds from water.[50,105] These two mechanisms are therefore ubiquitous and coexist in aqueous electrolytes for pH > 2,[50,105] as well as in organic electrolytes as shown **Figure II-2**, with the difference that a peak which intensity depends on the amount of H_2O is visible in organic electrolytes due to the limited concentration of water when compared to aqueous solution and/or the precipitation of a passivation layer, as discussed later in this chapter.

II.4 Free water vs. coordinating water

We then investigated the effect of cation hydrophilicity on the reduction of water in acetonitrile in the presence of 10 000 ppm (~ 400 mM) of water (**Figure II-3**). The experiments were done varying the nature of the cation for the supporting salt. Indeed, three cations that are expected to have very different interactions with water molecules, as suggested with their very different enthalpies of hydration (**Figure II-3 a**), were employed. Interestingly, three different electrochemical behaviors can be distinguished. While almost no cathodic current was observed with tetrabutylammonium (TBA^+) cations (orange), a large cathodic current was measured with Li^+ (purple) and Na^+ (green) cations (**Figure II-3 b**). Comparing these results with dry electrolytes for which no cathodic current is measured (Supplementary Figure II-1) and with the result obtained in aqueous electrolyte where a reduction event is measured in a similar potential range (< -0.75 V vs. SHE) (**Figure II-2 a**), this cathodic current can be attributed to water reduction: $H_2O + e^- = ½ H_2 + OH^-$. Second, the shape for the reduction current was found dependent on the cation. Hence, a reduction wave is observed for Na^+ while a reduction peak is seen for Li^+ cations. This difference is explained by the formation of a passivation layer (the so-called SEI). This passivation layer could result from the reaction of Li^+ with OH^- formed upon water reduction and the subsequent precipitation of LiOH ($Li^+ + H_2O + e^- = ½ H_2 + LiOH_{(s)}$), as previously observed in similar systems,[94,106,107] or from the possible reactivity of the organic solvent with OH^-. In both case, NaOH or any other Na-based product formed upon reduction is too soluble to passivate the electrode surface owing to the weaker affinity (weaker Lewis acidity) of Na^+ cations with OH^- anions or other anions than Li^+ cations.[106,108]

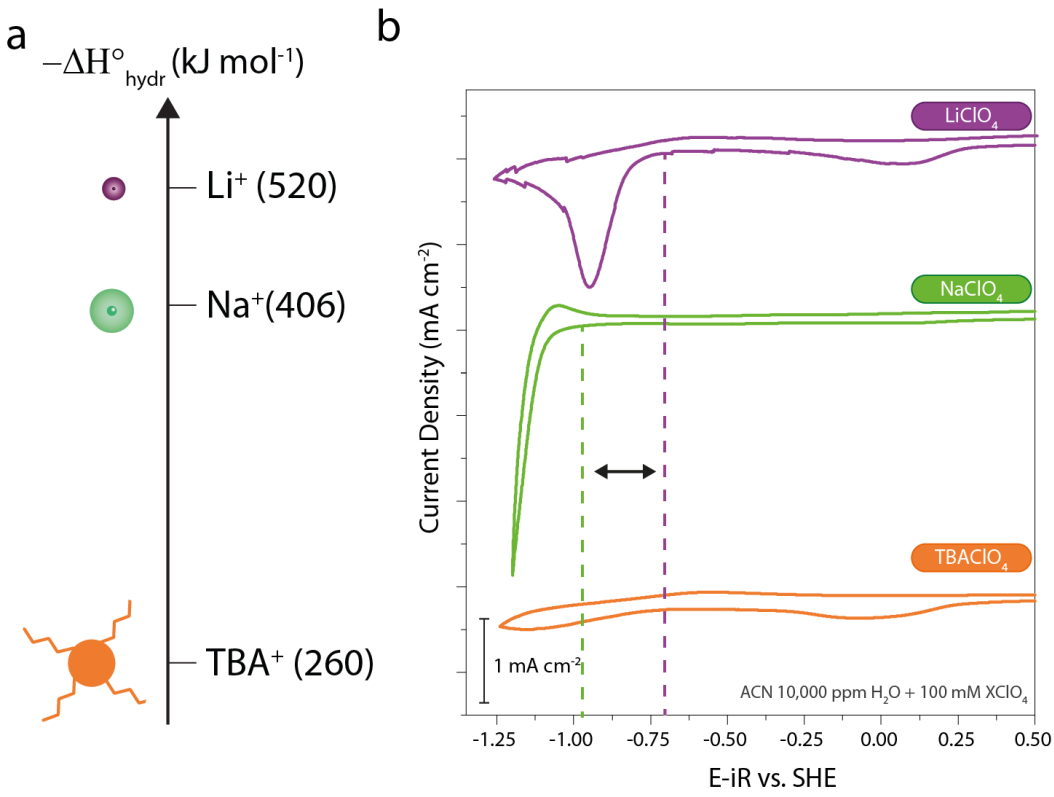

Figure II-3. a) Absolute enthalpies of hydration of gaseous cations for Li^+, Na^+ (data from ref. 109) and TBA^+ (data from ref. 110) and **b)** cyclic voltammograms recorded over a platinum electrode in acetonitrile electrolytes containing 10 000 ppm of water, in presence of $LiClO_4$ (purple), $NaClO_4$ (green), or $TBAClO_4$ (orange). Potentials were measured vs. a Ag^+/Ag electrode (see material and methods), are compensated for the ohmic drop (E-iR) and reported versus the Standard Hydrogen Electrode (SHE).

Intrigued by this difference of reactivity for water upon reductive conditions, the solvation structure for water molecules was analyzed for the different supporting salts by classical MD simulations. Indeed, because the solutions studied herein are very dilute, first principle calculations cannot be used. After selecting the proper force-fields, as detailed in the material and methods section, 100 ns trajectories were generated for each solution. To shed light on the cations first solvation shell, the radial distribution functions (RDFs) between the cations and the oxygen atom of water molecules were then calculated (**Figure II-4 a**). Li^+ and Na^+ cations have a stable first solvation shell (very sharp first peak in the RDFs), while only a broad low intensity peak at long distances is observed for the TBA^+ cation. In particular, the Li-O_{water} and Na-O_{water} first shell distances obtained in this work are 2.06 Å and 2.38 Å, respectively, consistent with those previously reported in the literature for aqueous solutions.[111–113] A good agreement was also found for Cation-N_{ACN} as shown in **Supplementary Figure II-2**, further validating the choice of the force

fields.[112,114] The number of water molecules in the first solvation shell of the cation is rather large (about 2.7) for Li^+, it slightly decreases for Na^+ and finally goes almost to zero for TBA^+ cation, which shows the possibility of accommodating a larger number of organic solvent molecules in its solvation shell (see **Figure II-4 b**). The direct consequence of this finding is that the percentage of "free" water molecules (*i.e.* water molecules that are not in the first solvation shell of a cation) rapidly increases moving from Li^+ to Na^+ and finally to TBA^+ cation, as shown in **Figure II-4 c**. The different complexing ability of the three cations with water thus reveals a different hydrophilic character following $Li^+ > Na^+ > TBA^+$. The marked passage from hydrophilic Li^+ cation to hydrophobic TBA^+ cation is also confirmed by the evaluation of the cation-water cage lifetime (**Figure II-4 d** and **Supplementary Figure II-3**), that indeed is one order of magnitude larger for Li^+ and Na^+ than for TBA^+, suggesting a reduced (almost zero) cation-H_2O affinity for the TBA^+ cation.

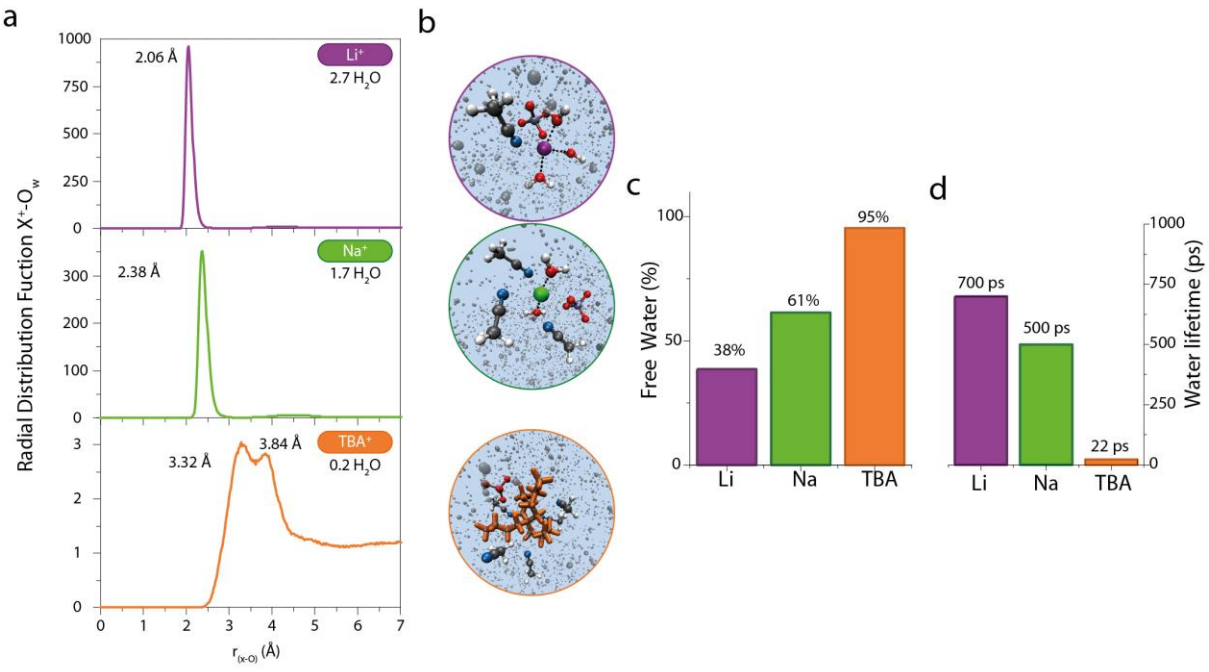

Figure II-4. a) Cation-O_{water} radial distribution functions. **b)** Snapshots of corresponding MD simulations illustrating the cation first solvation shell. **c)** Percentage of free water (left) and **d)** water molecules lifetime (ps) in the cation first solvation shell (right)

To experimentally assess these different interactions of water with the aforementioned cations, ^1H nuclear magnetic spectroscopy (NMR) was employed (**Figure II-5**). The ^1H signal from H_2O is found for TBA^+ (2.95 ppm) to not drastically differ from the one of water in

acetonitrile without any added salt (3.0 ppm). In contrast, it is found at higher chemical shifts (downfield) for Na^+ (3.1 ppm), and this shift is even greater for Li^+ (3.7 ppm). Since a downfield signal (higher chemical shift) traduces a weaker electronic density around protons, this observation corroborates a stronger Li^+-H_2O interaction than Na^+-H_2O. Instead, almost no interaction is observed between the hydrophobic TBA^+ cation and H_2O molecules. This experimental observation for the increased cation-H_2O affinity (or hydrophilicity) following $Li^+ > Na^+ > TBA^+$ is in agreement with the predictions made by MD simulations (**Figure II-4** c). As a result, this spectroscopic study demonstrates that the lower electronic density observed around protons for solvated Li^+ cations is due to the strong Lewis acidity of Li^+ cations, which also suggests a greater Brønsted acidity for these protons due to electron withdrawing from the water molecule.

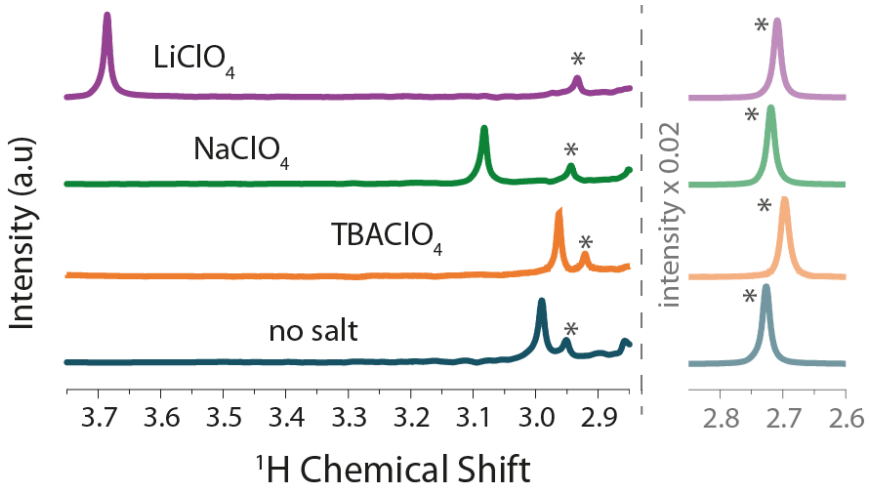

Figure II-5. NMR spectra of acetonitrile based electrolytes containing 100 mM of supporting perchlorate salt ($LiClO_4$ = purple, $NaClO_4$ = green, $TBAClO_4$ = orange) or no supporting salt (dark blue) and 10 000 ppm of water. The main peak is attributed to protons from H_2O while the peaks (and satellites arising from ^{13}C-^1H coupling) corresponding to acetonitrile labeled *.

Having demonstrated the different hydrophilicity for the cations considered in this work, its impact on the water reduction reaction can then be rationalized. As the electrode is negatively polarized, cations are migrating with their solvation shells toward the negative electrode. In the presence of TBA^+ cations, the resulting double-layer is hydrophobic (as shown by the short lifetime of water molecules in its first solvation shell, **Figure II-4 d),** and water cannot access the surface of the electrode even though the concentration of free water is found greater than for Li^+ and Na^+ cations. This explains the absence of cathodic current associated with the reduction of water for TBA^+ (**Figure II-3**). On the contrary, hydrophilic lithium and to lesser extent sodium cations

migrate to the electrochemical interface together with their solvation shell comprised of water molecules, allowing water to be reduced. Furthermore, not only the nature of the cation dictates the presence of water at the electrochemical interface, but the cation affinity for water also modifies the onset potential for water reduction. Hence, the considerable difference in the onset potential for H_2O reduction measured for Li^+ and Na^+ cations (~ 250 mV) in **Figure II-3** cannot be solely explained by the difference of water content or lifetime of water molecules in the cations solvation shell. Indeed, such a potential shift would result, applying the Nernst equation, in an interfacial concentration of water 4 orders of magnitude greater for lithium than for sodium, while MD simulations demonstrate that the ratio of water in the solvation shell of Li^+ and Na^+ cations is closer to 1.6:1 and the lifetime of water molecules in the solvation shell is not drastically modified (**Figure II-4 c, d**). Thus, this difference in onset potential can originate from kinetics limitations. As the initial Volmer step ($H_2O + e^- = H_{ads} + OH^-$) is expected to be the rate determining step for water reduction in these experimental conditions,[18,21,26] the electrochemical activity is going to be driven by its activation energy that, according to the linear free energy relationship approximation, must vary linearly with the difference of energy between the products states and the reactants states of this step.[8] The greater electronic withdrawing interaction between Li^+ cations and oxygen atom from H_2O could thus be partly responsible for a weakening of the O—H bond of water molecules (destabilization of the reactants state), in agreement with the ^1H NMR results that show more acidic protons (**Figure II-5**) and with previous experimental observations.[116] This is coherent with a recent *ab-initio* MD simulation study of aqueous solutions of alkali metal salts under applied electric field[117] which showed that the water dissociation threshold field is lowered in LiCl and NaCl with respect to bulk water (with an effect slightly more marked in the case of the lithium salt), but not in the less acidic KCl. This effect would thus facilitate water reduction by lowering the transition state energy as a result of an easier proton adsorption and a stronger association of Li^+ with OH^- produced during the HER (stabilization of the products state).

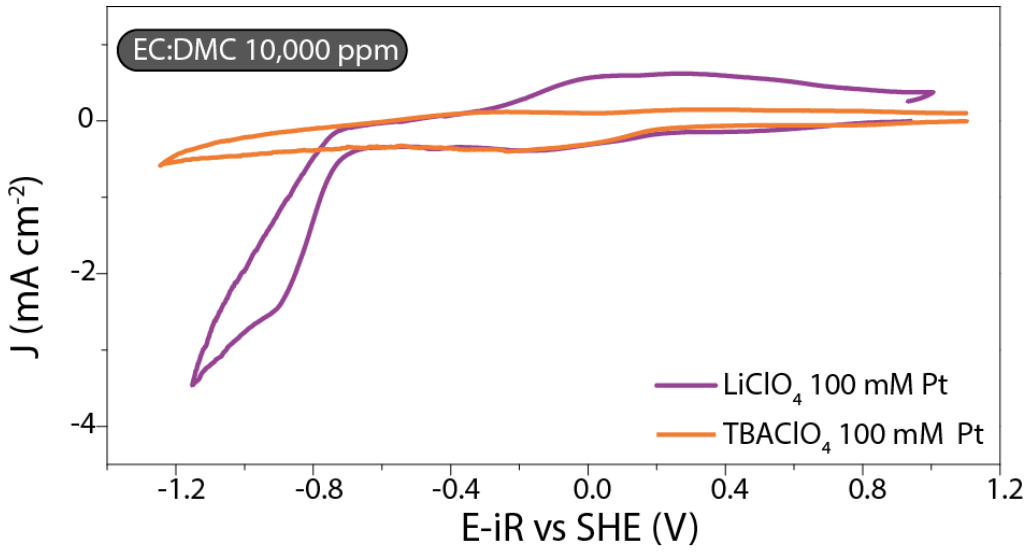

Figure II-6. Cyclic voltammograms recorded at 50 mV s^{-1} on a platinum electrode in ethylene carbonate : dimethyl carbonate (1:1 in mass) electrolytes containing 10 000 ppm of water and 100 mM of $LiClO_4$ (purple) or $TBAClO_4$ (orange).

Finally, we could show that the nature of the organic solvent on the double-layer formation and water reduction is weak. For that, ACN was replaced by a solvent with a greater dielectric constant, namely ethylene carbonate (EC) dissolved into dimethyl carbonate (DMC), and similar electrochemical observations were made with the presence of a reduction event starting at around -0.75 V vs. SHE with Li^+ while no reduction is observed with TBA^+ (**Figure II-6**).This result confirms that organic solvent molecules play a minor role under negative polarization at the electrochemical interface when compared to the role played by cations. In other words, the concentration of water is always greater at the negative electrochemical interface in presence of hydrophilic cations than in the bulk of the electrolyte independently of the polarizability of the solvent.

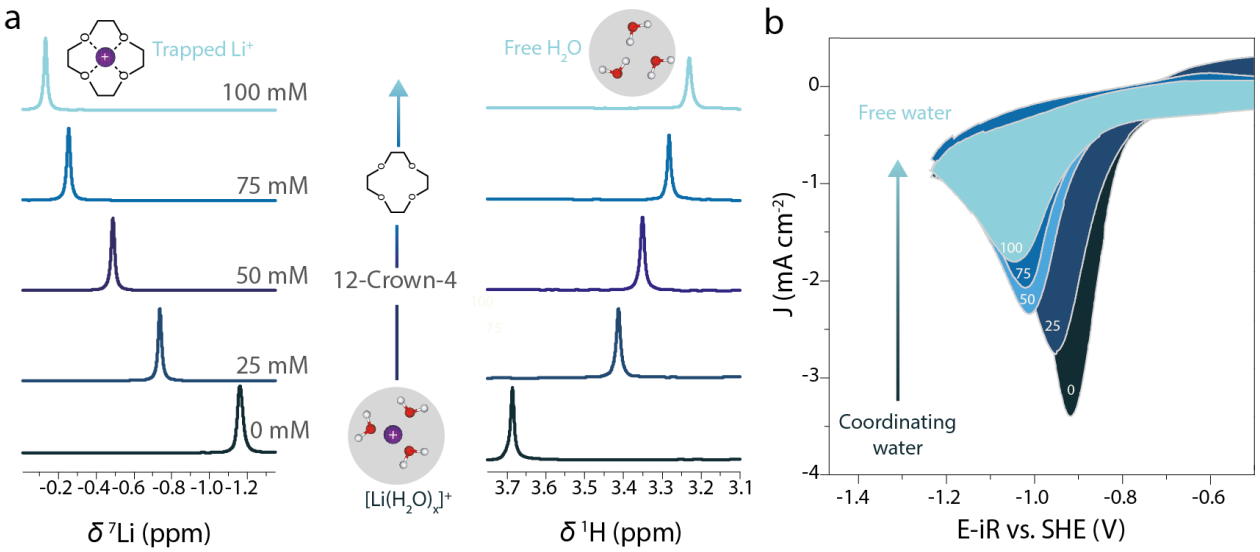

Figure II-7. Influence of the 12-Crown-4 concentration in 100 mM $LiClO_4$ in acetonitrile containing 10 000 ppm of water electrolytes on **a)** Li^+ (left) and H_2O (right) NMR chemical shifts and **b)** water reduction electrochemistry.

Having established that the use of hydrophilic cations such as Li^+ enables an easy reduction of water at the electrochemical interface under negative polarization, we then investigated the reactivity of "free" water molecules in organic solvent independently of the use of hydrophobic cation. For that, crown ether (12-Crown-4) was used as an additive to selectively "trap" Li^+ cations and therefore release water molecules from their solvation shell, thus making them "free". We first validated this strategy by studying the water solvation using ^7Li and ^1H NMR (**Figure II-7 a**). As the crown ether/Li^+ ratio increases closer to 1, the chemical shift for ^7Li was found to be downfield (higher chemical shift), indicating a change of the Li^+ solvation shell and its association with the crown ether molecules.[118] The opposite trend was found for the ^1H signal from H_2O for which the chemical shift undertakes an upfield, demonstrating a greater electronic density. From these observations, it can be concluded that "free" water molecules are released when adding 12-Crown-4 to the electrolyte, following the reaction: $[Li(H_2O)_x]^+ + Crown = [Li(Crown)_1]^+ + x\ H_2O_{"free"}$. The electrochemical behavior of these solutions was then studied, and a shift to more negative potentials as well as a decrease of the cathodic current were found with increasing 12-Crown-4 concentration (**Figure II-7 b**). Hence, we can conclude that "free" water molecules are more difficult to reduce than "coordinating" water molecules in organic media, as seen by the more negative potential required for their reduction. This finding is in agreement with the results discussed above for which water molecules strongly coordinating hydrophilic Lewis acid such as

Li^+ cations were found to be reduced at lower onset potentials. Furthermore, we can tentatively assign the decrease of the reduction peak intensity to a reduced concentration of "free" water molecules at the electrochemical interface when compared to $[Li(H_2O)_x]^+$.

II.5 Water as a solvent: H-bonds vs. water-cations interactions

Among the different interactions playing a role on the water reactivity, our attention first focused on the short-range A^+-H_2O and we could demonstrate that cations with a greater Lewis acidity may help the water-dissociation step. However, we restricted our study to a case at which water molecules are not interacting together because they were diluted. As water is not only the active molecule in aqueous electrolytes, but also the solvent, it would be prime of interest to understand its role as a solvent, *i.e.* to study the effect of water-water interactions. Looking back at our strategy highlighted **Figure II-1**, we decided to prepare electrolytes with water concentration ranging from 1% (~ 440 mM *i.e.* 4.4 molecules of water per cation) to 10% (~ 4.40 M *i.e.* 44 molecules of water per cation) in mass (the exact values for the compositions of these electrolytes are given in the **Methods Table II-1** and **Methods Table II-2)**. We first monitored the evolution of the ^1H chemical shift from H_2O molecules in these electrolytes as a function of the water concentration (**Figure II-8**). For electrolytes using TBA^+ and Na^+ cations, a monotonous increase of the proton chemical shift with the water concentration is measured. Monitoring that the shift of the peak related to the CH_3 group in ACN is almost unaffected, we can discard changes coming from a drastic modification of the electrolytes magnetic susceptibility as the origin for this shift (**Supplementary Figure II-4**). Thus, this downfield shift toward values closer of a bulk H_2O environment reflects a greater acidity for protons that matches well with their increased reactivity. In contrast, in the presence of $LiClO_4$, a "V-shaped" curve characterizes the evolution of the ^1H chemical shift for protons in water with its concentration (**Figure II-8**). Surprising at the first glance, such a behavior may originate from the existence of different water populations with an exchange rate high enough to observe the coalescence of their respective NMR signals.[119] This existence of different H_2O populations in the presence of Li^+ cations would confirm a stronger A^+-H_2O interaction in the latter case, consistently with what was observed previously in this chapter (**Figure II-4**).

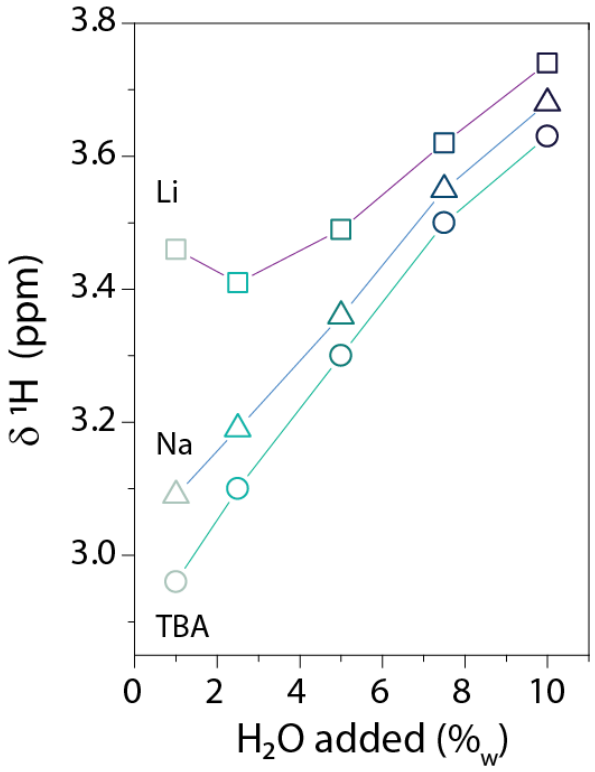

Figure II-8. Evolution of the ^{1}H chemical shift of the water molecules in acetonitrile electrolytes containing 100 mM of $LiClO_4$ (squares), $NaClO_4$ (triangles) or $TBAClO_4$ (circles) as a function of the water content. The lines are a guide for the eyes.

Having experimentally established that the water environment is drastically modified when the water concentration is tenfold increased, we investigated its electrochemical reactivity onto a platinum electrode embarked on a rotating disk electrode (RDE) setup. When using $TBAClO_4$ as a supporting electrolyte, no water reduction is measured at low water concentration (**Figure II-9 a**), which can be explained by the formation of a TBA^+-rich electrical double-layer (EDL). Indeed, since the water molecules hardly enter the solvation shell of TBA^+ cations, their presence in the EDL under negative polarization prevents water to access the interface and therefore to be reduced.[102–104,120] Nevertheless, by increasing the concentration of water in the organic electrolytes, water reduction slowly takes off with its onset potential shifting toward less negative values at higher water contents. Unlike for $TBAClO_4$, when using $LiClO_4$ as supporting salt, water reduction is measured even at a water concentration as low as 1% (**Figure II-9 b**). More surprising, the onset potential is not altered by the water concentration. Indeed, increasing the water concentration only gradually transforms the reduction event from a peak which arises from the passivation of the

electrode due to the precipitation of LiOH at low water content (as mentioned in the first part of this chapter), to a classical exponential event as expected for the catalytically activated HER. The absence of the electrode passivation at greater water content can be rationalized by the highest solubility of the LiOH, potentially formed after the Volmer step, in water than in pure acetonitrile. Finally, when the cation is changed to sodium (Na^+), the reduction of water is observed even at low water concentration, but at more negative potential than with Li^+ cations (**Figure II-9 c**). Furthermore, alike for TBA^+ cations, the increase of the water content in the electrolyte shifts the onset potential for H_2O reduction toward less negative potentials. While this shift observed for Na^+ and TBA^+ suggests that H_2O-H_2O interactions that presumably increase at greater water concentration are likely to influence the HER within these electrolytes, the different behaviors measured in the presence of these three different cations confirms a competing effect between H_2O-H_2O and A^+-H_2O interactions. Finally, it is noteworthy that changing the anion from ClO_4^- to $TFSI^-$ is not altering the aforementioned experimental trends (**Supplementary Figure II-5**), confirming that in these conditions the effect of water-water and water-cations interactions prevail on the reactivity of water.

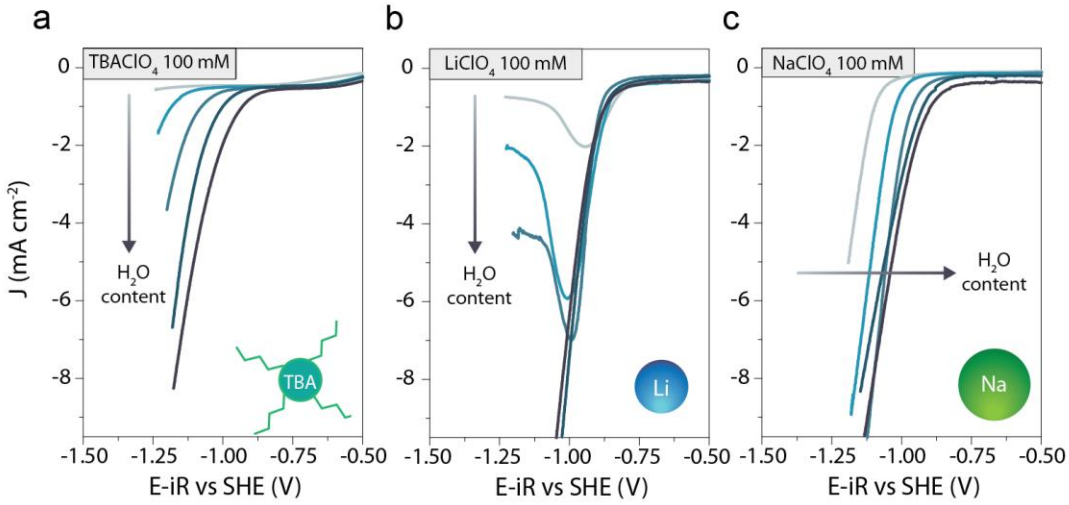

Figure II-9. Linear sweep voltammograms recorded in acetonitrile in the presence of **a)** 100 mM of $TBAClO_4$ **b)** 100 mM of $LiClO_4$ and **c)** 100 mM of $NaClO_4$ with different water contents (1, 2.5, 5, 7.5 and 10% in mass from light to dark blue, the exact values are given in the **Methods Table II-1** and **Methods Table II-2**) on a rotating disk (1 600 rpm) Pt electrode with a 50 mV s^{-1} sweeping rate. Potentials were measured vs. an organic Ag^+/Ag electrode (see methods), are compensated for the ohmic drop (E-iR) and reported versus the Standard Hydrogen Electrode (SHE).

Nevertheless, while NMR reveals a drastic influence of the water concentration on the protons environment, it fails to explain why an increase of the chemical shift for the Li^+ electrolytes does not lead to more facile water reduction, while the contrary is observed for TBA^+ and Na^+. Thus, additional understanding on the molecular environment of water molecules in these different systems was gleaned performing classical MD simulations for bulk electrolytes. To no surprise, for the $TBAClO_4$ electrolytes, the water environment is found drastically different at 1%, where isolated H_2O molecules exist, from the one observed at 10% where the formation of nanodomains of clustered water molecules can be found, as illustrated on the snapshots in **Figure II-10 a**. Furthermore, the coordination numbers, which is obtained by integrating the radial distribution function, between TBA^+ cations and water molecules (**Figure II-10 b**) at short distances only weakly depends on water concentration, confirming the absence of favorable interactions between H_2O and TBA^+ cations (as illustrated by the broadness of the first peak in the radial distribution functions, **Supplementary Figure II-6**). The rise of the coordination number between the water molecules (**Figure II-10 b**) with the water concentration pinpoints an increase of H-bond interactions between the water molecules at high water concentration. This increasing amount of interactions is confirmed by the growth of a peak at low-q in the computed O_{water}-O_{water} structure factor (**Figure II-10 c**), indicative of a long-range organization for water molecules and the formation of water clusters that results from the increase of H-bonds between water molecules. Thus, the average environment of the water molecules becomes more similar to a bulk water environment, which explains the downfield in the NMR ^1H chemical shift (**Figure II-8**). Here again, the more facile water reduction measured when nanodomains start to be formed provides the first experimental observation for previous *ab-initio* MD results. Indeed, early studies highlighted the need for a favorable H-bonding environment for the transfer of both the proton[121] and the hydroxide[122] ions. As a consequence, when autoprotolysis reaction occurs, the transfer of protons along a hydrogen bond "wire" allows the two ionic products to be separated by three or more neighbors. If this wire remains unbroken, the ions recombine rapidly.[123] A similar picture arise from a static DFT study of the palladium-water interface.[75] Here we can draw an analogy and propose that larger clusters facilitate the separation of the product of the Volmer step in the $TBAClO_4$ electrolyte.

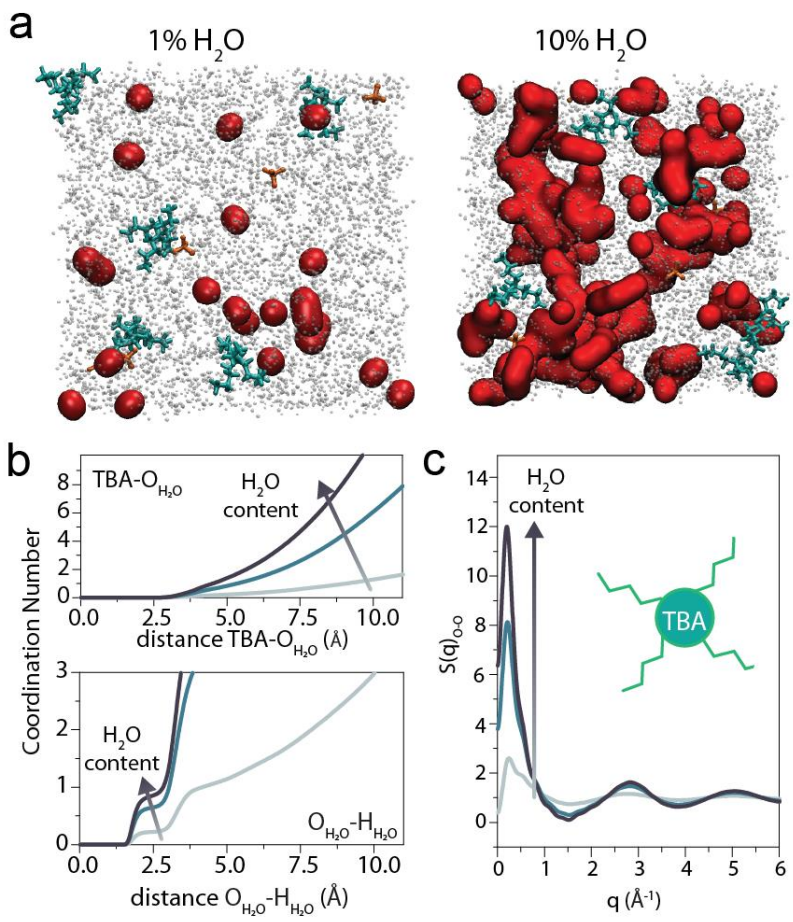

Figure II-10. a) MD snapshots for the systems containing 1% and 10% of water in mass in the presence of 100 mM $TBAClO_4$ in acetonitrile. Water molecules are represented in red, TBA^+ cations in green, ClO_4^- anions in orange and acetonitrile solvent with grey points. **b)** Coordination numbers for TBA^+-H_2O and H_2O-H_2O and c) structure factor for the oxygen atom of H_2O molecules at different water concentrations (1% in grey, 5% in blue, 10% in dark blue).

Puzzled by the different experimental trends observed for the $LiClO_4$ containing electrolytes, we also analyzed the water environment with MD simulations for the Li^+-containing systems. At low water concentration (1% in mass ~ 400 mM), water molecules are found to preferentially coordinate the Li^+ cations (**Figure II-11 a**), consistent with our previous observations. Unlike for TBA^+ cations that are hydrophobic, water is found to replace acetonitrile and perchlorate anions (**Supplementary Figure II-7**) in the first solvation shell of Li^+ cations (**Figure II-11 b**). This is further confirmed by observing a downfield shift of the ^7Li chemical shift in these electrolytes to values close to those observed in aqueous electrolytes (**Supplementary Figure II-8**). Thus, at intermediate water contents, water is either coordinating Li^+ cations (unshielded environment) or free in the electrolyte (shielded environment) (**Figure II-8**). Alike for

$TBAClO_4$, at higher water content, water clusters are forming in the electrolyte (**Figure II-11 a**) with the increase of the coordination between water molecules (**Figure II-11 b**) being responsible for this aggregation. Thus, the increase of H_2O-H_2O interactions explains the downfield observed in the NMR spectra at higher water content (**Figure II-8**).

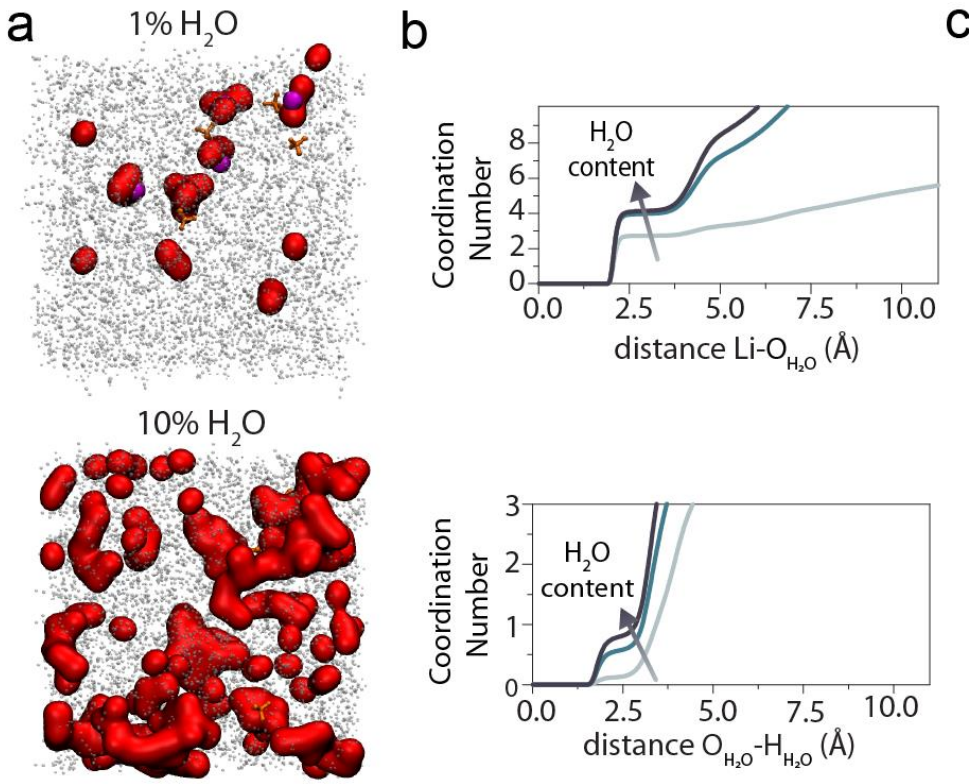

Figure II-11. a) MD snapshots for the systems containing 1% and 10% of water in mass in the presence of 100 mM $LiClO_4$ in acetonitrile. Water molecules are represented in red, Li^+ cations in blue, ClO_4^- anions in orange and acetonitrile solvent with grey points**. b)** Coordination numbers for Li^+-H_2O and H_2O-H_2O.

The MD simulations of the bulk of the electrolyte also reveal that the energy required to extract one water molecule from the Li^+ cation solvation shell (~200 meV) is greater when compared to the energy required to separate two water molecules (~80 meV) (**Figure II-12**), and that the strength of these weak H_2O-H_2O interactions is weakly affected by the water content. Hence, it confirms that the short-range H_2O-H_2O interactions are much weaker than Li^+-H_2O interactions, independently of the H_2O content in the electrolyte, finally providing the explanation for our initial observations (**Figure II-9 b**).

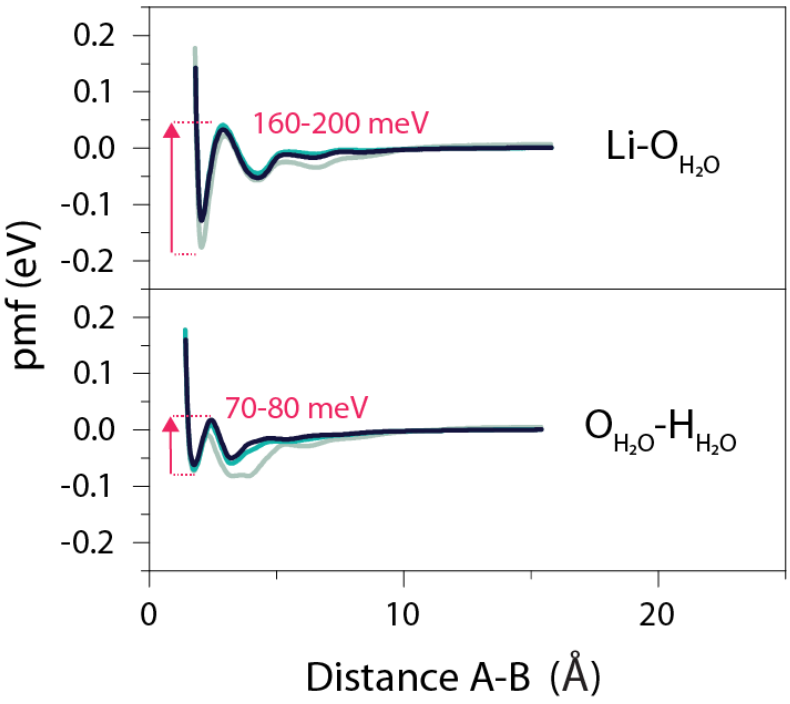

Figure II-12. Potential of mean force between Li^+ cations and O_{water} (top) and between O_{water} and H_{water} (bottom) derived from the g(r) functions. $\boldsymbol{pmf(r) = -k_B T \ln g(r)}$, where $\boldsymbol{k_B}$ is the Boltzmann constant and $\boldsymbol{T}$ the temperature (300 K) for different water contents (1% in light blue, 5% in blue and 10% in dark blue). Since the largest values are obtained for Li-O_{water}, independently on the water content, this indicates that it is more difficult to separate one Li^+ cation from a water molecule than a water molecule from another one.

In order to confirm that the different water environments isolated in the bulk of the organic electrolyte are maintained at the electrode interface, simulations were carried out applying constant voltages (of both 1.0 and 2.0 V) between two planar carbon electrodes to investigate the water structure within the EDL.[c] As shown in **Figure II-13 a**, the width of the EDL is of approximately 20 Angstroms and the electric field shows important fluctuations due to the formation of several well-structured layers of acetonitrile. Interestingly, despite this strong electric field, the water organization is found to be similar at the negative electrode as in the bulk of the electrolyte, independently on the applied potential. Hence, water molecules are found to coordinate Li^+ cations in both systems (**Figure II-13 b** and **c**), and some clusters of non-coordinating water are present in the water-rich electrode, surrounding the Li^+-$(H_2O)_x$ adducts. This undoubtedly establishes that the

[c] The simulations with a constant voltage applied were realized and analyzed in collaboration with M. Salanne, A. Serva, R. Berthin and G. Jeanmairet (PHENIX, Sorbonne Université Paris)

intensity of the short-range Li^+-H_2O prevails on H_2O-H_2O interactions and dictates the water reactivity at the interface.

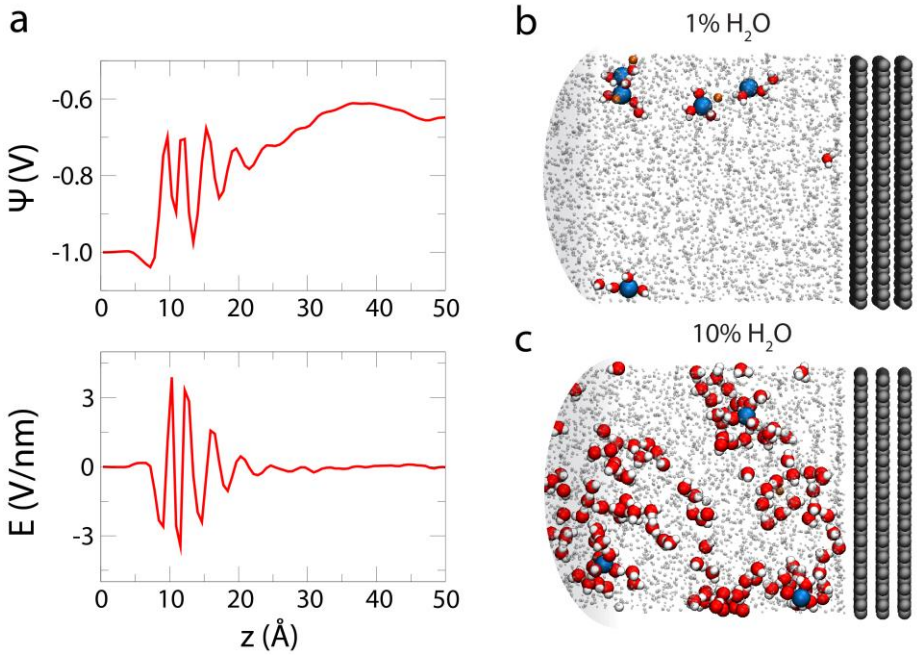

Figure II-13. a) Poisson potential and electric field in the vicinity of the negative electrode (which has a fixed potential of -1 V) for the system containing 10% of H2O and 100 mM LiClO4 and an applied potential of 2.0 V. MD snapshots of the double-layer structure at the negative electrode for **b)** 1 % or **c)** 10% of water in mass.

Finally, the case of the sodium electrolyte can be rationalized from these two extreme cases. Indeed, the solvation structure for the Na^+ cations are similar to the one of Li^+ in the most hydrated electrolyte, except that one water molecule is replaced by an acetonitrile molecule in the first solvation shell, as shown in **Figure II-14**. This weaker interactions between water molecules and Na^+ cations when compared to Li^+ cations is further assessed by comparing the potential of mean force (pmf) between the cations and a water molecule. Indeed, the activation energy to separate a sodium ion from a water molecule (which is the amplitude between the first minimum and the first maximum of the pmf) is found slightly lower than for Li^+ (130 mV for Na^+ vs. 162 for Li^+). Overall, because the Na^+-H_2O interaction is weaker than the Li^+-H_2O one, when water is added to the electrolyte H_2O-H_2O interactions become predominant and an electrochemical effect can be measured. Overall, this study suggests that while in presence of strong Lewis acids the short-range water-water interactions are negligible, they become predominant when no strong Lewis acid is present in the medium.

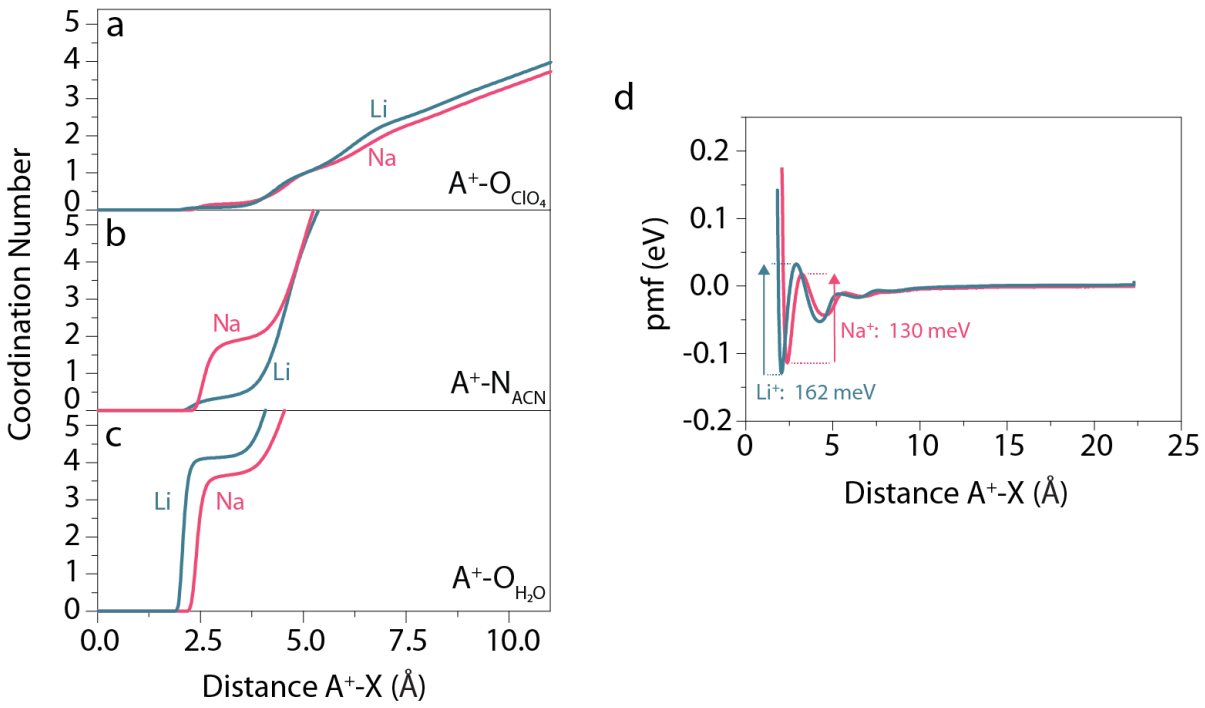

Figure II-14. Coordination number between Li^+ cation (blue) or Na^+ cations (pink) and **a)** oxygen atoms from ClO_4^- anions, **b)** nitrogen atoms from acetonitrile molecules (middle) and **c)** oxygen atoms from water molecules (bottom) in the presence of 100 mM of $AClO_4$ in acetonitrile containing 10% of water in mass. **d)** Potential of mean force between Li^+ or Na^+ cations and O_{water} (derived from the g(r) functions ($\boldsymbol{pmf(r) = -k_B T \ln g(r)}$, where $\boldsymbol{k_B}$ is the Boltzmann constant and $\boldsymbol{T}$ the temperature (300K)) in acetonitrile containing 10% of water in mass and 100 mM of $LiClO_4$ or $NaClO_4$ salt.

II.6 Nanostructuration of water at electrochemical interfaces

We managed so far to tune the nature of the cation-water interaction, and to study how increasing the H_2O-H_2O interactions is affecting the water reactivity. Nevertheless, while some long-range organization of water was found for the electrolytes with the highest water content, a direct correlation with water reduction could be drawn for the TBA^+ and the Na^+-based electrolytes only showing the importance of H-bonds between water molecules. Hence, we then extended our study for Li^+-based electrolytes by forming larger aqueous-rich domains to increase the long-range interactions within the electrolyte. We have previously demonstrated that Li^+ cations preferentially interact with water molecules. Thus, increasing the Li^+ concentration at fixed H_2O concentration (**Figure II-1**) can eventually lead to the formation of water/Li-rich nanodomains. While such nanodomains were already reported for water into acetonitrile at large H_2O content,[124–127] their formation is triggered (and enhanced) here by the addition of a salt at large concentration,[128] confirming our intuition.

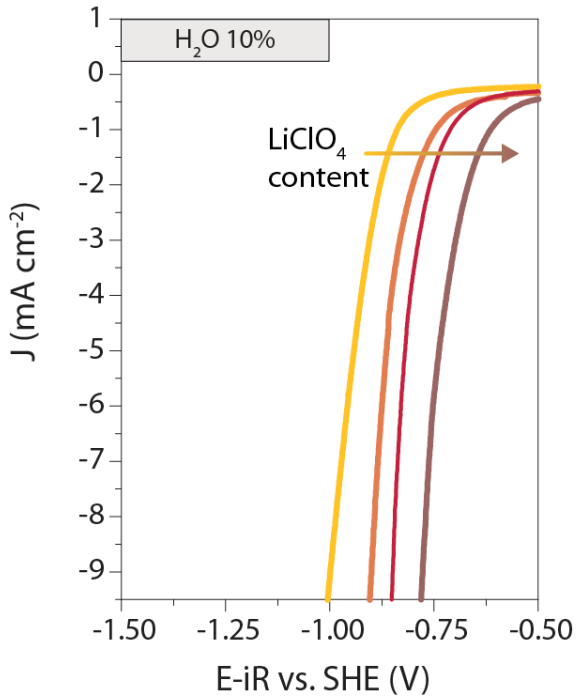

Figure II-15. Linear sweep voltammograms recorded in acetonitrile with 10% in mass of added H_2O in the presence of 100 mM (yellow), 500 mM (orange), 1 M (red), or 2 M (brown) $LiClO_4$ on a rotating disk (1 600 rpm) Pt electrode with a 50 mV s^{-1} sweeping rate. Potentials were measured vs. an organic Ag^+/Ag electrode (see material and methods), are compensated for the ohmic drop (E-iR) and reported versus the Standard Hydrogen Electrode (SHE).

The concentration of $LiClO_4$ was thus gradually increased from ~100 mM to ~2 M in the 10% H_2O in mass electrolytes (see **Methods Table II-3** for the exact values). Interestingly, as the $LiClO_4$ concentration increases, the onset potential for water reduction is shifted toward less negative values (**Figure II-15**). To better grasp the molecular origin for this enhanced reactivity, the electrolyte structure was thus analyzed with MD simulations. Doing so, we found that, at short-range, Li-H_2O interactions are gradually replaced by ion-pairing. Indeed, the increase of the $LiClO_4$ concentration results in an increased amplitude of the first plateau of the Li-O(ClO_4^-) coordination number, which suggests more ion-pairing, accompanied by a small increase of the acetonitrile in the first solvation shell of Li^+ cations and a small decrease of the water content in the first solvation shell (**Figure II-16 a**, **b** and **c**). These results are confirmed by the typical "bell-shape" curve obtained for the conductivity of these electrolytes (**Figure II-16 d**) as well as by the decrease of the ^{7}Li chemical shift (**Figure II-16 e**).

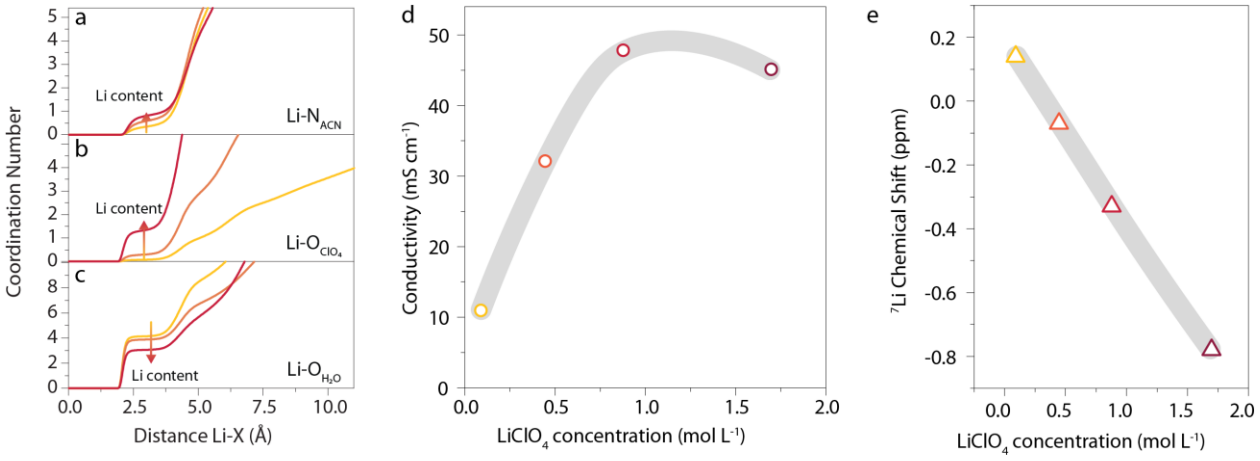

Figure II-16. Coordination number between Li^+ cations and **a)** nitrogen atoms from acetonitrile molecules, **b)** oxygen atoms from ClO_4^- anions and **c)** oxygen atoms from water molecules (bottom) in acetonitrile containing 10% of water in mass at different H_2O/Li ratio (44 yellow, 8.8 orange, 4.4 red). **d)** Conductivity of acetonitrile electrolytes with 10% in mass of added H_2O and in the presence of 100 mM (yellow), 500 mM (orange), 1 M (red), or 2 M (brown) $LiClO_4$. **e)** Evolution of the ^{7}Li chemical shift with the $LiClO_4$ concentration in these electrolytes.

However, the formation of water-rich domains at the nanoscale may result either in a fluctuation of the species concentration or in the microsegregation between these heterogeneities. The latter can be experimentally accessed by small-angle X-ray scattering (SAXS) at the low-q values which reflects changes in the structure factor.[127,129] Indeed, increase of the SAXS intensity at low-q values is observed with the $LiClO_4$ concentration (**Figure II-17 a**), which reveals the growth of nanodomains. This observation is corroborated by the increase of the X-ray-weighted structure factor calculated from the MD simulations at the low-q values (**Figure II-17 b**) that arises from the formation of oxygen-rich domains (*i.e.* rich in H_2O molecules and ClO_4^- anions), as shown when the structure factor analysis is restricted to oxygen atoms (**Figure II-17 c**).

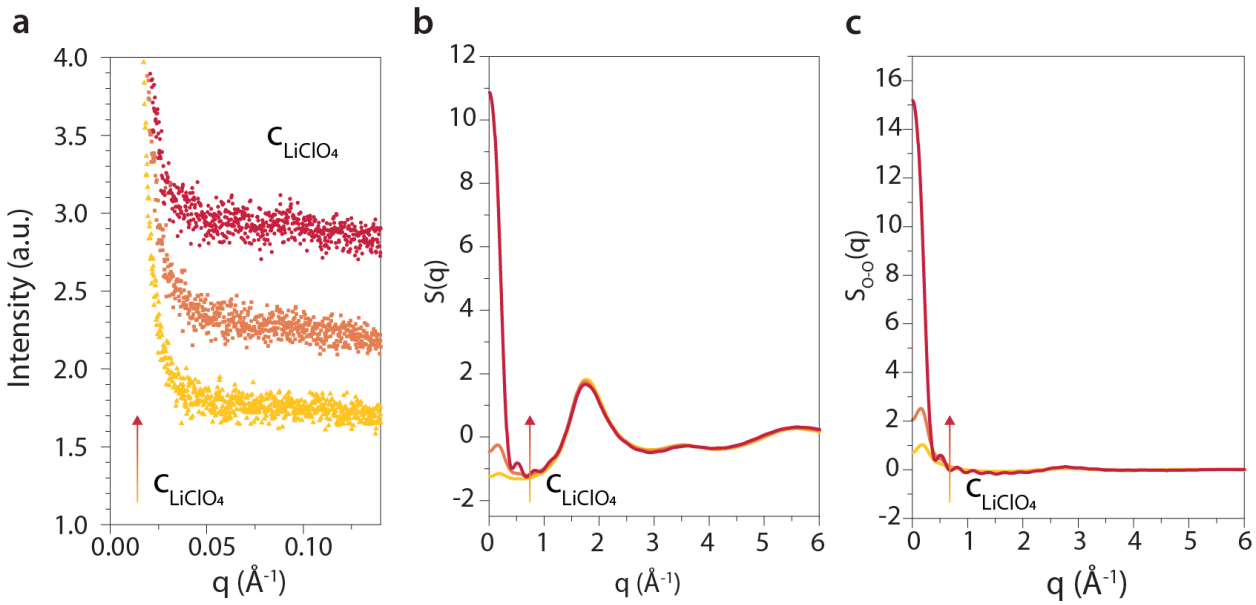

Figure II-17. a) Total X-ray-weighted structure factor of the electrolytes containing 10% H_2O, 100 mM (yellow), 500 mM (orange), 1 M (red) $LiClO_4$ as computed from the MD simulations. **b)** Small-angle X-ray scattering intensity experimentally measured for these electrolytes. **c)** X-Ray weighted contributions from the oxygen-oxygen pairs to the global X-ray-weighted structure factor as computed from the MD simulations.

Hence, these results suggest that increasing the $LiClO_4$ concentration enhances the size of the formed aqueous-rich nanodomains in the organic electrolyte. This conclusion is visually illustrated by MD snapshots of the electrolytes containing either 100 mM or 1 M of $LiClO_4$ and 10% in mass of H_2O, where larger aqueous domains are observed in the 1 M electrolyte (**Figure II-18 a** and **b**).

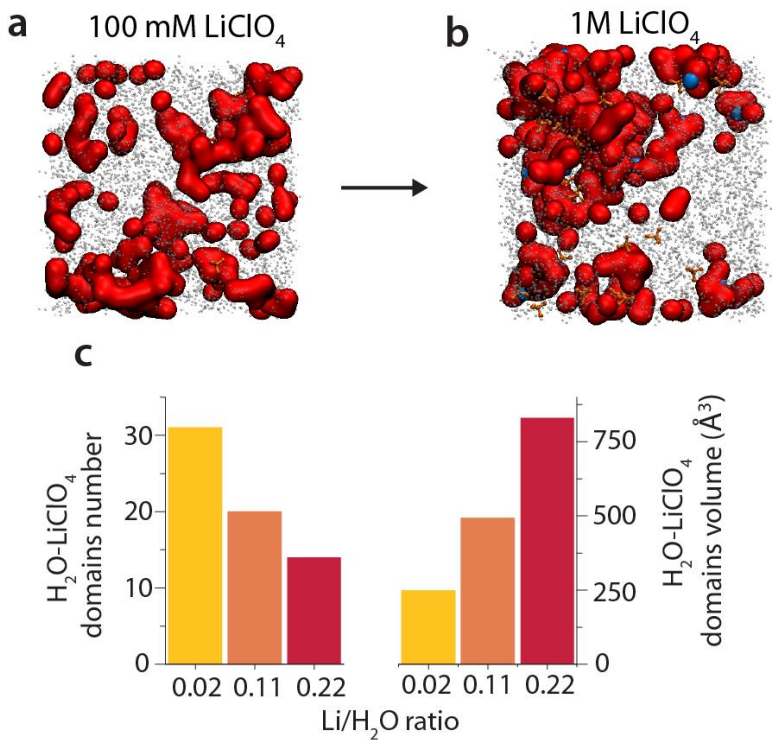

Figure II-18. MD snapshots of the **a)** diluted (100 mM $LiClO_4$ and 10% H_2O) and **b)** concentrated electrolyte (1 M $LiClO_4$ and 10% H_2O). **c)** Number of $LiClO_4$-H_2O domains and their average volume depending on the $LiClO_4/H_2O$ ratio at 10% in mass of water calculated from a domain analysis performed on the trajectories obtained from the classical MD simulations.

Furthermore, this interpretation is reinforced by observing that while activation energies for the Li^+ and H_2O diffusion measured by diffusion-NMR spectroscopy[d] (**Table II-1** and corresponding diffusion coefficients and Arrhenius fittings are reported in **Supplementary Figure II-9**) differ at low concentration ($E_{a,D_{Li^+}} = 42$ kJ. mol^{-1}and $E_{a,D_{H_2O}} = 31\ k$J. mol^{-1} at 100 mM $LiClO_4$), they become closer to each other when the $LiClO_4$ concentration is increased to 1 M ($E_{a,D_{Li^+}} = 32$ kJ. mol^{-1} and $E_{a,D_{H_2O}} = 28$ kJ. mol^{-1}). As a result, we can assume that the diffusion of both Li^+ and H_2O becomes correlated with the formation of these H_2O-$LiClO_4$ rich nanodomains in the electrolyte. Moreover, at greater $LiClO_4$ concentrations, a second population of Li^+ that exhibit lower diffusion coefficient is found, which is consistent with the ion-pairing observed in highly concentrated $LiClO_4$ electrolytes.

[d] The measurements and interpretation of the diffusion NMR experiments was realized by Elodie Salager and Benjamin Porcheron, in CEMHTI laboratory (Univerité d'Orléans).

Sample	10% H_2O 1 M $LiClO_4$	10% H_2O 100 mM $LiClO_4$
$E_a(\mathbf{H}_2O)$ (kJ.mol^{-1})	28±3	31±5
$E_a(C\mathbf{H}_3CN)$ (kJ.mol^{-1})	23±3	30±7
E_a(Li, fast) (kJ.mol^{-1})	32±6	42±4
E_a (Li, slow) (kJ.mol^{-1})	92±2	

Table II-1. Activation energies measured by pulse-field gradient NMR. Uncertainties were evaluated by fitting the data for all possible permutations of 4 temperatures out of 5.

More quantitative information is obtained by performing a domain analysis[130]: when $LiClO_4$ concentration is increased from 100 mM to ~1 M (at fixed water concentration), the number of H_2O-$LiClO_4$ domains follows a two-fold decrease while their average volume increases by a factor of 4 (**Figure II-18 c**). Interestingly, even at the electrified interfaces where strong electric fields are present, these large water-rich domains are conserved and migrate to the negative electrode forming aqueous-rich "channels" between the interface and the bulk (**Figure II-19**).

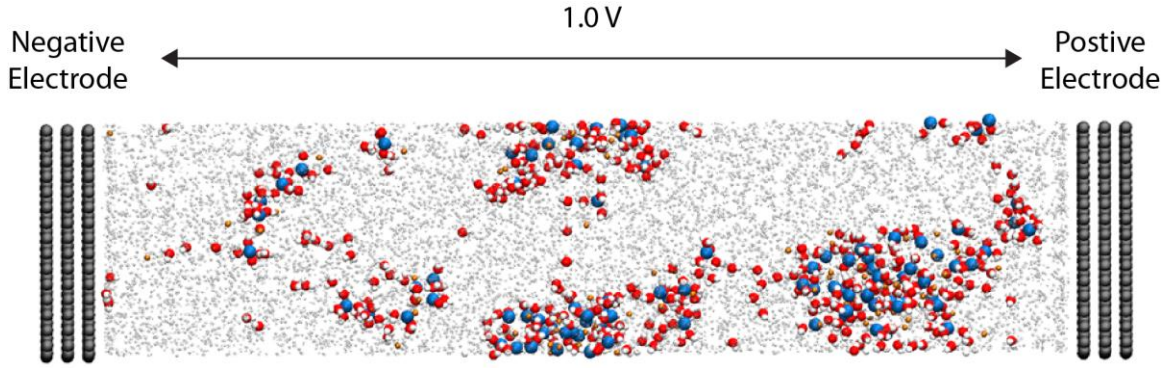

Figure II-19. Snapshot extracted from the MD simulation at constant applied potential of 1 V for the system rich in water and lithium (acetonitrile that contains 10% of water in mass with a H_2O/Li ratio = 4.4, see **Methods Table II-4**). The positive carbon electrode is on the left while the negative one is on the right. Lithium atoms are in blue, water molecules in red (O) and white (H), perchlorates molecules in orange (only the central Cl atom is represented) and acetonitrile in grey.

Furthermore, no significant variation is observed when the applied potential is increased from 1.0 V to 2.0 V. Indeed, similar density profiles showing water heterogeneities for the different species are observed at the different voltages, as illustrated in the **Supplementary Figure II-10** for the system containing 1% of H_2O and 100 mM $LiClO_4$. Hence, the presence of these large water-rich aggregates strikingly contrasts with our previous observations at low $LiClO_4$ content for which only small water clusters could be found in the bulk and at the EDL. While these results suggest that the long-range ordering of the aqueous phase within the electrolyte is likely to impact the water reduction, the environment of water at short-range conspicuously diverges between the different electrolytes studied. Indeed, when the H_2O/Li^+ ratio decreased (*i.e.* $LiClO_4$ is added to the

electrolyte), the analysis of the MD simulations have revealed the formation of ion pairs, and the loss of one water molecule in the first solvation shell of Li^+ cations. Hence, to finally assess whether the increase of the reactivity for water molecules at higher $LiClO_4$ concentrations emerge from a modification of short- or long-range environments, we decided to keep the H_2O/Li^+ ratio constant, *i.e.* to move along the third axis of the phase diagram in **Figure II-1**.

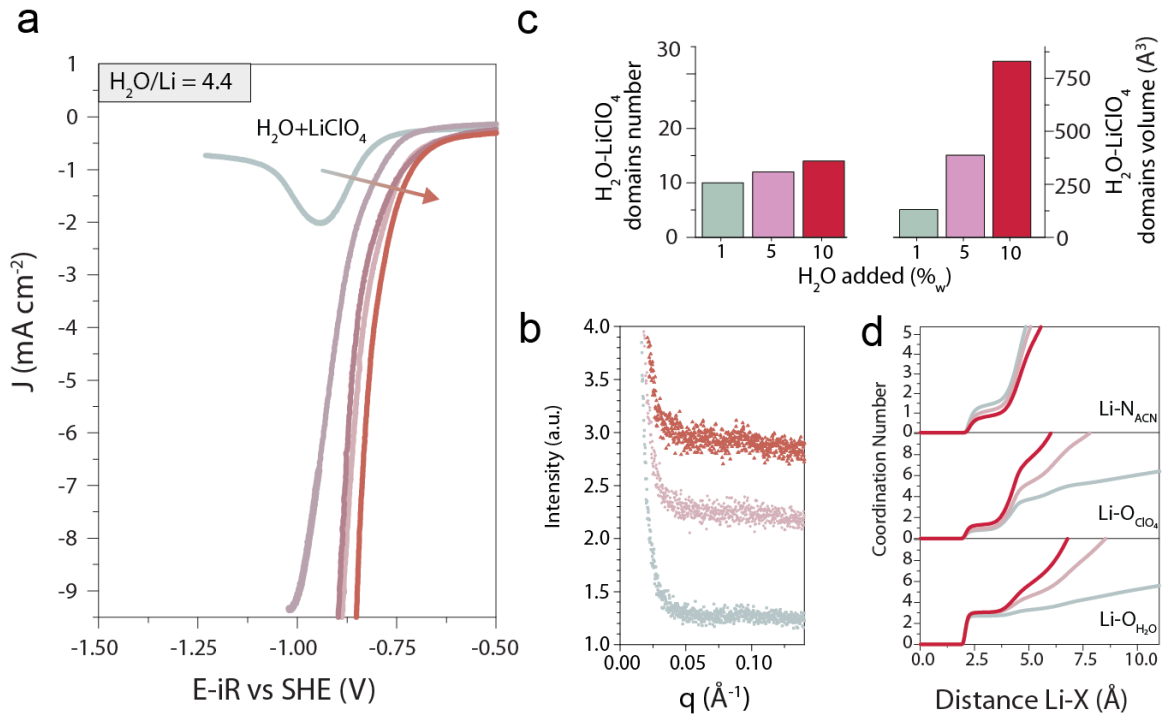

Figure II-20. a) Linear sweep voltammograms recorded in acetonitrile with a H_2O/Li^+ ratio of 4.4 at different water concentration (from 1% light grey, to 10% red) on a rotating disk (1 600 rpm) Pt electrode with a 50 mV s^{-1} sweeping rate. Potentials were measured vs. an organic Ag^+/Ag electrode (see material and methods), are compensated for the ohmic drop (E-iR) and reported versus the Standard Hydrogen Electrode (SHE). **b)** SAXS intensity in the low-q range of acetonitrile for the electrolytes with 1% (grey), 5% (rose) or 10% of added H_2O at constant H_2O/Li^+ ratio of 4.4 **c)** Number of $LiClO_4$-H_2O domains and their average volume depending on the $LiClO_4/H_2O$ ratio at 10% of water concentration extracted from the MD simulations and **d)** corresponding coordination numbers between the Li^+ cations and acetonitrile molecules (top), ClO_4^- anions (middle) and water molecules (bottom).

The linear-sweep voltammograms recorded with this series of electrolytes show 1) a gradual reduction of the electrode passivation and 2) a gradual shift of the onset potential for reduction toward less negative values when the concentration is increased (**Figure II-20 a**). Logically, this behavior directly results from a combination of the two extreme trends previously measured (**Figure II-9** and **Figure II-15**). Furthermore, a significant increase in the SAXS

intensity at low-q values with the Li-H_2O concentrations is observed, experimentally confirming the growth of these long-range $LiClO_4$-H_2O domains in this third series of electrolytes (**Figure II-20 b)** which is further assessed by a domain analysis: at high H_2O-$LiClO_4$ contents, the $LiClO_4$-H_2O rich domains numbers is not drastically altered while their volume is fivefold increased (**Figure II-20 c)**. Finally, the analysis of the coordination numbers for the cations in this series of electrolytes confirms that similar short-range environment for the Li^+ cations is maintained (**Figure II-20 d)**. Studying the water reactivity at fixed H_2O/Li^+ ratio confirms that the formation of water rich nanodomains, connecting the electrode interface to the bulk of the electrolyte triggers the water reduction at higher potentials.

Overall, the greatest reactivity measured for water in large water-rich domains can be explained with the current knowledge of the bulk water autoprotolysis mechanism[121,122] as well as the framework developed by Filhol *et al.* [75] which suggests that several "layers" of water are required to accomplish the Volmer step: the first one provides proton to the electrode, the second accepts the OH^- generated during the HER and the following ones allow the reactants and products to diffuse into solution following a Grotthuss diffusion mechanism. It is also noteworthy that a higher Li^+ concentration in the electrolyte may also drive the OH^- transport across the double layer and promote the cleavage of the water O—H bond, as previously suggested.[117,131] From these experimental and modeling observations, we can therefore conclude that the highest activity measured for water reduction in the presence of these nanodomains highlights the critical role of the long-range-interactions onto the water reactivity.

II.7 Conclusions of the chapter

From both an experimental and a modeling point of view, we have highlighted in this chapter the critical role played by the organization of water at both short and long-ranges on its reactivity upon electrochemical reduction. They provide a picture at the molecular scale of the complex role of the water at electrochemical interfaces. Indeed, by playing on the water content and the salt concentration/nature in the electrolytes, we could constrain the structure of water and sort out 3 different behaviors. First, we could clearly exhibit that the potential at which protons are adsorbed on the Pt electrode directly depend on the nature of the protons donor ($HClO_4$ vs. H_2O), which suggests that the alkaline HER mechanism (H_2O as the proton donor) differs from the acidic

one (H^+/H_3O^+ as the proton donor). Then, focusing on the water reduction, we clearly demonstrated that short-range interactions (water-water and water-cations) are competing. We find that when the H_2O-H_2O interactions are insignificant in the electrolyte (low water concentration), the strength of the water-cation interaction directly impacts the O—H bond strength and thus dictates the water reactivity upon reduction. This clearly suggest that the cleavage of the O—H bond of the water molecule, *i.e.* water autoprotolysis, may limit the water reduction, and thus the HER in alkaline media, kinetics and that adding strong Lewis acids in the electrolyte may help to overcome this issue. Moreover, employing this confinement strategy we could glimpse some insights on the role of water as a solvent for the water reduction. By creating H-bond interactions between water molecules at the short-range, small water clusters are formed which can impact the water reactivity only if the cation-water interaction is not too strong. Finally, when the size of these clusters is grown by increasing the salt concentration, thus creating nanodomains in the electrolyte as detected by SAXS, an increase of the water reactivity is measured. Classical MD simulation shows that these structural heterogeneities are conserved at the interface. Overall, this confirms at the molecular scale that the transport of hydroxides and hydroniums ions at the electrode-electrolyte interface through several layers of water is a key parameter controlling the water reactivity.

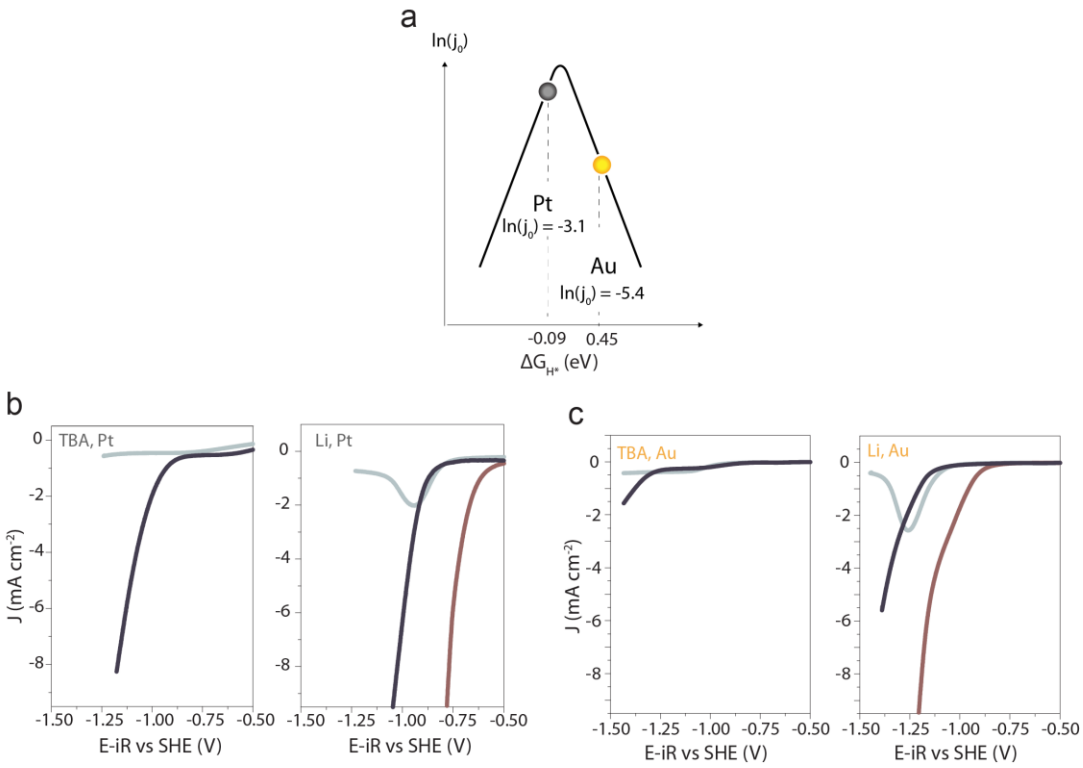

Figure II-21. a) Exchange current densities for the HER over platinum and gold electrodes compared with the computed free energy for the formation of the adsorbed hydrogen intermediate (Data taken from ref. **41)**. **b)** Linear sweep voltammograms (50 mV s^{-1}) recorded over a platinum rotating disk electrode (1 600 rpm) in acetonitrile with $TBAClO_4$ (left panel) at 100 mM with 1% (grey) or 10% (dark blue) in mass of water and with LiClO4 (right panel) at 100 mM with 1% of water (grey) or 10% of water (dark blue) or 2 M $LiClO_4$ with 10% of water (brown). **c)** Similar curves registered on a gold rotating disk electrode (1 600 rpm). Potentials were measured vs. an organic Ag^+/Ag electrode (see material and methods), are compensated for the ohmic drop (E-iR) and reported versus the Standard Hydrogen Electrode (SHE).

Importantly, we also demonstrate that similar electrochemical behaviors hold for different electrode materials. More precisely, while changing the HBE of the surface from a strong binding (Pt) to a weak binding surface (Au), thus covering both sides of the usual 2D-Volcano plots traditionally employed to describe the catalytic activity of metallic surface towards HER, effects of water and salt concentrations are found similar for ACN/$LiClO_4$/H_2O mixtures (**Figure II-21**). Therefore, we reveal that a third dimension, which would stand for the electrolyte structure, is required to capture the HER kinetics at the solid/liquid interface. Because both the short- and long-range environment of the water molecules impact its activity, this third dimension can only be described by the combination of different descriptors, as we demonstrate in this work. Indeed, our confinement strategy allows to scan each effect independently by moving alongside only one

"degree of freedom", thus highlighting different regimes in which one descriptor controls the HER kinetics. Hence, by tuning the salt nature, or the water concentration, the activation energy for the cation desolvation (as extracted from the potential of mean force) describes the HER kinetics which is thus dictated by short-range interactions (**Figure II-22**). When reaching large concentrations, a change of descriptor is needed with the size of the aqueous-rich domains found to correlate with the onset potential for the water reduction (**Figure II-22**). Overall, we demonstrate that adopting this confinement methodology can therefore allow rationalizing electrolyte effects previously observed (Li^+, double-layer rigidity, etc.) by providing a molecular picture.

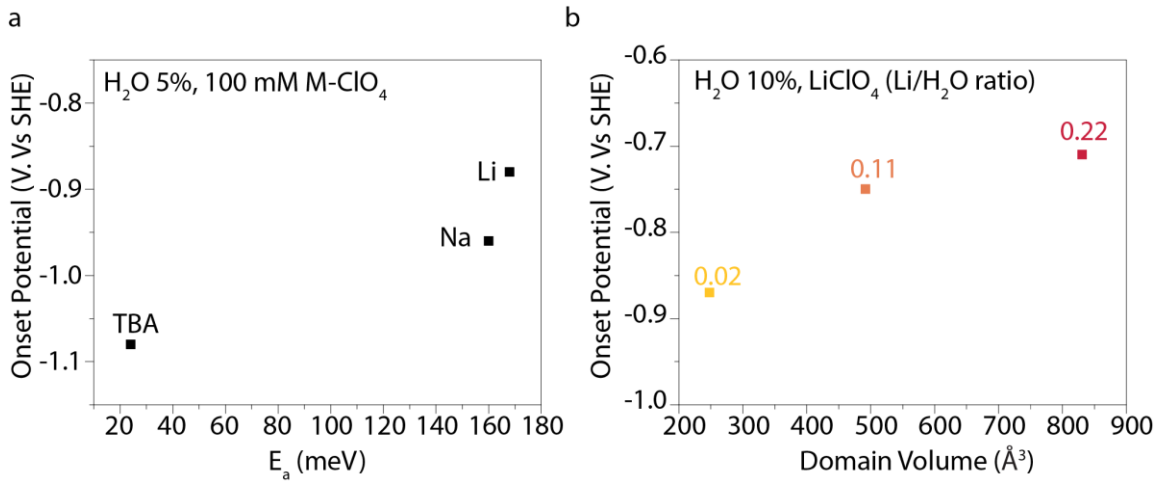

Figure II-22. a) Onset potential for the water reduction (at j = 1 mA cm^{-2}) in acetonitrile electrolyte with 5% in mass of water and 100 mM of TBA, Na or Li perchlorate expressed in function of the activation energy for the cation-water separation obtained from the cation-O_{water} potential of mean force. **b)** Onset potential for the water reduction (at j = 1 mA cm^{-2}) in acetonitrile electrolyte with 10% in mass of water at different Li/H_2O ratios expressed in function of the aqueous domain volume obtained from the domain analysis of the molecular dynamics simulations.

Mastering the water structure at the electrode-electrolyte interface has recently been highlighted both from theoretical[75,132] and experimental[5,15,35] studies as critical to improve the catalytic activity of a surface toward water splitting. The framework developed in this work presents a molecular picture of how short and long-ranges interactions can be employed to promote water reduction on conductive electrodes in non-aqueous electrolytes. This acquired knowledge may transpose beyond the HER to other domains such as the electrosynthesis of complex organic molecule where it was for instance recently theoretically predicted that the formation of domains at the electrode-electrolyte interface may drastically influence electrochemical synthesis kinetics.[133] Thus we believe that a similar approach that the one developed in this study may be

employed to confirm these theoretical predictions. This picture may also been of interest to explain the decrease of potential window stability measured in wet ionic liquids,[88,89,92] or explain the surprising poor cathodic stability of water-in-salt electrolytes that contains Li-H_2O rich domains as will be discussed more deeply in the next chapter.[134–138] Moreover, the creation of these kind of nanodomains in the electrolyte may also be used to tune the selectivity of reactions such as CO_2[139] or N_2[140] reduction by playing on the affinity of the reactants/products with an aqueous or hydrophobic nano-phase.

Chapter III - From *water-in-salt* electrolytes to aqueous biphasic systems [e]

III.1 Motivations

As mentioned in the introduction of this thesis, thanks to the development of high specific energy insertion materials, LIBs are nowadays well established as the leading technology to feature mobility and meet the renewable energy storage needs.[141] Today, typical LiBs materials are working at voltages higher than 4 V for positive electrodes, while negative electrodes operate at potential lower than 1 V (vs. Li^+/Li), well below the thermodynamic stability of carbonate-based electrolytes commonly employed. This is made possible thanks to the initial degradation of the electrolyte, either at the open-circuit voltage (OCV) or during the first initial cycles, forming an electronically insulating but ionically conducting layer on the surface of the electrode called the SEI.[97,142,143] In parallel with the development of LIBs based on carbonated electrolytes, the feasibility of aqueous LiBs has been investigated since the early 1990's,[20,21] motivated by environmental, safety and manufacturing cost challenges. However, the development of these aqueous devices faces two main challenges. First, the electrochemical window in which water is thermodynamically stable is limited to 1.23 V, well below typical organic electrolytes. Second, the formation of a stable and electronically insulating SEI in aqueous electrolytes appears challenging owing to the greater solubility of ionic compounds in water than in organic electrolytes and to the absence of organic solvent to decompose and gives the polymeric part of the SEI.[144] Nonetheless, inspired by organic superconcentrated electrolytes,[145,146] a new class of "aqueous" superconcentrated electrolytes emerged. They were described as Water-in-Salt Electrolytes (WiSEs)[147] or hydrate melt electrolytes.[135] Such aqueous superconcentrated electrolytes are obtained by dissolving large quantities of organic salt such as LiTFSI salt in water (more than 20 moles per kilogram of water). Interestingly, the formation of fluorinated based SEI was reported to be formed on the surface of the negative electrode,[147,148] allowing the assembly of 3 V and even

[e] This chapter is based on three articles that I co-authored: (1) Dubouis, N.; Lemaire, P.; Mirvaux, B.; Salager, E.; Deschamps, M.; Grimaud, A. The Role of the Hydrogen Evolution Reaction in the Solid–Electrolyte Interphase Formation Mechanism for " Water-in-Salt " Electrolytes. *Energy Environ. Sci.* 2018, 11 (12), 3491–3499, (2) Dubouis, N.; Park, C.; Deschamps, M.; Abdelghani-Idrissi, S.; Kanduč, M.; Colin, A.; Salanne, M.; Dzubiella, J.; Grimaud, A.; Rotenberg, B. Chasing Aqueous Biphasic Systems from Simple Salts by Exploring the LiTFSI/LiCl/H_2O Phase Diagram. *ACS Cent. Sci*. 2019, 5 (4), 640–643 and (3) Dubouis, N.; France-Lanord, A.; Brige, A.; Salanne, M.; Grimaud, A. Anion Specific Effects Drive the Formation of Li-Salt Based Aqueous Biphasic Systems, *The Journal of Physical Chemistry B,* 2021.

higher[135,147] aqueous batteries. Thus, these so-called WiSEs have recently been investigated in depth for the realization of practical LiBs[135,149–152], but also for other applications such as sodium-ion,[153] potassium-ion,[154] lithium-air[155] batteries or even supercapacitors.[156]

However, the origin for the electrochemical stability of these electrolytes has been widely discussed. While it is well established and admitted that upon positive polarization, the large hydrophobic anions are crowding the electrochemical interface and repulsing water molecules from the positive electrode,[138,147,151,157–160] thus postponing the OER towards higher potential, the mechanism explaining the improved cathodic stability of the electrolyte (*i.e.* stability at the negative electrode of the battery, so called the anode) has been widely debated. Moreover, while the formation of a fluorinated-rich SEI is well accepted,[147,148] its formation mechanism remains questioned. Indeed, based on first principle calculations showing a shift of the organic anions lowest unoccupied molecular orbital (LUMO) towards more negative energies, it was proposed that the direct electrochemical reduction of these anions leads to the formation of a fluorinated-rich SEI.[147,148,161–163] However, despite such analysis being widely admitted in the batteries electrolytes field, it is not straightforward to correlate the electronic structure of the electrolyte with the thermodynamics and kinetics of electrochemical reactions, as previously discussed in great extent.[164] Especially, the thermodynamics of a reaction depend on both the reactants' and the products' energies, the latter being totally omitted when electrolyte electronic structures are computed. Moreover, it is not so clear whether the pure electronic transfer from the electrode to the anion is the rate determining step of the reaction and thus governs its kinetics. Also, it was demonstrated that the potential at which the reduction occurs in these electrolytes strongly depends on the nature of the electrode material,[135,165] suggesting that these reactions are electrocatalyzed. Hence, the nature of the intermediate species is likely to tune the reaction kinetics, as widely discussed in the previous chapters.

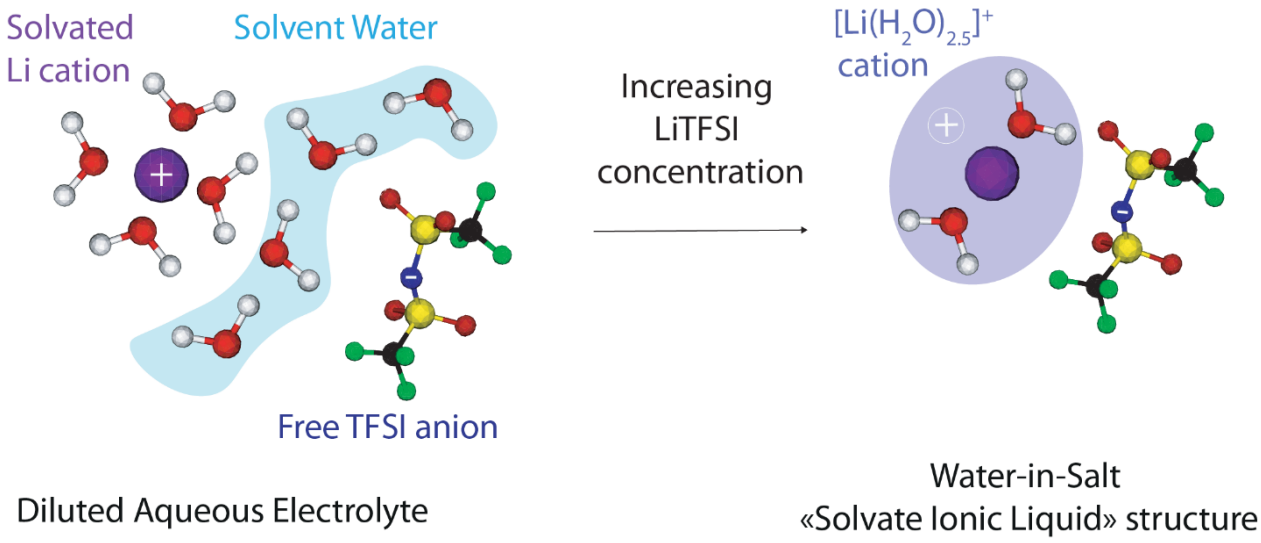

Figure III-1. Schematic structure of the environment for water molecules, Li^+ cations and organic $TFSI^-$ anions in diluted or superconcentrated aqueous electrolytes. The following color code is used to describe the different atoms: H = grey, C = black, N = blue, O = red, F = green and S = yellow.

Importantly, the water structure in WiSEs has been proven to drastically differ compared to traditional diluted aqueous electrolytes. Indeed, in such highly concentrated electrolytes, most of the water molecules are found as "coordinating-water" (*i.e.* in the first solvation shell of a cation),[135,147] as schematized in **Figure III-1**, eventually leading to a structure similar to the one found in solvate ionic liquids, with the positive charge of the cations being delocalized within its solvation shell.[166,167] Moreover, the formation of Li-H_2O rich domains at the nanoscopic scale was demonstrated in these WiSEs.[136,138,168] This allow us to describe/discuss the results obtained on WiSEs using the framework developed in **Chapter II -**. Hence, the first part of this chapter will be dedicated to the study of the cathodic stability of these systems.

From a practical point of view, the cost of organic fluorinated salts used in WiSEs is prohibitive compared to the one of inorganic salts such as those obtained from brines (LiCl). In an attempt to decrease the amount of expensive organic salt used in these aqueous electrolytes,[169] we also investigated mixtures with inexpensive lithium salts and observed an unusual phenomenon, namely the formation of an aqueous biphasic system (ABS). When two liquids with very different physicochemical properties, such as water and oil, are put in contact, they usually coexist as separate phases with a sharp interface. This fact has long been exploited *e.g.* for the separation of

aqueous solutes via liquid-liquid extraction using organic phases or ionic liquids.[170–172] While first ABS based on polymers were discovered in the late 19th century,[173] the coexistence of two aqueous solutions of different salts has only been reported much more recently and the range of such ABS remains comparatively limited.[174–176] Their composition usually involves a concentrated inorganic salt and an ionic liquid. The resulting phases both contain a sizeable amount of water (hence their name) and the origin of the phase separation is thought to result from the simultaneous presence of water hydrogen bond network structuring (kosmotropic) or disordering (chaotropic) ions.[175] This raises the fundamental question: how "different" should the components of the mixture be for such a liquid-liquid phase separation to occur -- *i.e.* in the aqueous case, for an ABS to form? Studying a large variety of Li-based salts, we will thus discuss in the second part of this chapter which physical descriptors can be used to predict the formation of ABSs. We will also show that ABSs reveal promising as electrolytes for new generation of batteries.

III.2 Reactivity of water in superconcentrated electrolytes

Evaluation of the impact from the salt concentration on the electrochemical reactivity of aqueous superconcentrated electrolytes

To assess the stability of WiSEs, we first employed two flat model electrodes, glassy carbon (GC) and polycrystalline platinum, respectively known to possess poor and good electrocatalytic activity towards water reduction. The electrochemical results presented in **Figure III-2 a** confirm that the anodic stability of water increases with the LiTFSI concentration, independently on the electrode material (Pt and GC). As proposed by Coustan *et al.*[157] and latter on rationalized by others,[138,158,166] the screening by $TFSI^-$ anions of the positively charged electrode prevents the migration of water to the surface of the electrode, which increases the onset potential for the oxygen evolution reaction (OER: $H_2O = 2H^+ + ½\ O_2 + 2e^-$). Regarding the cathodic behavior, no real trend was found, as the cathodic currents are similar within the range of error bars due to ohmic drop compensation (between 15 Ω for 1 m electrolytes up to 125 Ω for 20 m electrolytes).

Intrigued by the lack of modification of the cathodic behavior with increased LiTFSI concentration, the electrochemical window was widened and rotating disk setup was used to avoid limitations related to mass diffusion. First, when the salt concentration is increased from 1 m to 20 m, only a small negative shift of the onset potential for the electrolyte reduction (~100 mV) is

measured on GC electrode, while the onset potential measured on a Pt electrode is found not to be sensitive to the salt concentration (**Figure III-2 b**). More importantly, similar measurements performed in highly concentrated inorganic salts ($LiNO_3$ and LiCl, **Figure III-2 c**) reveal that the onset potential for the electrolyte degradation is the same, whatever the salt ($LiNO_3$, LiCl, LiTFSI). Surprisingly, a broad and large reduction peak was observed for 20 m LiTFSI on both Pt and GC electrodes, followed by another reduction event at more negative potentials (**Figure III-2 b**). Since rotation is applied, this phenomenon is unlikely arising from a diffusion-limited process for which a plateau would be observed. Inspired from the observations from **Chapter II -**, a passivation of the electrode can explain such behavior. Another specific feature noticed for 20 m LiTFSI is the quasi absence of reduction current observed during the backward scan which could further indicate the deposition of a passivating layer, as already noticed in ionic liquid.[177] Nevertheless, the apparition of this cathodic peak was measured only in presence of $TFSI^-$ anions, excluding the simple electrode passivation by LiOH precipitation ($Li^+ + H_2O + e^- = LiOH_{(solid)} + ½\ H_2$).

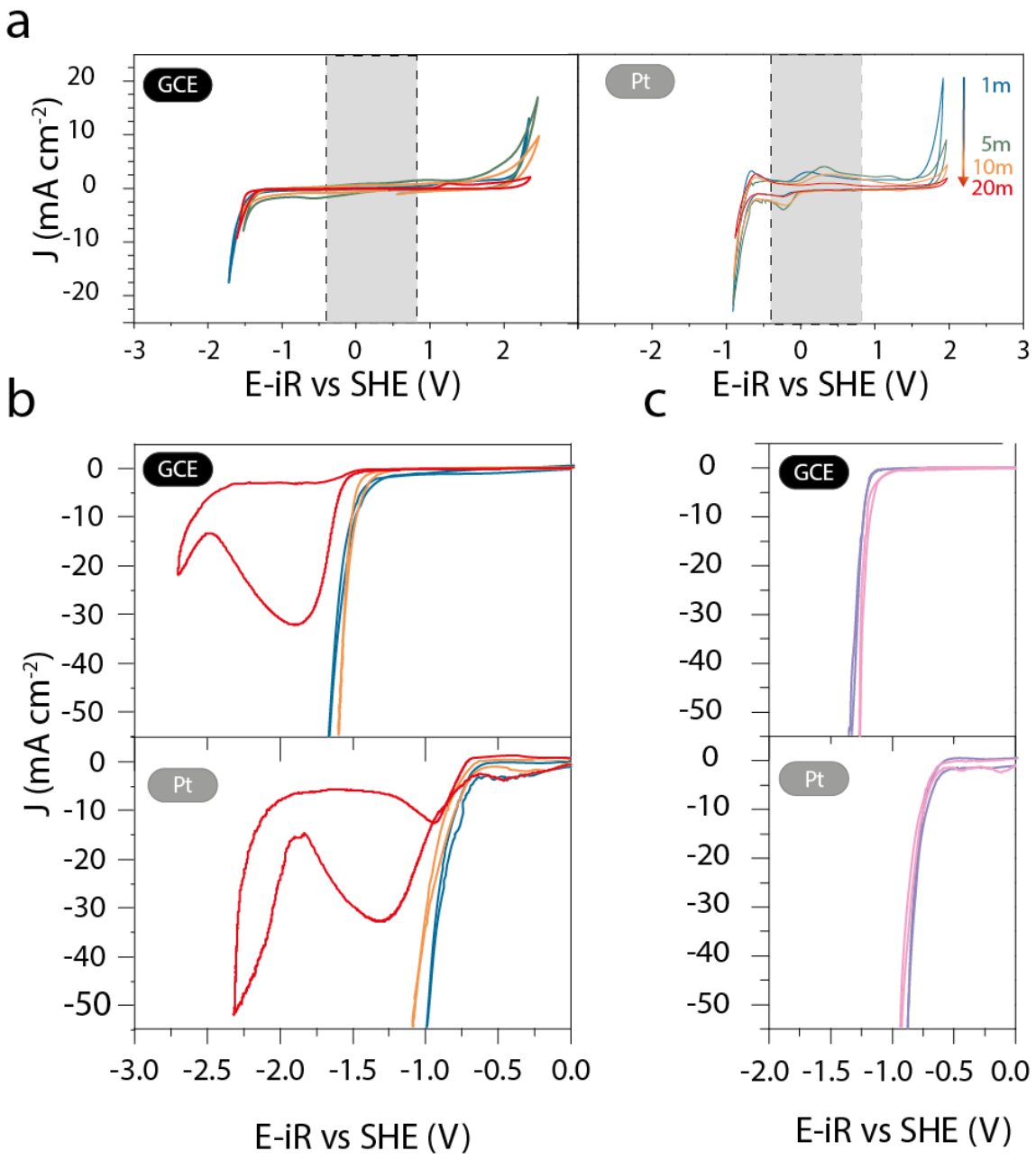

Figure III-2. Cyclic voltammograms recorded at 100 mV s^{-1} **a)** in static conditions over glassy carbon (left) and platinum (right) electrodes in 1 m (blue), 5 m (green), 10 m (orange) and 20 m (red) LiTFSI aqueous electrolytes and **b)** on glassy carbon (top) and platinum (bottom) disk electrodes rotated at 1 600 rpm in 1 m (blue) 10 m (orange) and 20 m (red) LiTFSI aqueous electrolytes and **c)** same rotating disk experiment performed in $LiNO_3$ saturated solution (~ 11 m, rose) and LiCl saturated solution (~ 18 m, purple). On a) grey area represents the thermodynamic stability window of water in the considering of pure water at pH = 7.

Growth of a passivating layer on the electrodes upon water reduction and LiOH formation.

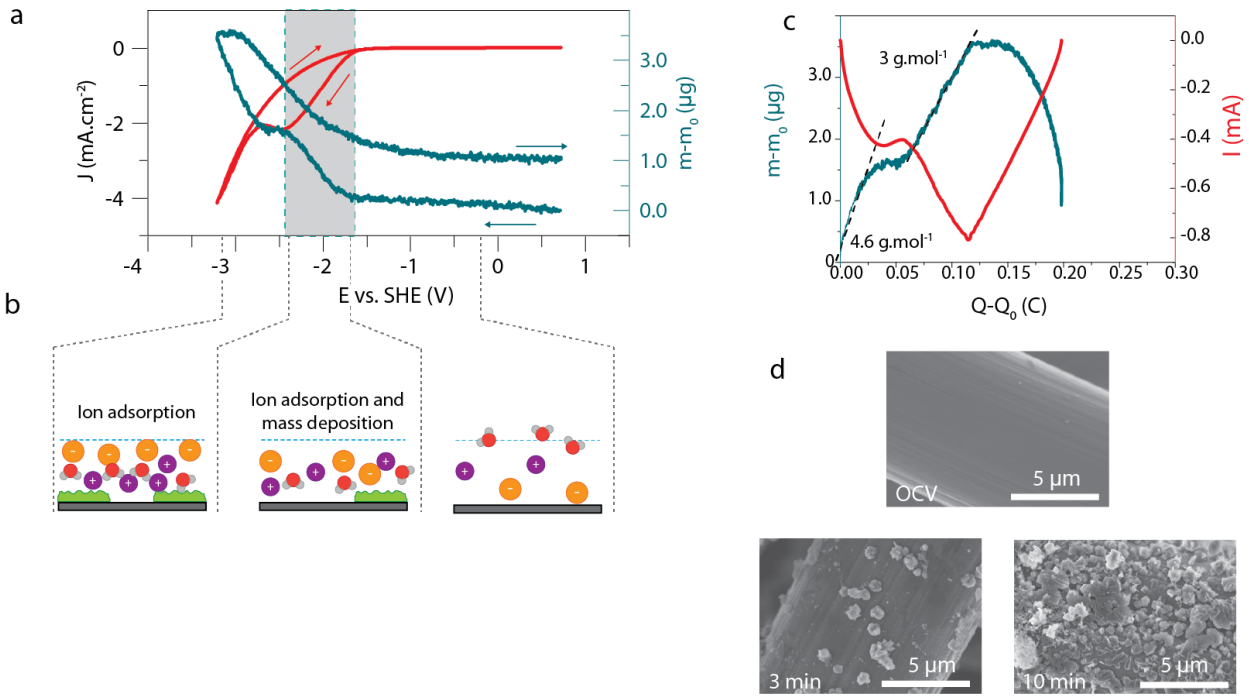

Figure III-3. a) Cyclic voltammogram recorded at 5 mV s^{-1} on a carbon electrochemical quartz microbalance electrode in 20 m LiTFSI solution showing the intensity (red) and the mass deposited on the electrode (blue). **b)** Schematic representation of the phenomena taking place during the forward scan of the cyclic voltammogram. **c)** Evolution of the mass of the electrode (blue) and of the current (red) in function of the electrical charge passed through the electrode. The dashed lines indicate areas in which a fitting of the mass of the electroactive species can be obtained thanks to the Faraday law. **d)** Scanning electron microscopy pictures of gas diffusion layer electrodes just wetted in 20 m LiTFSI and rinsed (left), hold at -1.8 V vs. SHE for 3 min (middle) and for 10 min (right) and rinsed.

To confirm the passivation hypothesis, electrochemical quartz crystal microbalance (EQCM) was used (**Figure III-3 a**). At relatively mild reducing potential, no current and no modification of the quartz resonance frequency is observed. When lowering the potential below -1.7 V vs. SHE, a concomitant increase of the cathodic current and a decrease of the quartz resonance frequency are measured, indicative of a gain of mass. When reaching the cathodic plateau, the mass stabilizes before to further increase when entering the solvent reduction region at potential lower than -2.5 V vs. SHE. On the backward scan, a continuous loss of weight is measured, revealing the desorption of ions previously adsorbed at the interface under negative polarization.[178–181] Indeed, below the pzc of the electrodes, Li^+ cations are continuously adsorbed to screen the negative charge on the surface of the electrode. For WiSEs, these solvated $[Li(H_2O)_{2.x}]^+$ cations are not only surrounded by water molecules, but form pairs with TFSI anions.[158,182] Thus, $TFSI^-$ anions can absorb on the electrode surface together with $[Li(H_2O)_{2.x}]^+$

cations. Finally, after reaching back a potential at which no current is measured, the mass stabilizes with an irreversible gain of 5 μg cm^{-2} (**Figure III-3 b)**. This irreversible gain of mass takes place in the potential range highlighted by the grey area, which matches well with the potential at which a reduction peak is observed during the cyclic voltammetry. Analyzing the evolution of the mass with the charge passed during the cathodic process the presence of at least two distinct processes are confirmed. Unfortunately, the exact molecular weight of the deposited product could not be extracted since the values for the molecular mass found using the Faraday law are very low (**Figure III-3 c)**. Furthermore, it is worth mentioning that all the electrochemical measurements show that the passivation of the electrode is only partial. Indeed, the formation of this film does not totally suppress the electrolyte degradation at very low potentials below -2.5 V vs. SHE where large cathodic current is measured. As discussed by Suo *et al.*, this can be in part explained by the increased probability for electrons to undergo a tunneling process through this poorly conductive thin layer when going towards more negative potentials.[148] To confirm that the gain of mass observed in this potential range was due to the deposition of a film on the electrode surface, porous gas diffusion layer (GDL) electrodes were held at -1.8 V vs. SHE in 20 m LiTFSI solution and analyzed *post mortem* by scanning electron microscopy (SEM). After holding the GDL electrode for 3 min (**Figure III-3 d**), small deposits that are not observed when simply soaking the electrode at the OCV could be seen. After 10 minutes holding, the fibers are almost fully covered by a film made of aggregates of particles (**Figure III-3 d**).

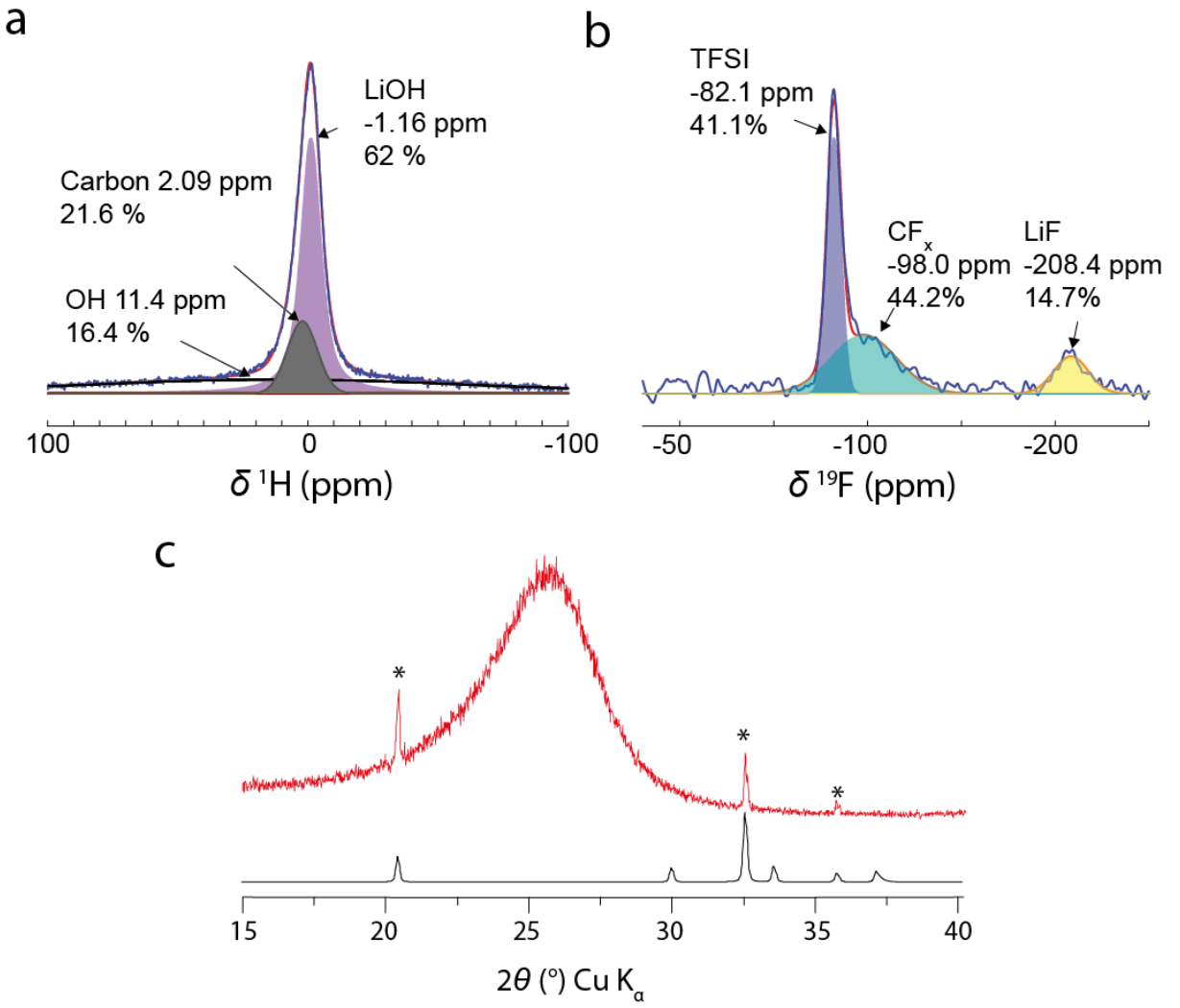

Figure III-4. a) ^{1}H and **b)** ^{19}F MAS NMR spectra of a gas diffusion layer hold at -1.8 V vs. SHE in 20 m WiSE for 30 min (blue curve and red curve showing the raw and fitted data, respectively). **c)** XRD pattern of a similar gas diffusion layer hold at -1.8 V vs. SHE in 20 m WiSE for 10 min compared with LiOH (black) reference pattern. The "*" symbols show the peaks matching those of LiOH reference pattern.

The chemical nature of the decomposition phases was thus analyzed by ex-situ solid-state NMR[f] on a GDL electrode discharged at -1.8 V for 30 min. First, ^{1}H NMR spectrum (**Figure III-4 a**) reveals the presence of LiOH as indicated by the broad peak centered at around - 1 ppm and confirmed by X-ray diffraction (XRD, **Figure III-4 c**), while other environments could be assigned to residual water. The ^{19}F spectrum (**Figure III-4 b**) shows several peaks, with the most intense one around -82 ppm assigned to residual LiTFSI trapped in the SEI. Additionally, two other environments could be observed. The first one at around -207 ppm originates from LiF,[183,184] while

[f] The measurement and analysis of the NMR spectra was realized by M. Deschamps (CEMHTI Orléans)

the one at -98 ppm may correspond to CF_x groups. Hence, the simultaneous presence of CF_x groups together with LiF indicates fragmentation of CF_3 groups during the formation of the amorphous part of the SEI. Overall, these first electrochemical studies combined with characterization of cycled model electrodes confirmed that the cathodic pic observed at high LiTFSI concentration originates from a passivation mechanism, that involves the degradation of the $TFSI^-$ anions.

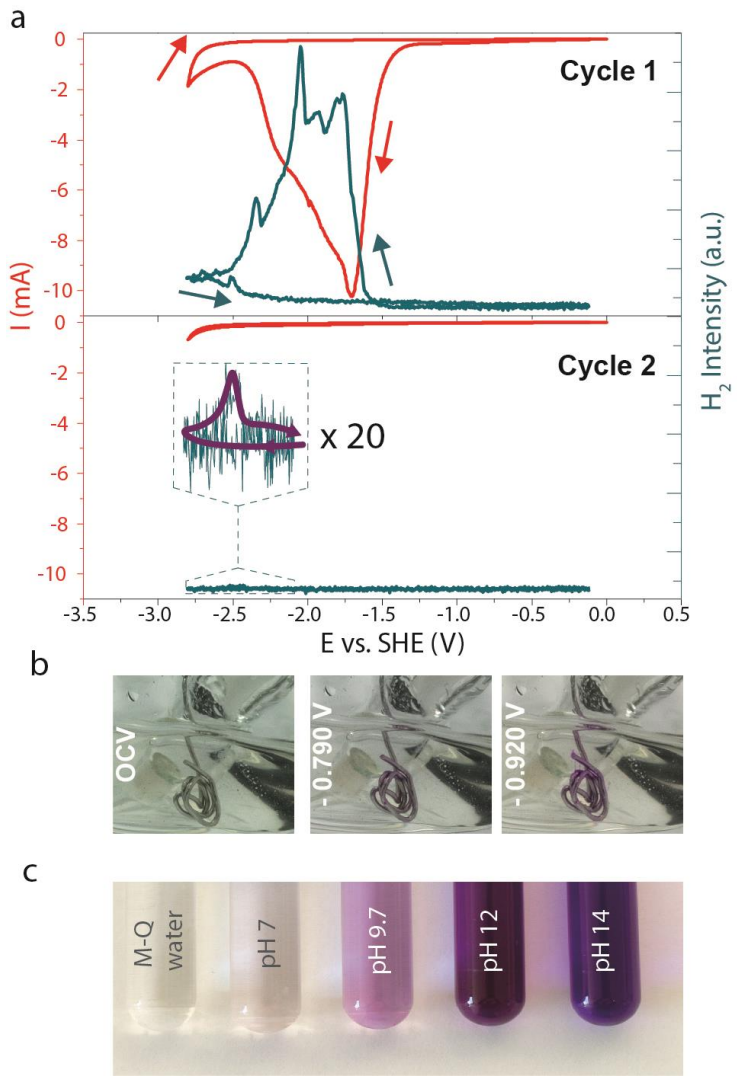

Figure III-5. a) Cyclic voltammograms recorded on a glassy carbon plate electrode in 20 m LiTFSI electrolyte at 0.5 $mV.s^{-1}$ under a continuous argon flow and online electrochemical mass-spectrometry H_2 generation monitoring for the first (top) and a second (bottom) cycle, arrows showing forward (reduction) and backward (going back to OCV) scans, purple plain line serves as a guide for the eyes **b)** pictures of a platinum wire cycled in reduction with a 5 $mV.s^{-1}$ sweep rate in 20 m LiTFSI electrolyte in presence of a pH indicator presenting a purple color in alkaline media, the pH scale being shown in **c)**.

Having established the nature of the materials constituting the SEI, we decided to further investigate the mechanism for its formation. Since LiOH was found as one of the SEI components, the mechanism for the SEI formation must involve the reaction of water molecules. Indeed, two paths can be envisioned for the formation of LiOH. First, it could be the result of an acid-base reaction between an organic base formed during $TFSI^-$ anions reduction and water molecules ($R^- + H_2O = B\text{-}H + OH^-$). Second, it could originate from the reaction of Li^+ with OH^- generated during the water reduction following the reaction $2\ H_2O + 2\ e^- = H_2 + 2\ OH^-$. Hence, to discriminate between these two pathways, on-line electrochemical mass spectrometry (OLEMS) measurements were conducted in 20 m LiTFSI electrolyte to detect if gaseous H_2 is evolved under reductive conditions. As shown in **Figure III-5 a**, during the first cycle, an important generation of H_2 is recorded during the cathodic peak previously described. Interestingly, in the following cycle, H_2 evolution is nearly suppressed, which confirms the passivating role of the layer formed concomitantly with the HER in the first cycle. We could then demonstrate, following the change of color of o-Cresolphtahalein complexone used as a pH indicator, that a strong basification occurs on the surface of the electrode upon HER owing to the generation of OH^- at the electrochemical interface following the water reductive dissociation. Hence, with the presence of Li^+ cations at the electrochemical interface[138,158] as well as the generation of OH^- during the HER (**Figure III-5 b and c**), and owing to the limited solubility of LiOH in water (approximatively 5 m) compared to LiTFSI, the common ion effect and the large ion activity coefficients in superconcentrated electrolytes[185] can easily explain the precipitation of crystalline LiOH observed by XRD (**Figure III-4**). Hence, the following mechanism is proposed:

$$H_2O + e^- = \tfrac{1}{2} H_2 + OH^- \qquad \text{(III-1)}$$

$$OH^- + Li^+ = LiOH_{(cryst)} \qquad \text{(III-2)}$$

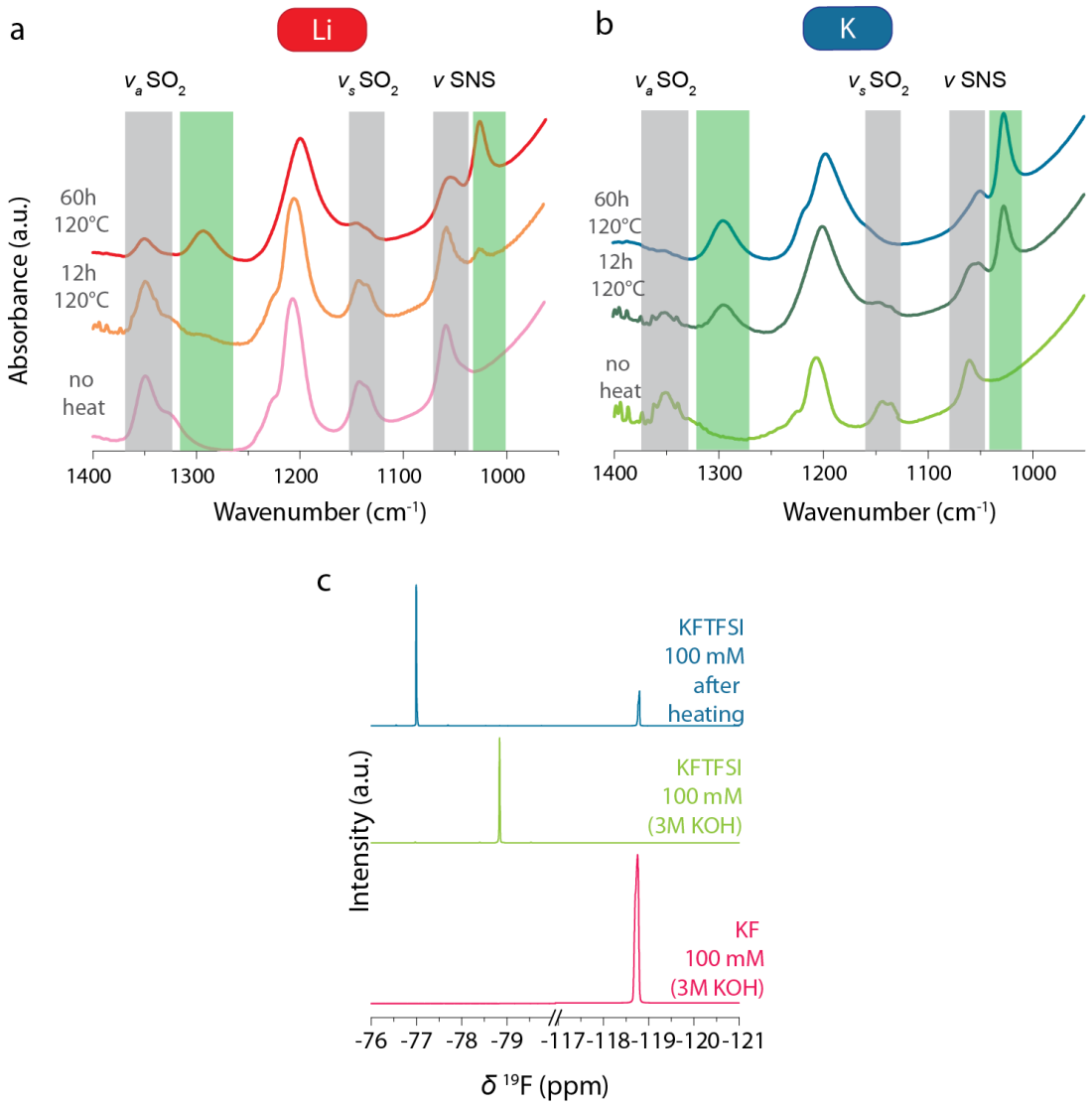

Figure III-6. a) Fourier transform infrared spectroscopy analysis of the 100 mM TFSI solution in 3 M LiOH and **b)** in KOH) before heating and after 12 and 60 hours at 120°C (spectra are not normalized). **c)** 19F NMR analysis of the 100 mM KTFSI in 3 M KOH solution before (green) and after 60 hours at 120°C (blue) compared with the same analysis replacing KTFSI by KF (pink).

However, none of these steps could explain the traces of fluorine and sulfur that were observed by solid-state NMR (**Figure III-4 a**) and that were previously reported on the surface of Li^+ insertion materials.[135,147,148] Even though $TFSI^-$ anions were previously described as stable in a wide range of pH, including strong alkaline media,[186] electro-generated species are often more reactive than their chemical counterparts owing from the slow solvent reorganization when compared to the electron transfer,[187,188] which can render $TFSI^-$ anions unstable towards OH^-

species generated during the HER. To mimic this increased reactivity, the stability of $TFSI^-$ anions in alkaline environment was studied at temperature above room temperature. Thus, 3 M LiOH (resp. KOH) solutions containing 100 mM of LiTFSI (resp. KTFSI) were introduced in hydrothermal bombs and heated for 12 h and 60 h at 120°C. Resulting solutions were analyzed by Fourier transform infrared spectroscopy (FTIR) and ^{19}F liquid state NMR spectroscopy. FTIR results presented in **Figure III-6 a and b** reveal that $TFSI^-$ anions undergo a chemical degradation in these strong alkaline conditions. Indeed, after 60 hours of heating, the FTIR bands assigned to SO_2 (1,350 cm^{-1} and 1,175 cm^{-1}) and SNS (1,160 cm^{-1}) bonds almost disappeared for both solutions,[189] while new bands at around 1,290 and 1,025 cm^{-1} appears. However, looking at the reaction mixture after only 12 hours in these conditions, different kinetics for the degradation of $TFSI^-$ anions are observed for Li^+ and K^+, with the degradation being faster with K^+ than with Li^+. This result provides useful indications on the mechanistic pathway for TFSI degradation in alkaline conditions. Indeed, as Li^+ is a much stronger Lewis acid than K^+, the nucleophilicity of OH^- anions is greatly diminished in the presence of Li^+ cations.[190] Hence, a nucleophilic attack of OH^- on the sulfur atom of the TFSI, which were previously shown to possess a large Mulliken charge,[191,192] can be proposed as a possible mechanism for TFSI alkaline hydrolysis. To confirm this hypothesis, proton decoupled ^{19}F NMR spectra were recorded after TFSI hydrolysis (**Figure III-6 c**). As expected, the solution before hydrolysis shows only one peak at -79.8 ppm, corresponding to the CF_3 groups of $TFSI^-$ anions. After heating for 60 hours, two peaks at -77.0 and -118.8 ppm were observed in the ^{19}F NMR spectrum. Comparing with a solution of 100 mM KF in 3 M KOH, the peak at -118.8 ppm can be attributed to the presence of F^- anions. This control experiment shows that under strong alkaline conditions such as the ones encountered during initial HER at the negative electrode in WiSEs, TFSI is unstable and some LiF is generated by its slow reaction with OH^- anions. These results are in line with the solid-state NMR results discussed previously and confirm the presence of two fluorine environments arising from the chemical fragmentation of the CF_3 groups from TFSI under alkaline conditions.

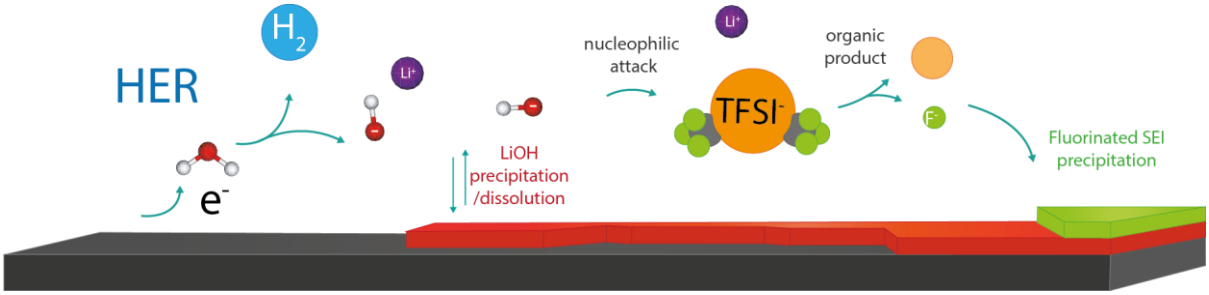

Figure III-7. Schematic illustration of the formation of the SEI following a "water reduction mediated mechanism" occurring in 20 molar LiTFSI WiSE.

Gathering all these observations, we propose the following mechanism that contributes to the formation of the passivating layer at the negative electrode in WiSEs (**Figure III-7**). First, as demonstrated by OLEMS, water is reduced at negative potential which leads to the formation of gaseous H_2 and the release of OH^- at the surface of the negative electrode. This process leads to the precipitation of LiOH on the surface of the electrode. Combining FTIR and ^{19}F liquid NMR, we could then demonstrate that TFSI is decomposed in the presence of either solid LiOH or OH^- ions in solution which react with the electrophilic sulfur atom of $TFSI^-$ anions through a nucleophilic attack. This attack generates F^- anions as well as some organic compounds that precipitate with Li^+ cations thanks to the common cation effect. Hence, a fluorinated SEI is eventually formed and allows cycling anode materials outside of the thermodynamic potential of the water.

From a fundamental point of view, the poor cathodic stability of such superconcentrated aqueous electrolytes can be rationalized within the framework developed in **Chapter II -**. Indeed, in these electrolytes water is mostly found as "coordinating water".[135,147] Moreover, it is clearly established that the bulk of the electrolyte, Li^+-H_2O nanodomains are formed,[136] and these large domains enriched in "coordinating water" are found to migrate to the negative electrode when an electrical field is applied.[138,158] Hence, a parallel can be drawn with the water-rich/salt-rich electrolytes studied in **Chapter II -** owing to their similar molecular edifices. Since the water reduction was found to be "facile" in presence of these Li-H_2O aggregates, it comes to no surprise that water reduction is not delayed to more negative potentials in aqueous superconcentrated electrolytes when compared to their more diluted counterparts. Overall, in this work we revealed that cathodic stability of WiSEs is mostly explained by the formation of a passivating SEI that prevents further electrolytes degradation rather than by a diminished water reactivity due to the modification of the water environment.

III.3 Immiscibility of aqueous superconcentrated electrolytes

Formation of aqueous biphasic systems

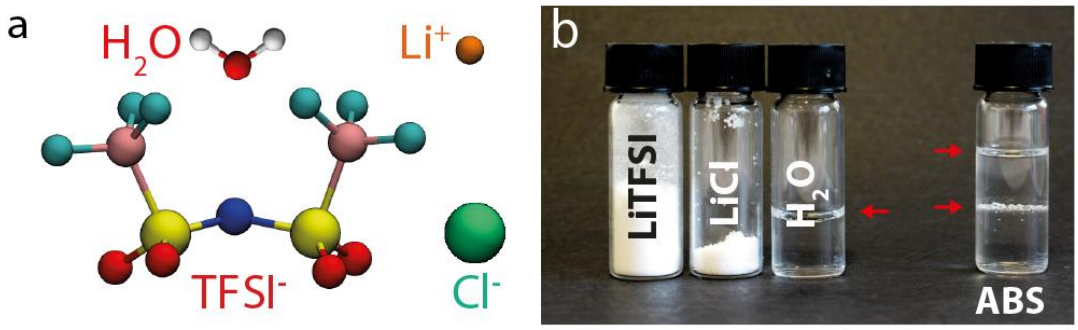

Figure III-8. a) Constituents of the system: water molecule, Li^+ cation, $TFSI^-$ and Cl^- anions. **b)** Stoichiometric amount of LiTFSI, LiCl and water to prepare the 12 m LiCl – 5 m LiTFSI Aqueous Biphasic System. The red arrows show liquid-air or liquid-liquid phase separations.

The formation of the SEI in WiSE has been identified as the key to increase the cathodic stability of aqueous electrolytes. Especially, the absence of a passivating layer in $LiNO_3$ or LiCl superconcentrated electrolytes (**Figure III-2**) clearly establishes the need of having a fluorine source in the electrolyte. Moreover, we could also establish that the precipitation of the inorganic components of the SEI cannot occur in a diluted electrolyte but requires a superconcentrated regime. Indeed, it is achieved thanks to the common ion effect and modification of the activity coefficients in WiSEs.[185] While elegant, such fundamental studies however do not address the scalability of WiSEs which is hampered by the use of large quantities of very expensive organic anions (TFSI). Moreover, such superconcentrated aqueous electrolytes contain more organic species than water, questioning the validity of the sustainability argument. Thus, we aimed at designing cheaper and more sustainable electrolytes, by using a cheap inorganic Li salt (LiCl) as a source of Li^+ cations (solubility ~ 18m) while LiTFSI would be added only as an additive for its ability to form a passivating SEI (SEI former). Surprisingly, when such mixture with a global composition of 12 m of LiCl and 5m of LiTFSI was prepared, we observed at room temperature the formation of two coexisting liquids separated by a sharp interface (**Figure III-8**).

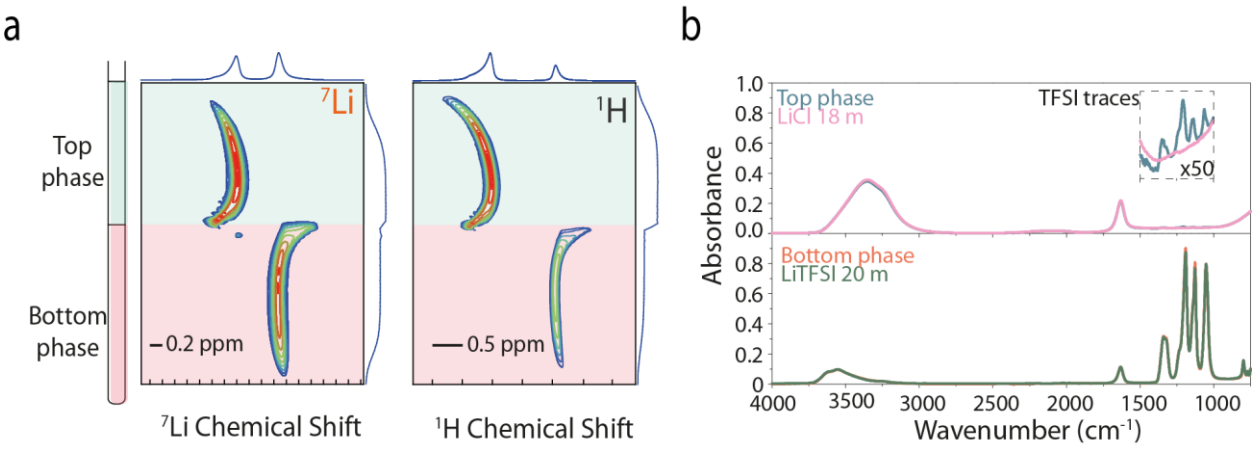

Figure III-9. a) Chemical Shift Imaging of an NMR tube containing the 12 m LiCl – 5 m LiTFSI ABS, revealing distinct local environments for Li^+ cations and water in the two phases. The color indicates the intensity (from blue for low to red for high) as a function of chemical shift and position, while the shape of the peaks reflects the distortion of the magnetic field near the liquid-liquid and liquid-air interfaces. **b)** FTIR spectra of the top and bottom phases of the 12 m LiCl – 5 m LiTFSI ABS compared with those of a 18 m LiCl solution and a 20 m LiTFSI solution, respectively.

To better understand the composition of each phases, we employed ^7Li and ^1H chemical shift imaging (CSI) NMR[g] to provide specific information of the chemical environment of the different species (**Figure III-9 a**). The evolution of the chemical shifts across the interface indicates that Li^+ cations and water molecules are present in the two phases and adopt distinct local environments in each of them. Moreover, the distortion of the signal at the interface results from a change of dielectric constants between the two liquid phases. In addition, FTIR spectroscopy allows us to probe the local environment of water in both phases, which in turn provides indirect information on their composition. As shown in **Figure III-9 b**, water molecules from the top phase exhibit O—H bond stretching modes (broad signal around 3 400 cm^{-1}) similar to those in an aqueous 18m LiCl solution, while weak absorbance peaks around 1 250 cm^{-1} reveal traces of TFSI in solution.[189] A similar resemblance between the bottom phase and aqueous 20 m LiTFSI can also be deduced from their FTIR spectra.

[g] The NMR experiments for the aqueous biphasic systems characterization were realized in the CEMHTI Orléans with the help of Michael Deschamps.

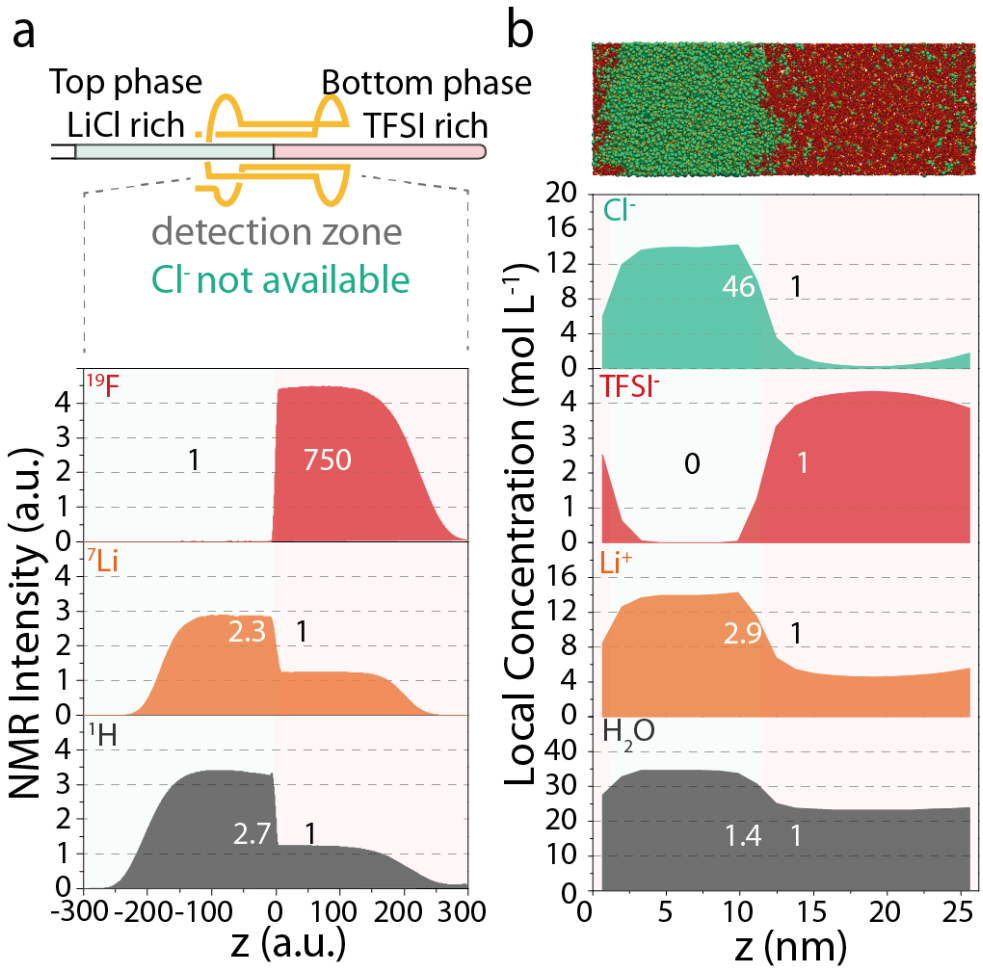

Figure III-10. a) Density profiles for ^{19}F, ^{7}Li and ^{1}H obtained by NMR for the 12m LiCl – 5m LiCl ABS compared with **b)** those obtained by Molecular Dynamics simulations for Cl^-, $TFSI^-$, Li^+ and H_2O for the same system. On the top of panel **b)**, a snapshot extracted from the simulation (Li^+ ions are in orange, Cl^- anions in green, $TFSI^-$ anions in red, and water molecules are not shown) illustrates the presence of a sharp interface.

The liquid-liquid phase separation is further quantitatively examined in **Figure III-10**, which compares the equilibrium density profiles for various elements probed by NMR imaging experiments and computed by MD[h] simulations. Despite the difference in length scales probed by both approaches (~1cm for NMR, ~10 nm for MD), they provide a consistent picture of a sharp interface between two coexisting liquids. The compositions are in good agreement for the species that we could probe experimentally (all but Cl^- anions), which validates the MD simulations. In

[h] The molecular dynamics simulations were conducted in collaboration with M. Salanne and B. Rotenberg from PHENIX (Sorbonne Université, Paris) and C. Park, M. Kanduč and J. Dzubiella from Research Group for Simulations of Energy Materials (Humboldt-Universität zu Berlin, Berlin)

particular, MD simulations predict almost quantitatively the ratio of Li^+ concentration in both phases, as well as the virtual absence of $TFSI^-$ in the Cl-rich phase. The predicted water content in the TFSI-rich phase is smaller than in the other one, even though the ratio is slightly larger than the experimental one.

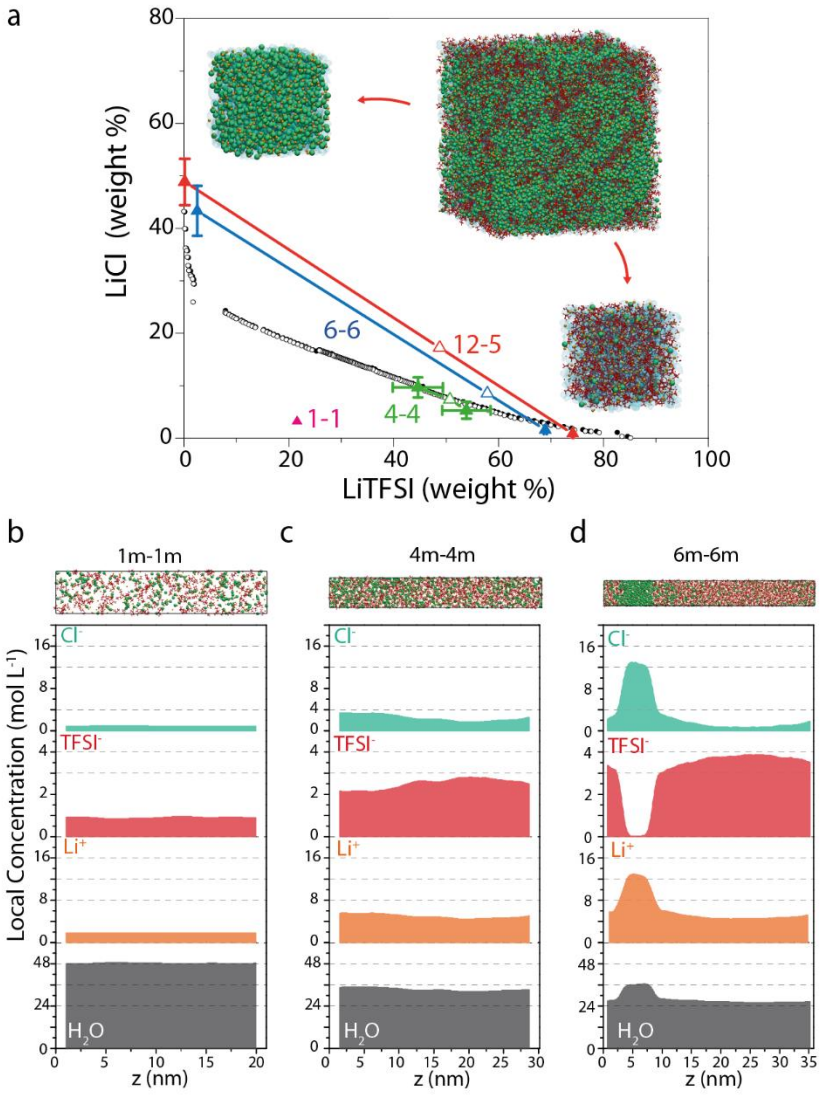

Figure III-11. a) Phase diagram of the ternary LiCl-LiTFSI-H_2O mixture. The phase boundary is located by cloud point experiments between full black circles correspond to a biphasic system and empty circles corresponding to a monophasic system. Tie lines are obtained by MD simulations for 12 m-5 m (red), 6 m-6 m (blue), 4 m-4 m (green) and 1 m-1 m (magenta) LiCl-LiTFSI systems and relate the global composition of the system (empty triangles) to that of the resulting phases (full triangles). The corresponding density profiles are shown in **b)** 1 m - 1 M, **c)** 4 m-4 m and **d)** 6 m-6 m. The 12 m-5 m tie line was deduced from the density profiles presented in **Figure III-10**. MD simulation snapshots illustrate the initial system for the 12 m LiCl – 5m LiTFSI composition and resulting LiCl and LiTFSI rich phases.

The formation of an ABS, *i.e.* a phase separation between two liquid phases, depends on the global composition of the system. The boundary between the monophasic and biphasic regions of the phase diagram was determined by cloud point measurements and is shown in **Figure III-11 a.** Briefly, the cloud point titration consists in introducing a precise mass (m_I) of a concentrated solution of LiTFSI (20 m) or LiCl (18 m) in a test tube, which was weighted before used to tare the scale. The other solution is introduced dropwise, until a cloudy solution is observed. The tube is weighted again (m_C) so that the mass of the added solution can be deduced ($m_S = m_C - m_I$) and the composition of the system is reported as a point of coexistence (biphasic system). Then, water is added dropwise until the solution turns limpid. The tube is then weighted (m_L) to determine the mass of added water ($m_W = m_L - m_C$) and the point corresponding to the monophasic system is reported on the phase diagram. As for the above-mentioned system (12 m LiCl + 5 m LiTFSI), we also observed a phase separation in the MD simulations for a global composition of 6 m + 6 m, while for a more dilute system (1 m + 1 m) the system remains monophasic. At a global composition of 4 m + 4 m, the system is close to the transition between the one- and two-phase behaviors. The resulting compositions of the coexisting liquids in the phase-separating cases, obtained from the MD density profiles **Figure III-11 b, c and d**, are thus very close to the experimental phase boundaries **Figure III-11 a**. Such an agreement is remarkable considering the complexity of the system. This further supports the validity of the MD simulations, which in turn complements the experimental phase boundaries with the tie lines (which could in principle be obtained by separating and weighting both phases, but would require larger volumes and therefore be much more expensive).

We finally turn to the physical origin of the phase separation. In contrast to previously reported ABS,[175,176] in the present systems the salts share a common cation. In agreement with previous MD studies of bulk WiSEs,[147] we find that in our case the relevant cationic species in both phases is the hydrated Li^+, despite the observed partial desolvation in this high concentration regime (**Figure III-12**). This indicates that the phase separation is essentially driven by the different properties of the anions.

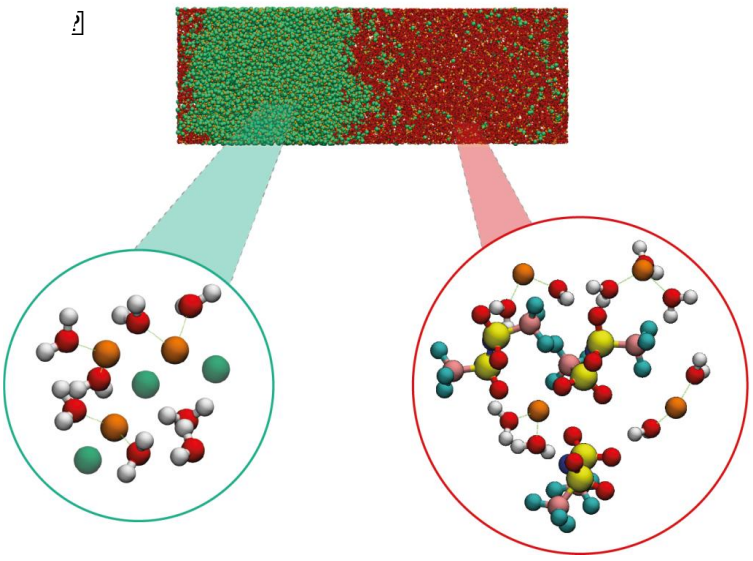

Figure III-12. MD snapshot of the 12 m LiCl – 5 m LiTFSI system, showing the solvation structures of Li^+ cations (orange) in the LiCl (Cl^- in green in top panel and bottom left panel) and LiTFSI ($TFSI^-$ in red in top panel, with separate colours for each atom in bottom right panel) rich phases. Li^+ cations remain partially solvated by water molecules (O in red, H in white) in both phases.

The driving force to form an ABS was previously proposed to result from the difference in interaction with water molecules between two salts: one structuring water (kosmotropic) and the other disordering the hydrogen bond network of water (chaotropic),[175] a phenomenon classically evidenced by viscosity measurements.[193] Indeed, a common way to assess individual ions effect on water structure is to measure the viscosity of dilute solutions (from 5 mM to 500 mM) and to determine the B-coefficient in the Jones-Dole equation ($\eta/\eta_{water} - 1 = Ac^{1/2} + Bc$) by comparing with the results obtained for KCl, assuming the additivity of ionic contributions (and using the fact that $B(K^+)$ = - $B(Cl^-)$.[193,194] Actually, this empirical equation accounts for the influence on the electrolyte viscosity of both the ion-ion interactions with the A term (that can be theoretically computed from Debye-Hückel theory) and the solute-solvent interaction with the B term. For a given solute, if the B term is positive it is commonly accepted that the solute will structure the H-bond network of the water molecules in its close surrounding (kosmotropic), and a negative B coefficient should result in a disruption of the H-bond network in the solute vicinity.[193] The viscosity measured for LiTFSI, LiCl and KCl solutions from 50 mM to 1 M are well described by the Jones-Dole equation for the three salts, which allows us to determine the corresponding A and B parameters (**Figure III-13**). An almost null B-coefficient is measured for KCl, for which it can be deduced $B(K^+)$ = - $B(Cl^-)$ = 0.00 $dm^{3/2}$ $mol^{-1/2}$. The positive B-coefficient of

+0.18 $dm^{3/2}$ $mol^{-1/2}$ found for Li^+ cations indicates its water-structuring role (kosmotropic) and is in excellent agreement with the literature (+0.15 $dm^{3/2}$ $mol^{-1/2}$).[193] Finally, a B-coefficient for $TFSI^-$ anions of + 0.59 $dm^{3/2}$ $mol^{-1/2}$ can be deduced from the slope obtained for LiTFSI and the above value for Li^+. While $TFSI^-$ was reported to be chaotropic,[61] our viscosity measurements reveal that it would rather be a kosmotropic salt owing to its positive B-coefficient (**Figure III-13**). This could result from the large size and hydrophobic character of $TFSI^-$ anion.[193,194] However the concept of chao/kosmotropicity, which underlines the effect of individual ions on water H-bond network, should be taken with some caution at such high concentrations. This is particularly true for WiSEs where the salt-to-water ratio is larger than one, since in this regime the effects of ion-water interactions are not additive.[136,196]

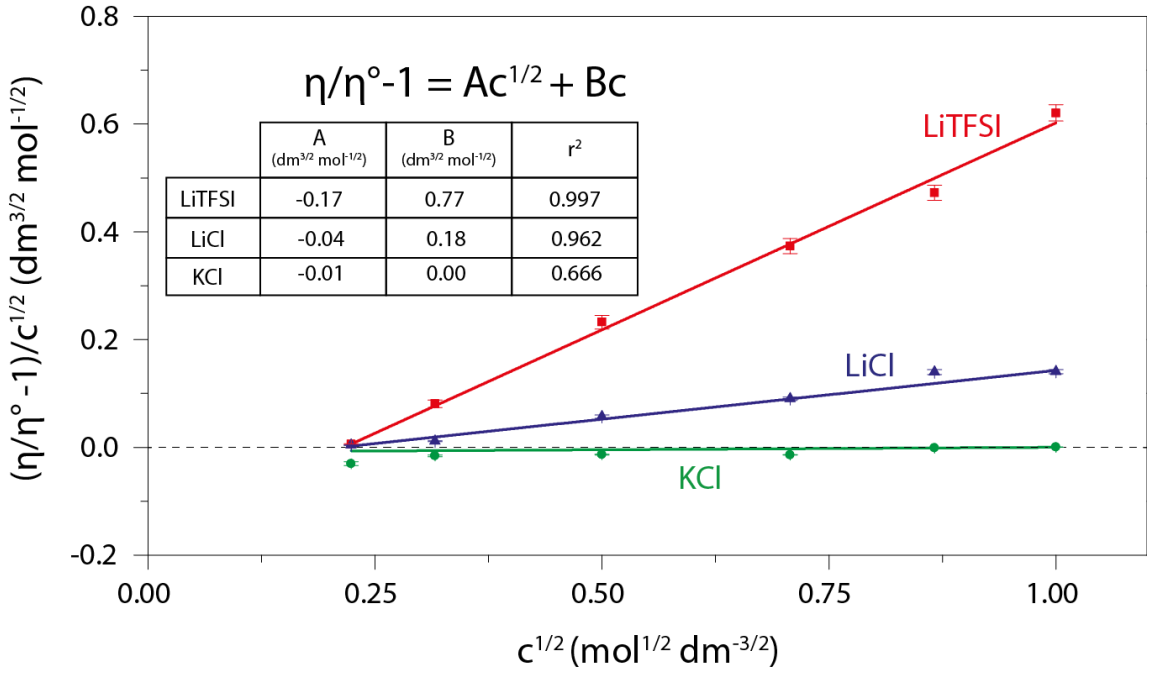

Figure III-13. Viscosity measurements for low concentrations (0 to 1 mol L^{-1}) aqueous solutions of LiTFSI (red), LiCl (blue) and KCl (green). Straight lines represent a linear fitting with the Jones-Dole equation.

From a thermodynamic point of view, a mixture of a solvent with two salts sharing a common ion can be considered as a ternary mixture, due to the constraint of electroneutrality. Using integral equations, Lo Celso *et al.* analyzed the phase behavior of such mixtures for neutral (solvent) and charged (ions) hard spheres[197] and found that an asymmetry in the size of the counterions can be sufficient to induce a phase separation, for a range of compositions and temperatures. On the microscopic scale, this means that the liquid structures satisfying both the

local electroneutrality and packing constraints with each counterion separately are more stable than for the case when all ions are mixed. This is not to say that water does not play a role in the mixing free energy, which determines whether or not the phase separation occurs: it does contribute both energetically (via ion solvation and screening of electrostatic interactions) and entropically (configurational entropy via the composition of each phase). However, this contribution may not be the dominant one. This claim is further supported by the low solubility of alkali halides in conventional ionic liquids in which there is no solvent, revealing an intrinsic immiscibility between large organic anions and halides.[198]

Geometrical descriptors for the formation of ABSs

This first part of the study of ABSs was limited to a single halide and a single organic anion. Moreover, the anion size mismatch was inferred from a simple chemical intuition looking at the chemical formulas of the different anions, but not directly assessed since the anion size was not measured. Therefore, our initial finding calls for a deeper study to check if such explanation based on the size mismatch holds true or not. We thus studied a series of aqueous Li-salt binary mixtures with a series of anions spanning a wide range of geometries: Cl^-, Br^-, I^-, NO_3^- and ClO_4^- on the one hand, and three fluorinated sulfonylimide anions on the other hand, and determined which pairs form ABS.

In order to test the influence of the geometry of the anions, we decided to first investigate the effect of the nature of the fluorinated sulfonylimide anion on the formation of ABSs while keeping the Cl^- anion for the second salt. Hence, two additional organic symmetric fluorinated anions with the following formulas $N(SO_2)_2F_2^-$ (bis(fluorosulfonyl)imide, FSI) and $N(SO_2CF_2CF_3)_2$ (bis(pentafluoroethanesulfonyl)imide, BETI) were selected from the sulfonylimide family. Their chemical formulas is shown in (**Figure III-14 a**). For the former, no formation of a biphasic solution could be spotted even for a highly concentrated solution of the two salts (18 mol kg^{-1} each) at room temperature. Aqueous LiFSI and LiCl thus coexist over the whole range of compositions within a single aqueous phase at room temperature. In contrast, when a concentrated solution of LiBETI (15 mol kg^{-1}) was combined with a concentrated LiCl solution (18 mol kg^{-1}), a phase separation could be triggered. The phase diagram for the LiCl-LiBETI-H_2O

system was constructed using the cloud point method. When compared to the one of LiCl-LiTFSI-H_2O (**Figure III-14**), a larger biphasic region is measured.

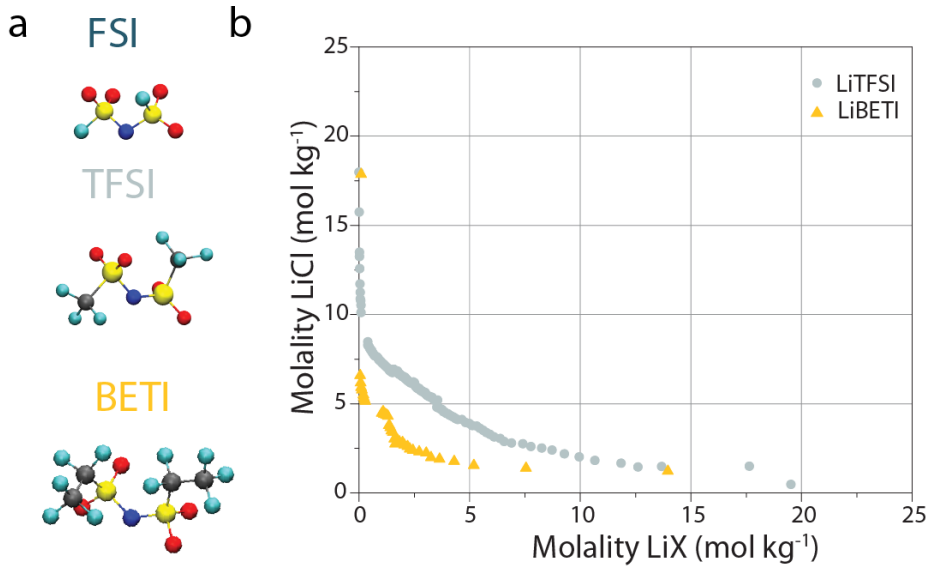

Figure III-14. a) Chemical formulas of FSI^-, $TFSI^-$ and $BETI^-$ anions with N atoms in dark blue, S atoms in yellow, O atoms in red, C atoms in black and F atoms in light blue. **b)** Phase diagrams of the LiCl-LiTFSI-H_2O (grey circles) and LiCl-LiBETI-H_2O (yellow triangles) systems at room temperature, constructed using the cloud point method. The regions under the lines are the monophasic regions.

Then, to test the influence of the size of the second anion on the formation of ABSs, we varied the nature of the halide (X^- = Cl^-, Br^-, I^-) while keeping $TFSI^-$ as organic anion. In all cases, phase separations could be observed at large salt concentrations. Thus, the phase diagrams for the various LiX-LiTFSI-H_2O systems were constructed using the cloud point titration method. When plotted in the mass scale (**Figure III-15 a**), the extent of the monophasic region reduces when going from I^- to Br^- and then Cl^-. Nevertheless, to properly assess those physical effects at the molecular level, the molality scale appears more adequate. Indeed, two electrolytes sharing the same molality also share the same ion-pairs over water molecules ratios, making it possible to discuss the role of ions and solvent molecules. Interestingly, when the different phase diagrams are plotted in the molality scale (**Figure III-15 b**), the boundary lines that separate the monophasic region from the biphasic region almost perfectly overlap for the three different halides.

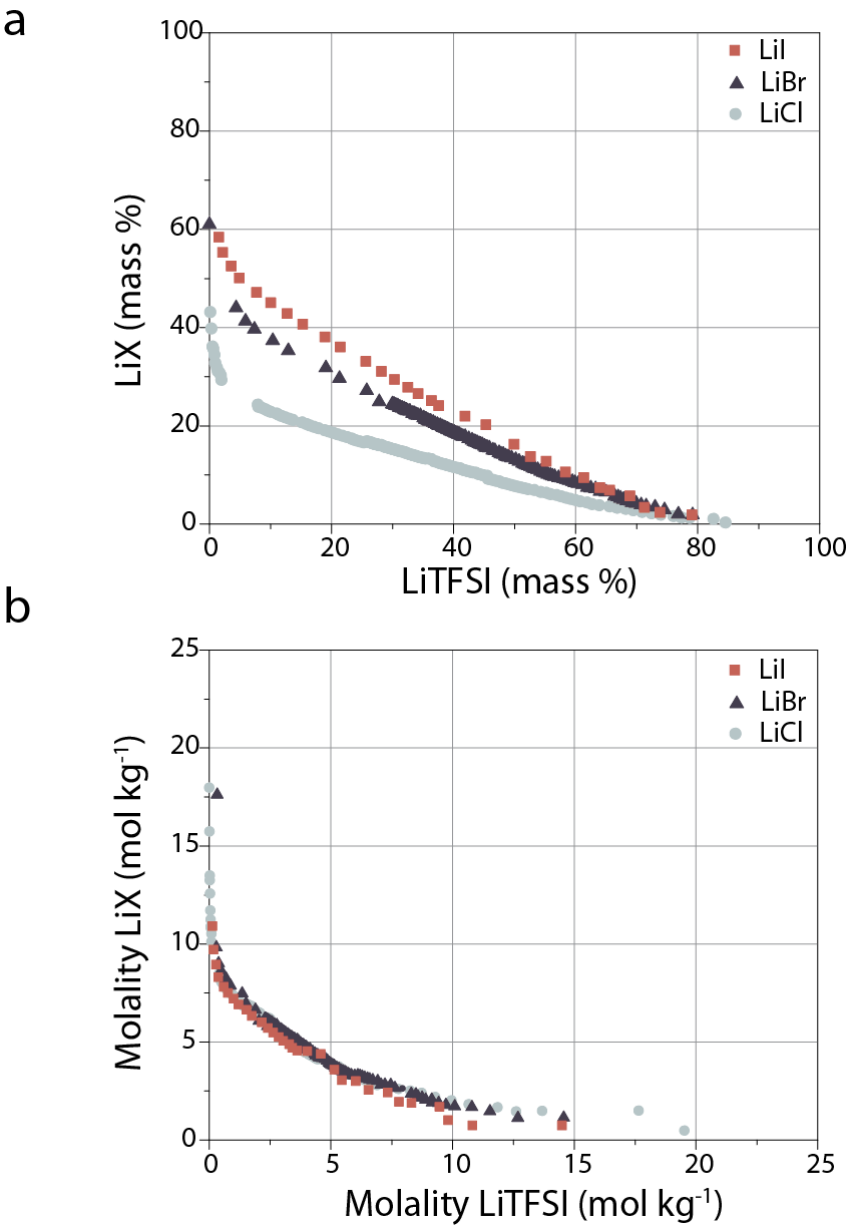

Figure III-15. Phase diagram for LiX-LiTFSI-H_2O systems, with X = Cl (grey), Br (blue) or I (red). The phase diagrams were constructed using the cloud point method and plotted **a)** in the mass scale or **b)** in the molality scale. The region under the line is the monophasic region.

In order to complement the results with another family of compounds, a similar study was carried out using inorganic anions, *i.e.* perchlorate and nitrate, that do not belong to the inorganic halides or organic sulfonylimide families and thus show different chemistries and geometries. In both cases, no ABS was formed when they were mixed with concentrated LiTFSI solutions, unlike what was previously observed for halides. The results obtained for the formation of the ABS are

summarized in **Table III-1**. In the following, we will assess the ability of various geometric descriptors to predict the occurrence of ABS.

	LiCl	**LiBr**	**LiI**	**LiNO3**	**LiClO4**
LiFSI	X	n.a.	n.a	n.a	n.a
LiTFSI	+	+	+	X	X
LiBETI	++	n.a.	n.a.	n.a	n.a

Table III-1. Summary on the formation of ABS. The natures of the first and second salts are given in the columns and lines respectively. Symbol code: (X) = no ABS observed , (+) formation of an ABS, and (++) formation of an ABS with a small monophasic region. The systems that were not investigated are indicated as "n.a.". All these data are at room temperature.

Probing the influence of the anion size from simple density measurements

In order to be effective, chemical descriptors should be simple to measure. Based on the theoretical model developed by Lo Celso *et al*. who studied the mixing behavior of charged hard spheres[199] (in the absence of solvent), we expect the relative size of the two anions (or their ratio) to play an important role on the formation of an ABS. However, there is currently no consensus on the best method to determine the size of ions in solution. For example, the ion-water distances can be probed by diffraction methods or molecular simulations,[200] but these two methods are rather complex to implement. A simpler approach to sense the mean ion diameters (d_{ion}) of the ions composing a salt is to measure the densities of several solutions prepared with a precisely known concentration of salt and water.[201,202] Briefly, the densities d of solution containing a precisely known amount of a salt (m_{salt}) and water (m_{H_2O}) were measured with an electronic densitometer. Thus, the c_{salt} and c_{H_2O} were extracted following the equations: $c_{salt} = \frac{d}{M_{salt}\left[\frac{m_{H_2O}}{m_{salt}}+1\right]}$ and $c_{H_2O} = \frac{d}{M_{H_2O}\left[\frac{m_{salt}}{m_{H_2O}}+1\right]}$ and were further converted to the nm^{-3} scale. The partial molar volume of an ion pair V_{IP} is then extrapolated by taking the intercept at $c_{H2O} = 0$ of a linear regression, as shown in **Figure III-16 a** for the lithium halide salt, **Figure III-16 b** for the lithium fluorosulfonylimide salts and

Figure III-16 c and d for $LiNO_3$ and $LiClO_4$, respectively. The mean ion diameter (d_{ion}) is then taken as half the diameter of the sphere with a volume V_{IP}. The d_{ion} thus obtained are given in **Figure III-16 e**.

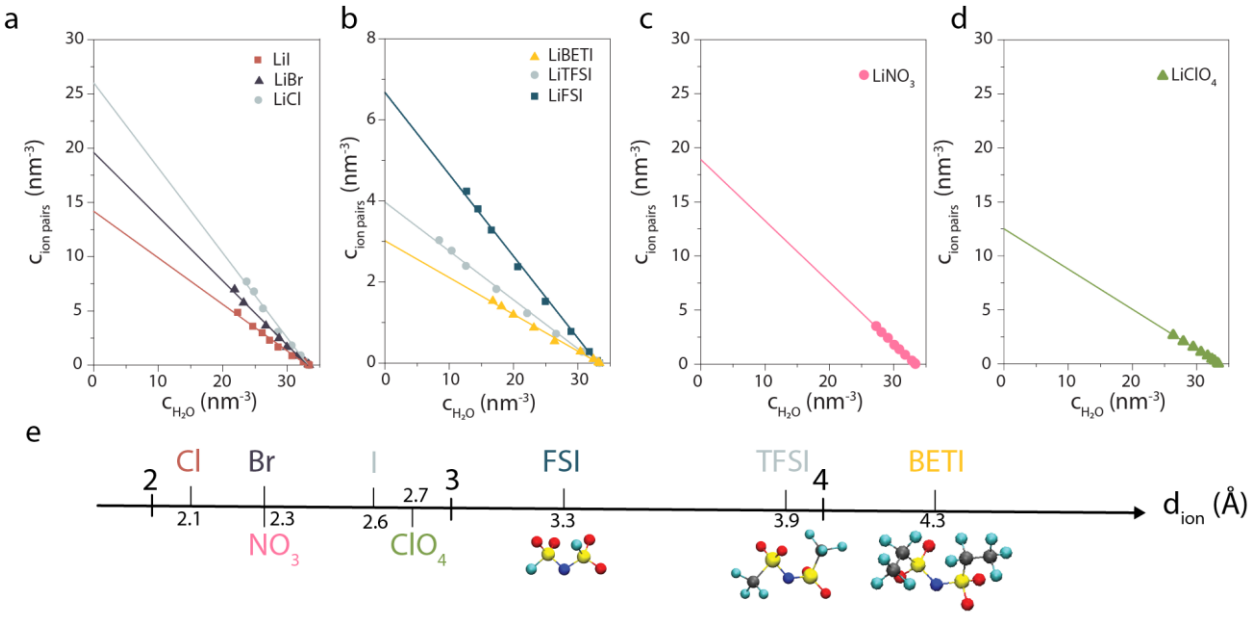

Figure III-16. a) Concentration of ion pairs (ions pair per unit of volume) as a function of the water concentration for LiCl (grey circle), LiBr (blue triangle) and LiI (red squares) determined by measuring the density of solutions with different molalities. **b)** Concentration of ion pairs for LiFSI (blue squares), LiTFSI (grey circles) and LiBETI (yellow triangles). **c)** Concentration of ion pairs for $LiNO_3$. **d)** Concentration of ion pairs for $LiClO_4$. **e)** Mean ion diameters (Å) for all the anions computed from the apparent ion pair volume extrapolated from the concentration of ions at c_{H2O} = 0. Molecular representations are given for the organic anions with N atoms in dark blue, S atoms in yellow, O atoms in red, C atoms in black and F atoms in light blue.

If first looking at the large organic anion series (**Figure III-16 e**), the size argument seems to provide a qualitatively good descriptor for the formation of the ABS. Indeed, no ABS would be formed for the LiCl-LiFSI-H_2O system due to the small diameter of the FSI anion (3.3 Å according to our estimate), and the larger the fluorosulfonylimide, the larger the immiscibility domain **(Figure III-14 b**). However, the situation is much less clear when looking at the small inorganic anion series. Indeed, the three halides show similar phase diagrams when using the molality scale despite the increase of their radius with their atomic number (**Figure III-15 b**). This could point towards a "threshold" size below which an ABS is formed independently of the diameter of the small ion. Nevertheless, it is worth noting that d_{ion}(I) is found to be only 1.25 times larger than d_{ion}(Cl). This small difference, presumably not significant compared to the size of the organic $TFSI^-$ anion, may explain why no effect of the halide size is observed on the phase diagrams.

However, as seen on **Figure III-16 e,** the diameters of the nitrate and perchlorate anions are very similar to the ones of Br^- and I^-, respectively, which is either due to a poor determination of the ion diameter or to the failure of ion diameter as a sole descriptor for the formation of ABS. Concerning the first hypothesis, it is certain that the diameters obtained herein from density measurements are approximate. For example, they are twice smaller than those of the same anions within pure ionic crystals.[203] This observation surely results from the small size of the Li cation (d = 1.80 Å in pure ionic crystals),[203] even compared to those of the halides (at least twice larger), which results in a systematic underestimation of d_{ion} for the anions. Indeed, the d_{ion} value estimated by this method is the average ion diameter for a given ion-pair, e.g. considering similarly the anion and the cation. In order to assess this effect, the diameter was also estimated using density measurements of sodium halide and potassium halide salts dissolved in water (**Figure III-17**).

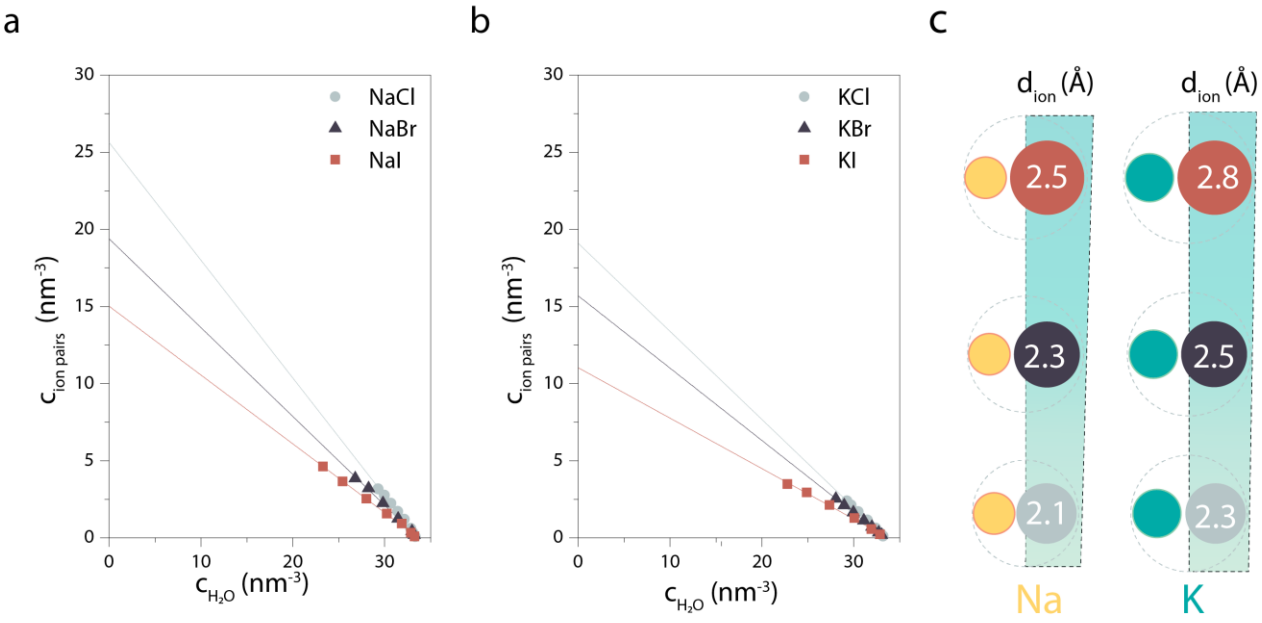

Figure III-17. a) Concentration of ion pairs in function of the water concentration for NaCl (grey circle), NaBr (blue triangle) and NaI (red squares). **b)** KCl (grey circle), KBr (blue triangle) and KI (red squares) determined by measuring the density of solutions with different molalities. The lines correspond to linear extrapolations of the ion concentrations. **c)** Extrapolated mean ion diameters for the different ion-pairs (in Å)

The diameters are almost invariant between LiX, NaX and KX salts (X being the halides) while the cation size should increase, thus showing that the anion contribution to the d_{ion} largely dominates the one of the cation and validating this experimental method as a good estimation of

the relative anion sizes. In addition, a spherical geometry for the ion-pairs was assumed in order to determine the d_{ion}. While this assumption may roughly hold for simple spherical anions such as the halides, it probably fails for ions with more complex geometries. Indeed, the NO_3^- anion has a triangular shape while the ClO_4^- one forms a tetrahedron. It is thus possible that the Li^+ ions can approach closer to the anion center along specific directions (for example between the two tips of the triangle in the case of the nitrate), thus resulting in an underestimation of the anion diameter using the density measurement method. It is probably even more irrelevant for the organic anions since their spatial conformation may depend on their concentration. Indeed, it was demonstrated that in so-called water-in-salt electrolyte (LiTFSI at 20 mol kg^{-1}) developed for aqueous LIBs, the formation of contact ion-pairs and ion-aggregates at such large ionic concentration leads to different conformation of the $TFSI^-$ anions.[147] Such observation further highlights the difficulties in determining which characteristic distance should be used to describe ionic sizes (interatomic distances, radius, etc.). This calls for the use of more involved descriptors to analyze the formation of ABSs when the anions' characteristic sizes are too similar.

Probing the influence of the anion hydrophobicity using gas phase DFT calculations[i]

Further complicating such study, an analysis solely based on the ion size also misses features such as differences in hydrophobicity between anions. Originally, ABS formation was thought to be determined by the structure-forming (kosmotropic) or structure-breaking (chaotropic) nature of the ions; however, we recently showed that such a criterion is not sufficient.[204] An ion's structure making or breaking behavior is intimately related to how an ion interacts with its surroundings. In the case of a dilute aqueous solution, this is generally characterized by the hydrophilic or hydrophobic character of an ion. We therefore investigated if differences in the anions' hydrophobicity behavior could rationalize the cases for which the sole difference in anions size cannot explain the ABS formation.

[i] The DFT calculations were realized in collaboration with A. France-Lannord and M. Salanne from PHENIX (Sorbonne Université, Paris)

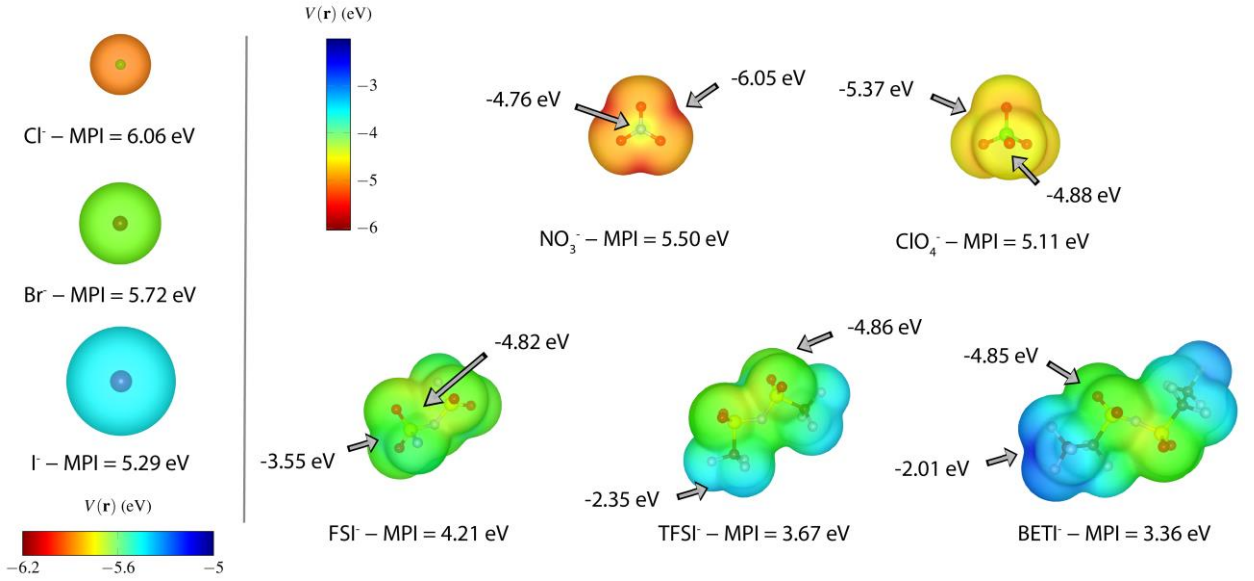

Figure III-18. Electrostatic potential $\boldsymbol{V(r)}$ mapped to the 0.001 e/Å^3 isosurface of the electron density for a series of anions (Cl^-, Br^-, I^-, NO_3^-, ClO_4^-, FSI^-, $TFSI^-$, $BETI^-$) obtained from gas phase quantum chemistry calculations, along with the molecular polarity index (MPI). For non-spherical anions, extrema values of the electrostatic potentials are indicated along with their location on the isosurfaces.

To do so, the simplest approach would consist in using the hydration free energies of the anions as a descriptor. However, experimental measurements show significant variability which can be attributed to the various assumptions required for extrapolating such values.[205] Nevertheless, the experimentally determined Gibbs free energy of hydration[206] do place NO_3^- as more hydrophilic than I^-, which seems to indicate that this descriptor is also deficient for explaining their different abilities to form ABSs. Molecular polarity index (MPI) obtained from the electrostatic potential calculated at the quantum chemistry level has also been proposed to correlate with the ion hydrophilicity, the larger value of the MPI corresponding to a more hydrophilic character.[207] Results obtained for MPI computed for the different anions are shown on **Figure III-18**. Here again, it is clear that this descriptor is not able to catch differences between the Br^-, NO_3^-, I^- and ClO_4^- since they all display very similar MPIs.

Probing the solvated anions geometry using ab initio molecular dynamics simulations[j]

In order to clarify the differences existing between halides and perchlorate or nitrate ions, we then computationally investigated the shape of these ions in solution. For that, *ab initio* MD simulations were performed in order to avoid any pitfall associated to the choice of a particular force field. The computed radial distribution functions between the halide anion or the central atom of the nitrate and perchlorate anion and the hydrogen atoms from the water molecules are shown **Figure III-19**. We observe that this function hints towards a larger diameter for the NO_3^- anion compared to our experimental estimate, since it is almost superimposed with the one of the I^- anion (while density measurements gave similar diameters for NO_3^- and Br^-, as shown **Figure III-16**). In addition, the ClO_4^- anion displays the largest preferred distance to the water molecules. However, the differences observed here are too small to conclude further on a diameter effect.

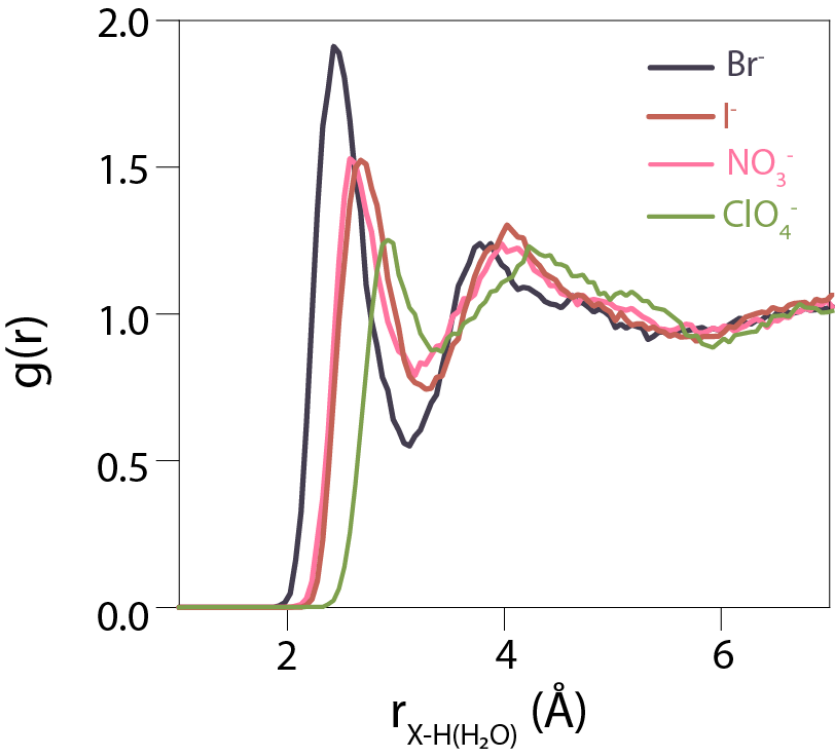

Figure III-19. Radial distribution function between the halide anion or the central atom of the nitrate and perchlorate anion and the hydrogen atoms from the water molecules.

[j] The ab-initio molecular dynamics simulations were realized in collaboration with A. France-Lannord and M. Salanne from PHENIX (Sorbonne Université, Paris)

MD simulations allow us to go further and determine the shape of the solvation shell. This was done using a domain decomposition analysis of the trajectory, using the Voronoi tessellation method.[130] Doing so, the shape of the anions could be characterized, assuming the anion to occupy the ensemble of Voronoi cells containing the anion and no other atom from the local environment. Results are presented in **Table III-2.** It is worth noting that the surface area and volume of the calculated domains are only estimated since they strongly depend on the metrics used as Voronoi radii (in our case, van der Waals radii). However, the use of different parameters would lead to qualitatively similar results. It is therefore clear that, owing to their molecular character, the nitrate and perchlorate anions occupy significantly more space than their halides counterparts. This result therefore reinforces the argument following which ABS are formed when the two anions have different sizes due to packing constraints, albeit this cannot always be cast in a simple descriptor as initially attempted in this work.

Anion	S (Å^2)	V (Å^3)	Q	N
Br^-	62.68±2.93	38.70±2.41	0.829±0.020	28.4+4.0
NO_3^-	93.26±4.44	61.87±4.00	0.731±0.020	70.4±5.7
I^-	70.08±2.57	47.24±2.24	0.856±0.016	32.4±3.7
ClO_4^-	114.46±4.57	84.14±4.33	0.731±0.023	85.8±5.6

Table III-2. Geometrical characteristics of the anion-containing domains: surface area (S), volume (V), isoperimetric quotient (Q), and number of facets (N). Reported values are averages with associated standard deviations calculated over the trajectories.

A third important quantity which can be extracted is the sphericity of the calculated domain, through the introduction of the isoperimetric quotient Q defined as:

$$Q = 36\pi \frac{V^2}{A^3}.$$

For a spherical domain, $Q = 1$, while the asphericity increases with decreasing Q value. As seen in **Table III-2**, halide domains show high Q values. Such a result is not trivial, as this method probes the imprint of the anion in its environment rather than the shape of its electronic cloud. In details, the I^- domain is slightly more spherical than the Br^- one, mostly because it is larger and composed of more facets (N values in **Table III-2**). On the other hand, both nitrate and perchlorate domains show significantly larger asphericities. Since $TFSI^-$ anion exhibits a highly non-spherical

geometry, its Q value should certainly be low as well, explaining its mixing with low Q-values anions such as ClO_4^- or NO_3^- and the formation of ABS in presence of highly spherical halide anions. Overall, this means that this quantity may be seen as a secondary descriptor for systems in which the diameter is not sufficient.

Can ABSs be used for electrochemical applications?

Our investigation of ABSs started from electrochemistry related interrogations. Despite the fact that ABSs found various applications in life-science or recycling, their use remains relatively limited as potential electrolytes for batteries. However, as they can be prepared from two conductive salts, they could reveal useful to design batteries. For instance, Navalpotro *et al*. recently took profit of the difference of solubility for organic redox molecules in the different phases of an ABS to assemble a membrane-free aqueous redox(-flow) battery.[208] In our case, both phases forming the ABSs contain Li^+ cations commonly used in intercalation batteries. Moreover, while one phase contains an organic ion, the other is mainly composed of a halide salt. Because chloride-ion batteries using polypyrrole polymer (PP) electrodes have been previously investigated,[209] we assembled a prototype of dual-ion (Li^+/Cl^-) battery using a PP cathode, a Mo_6S_8 anode able to intercalate Li^+ cations and a LiCl/LiTFSI (18 m / 20 m) ABS electrolyte, as schematized in **Figure III-20**.

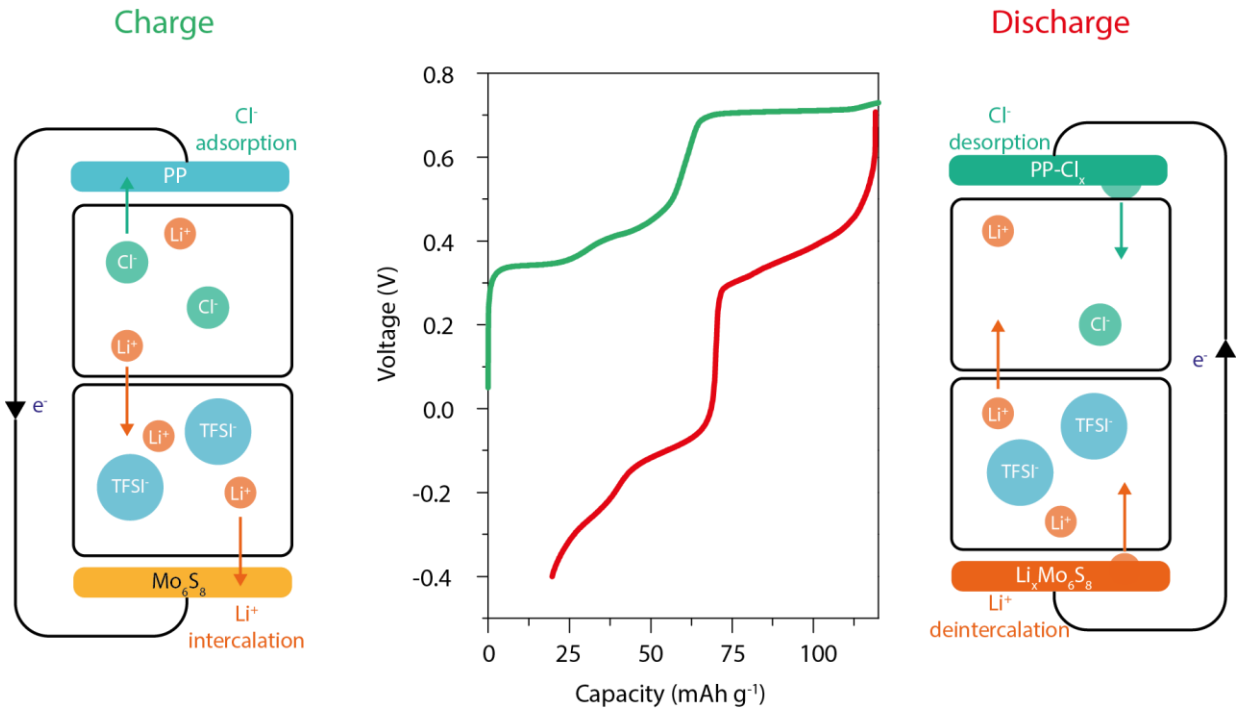

Figure III-20. First charge (green) and discharge (red) cycle obtained for a dual ion battery using a 20 m LiTFSI-18 m LiCl ABS electrolyte with a polypyrrole chlorine adsorption positive electrode and a negative Mo_6S_8 negative electrode. Capacity is expressed based on the Mo_6S_8 mass. Cycling was done at a C-rate of 1 (one mole of electron per mole of active material per hour), based on Mo_6S_8 mass.

During the charge of the device, chloride ions can undergo an oxidative adsorption on the PP electrode:

$$x\ Cl^- + PP = PP - Cl_x + x\ e^- \quad \text{(III-3)}$$

while Li^+ ions are intercalated in the Mo_6S_8 anode:

$$x\ Li^+ + Mo_6S_8 + x\ e^- = Li_xMo_6S_8 \quad \text{(III-4)}$$

On the contrary, the discharge of the cell must involve the reductive desorption of chloride ions and the oxidative deintercalation of lithium cations. Thus, such system requires the presence of chloride ions at the PP electrode. However, the negative electrode Mo_6S_8 cannot be cycled in regular aqueous electrolytes such as LiCl-H_2O as it operates at voltages below the HER. Nevertheless, this issue can be alleviated by cycling in WiSEs thanks to the formation of a

fluorinated SEI, as discussed above in this chapter.[147] Hence, this system appears as a good prototype to test the viability of ABSs as electrolytes for dual-ion batteries. Since a reversible electrochemical trace is obtained, this experiment confirms the possibility of using ABS to develop dual-ions batteries with different anolyte and catholytes in absence of any membrane. In particular, the interface between the two phases remains stable even when an electric field is applied. Because a liquid-liquid interface is present, the transfer of Li^+ cations between the two aqueous phases is expected during the battery operation to maintain the charge neutrality in the both phases, raising questions about the mechanism for the ion transfer at a water-water interface. From a practical point of view, further improvements, such as stability of the positive current collector in presence of Cl^- and reducing the large hysteresis observed in this preliminary experiment, would be required to assemble an effective dual ion battery based on ABS electrolytes.

More recently, transition-metal free batteries based on a new "intercalation-conversion" chemistry were proposed.[210] To assemble these batteries, a water-in-bisalt[149] electrolyte (WiBSEs) consisting in a mixture of LiTFSI and LiOTf (lithium triflate) is employed. Regarding the electrode materials, the prototypical anode material, *i.e.* graphite in this case (coated with a polymer to ensure the stability with the WiBSEs),[151] is used as the negative electrode to reversibly intercalate Li-ions. However, the choice of the positive electrode is more novating: it consists in a composite made from graphite, lithium chloride and lithium bromide allowing the intercalation and conversion of chloride and bromide ions into the graphite and so called LBCG (**Figure III-21 a**). Indeed, it was proven by various material characterization techniques (Raman, XAS, etc.) that the bromide and chloride ions can undergo successive oxidative intercalation into graphite positive electrode:

$$Br^- + C_n = C_n[Br] + e^- \quad \text{(III-5)}$$

$$Cl^- + C_n[Br] = C_n[BrCl] + e^- \quad \text{(III-6)}$$

while lithium is intercalated into graphite at the negative electrode:

$$2\,Li^+ + C_n + 2\,e^- = Li_2C_n[BrCl] \quad \text{(III-7)}$$

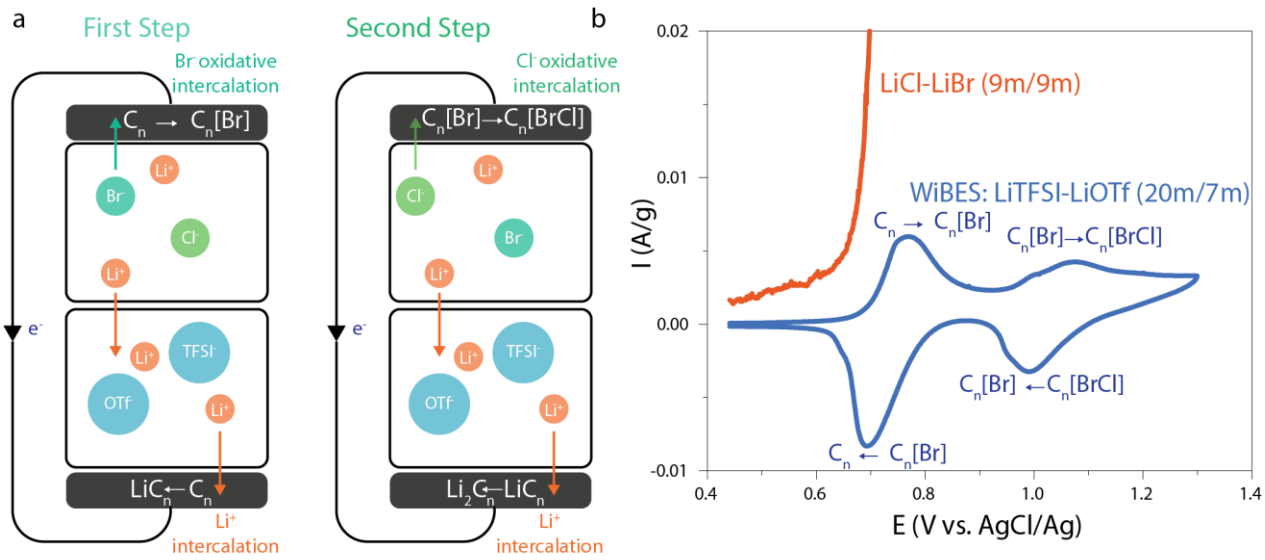

Figure III-21. a) Schematic representation of the two electrochemical steps occurring during the operation of the LBCG battery. **b)** Cyclic voltammogram of the LBCG composite (LiCl, LiBr and graphite powder mixed with PVDF binder) in (blue) WiBSE (LiTFSI/LiOTf) or (orange) in a superconcentrated LiCl-LiBr (7m/7m) electrolyte. The composite electrodes were pressed on a Ti-gauze and the potentials were measured against a 3M AgCl/Ag electrode. The current densities are normalized with the mass of composite. Because intercalation processes are relatively slow, a 0.05 mV scan-rate was employed for both experiments. A large excess of capacitive carbon YP50 composite was used as a counter electrode.

Because these aqueous batteries theoretically outperform the state of the art organic Li-ion, it would be prime of interest to rationalize how they operate. Especially, the operation of the cathode is not straightforward. It was indeed reported that upon dissolution of a tiny amount of lithium halide when in contact with the electrolyte, an ABS is locally formed at the cathode. Nevertheless, it was not proven that the formation of an ABS is required to suppress the electrolyte irreversible oxidation (OER or chlorine/bromine evolution reactions). To further test this hypothesis, we assembled different three electrode cells (**Figure III-21 b**). The first one is a replicate of the cell proposed in the original study, using a WiBSE electrolyte (LiTFSI 20 m combined LiOTf 7 m) while a second one was built using a concentrated LiCl/LiBr (9 m/9 m) solution as electrolyte. The reversible intercalation conversion of bromide and chloride was only observed in presence of the WiBSE, while an exponential wave corresponding to irreversible electrolyte oxidation was observed in presence of the LiCl/LiBr electrolyte. These experimental observations prove that the formation of an ABS at the cathode is required to trigger the bromide-chloride intercalation conversion reactions and opens questions about the exact role of the ABS at the cathode, which will be the object of further studies in the group.

III.4 Conclusion of the chapter

In this chapter we investigated the water reactivity in superconcentrated aqueous electrolytes. While WiSEs are known to have a larger intrinsic oxidative stability related to double-layer effects, we found that their negative stability is rather related to the formation of a SEI. Indeed, we could not observe drastic shift of the water reduction onset potential depending on the concentration or on the nature of salt in the electrolyte. Combining *operando* electrochemical measurements with material characterization techniques, we could demonstrate that despite water reduction occurs, the OH^- generated during the HER degrades $TFSI^-$ anions into fluorine containing products that precipitate due to the common ion effect to form the SEI. Thus, the aging properties of the SEI will govern the long-term stability of this aqueous superconcentrated electrolytes. Recent studies show that despite a good passivation of the negative electrode is obtained during the first cycles, the efficiency of WiSEs based systems decreases when cells are not operated or are cycled at higher temperatures.[211] During the time of this thesis, new generations of WiSEs were developed, with even greater salt concentrations.[212–215] Nevertheless, despite these aqueous electrolytes exhibiting electrochemical stability windows greater than the one measured for pure water, they are mainly constituted of organic salts, water representing less than 15 w% of the electrolyte (**Table III-3**), killing the cost and sustainability advantages initially conferred to WiSEs when compared to classical organic electrolytes.

System	Stability	Water (w%)
WiSE[147]	2.7 V	15 %
Hydrate-Melt[135]	3.0 V	10%
Asymmetric [214,215]	5.0 V	5%

Table III-3. Electrochemical stability window and water weight content of various superconcentrated electrolytes.

In order to overcome the drawbacks related to the high concentration of WiSEs, we tried to dilute organic anions and to formulate them in superconcentrated brines. Doing so, we observed the formation of ABSs. Interestingly, the formation of ABSs was reported to strongly depend on

how ions interact with water molecules surrounding them.[175] Nevertheless, viscosity measurements revealed that such explanation does not hold for the salts we used (lithium halides and sulfonylimides). Combining density measurements with molecular simulations, we investigated numerous physical parameters as potential descriptors to predict the formation of ABSs. The size of the largest (organic) anion appears to be critical to determine how "easy" it is for two salts to segregate into two coexisting aqueous phases, but the results are less clear concerning the impact of the size of the smallest (inorganic) anion. The comparison between Br^-, I^-, NO_3^- and ClO_4^- in which the two halides form ABSs with LiTFSI while the two others do not, shows that the local interaction with the water molecules, as described by their hydrophilic character or through the corresponding radial distribution functions, does not play a crucial role. Instead, a geometrical analysis of the solvation shell shows important differences between the two pairs of ions in terms of occupied volume and asphericity, which hints towards an important role of the packing ability of the ions, hence their overall shape, on the formation of ABSs.

Also, this study helped us to better understand how water molecules behave in electrolytes that are prime of interest for electrochemical energy storage devices. While models such as "water fingers" rationalizing the physics for the transfer of ions at the liquid-liquid interfaces have already been proposed,[216,217] it would be important to adapt them and explain how ion-transfers occur at ABSs interfaces where the solvent is the same in both phases. Despite this chapter showing that at that stage superconcentrated electrolytes and ABS remains a curiosity for electrochemical devices, we utilized the fundamental questions that their formation raised to tackle practical challenges related to intercalation electrode dissolution in rechargeable batteries as discussed in the next chapter.

Chapter IV - Reversible intercalation in vanadium halides enabled by the use of superconcentrated electrolytes[k]

IV.1 Motivations

The previous chapters were mainly devoted to the understanding of the environment and reactivity of water molecules in complex electrolytes. Our focus was paid on understanding the impact of the electrolyte structure on the kinetics at the electrode/electrolyte interface, but fixing the electrode to metallic ones without focusing on the effect of the electrolyte on the stability of the electrode. However, recent developments in batteries and electrocatalysis fields clearly highlight the need to take the electrolyte/electrode stability into account when designing a new electrode material. Such paradigm is well illustrated by the absence of cheap/abundant transition-metal based materials for the OER in acidic electrolytes, because such materials would readily dissolved in such corrosive conditions. Also, similar dissolution issues find applications in other fields such as LIBs.

Indeed, throughout its history, LIB research has witnessed a frenetic race for designing new intercalation compounds, so that most of the crystallographic families with open framework have been investigated and though chances to discover new promising phases are slim. Nevertheless, some compounds sharing similar structures with those of archetypal LIBs cathode materials have never been envisioned as potential host materials. For instance, while transition metals oxides and sulfides have been widely studied, members of the vanadium tri-halide family VX_3 (X = Cl, Br or I) were never investigated as battery intercalation compounds despite sharing similar structure with the iconic Li-ion cathode layered materials TiS_2 and $LiCoO_2$. Yet, recent studies highlight the interesting physical properties of theses vanadium halide phases.[218,219] For instance their magnetic and electronic structures can be finely tuned by playing with the interlayer coupling between the Van der Walls gap.[220] Such structural modifications are easily achieved through cation intercalation,[221] reinforcing our motivation for testing these materials as Li intercalation hosts.

[k] This chapter is based on the peer-reviewed article I co-authored: Dubouis, N.; Marchandier, T.; Rousse, G.; Marchini, F.; Fauth, F.; Avdeev, M.; Iadecola, A.; Porcheron, B.; Deschamps, M.; Tarascon, J.-M.; Grimaud, A. Superconcentrated Electrolytes Widens Insertion Electrochemistry to Soluble Layered Halides, *Nature Materials*, **2021**.

However, the absence of reports on layered halides intercalation compounds is partially explained by their high solubility in polar solvents, as highlighted by their use as vanadium precursors in redox-flow batteries.[222]

As briefly explained in the introduction, the (un)stability of materials in liquid electrolyte was already one of the main hurdles that has delayed the commercialization of secondary lithium-ion batteries relying on insertion reactions. Indeed, the physical and chemical integrity of carbonaceous electrodes were found altered upon lithium intercalation in polypropylene carbonate (PC) based electrolytes initially employed.[223] Such difficulty was later on addressed by tuning the lithium solvation shell with the use of EC, suppressing the co-intercalation of PC and forming a stable passivating layer onto the carbon anode,[224] or more recently by using superconcentrated electrolytes.[225–227] In turn, this example demonstrates that an electrolyte engineering approach can be used to unlock lithium intercalation in phases hitherto believed to be too unstable for the application. Besides graphite intercalation, superconcentrated electrolytes have also shown helpful functionalities to solve most fundamental drawbacks relative to the use of carbonate based electrolytes, such as incompatibility with Li-metal, instability at high voltages, flammability or dissolution of transition metals from the cathode.[134,135,145,146,228–231] One can legitimately wonder whether recent advances made in the comprehension of electrolytes' properties could help to overcome stability issues that have hampered the reversible intercalation of Li cations into halide-based compounds, such as the members of the VX_3 family.

In this chapter, in the light of what we observed in the previous chapter, *i.e.* that halides do not mix with sulfonylimide, we investigated the electrochemical insertion of lithium into VX_3 compounds using superconcentrated electrolytes. For that, we studied the electrochemical behavior of three vanadium-based halides: VCl_3, VBr_3 and VI_3. Combining electrochemical measurements with structural (synchrotron X-ray and neutron diffractions) and solubility measurements, we demonstrate that Li^+ can be reversibly intercalated into these halides unlike in classical diluted electrolytes or ionic liquids into which they readily dissolve. Doing so, we open the door to new intercalation chemistries going beyond our current knowledge regarding oxides, sulfides or polyanionic compounds, which will serve the field of materials science to develop *à façon* materials with tunable physical properties.

IV.2 Synthesis and characterization

While VCl_3 is commercially available, VI_3 and VBr_3 were grown in evacuated quartz sealed tubes by reacting elemental vanadium, iodine and bromine, with a slight excess of halides. After heating, single crystals were obtained and further purified under dynamic vacuum to remove halides impurities (methods for details). The structure[l] of the as synthetized materials was obtained from Rietveld refinements of XRD patterns (**Figure IV-1**, **Supplementary Table IV-1** and **Supplementary Table IV-2**) was found to match those reported in the literature,[218,219] where edge-shared VX_6 octahedra form honeycomb layers stacked along the *c* direction with a AB sequence (O1 type structure[232]).

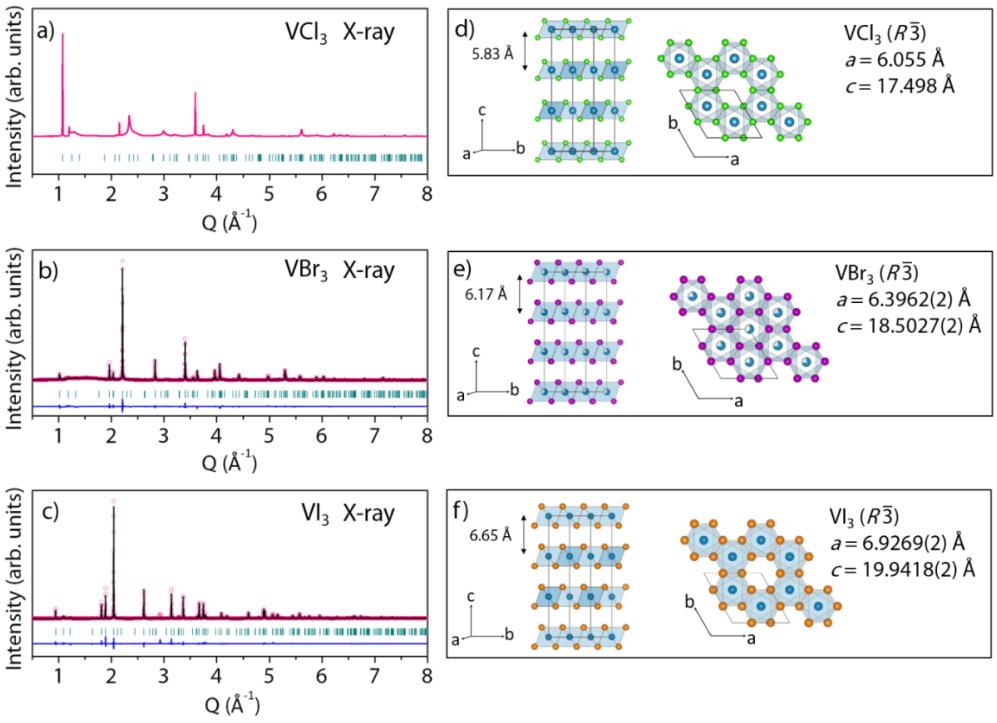

Figure IV-1. a) Indexed synchrotron XRD (λ = 0.41378 Å) pattern for VCl_3 where vertical green tick bars stand for the Bragg positions. **b)** Rietveld refinement of VBr_3 and **c)** VI_3 synchrotron patterns (λ = 0.41378 Å). The corresponding structural models are reported in the **Supplementary Table IV-1** and **Supplementary Table IV-2**. The pink circles, black continuous line, and bottom blue line represent the observed, calculated, and difference patterns, respectively. Vertical green tick bars stand for the Bragg positions. Corresponding structures for **d)** VCl_3, **e)** VBr_3 **and f)** VI_3 where vanadium, chlorine, bromine and iodine atoms are represented in blue, green, purple and orange, respectively.

[l] The analysis of the diffraction data was conducted by T. Marchandier and G. Rousse from our lab

IV.3 Electrochemical activity of VX_3 in various electrolytes

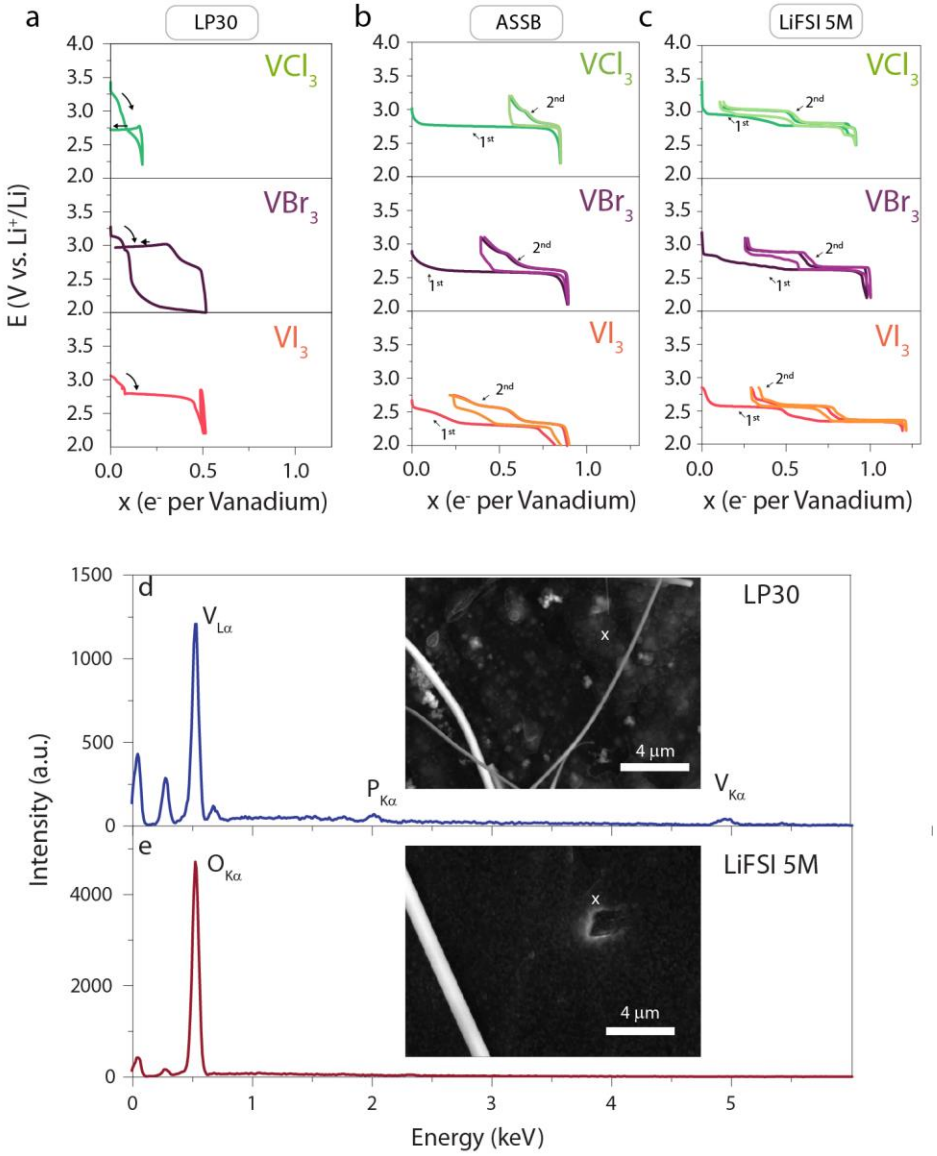

Figure IV-2. a) Galvanostatic cycling of VCl_3 (green), VBr_3 (purple) and VI_3 (red) at C/40 using LP30 electrolyte and a $Li_{(Metal)}$ negative electrode. **b)** Galvanostatic cycling of VCl_3 (green), VBr_3 (purple) and VI_3 (red) at C/40 in a solid-state configuration using argyrodite electrolyte and InLi negative electrode. **c)** Galvanostatic cycling of VCl_3 (green), VBr_3 (purple) and VI_3 (red) at C/40 using a 5 M LiFSI in DMC electrolyte and a $Li_{(Metal)}$ negative electrode. For **b)** and **c)** the first two cycles are plotted. The "x" axes represents the arithmetic number of mole of electrons exchanged per mole of active material. If the current density is negative (discharge) x increases (reduction of the active material), while x decreases during the charge (oxidation of the material). **d)** Electron dispersive X-ray (EDX) spectra recorded for Li negative electrodes after the full discharge of VI_3 half-cells at C/40 in LP30 and **e)** LiFSI 5 M. The corresponding scanning electron microscopy images are given in insets. The white cross shows the point where the EDX spectra were recorded.

These materials were tested by assembling battery half-cells to investigate their ability to electrochemical insert lithium cations (Li^+), using state-of-the-art LIB electrolyte LP30 (1 M of lithium hexafluorophosphate in an equivolume mixture of dimethyl carbonate, DMC). For these three compounds (**Figure IV-2 a**), a relatively small discharge capacity is obtained and the process is clearly irreversible as no capacity is observed during the subsequent charge. Moreover, the electron dispersive X-ray (EDX) spectra of the lithium negative electrode after discharge (**Figure IV-2 d**) shows signals at energies characteristic from $V_{L\alpha}$ and $V_{K\alpha}$ pointing to the dissolution of the cathode material and an irreversible solution process as the origin for the limited discharge capacity. Hence, there is a need to develop a new strategy to overcome these dissolution issues.

The first attempt consists in replacing the liquid electrolyte by a solid-state electrolyte in which no dissolution can occur. Effectively, when composite cathodes are prepared and tested in an all-solid-state battery configuration (see methods), the electrochemistry is greatly improved compared to that in LP30, thus hinting towards the electrochemical intercalation of Li^+ into VX_3 compounds (**Figure IV-2 b**). However, in such configuration the complex interplay between ionic conductivity of the solid electrolyte, chemical compatibility between components and electrode microstructure requires a separate optimization of electrode formulation and testing conditions for each compound. This is indeed exemplified in the chemical incompatibility found between VBr_3 or VI_3 and argyrodite solid-state electrolyte, evidenced as a clear color change-upon mixing. This observation, combined with the difficulty of assembling ASSB and characterizing active materials in such configuration, renders critical the search for an adequate liquid electrolyte in which halides would be stable.

To select the correct electrolyte, reconsidering the physico-chemical properties of classical aprotic LIBs electrolytes proves to be insightful. Commercial LP30 electrolyte is made from a mixture of carbonate solvents (EC and DMC) in which a salt ($LiPF_6$) is dissolved. While EC is a polar component essential to ensure both ion-pairs dissociation and the formation of a stable solid SEI at the negative electrode, its high dielectric constant is presumably responsible for the VX_3 dissolution. Hence, not only the chemical composition of the electrolyte must be modified to prevent vanadium cations and/or halides solubility but also its solvation properties. Inspired by the recent observation of the non-miscibility of lithium halides salts with lithium imide salts,[167,233] we

then investigated the electrochemical behavior of vanadium halides in superconcentrated electrolytes. As shown in **Figure IV-2 c**, when LP30 is substituted with a 5 M LiFSI in DMC electrolyte (denoted LiFSI 5 M hereafter), the electrochemical behavior of the three different phases is drastically even at C-rates as low as C/40[m], indicating that superconcentrated electrolytes can tackle the solubility issue observed in LP30. Indeed, albeit some initial irreversible capacity being observed in the first cycle, these results suggest that almost 1 Li^+ per formula unit can be reversibly inserted into these hosts. Furthermore, no vanadium was found at the negative electrode at the end of discharge (**Figure IV-2 e**) as indicated by the absence of signals at the $V_{K\alpha}$ energy. Overall, switching from regular diluted carbonate-based electrolytes to a superconcentrated electrolyte appears as a key to unlock the electrochemical intercalation of Li^+ into halide layered compounds.

IV.4 Determination of the mechanism for the phase transformation upon cycling

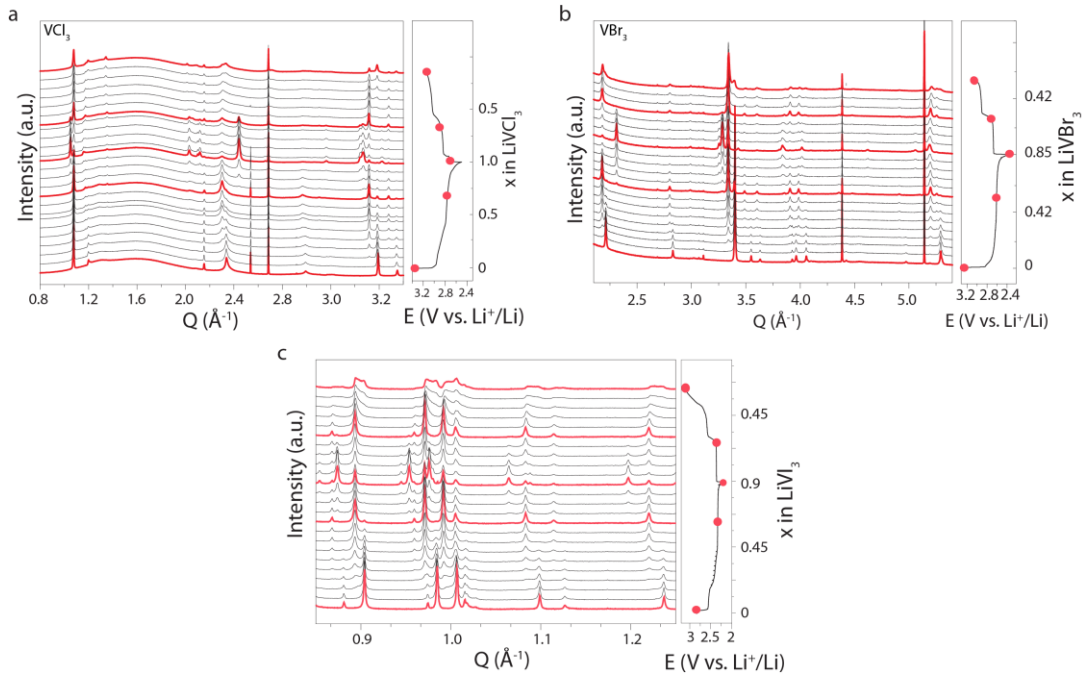

Figure IV-3. *Operando* synchrotron X-ray diffraction patterns recorded for **a)** VCl_3 **b)** VBr_3 and **c)** VI_3 upon cycling (left). The electrochemistry was conducted at C/20. The potential profile recorded during the *operando* measurement is plotted on the right panel.

[m] As for a note, a C-rate of C/x means that the current density is set in order to insert (reduction) or remove (oxidation) 1 mol of electron per mol of active material in x hours.

To grasp further insights into the behavior upon cycling of these halides, their structural evolution was monitored by *operando* synchrotron X-ray diffraction (SXRD). For Li_xVCl_3 (**Figure IV-3 a**), two successive biphasic processes can be distinguished upon discharge, consistent with the two plateaus previously observed (**Figure IV-2 d**). For $0 < x < 0.6$, the pristine phase disappears at the expense of an intermediate phase which is then replaced by a fully lithiated phase. On charge, the process is found reversible with the discharged phase being converted back to the pristine one; similar reversible bi-phasic intercalation processes are observed for both VBr_3 and VI_3 (**Figure IV-3 b and c).** Having proved the full structural reversibility of the insertion process and the absence of vanadium dissolution, we believe that part of the observed irreversibility capacity is mostly nested in minute amounts of amorphous impurities of chemically absorbed I or Br in our starting materials that were made by gas phase reactions using an excess of halides. The structure of every intermediate and fully lithiated phases were then determined by Rietveld refinement. This analysis reveals that the O1-type layered structure ($R\bar{3}m$ space group) of the pristine is preserved for every intermediate phases, with the sole evolution of the lattice parameters (**Figure IV-4** and **Supplementary Table IV-3** and **Supplementary Table IV-4**).

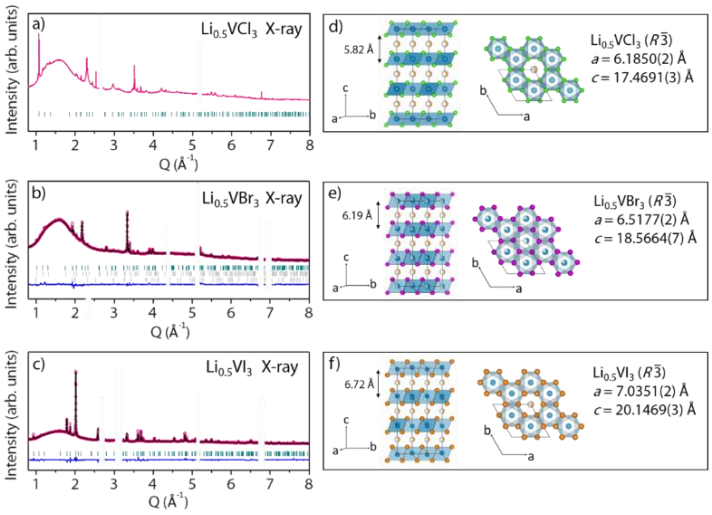

Figure IV-4. a) Indexed synchrotron XRD (λ = 0.41378 Å) pattern for $Li_{0.5}VCl_3$ where vertical green tick bars stand for the Bragg positions. **b)** Rietveld refinement for $Li_{0.5}VBr_3$ and **c)** $Li_{0.5}VI_3$ synchrotron XRD **c)** patterns (λ = 0.41378 Å), corresponding to the structural model reported in the **Supplementary Table IV-3** and **Supplementary Table IV-4**. The pink circles, black continuous line, and bottom blue line represent the observed, calculated, and difference patterns, respectively. Vertical green tick bars stand for the Bragg positions. Structure of **d)** $Li_{0.5}VCl_3$, **e)** $Li_{0.5}VBr_3$ and **f)** $Li_{0.5}VI_3$. Vanadium, chlorine, bromine, iodine and lithium atoms are represented in blue, green, purple, orange and yellow, respectively. Some parts of the pattern have been excluded due to the presence of Li or Be diffraction peaks.

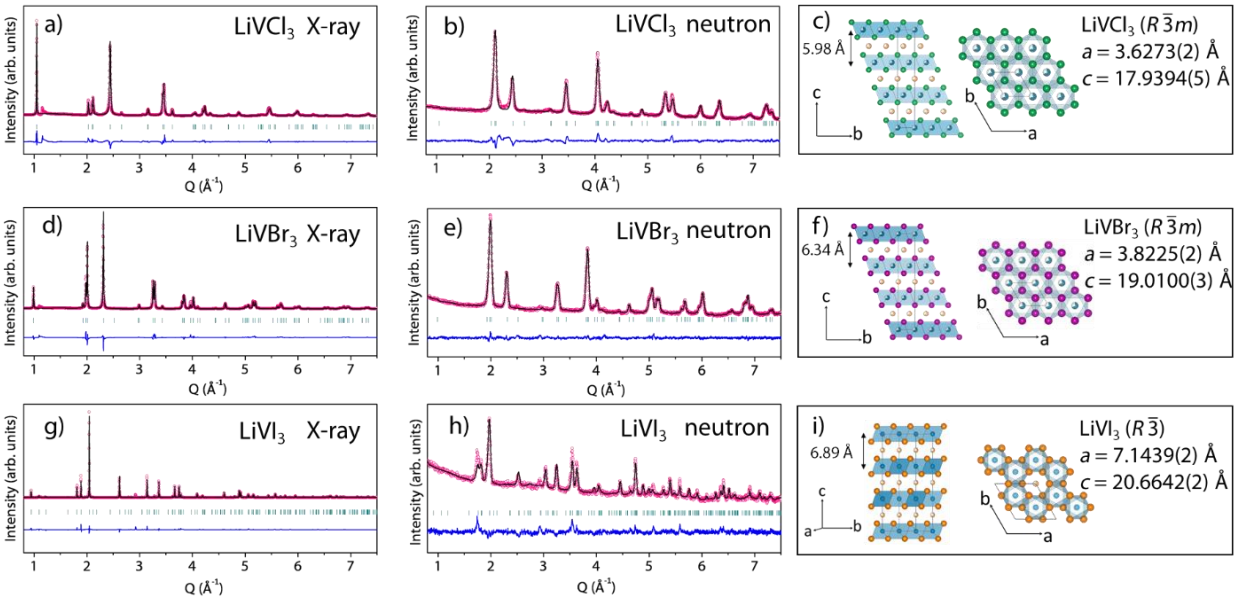

Figure IV-5 a) Synchrotron XRD (λ = 0.41378 Å) Rietveld refinement for $LiVCl_3$, **b)** $LiVBr_3$ and **c)** $LiVI_3$. **d)** Neutron diffraction (λ = 1.6220 Å) Rietveld refinement for $LiVCl_3$, **e)** $LiVBr_3$ and **f)** $LiVI_3$. The corresponding structural models are reported in the **Supplementary Table IV-5**, **Supplementary Table IV-6** and **Supplementary Table IV-7**. The pink circles, black continuous line, and bottom blue line represent the observed, calculated, and difference patterns, respectively. Vertical green tick bars stand for the Bragg positions. **g)** Structure of $LiVCl_3$, **h)** $LiVBr_3$, **i)** $LiVI_3$. The vanadium, chlorine, bromine, iodine and lithium atoms are represented in blue, green, purple, orange and yellow, respectively.

Unlike for the intermediate phases, the structure of the fully discharged phases is dependent on the nature of the anion. Hence, while for VI_3 the fully discharged phase possesses the O1 structure, for VCl_3 and VBr_3 a distortion to an O3 layered structure ($R\bar{3}m$ space group) is observed (**Figure IV-5**, **Supplementary Table IV-5**, **Supplementary Table IV-6** and **Supplementary Table IV-7**), in agreement with a previous report on a VCl_3 lithiated phase prepared by a solid-state route.[234] Such a subtle Li-driven structural difference depending upon the nature of the halide may simply be rooted in their size, following the ionic radii Cl < Br < I. Finally, and to no surprise for layered compounds, it was confirmed by neutron diffraction experiments that lithium cations sit in the interlayer of the phases (**Figure IV-5**).

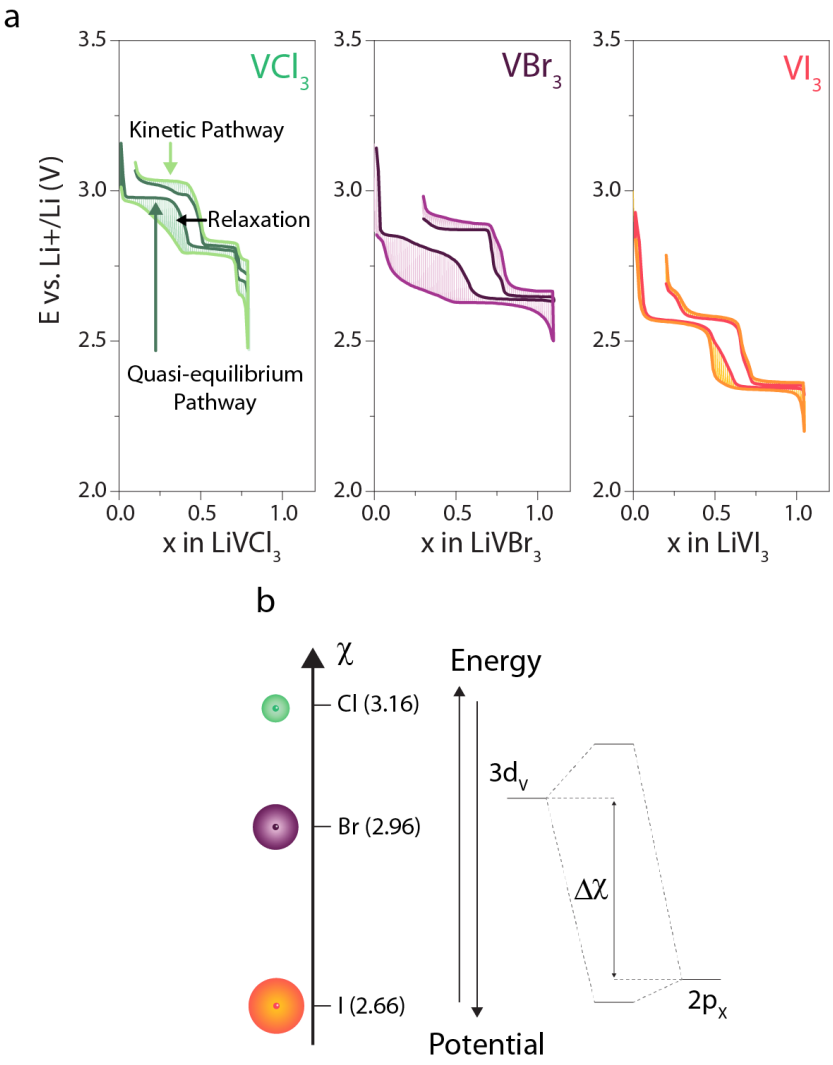

Figure IV-6. a) Galvanostatic intermittent titration technique measurements of VCl_3 (green), VBr_3 (purple) and VI_3 (red) at C/40 alternating between 30 min galvanostatic and 2 hours of relaxation. b) Electronegativity of the halide ligands according to the Pauling scale and impacts on the orbital structure.

To gain a deeper understanding of the kinetics of the redox process taking place during intercalation, galvanostatic intermittent titration technique (GITT) was performed. Briefly, a constant current pulse is applied (here for 30 min), followed by a relaxation time in which no current is passed through the cell (here 2 hours). Monitoring the cell voltage during both sequences allow to compare the "kinetic" pathway (**Figure IV-6 a**) with a quasi-equilibrium pathway obtained by recording the potential after the relaxation (**Figure IV-6 a**). Interestingly, the quasi-equilibrium path is almost identical for the three halides. Two discharge plateaus are observed, only differing in their potentials which correlate nicely with the ligand electronegativity (the more

electronegative the halide, the higher the potential, **Figure IV-6**). This result suggests that the electrochemical activity is solely related to the redox potential of the V(III)/V(II) couple. As for a note, the hysteresis (*i.e.* overvoltage) can be approximated by the difference of voltage at a given "x" between the kinetic and quasi-equilibrium pathways. Such hysteresis can originate from different physical parameters (iR-drop, ion-diffusions, electronic conductivity, structural rearrangements, etc.). Here, the kinetic pathway was found to strongly depend from the batch of VBr_3 and VI_3 synthetized materials. Because single crystals were obtained, the main difference between the batches is probably related to a difference in the particle sizes. Hence, the hysteresis estimated herein probably takes its origin from ion-diffusion and/or electronic conductivity issues.

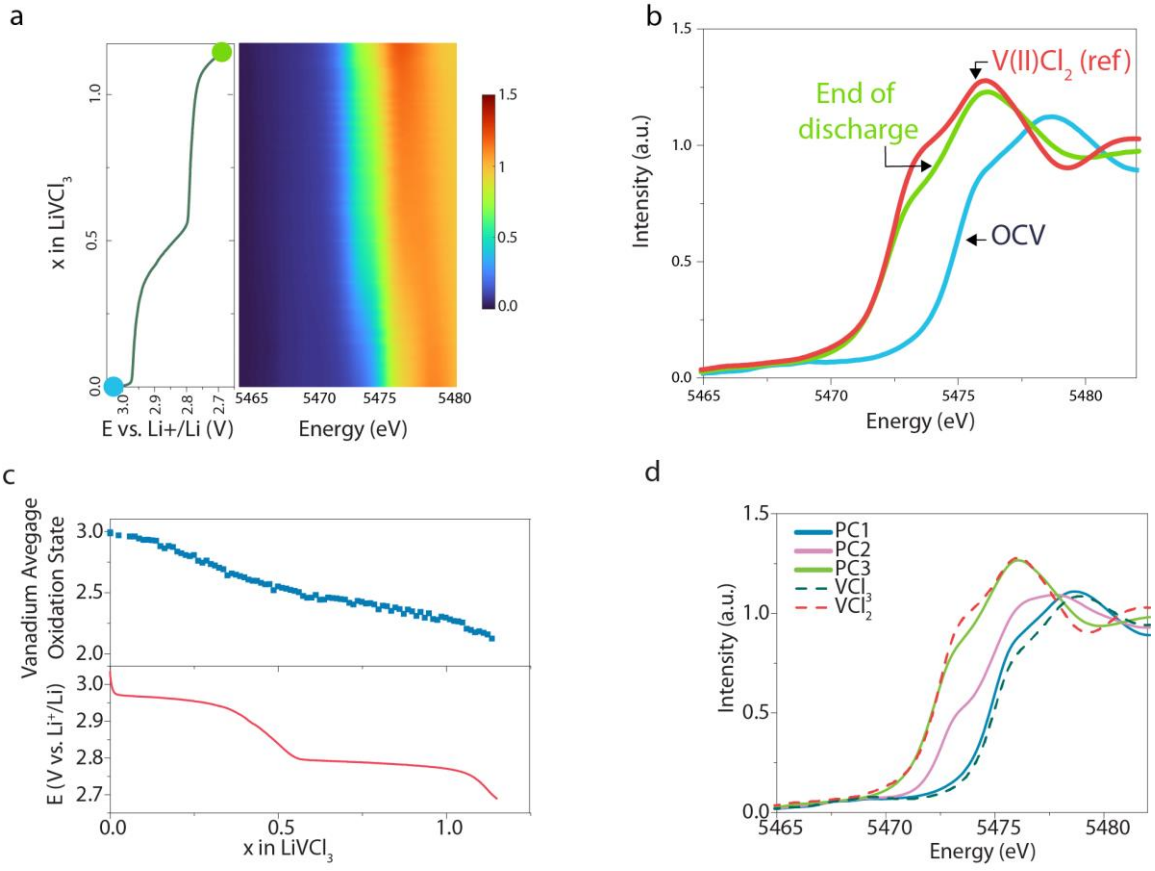

Figure IV-7. a) *Operando* evolution of the V K-edge spectra measured by X-ray absorption spectroscopy during the discharge of VCl_3 at C/20. **b)** Comparison of the spectra recorded at the open circuit voltage (blue), end at the end of discharge (green) with VCl_2 reference material (red). **c)** Evolution of the vanadium average oxidation state as a function of the electrochemical cycling for VCl_3 obtained from PCA analysis conducted on V K-edge *operando* XAS dataset. The cycling was done at C/20 in 5 M LiFSI DMC. d) Reconstructed principal components 1 (blue), 2 (pink), 3 (green) obtained by MCR-ALS analysis compared to VCl_3 (dark green) and VCl_2 (red) references.

To validate this charge compensation mechanism, *operando* XAS[n] was performed on VCl_3 (**Figure 3 c**). During the discharge, a shift of the V K-edge position to lower energy (**Figure IV-7 a)** reveals a shift from V(III) (pristine) to V(II) (**Figure IV-7 b**). Indeed, the end of discharge spectra K-edge position matches almost perfectly the one of the $V(II)Cl_2$ reference. The overall evolution during the discharge can be fully described using three principal components: the pristine phase, the end of discharge phase and an intermediate phase (**Figure IV-7 c** and **d**), confirming the existence of an intermediate phase as previously observed during *operando* synchrotron XRD. The whole *operando* XAS dataset was used as an input for the principal component analysis (PCA) to determine the number of independent. The XAS spectrum of these principal components was thus reconstructed using multivariate curve resolution−alternating least-squares (MCR-ALS) analysis.[235] Three principal components are needed to describe the whole evolution of the XAS spectra during the Li^+ intercalation. They are reported along the references in **Figure IV-7 d**. The first principal component (PC1) corresponds to the first *operando* XAS spectrum for which the V oxidation state is found close to the expected V(III). On the other hand, the edge position of the third principal component (PC3) agrees with that of VCl_2, confirming the V(III)/V(II) redox mechanism upon Li insertion. The second component (PC2) cannot be expressed as a linear combination of PC1 and PC2, and corresponds to a vanadium +2.55 oxidation state. The details (variance plot and evolution of up to 8 PCs during the discharge) for the PCA analysis are given in **Supplementary Figure IV-1** and **Supplementary Figure IV-2**. Because the evolution of the vanadium redox number should counter balance the quantity of lithium inserted in the phase, the determination of the oxidation state for the intermediate phase further suggests its composition: $Li_{0.45}VCl_3$, leading to a better understanding of the Li/V stoichiometry in the intermediate phase.

IV.5 Rationale for the decreased solubility of halides in superconcentrated electrolytes

In summary, we directly proved that superconcentrated electrolytes can be used to explore new intercalation compounds and synthesize novel phases for chemistries previously disregarded as highly soluble in liquid electrolytes. To rationalize this effect, the solubility of VCl_3 was measured at different concentrations of LiFSI as supporting salt in DMC by inductively coupled plasma mass spectrometry (ICP-MS). To do so, the powders were stirred during 3 days at room

[n] A. Iadecola measured and analyzed the data from the *operando* XAS cells

temperature (~25°C in an Ar filled glovebox) and the solutions centrifuged and filtered. The organic solutions obtained were then extracted/diluted in 2w% HNO_3 solutions in order not to saturate the ICP-MS detector (c_V < 1 ppm).

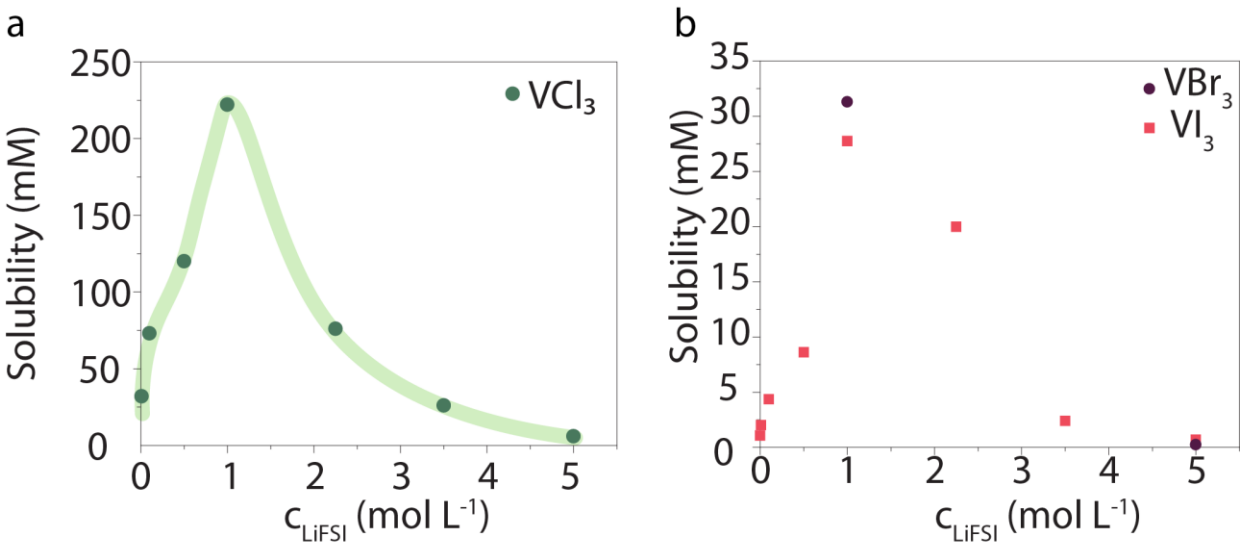

Figure IV-8. a) Evolution of VCl_3 solubility measured by ICP-MS LiFSI/DMC electrolytes as a function of the LiFSI concentration. **b)** Same for VBr_3 (purple) and VI_3 (red)

The results, shown **Figure IV-8 a,** reveal an initial increase of the vanadium solubility as a function of the LiFSI concentration followed by a drastic decrease when LiFSI concentration is higher than 1 M, reaching values as low as few mM for the LiFSI 5 M superconcentrated electrolyte. Furthermore, vanadium chloride powder was mixed with 5 M LiFSI in DMC solutions for 3 days at 55°C and 85°C, before allowing the solutions to rest at room temperature and monitoring the amount of dissolved vanadium. Since the measured concentrations were extremely close to the ones obtained at room temperature (c_V(RT) = 6.3 mM, c_V(55°C) = 7.6 mM and c_V(85°C) = 5.5 mM), any scattering of the results due to a kinetic hindering of the powder dissolution can be discarded to explain the aforementioned trend. Moreover, similar results showing a lower solubility at high LiFSI concentrations were obtained for VI_3 and VBr_3 (**Figure IV-8 b**). Thus, this peculiar bell shape reflects a thermodynamically-driven phenomenon.

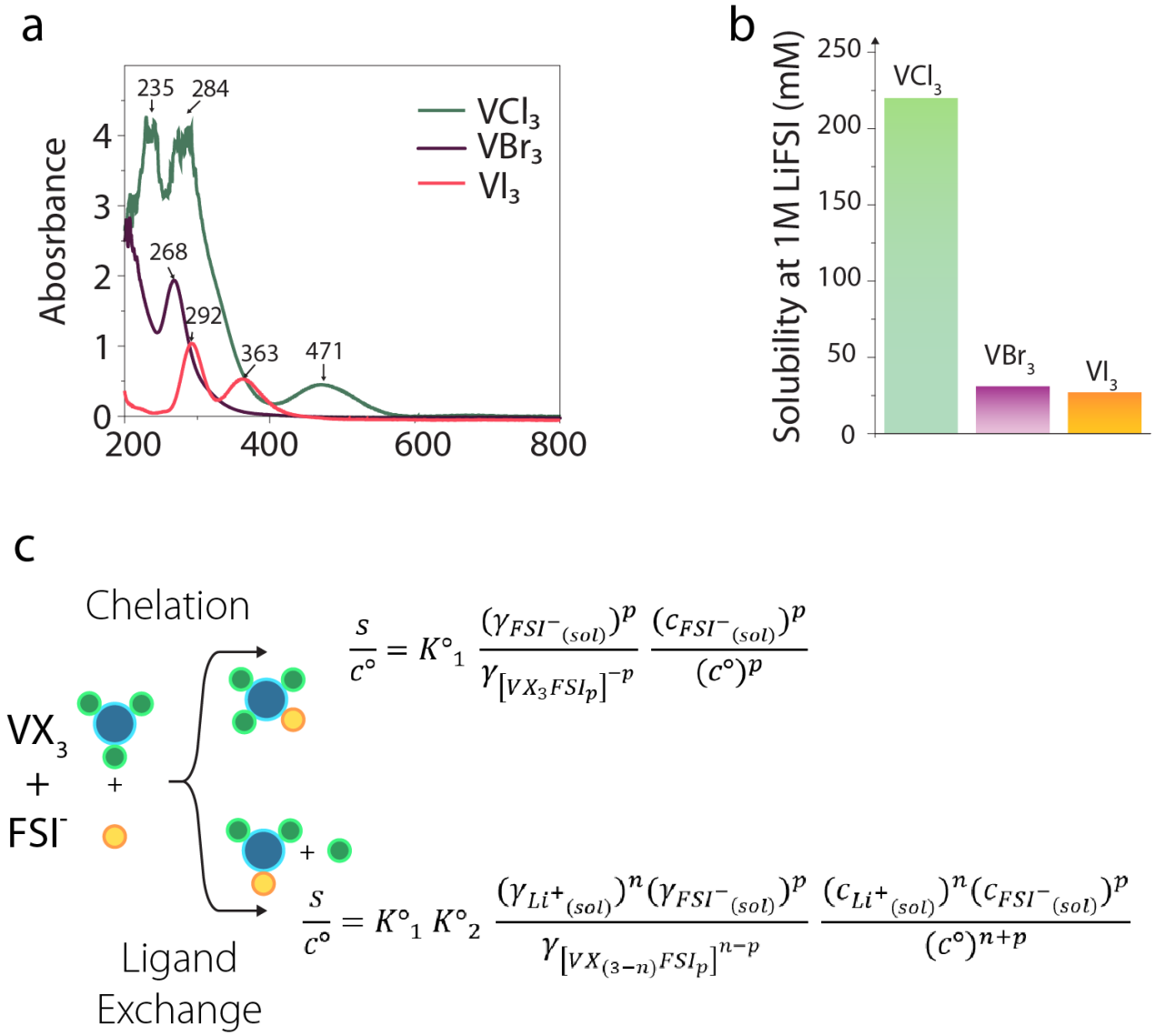

Figure IV-9. a) UV-vis spectra for 1 M LiFSI in DMC solutions saturated in VCl_3 (green), VBr_3 (purple), and VI_3 (red). The spectrum for VCl_3 shows some saturation, which is related to the high vanadium concentration, even when measured in a 0.1 mm optical pathway cuvette. **b)** Solubilities measured for VCl_3 (green), VBr_3 (purple) and VI_3 (orange) by ICP-MS in a 1 M LiFSI in DMC electrolyte. **c)** Expression of the vanadium halide solubility as a function of the dissolution mechanism (chelation or ligand exchange).

To derive the equilibrium law that governs the solubility of vanadium at different supporting salt concentrations, we first need to understand the nature of the dissolution reaction by identifying the chemical environment of the vanadium cations dissolved in solution. Visually, every 1 M LiFSI solution saturated with VX_3 exhibits a pronounced coloration, as evidenced by the presence of absorption peaks in their UV-vis spectra (**Figure IV-9 a**). Interestingly, the

wavelengths of the absorption peaks are halide-dependent, suggesting the formation of a vanadium-halide complex in solution. Moreover, the initial increase of the solubility with LiFSI concentration (at concentrations below 1 M) advocates for the participation of the salt anion in the formation of this complex. Such observations can be rationalized by the formation of adducts in solution in the form of $[VX_{3-n}FSI_p]^{n-p}$, through a chelation or a ligand exchange mechanism, as proposed below:

$$VX_{3\,(crist)} + p\ FSI^-_{(sol)} = \left[VX_{(3-n)}FSI_p\right]^{n-p} + n\ X^- \qquad \text{(IV-1)}$$

where n and p are integers with $0 \leqslant n \leqslant 3$ and $p > 0$ ($n = 0$ for the chelation mechanism).

Moreover, the solubility of LiCl is very low in DMC (1.3 mM in pure DMC).[236] Hence, since the VCl_3 solubility in 1 M LiFSI electrolyte is around 100 times greater than this value, Cl^- ions must be generated from the VCl_3 dissolution and should undergo an almost complete re-precipitation:

$$Li^+_{(sol)} + Cl^-_{(sol)} = LiCl_{(crist)}\ (K^\circ_2 \gg 1) \qquad \text{(IV-2)}$$

This second step, however, can hardly be observed due to the very limited amount of LiCl precipitated. Indeed, when the exact quantity of VCl_3 is added to a 1 M LiFSI solution to reach the limit of solubility (s), the quantity of chloride ions that would precipitate into LiCl can roughly be estimated to be ~ 10 mg in 1 mL of electrolyte (quantities used in this study). Such small quantity is evidently too low to be easily washed and separated by centrifugation and be further characterized by XRD, for instance.

The existence of a precipitation step can drastically shift the first equilibrium towards the formation of the product, as expressed by the equation below:

$$VX_{3\,(crist)} + p\ FSI^-_{(sol)} + n\ Li^+_{(sol)} = \left[VX_{(3-n)}FSI_p\right]^{n-p} + n\ LiX_{(crist)}\ (K = K^\circ_1\ K^\circ_2) \qquad \text{(IV-3)}$$

At the thermodynamic equilibrium, the Guldberg and Waage law of mass action gives:

$$K = K^\circ_1\ K^\circ_2 = \frac{a_{\left[VX_{(3-n)}FSI_p\right]^{n-p}}}{(a_{Li^+_{(sol)}})^n (a_{FSI^-_{(sol)}})^p} \qquad \text{(IV-4)}$$

Thus, considering the activity of a solute as the product of its concentration *c* and its activity coefficient γ, divided by the standard concentration (c° = 1 mol L^{-1}), the solubility *s* of the VX_3 salt can be expressed by the following equation:

$$\frac{s}{c^\circ} = K^\circ_1 \, K^\circ_2 \, \frac{(\gamma_{Li^+_{(sol)}})^n (\gamma_{FSI^-_{(sol)}})^p}{\gamma_{[VX_{(3-n)}FSI_p]^{n-p}}} \, \frac{(c_{Li^+_{(sol)}})^n (c_{FSI^-_{(sol)}})^p}{(c^\circ)^{n+p}} \qquad \text{(IV-5)}$$

Since the solubilities of LiBr (s_{LiBr}) and LiI (s_{LiI}) are expected to be greater than the one of LiCl in nonpolar solvents (e.g. s_{LiBr} = 4 mM in DMC at 25°C, 3 times that of LiCl)[236], one would expect $K^\circ_2(Cl) > K^\circ_2(Br) > K^\circ_2(I)$, which is consistent with the trend observed for the solubilities of the VX_3 compounds that follows $VCl_3 > VBr_3 > VI_3$ (**Figure IV-9 b**). For a chelation mechanism, $K^\circ_2 = 1$ and the solubilities of the different vanadium halides are expected to vary less than for the ligand-exchange mechanism. Hence, our experimental observations **Figure IV-9 b** point towards dissolution through a ligand-exchange mechanism.

Neglecting a variation of the activity coefficients, hypothesis which usually holds for low salt concentrations,[185] the VX_3 solubility should thus increase with the LiFSI concentration, in agreement with our experimental observations made for concentrations < 1 M (**Figure IV-8**). However, such explanation does not hold anymore at high ionic strength, regime in which activity coefficients are known to be modified.[185] First, as expressed in Equation (IV-6), a large decrease of γ_{Li^+} and γ_{Cl^-} could potentially explain the lowering of the VX_3 solubility. Nevertheless, as suggested in a recent theoretical work, the average activity coefficient of single ions is more likely to be greater at high salt concentrations.[185] Hence, the decreased solubility is rather explained by a large increase of $\gamma_{[VX_{(3-n)}FSI_p]^{n-p}}$ which, owing to the interaction of the vanadium adduct with surrounding solvent molecules, would require developing a refined model to accurately account for the variation of its activity coefficient with the ionic strength. We should further emphasize that independently on the dissolution mechanism (ligand-exchange or chelation), the VX_3 solubilities are expected to vary in a similar manner depending on the LiFSI concentration.

Our study provides the rationalization for the observed bell shape behavior: the initial increase of the solubility originates from the increased concentration of FSI^- anions, while the decrease observed in the concentrated regime arises from a large deviation from unity of the

transition-metal complex activity coefficient value. More importantly application-wise, the solubility of the fully discharged $LiVCl_3$ phase shows similar bell shape (**Figure IV-10 a**), albeit the solubility is found lower than for VCl_3 which ensures a good resistance to dissolution for the material even upon reduction. However, we note that upon long cycling a severe capacity decay is observed and can be attributed to vanadium dissolution accumulated over time (**Figure IV-10 b**). Indeed, since the cycle numbers for a similar capacity retention are much greater (approximatively threefold) when the cycling is operated at C/10 compared to C/40, part of the capacity loss is likely to be related to vanadium dissolution upon time. Obviously, future work range in better tuning the delicate electrolyte-solvent balance to improve the capacity retention both at RT and 55°C. In conclusion, these findings confirm that the fundamental framework developed in this work captures every stage of lithiation and can be transposed to the study of other intercalation compounds.

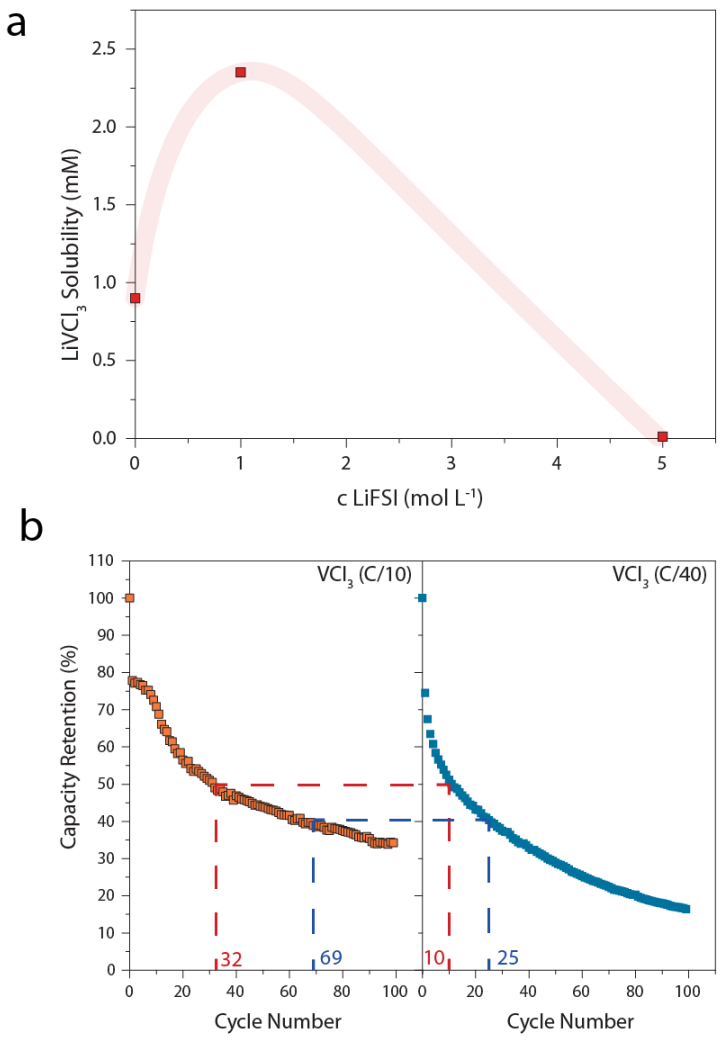

Figure IV-10. a) Evolution of $LiVCl_3$ solubility measured by ICP-MS in LiFSI/DMC electrolytes as a function of the LiFSI concentration. **b)** Discharge capacity retention obtained for VCl_3 cycled either at C/10 (orange) or C/40 (blue). The dashed lines indicate the number of cycles attained with similar capacity retention values depending on the cycling rate.

IV.6 Conclusions of the chapter

Overall, we established the use of superconcentrated electrolyte as a platform to discover new families of materials for Li^+ intercalation. Driven by the broad interest for their physical properties, we (reversibly) intercalated Li^+ into layered vanadium halides to form new layered phases, the impact of which goes beyond the sole development of intercalation electrodes for secondary batteries. Indeed, preliminary NMR suggest a fast exchange of Li^+ cations between different crystallographic sites, which does not come as a total surprise owing to the ongoing interests for halides as solid state ionic conductors. Moreover, these layered halides have been

widely investigated for their promising magnetic properties, and preliminary magnetic susceptibility measurements show that Li+ intercalation can be used to tune their magnetic structure. Aside from unlocking the synthesis of new layered structures, our study also lays the fundamental background to comprehend a so far ill-understood effect related to the use of superconcentrated electrolytes, *i.e.* the decreased solubility of active material. Indeed, we demonstrate that the low solubility of transition metal compounds in superconcentrated electrolytes originates from a shift of the solubility equilibrium, *i.e.* from a thermodynamic effect rather than a kinetics one, which also applies to current collectors whose stability in presence of corrosive anions (FSI, TFSI, etc.) was observed to increase in superconcentrated electrolytes. In general, our study highlights the critical need for solid-state chemists to include knowledge about the physical chemistry of liquids when developing novel intercalation compounds. Evidently, the future success of such explorative and collaborative work will rely on answering fundamental questions regarding equilibrium and ion activities in this novel class of electrolytes.

General conclusion and perspectives[o]

During this thesis, we developed a fundamental understanding of how the structure of liquid electrolytes may dictate their use for electrochemical applications such as water electrolysis and Li batteries. After recalling that both water electrolysis and Li batteries largely benefited from intensive research in solid-state chemistry that brought knowledge about the best electrode materials/electrocatalyst that should be used for various applications, we highlighted that one of the greatest challenges to further improve electrochemical energy conversion devices lies in our understanding of the impact of the electrolyte on the interfacial processes happening upon operation.

Especially, we first focused on the understanding of the role of water as an active molecule or as a solvent for the HER. Because in aqueous electrolytes water molecules found at the electrochemical interfaces are subject to many non-covalent interactions, we developed a fundamental framework to separately investigate how water molecules environment may modify the water reactivity. Toward that goal, we explored systems that are comparatively less studied and in which water is confined in an organic matrix, acetonitrile in our case. First focusing on short-range interactions, systems were prepared by dissolving a very scarce amount of water in acetonitrile. This confinement strategy coupled with MD simulations, and experimental characterization techniques allowed us to sketch a structure-reactivity correlation for the water molecules. We revealed that when the electronic density of water molecules is decreased by the presence of a Lewis acid or other water molecules for instance, water molecules reduction is more facile. Such results may explain why the addition of Li^+ cations may boost the kinetics for the HER in alkaline electrolytes. Furthermore, we also managed to tune the environment of the water molecules at the nanoscale. Indeed, increasing the salt concentration in these electrolytes led to the formation of aqueous rich nanodomains, in which water reactivity is exacerbated compared to the diluted case. The presence of such nanodomains at the electrochemical interface may help to transfer water-ions between the bulk of the electrolyte with the electrode-electrolyte interface,

[o] This General conclusion and perspective part is partly based on the following paper I co-authored: Serva, A.; Dubouis, N.; Grimaud, A.; Salanne, M. Confining Water in Ionic and Organic Solvents to Tune Its Adsorption and Reactivity at Electrified Interfaces. *Acc. Chem. Res.* **2021**.

which could explain the more facile water reduction observed in these electrolytes. Overall, our observations confirm that when water is the reacting molecule for the HER, the kinetics for its dissociation (*i.e.* cleavage of the OH bond) are likely to govern the HER kinetics.

Nevertheless, these observations also raised numerous questions. First, from a fundamental point of view, while insights were gained on how the water environment modifies its reactivity upon reduction, we could not directly translate it for the water oxidation reaction. Because the OER is the main source of energy penalties for the water splitting, this direction of research would probably help to further increase electrolyzers' performances. Nevertheless, one of the main experimental hurdles to be tackled is the absence of model catalyst to study the water oxidation in organic electrolytes. From a more applied point of view, we demonstrated the possibility to prepare organic electrolytes that contain aqueous nanoreactors with tunable sizes that could prove very useful for a wide variety of applications. For instance, such aqueous−organic mixtures have already been employed in CO_2 reduction.[237,238] Indeed, apolar small molecules such as CO_2 and N_2 have poor affinities for water molecules and thus low solubilities in aqueous phases, which drastically hampers the reaction rates for CO_2 or N_2 reduction. Nevertheless, a proton source is required to achieve the transformation of CO_2 into high-added-value compounds such as methane, methanol, ethanol, ethylene, etc. Thus, one could seize the opportunity of tuning the size of aqueous domains that form in aprotic solvents to enhance the selectivity and/or rate toward high-value-added products while sustaining a sufficient CO_2 solubility. This stratagem could even be pushed toward more complex processes, such as synthetic electrochemistry. Indeed, changing the size and composition of the aqueous and/or organic nanodomains formed in the electrolytes could allow polar and apolar reactants to be brought together at the electrochemical interface and thus increase the molecular complexity of products that could be formed.[133]

Outside of the electrocatalysis field, these findings can also reveal helpful in understanding the parasitic reactions due to water contamination in carbonate-based LIBs. Indeed, the "perfect" water content for organic-based LIBs was long debated, as water contamination may modify the SEI composition on anode materials and thus enhance or deteriorate their performances.[98,99,239] The approach we deployed to understand how water speciation may impact its reactivity at electrified electrodes may thus help to rationalize these experimental observations. For instance, it was recently suggested that because water and Li^+ are strongly bonded, they can co-absorb on a metallic

surface upon negative polarization, leading to the formation of oxide species and the evolution of molecular hydrogen, both being detrimental for battery cycling.[240] Water is also used as an additive in organic electrolytes for divalent ion batteries to boost the kinetics for intercalation of divalent anions into oxides.[100] However, divalent cations such as Mg^{2+} are strong Lewis acids and strongly bind water molecules, which facilitates their electrochemical reduction and drastically limits the tolerable amount of water in these systems. Moreover, this strong cation-water affinity may also lead to co-intercalation of water molecules in the bulk of the electrode, limiting the effective capacity of these devices.

Playing on the solvation structure of water molecules was also recently discussed to propose high-voltage aqueous LIBs using superconcentrated aqueous electrolytes. In these electrolytes, most of the water molecules are found in the first solvation shell of a Li^+ cation, and Li-H_2O rich nanodomains can be observed. Measuring the intrinsic electrochemical stability of these new electrolytes, we could find that their greater cathodic stability originates mainly from the growth of a passivation layer, onto the electrode surface, formed upon decomposition of water molecules and organic anions. These findings are in line with what was observed when studying water reactivity in organic electrolytes. Indeed, in WiSEs, water molecules are mostly found in the first solvation shell of Li^+ cations, and the presence of H_2O-Li nanodomains in these superconcentrated aqueous electrolytes is well established, and advocates for a facile water reduction in light of what we measured in organic electrolytes. Nevertheless, the superconcentrated regime is required to facilitate the precipitation of the inorganic components of the passivating layer. Trying to blend different Li salts at large concentrations, we found that when two salts sharing the same cation but very different anions are mixed together in water, the formation of an ABS can occur. Screening a large variety of salts with different anions, we could find some pre-requisite to predict the formation of ABSs in presence of two Li-salts: the size of the anions must be very different and we also highlighted that difference in geometries (e.g. spherical vs. ovoid) is a prerequisite to trigger the ABSs formation. We also highlighted that ABSs formation can be used to design innovative aqueous based batteries. Our first attempts to design a membrane-free dual-ion battery were very preliminary and more is needed fully to appreciate the stability of the liquid-liquid interface formed in ABSs. Moreover, despite recent reports that the ABS can trigger novel intercalation chemistries,[210] nothing is known regarding why ABSs must be used as electrolyte in this case.

Aside from batteries, such systems may prove useful for electrochemical synthesis. Indeed, multiphasic electrolytes (made by emulsion) have been investigated as a way to unlock new synthesis paths because of their ability to tune the reaction processes at the triple phase boundary.[241] Actually, the presence of *in-situ* liquid-liquid extraction phenomena in these systems may help to extract the products of the reaction, and improves yields of electrochemical reactions. Because ABSs do not contain any organic solvent they can thus be envisaged to develop even greener organic electrosynthesis processes. Moreover, ABSs seem promising to recycle transition metals used in LIBs cathodes such as cobalt.[242] Hence the systems we studied may further serve the LIB recycling field since anions from the electrolytes salts could be recovered as well.

Studying electrochemistry in these superconcentrated electrolytes also raised fundamental questions. While in diluted electrolytes, the thermodynamic potentials for coupled proton-electron transfers reactions such as the HER or OER can be simply estimated from the Nernst equation and the solution pH, it is not so obvious to translate these concepts for superconcentrated electrolytes. Indeed, in such solutions, the activity coefficients of ions is known to largely deviate from unity,[185] which raises questions about the pH definition and measurement in WiSEs. Attempts to measure the pH in WiSEs did not reach consensus: based on measurements using a combination of glass-electrodes and pH-meters, it was proposed that WiSEs can be slightly more acidic than neutral water,[134,243] or even very acidic (pH ~ 2).[244] Because glass-electrodes may not show an accurate response in concentrated media, such measurements should be confronted to other experimental techniques that assess the ions activity coefficients. Thus, preliminary measurements of the HER and HOR on a Pt RDE were carried out during this thesis, and suggested that the concentration of protons in WiSEs is not increased compare to diluted electrolytes. However, the reversible HER/HOR potential compared to a calomel reference was observed to largely shift to more positive values at high ionic strength, suggesting that the activity coefficients of protons may reach very large values. Hence, the determination of the ions activity in these superconcentrated solutions will be the subject to a further study in our lab. Indeed, it can help to better understand the (un)stability of aqueous based electrolytes, but applies far beyond aqueous batteries field. It may actually help to better grasp why a different SEI formation mechanism is observed switching from diluted (reduction of the solvent) to superconcentrated (reduction of the anion) organic electrolytes.[229]

Outside of the battery field, we believe that, desalinization devices or chloroalkali electrolyzers operating in brines could benefit from this fundamental understanding.

Interestingly, we could also apply our understanding of the intrinsic non-miscibility of halides with sulfonylimides anions to develop an electrolyte engineering approach and widen the known insertion electrochemistry to layered vanadium halides. Doing so, we synthetized new $LiVX_3$ (X = Cl, Br, I) phases, recalling the interest for solid-state chemists to dialog with the physical chemists working on physical chemistry of liquids. Also, throughout this study we developed the fundamental understanding to explain the mechanism preventing the dissolution of transition metals into superconcentrated electrolytes. Indeed, we found that the corrosive character of fluorinated organic anions is inhibited in the superconcentrated regime because the formation of complexes based on transition metal and anions is prevented. We hypothesized that activity coefficients of such complexes in solutions drastically deviate from unity, opening the door to deeper thermodynamic modelling studies.

Closing the loop with the beginning of this thesis, the understanding of the influence of the electrolyte concentration on the stability of electrodes we developed for batteries could also reveal crucial for the electrocatalysis community. Indeed, despite the recent development of elegant *operando* approaches tracking the catalysts dissolution using RDE setups,[245] the conditions of such studies are far from those used in industrial devices operating at higher temperature, with large salt concentrations and very different mass/volume ratio for the catalyst and the electrolyte.[10] Gaining some general knowledge on how ions dissolve in concentrated electrolytes would surely help to design more resilient electrolyzers.

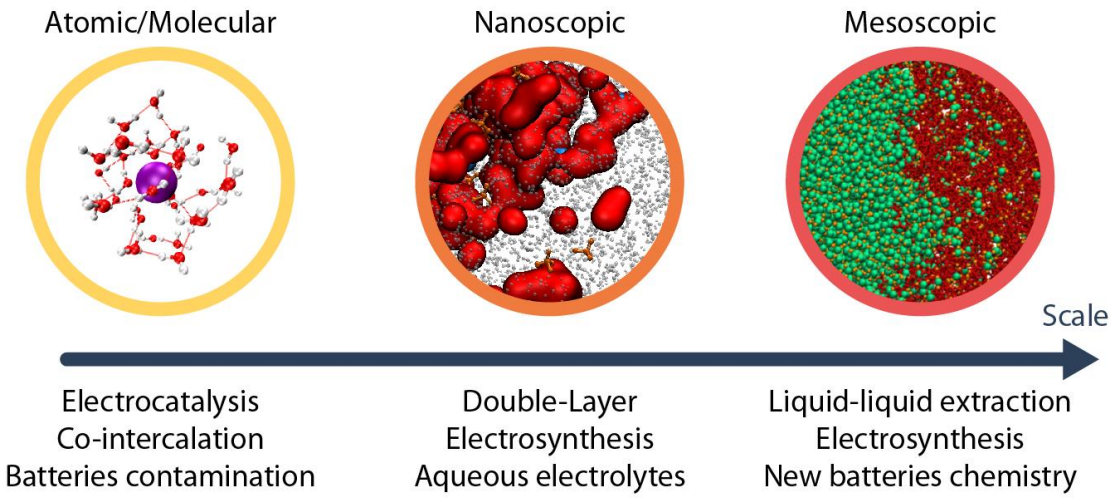

Conclusion and Perspective Figure 1. Tuning the solvent environment at the atomic, nanoscopic, or macroscopic scale is a promising strategy to unlock new electrochemical technologies.

Altogether, the findings of this thesis highlight that mastering the electrolyte solvation structure at the atomic, nanoscopic, or macroscopic scale is a key to unlock new electrochemical technologies for electricity storage, electrocatalysis, or electrosynthesis as illustrated in **Conclusion and Perspective Figure 1**.

List of abbreviations

Abbreviation	Signification
κ_{el}	electronic transmission coefficient
ABS	aqueous biphasic system
ACN	acetonitrile
APXS	ambient-pressure X-ray photoelectron spectroscopy
BETI	bis(pentafluoroethanesulfonyl)imide
c	concentration
CSI	chemical shift imaging
CV	cyclic voltammogram
DFT	density-functional theory
DMC	dimethylcarbonate
d	density
d_{ion}	mean ion diameter
EC	ethylene carbonate
EDL	electrical double-layer
EQCM	electrochemical quartz crystal microbalance
F	Faraday constant
FSI	bis(fluorosulfonyl)imide
FTIR	Fourier transform infrared spectroscopy
γ	activity coefficient
GC	glassy carbon
GHG	greenhouse gases
HBE	hydrogen binding energy
HER	hydrogen evolution reaction
HOR	hydrogen oxidation reaction
IHP	Inner-Helmholtz plane
IL	ionic liquid
k	reaction rate constant
K°	reaction thermodynamic equilibrium constant
k_B	Boltzmann constant
LBCG	Lithium bromide chloride graphite composite
LIB	Lithium-ion battery
LUMO	lowest unoccupied molecular orbital
M	mol L^{-1}
m	molality (mol kg^{-1})
m	mass
MD	molecular dynamics
MEA	membrane electrode assembly

MPI	molecular polarity index
NMR	nuclear magnetic spectroscopy
OER	oxygen evolution reaction
OHP	Outer-Helmholtz plane
OLEMS	on-line electrochemical mass spectrometry
OTf	triflate
Pc	polycrystalline
PC	propylene carbonate
pmf	potential of mean force
PP	polypyrrole polymer
ppm	part per million
pzc	potential of zero charge
pzfc	potential of zero free charge
Q	isoperimetric quotient
R	universal gas constant
RDE	rotating disk electrode
RHE	reversible hydrogen electrode
SAXS	small-angle X-ray scattering
SEI	solid electrolyte interphase
SHE	standard hydrogen electrode
SXRD	synchrotron X-ray diffraction
T	Temperature
TBA	tetrabutylammonium
TEY	total electron yield
TFSI	bis(trifluoromethanesulfonyl)amide
TST	transition-state theory
UHV	ultra-high vacuum
w%	weight percentage
WiBSE	water-in-bisalt electrolyte
WiSE	water-in-salt electrolyte
XAS	X-ray absorption spectroscopy
XRD	X-ray diffraction
ΔG^*	activation free energy
υ_n	nuclear tunneling factor

Supplementary data and methods

Chapter II -

Supplementary Data

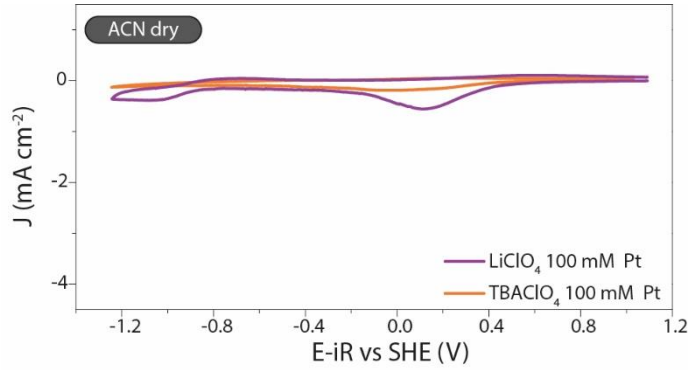

Supplementary Figure II-1. Cyclic voltammograms recorded at 50 mV s^{-1} on a platinum electrode in dry acetonitrile electrolytes containing 100 mM of $LiClO_4$ (purple) or $TBAClO_4$ (orange). The cathodic current at ~ 0.3 V vs. SHE can be attributed to platinum surface electrochemistry (for instance, Pt-OH desorption).

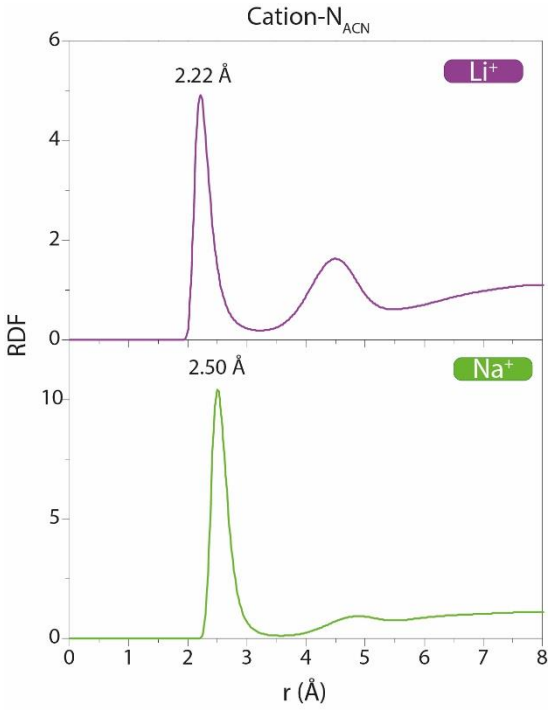

Supplementary Figure II-2. Cation-N_{ACN} radial distribution functions (RDFs calculated from the MD simulations of Li/$NaClO_4$ in H_2O/ACN).

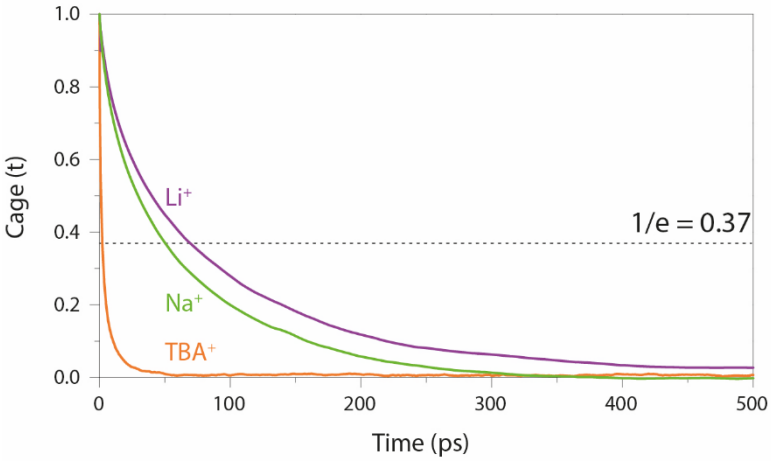

Supplementary Figure II-3. Cage correlation function used to determine the residence lifetime of H_2O in cations first solvation shell for the $LiClO_4$ (purple), $NaClO_4$ (green), $TBAClO_4$ (orange) simulations. The characteristic time of the exponential decay was measured at 37% of the cage function value for t=0 ps.

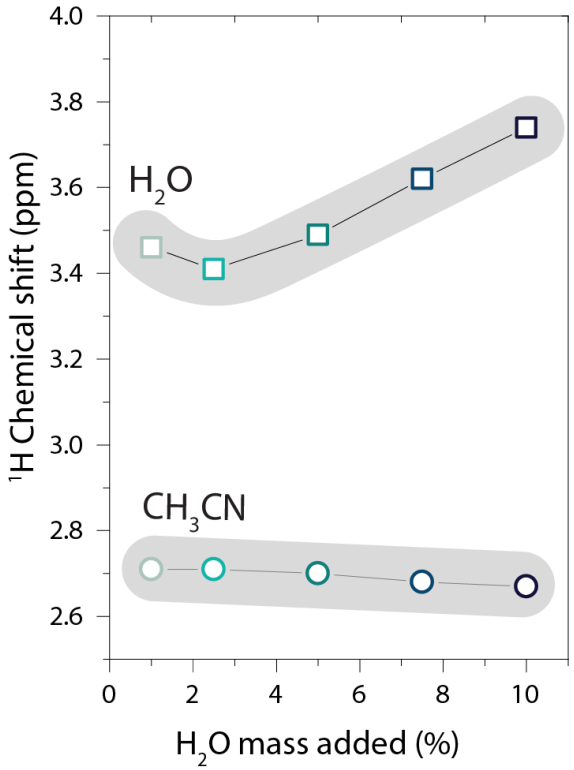

Supplementary Figure II-4. ^1H chemical shift for H_2O (squares) and acetonitrile CH_3CN (ACN, circles) molecules for different water contents in acetonitrile with 100 mM $LiClO_4$. The almost steady chemical shift of the $–CH_3$ group of acetonitrile as a function of the water concentration confirms that the trend measured for the ^1H chemical shifts of protons from H_2O is not related to a change in the electrolytes magnetic susceptibility. The lines are guide for the eyes.

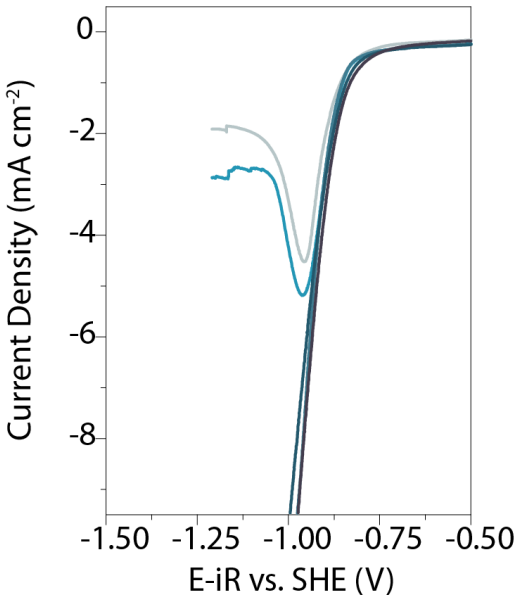

Supplementary Figure II-5. Linear sweep voltammograms recorded in acetonitrile in presence of 100 mM LiTFSI with different water contents (1, 2.5, 5, 7.5 and 10% from light to dark blue) using a rotating disk (1 600 rpm) Pt electrode with a 50 mV s^{-1} sweeping rate. No modification of the onset potential at which water is reduced was observed, independently of the water content, confirming that the trend previously measured for $LiClO_4$ is independent on the nature of the anion.

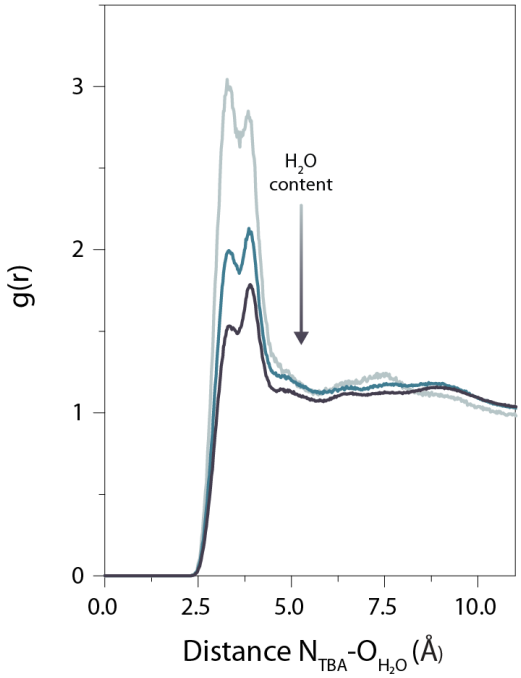

Supplementary Figure II-6. TBA-O(H_2O) radial distribution functions, g(r)'s, computed from the MD simulations for electrolytes containing 100 mM $TBAClO_4$ at different water contents (1% in light blue, 5% in blue and 10% in dark blue) in acetonitrile. The broadness of the first peak in the g(r) reflects the hydrophobic character of TBA^+ cations.

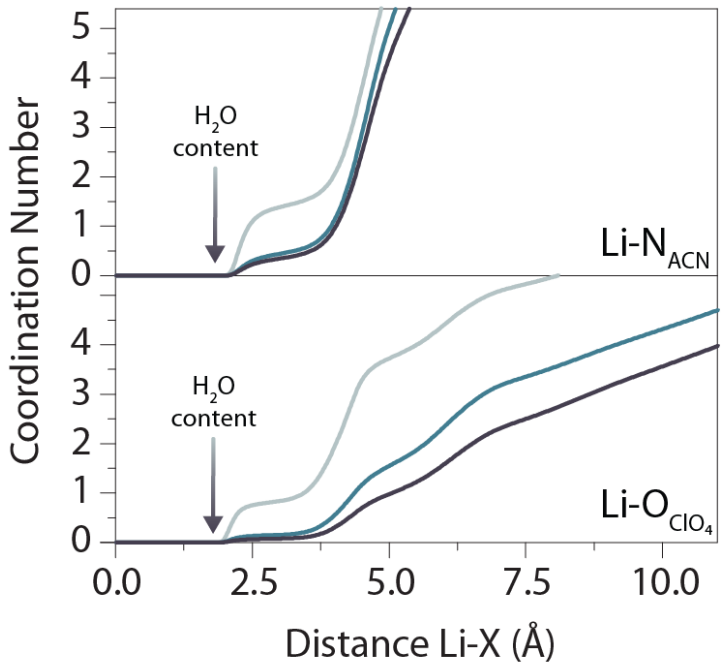

Supplementary Figure II-7. Coordination number between Li^+ cations and nitrogen atoms from acetonitrile molecules (top) and oxygen atoms from ClO_4^- anions (bottom) in the presence of electrolytes containing 100 mM $LiClO_4$ at different water content (1% in light blue, 5% in blue and 10% in dark blue) in acetonitrile. The decrease of the first plateau intensity with the water content shows that water molecules replace acetonitrile and perchlorate anions in the Li^+ cation first solvation shell when the concentration of water is increased in the electrolytes.

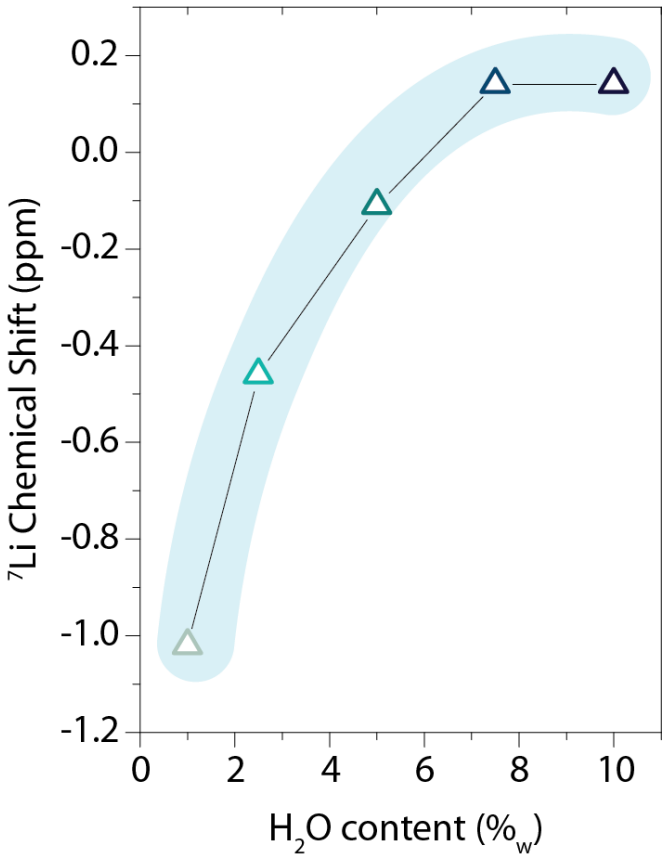

Supplementary Figure II-8. Evolution of the ^{7}Li chemical shift in the presence of 100 mM $LiClO_4$ in acetonitrile as a function of the water content. The chemical shifts measured at high water contents (> 7.5%) slightly above 0 ppm are close to values measured in aqueous electrolytes (0 ppm is defined by the ^{7}Li resonance frequency in a 1 M LiCl aqueous solution). The negative values measured at lower water-content may result from a shielding from the ACN or ClO_4^- anions.[118] The line is a guide for the eye.

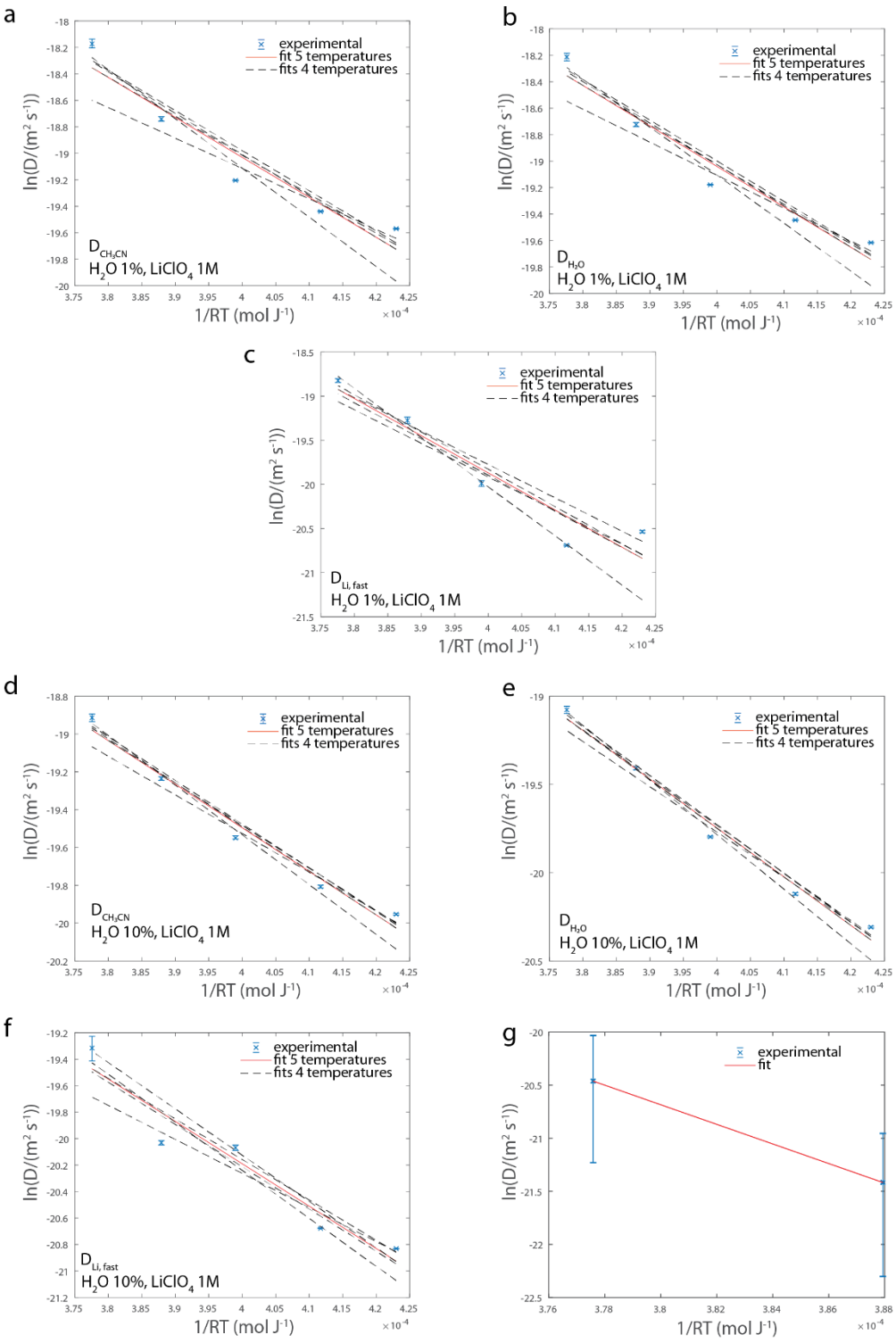

Supplementary Figure II-9. Arrhenius fits for the self-diffusion coefficients in the 10% H_2O 100 mM $LiClO_4$ electrolyte for **a)** CH_3CN, **b)** H_2O, **c)** Li^+ and in the 10% H_2O 1 M $LiClO_4$ electrolyte for **d)** CH_3CN, **e)** H_2O, **f)** Li^+ (fast) and **g)** Li^+ (slow).

The data were processed and integrated in the Bruker Topspin software. The water and acetonitrile ^1H peaks are well resolved and were fitted independently. The self-diffusion

coefficients were obtained in Matlab (The Mathworks, Inc.), using a weighted least-square-fit (polyfitweighted, 2006, S.S. Rogers) to the equation $\ln(A) = \alpha - BD$, with A the area of the signal, D the self-diffusion coefficient and $B = (\Delta - \frac{\delta}{3})(2\pi\gamma G\delta)^2$, Δ the effective diffusion time, δ the effective gradient duration, γ the gyromagnetic ratio and G the PFG strength. For the (ACN 10% of H_2O, 1 M LiClO4) sample at 310 K and 318 K, the ^{7}Li data required 2 components and a non-linear fit to $A = \propto_1 \exp(-B_1D_1) + \propto_2 \exp(-B_2D_2)$ was performed using the nlinfit Matlab function. The uncertainties are given as ±2 standard deviations in the figures. The activation energies were then obtained using a least-square fit (Arrhenius law) in Matlab.

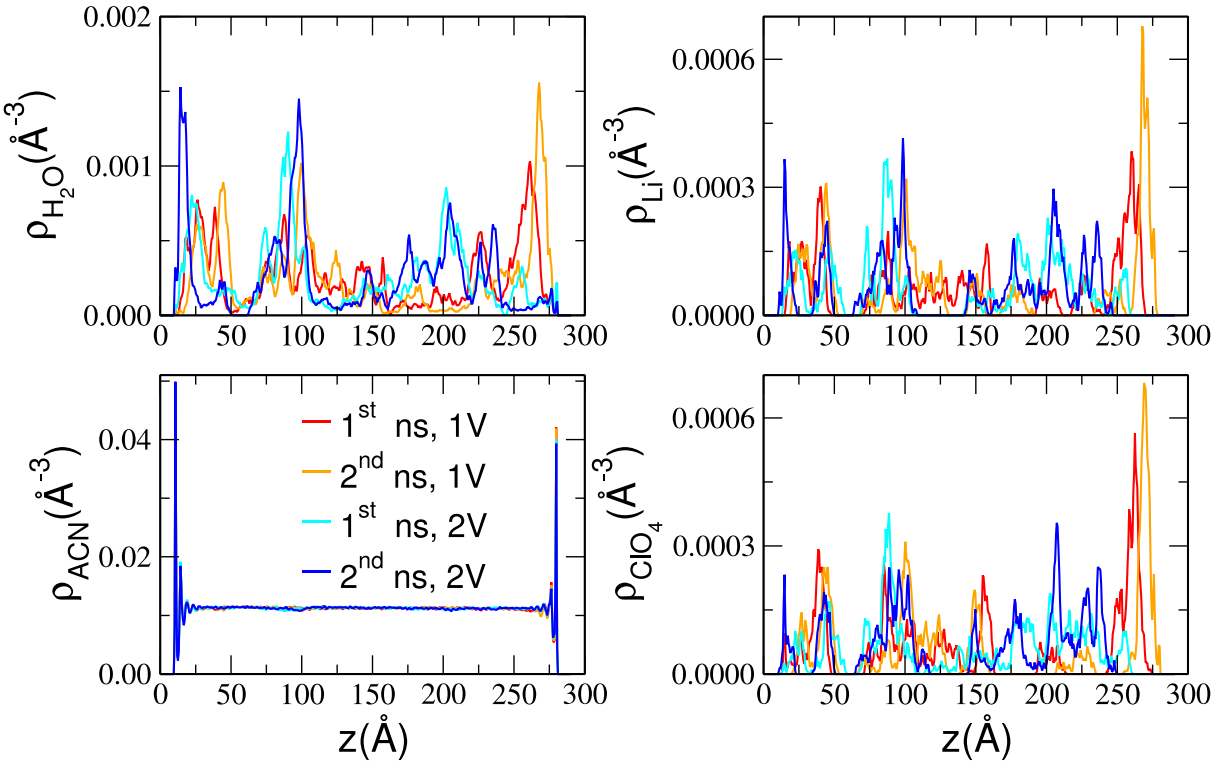

Supplementary Figure II-10. Molecular density profiles along the simulation cells for the constant applied potential (1V and 2V) simulations of system 1 (1% H_2O + 100 mM $LiClO_4$). The negative electrode is located on the left. Two trajectories of 1 ns each are shown in each case to highlight the fluctuations. For the acetonitrile, the profile is flat, which highlights a homogeneous distribution. On the contrary the water and the ions form heterogeneities that move with time across the cell, which leads to large local density peaks. The variations between the 1.0 V and the 2.0 V cases are not significant since similar profiles are obtained.

Methods

General procedures

All the experiments were carried out in an Ar-filled glovebox (MBraun, O_2 < 0.5 ppm H_2O < 0.5 ppm). All the salts were dried under vacuum for 24h in a Büchi oven at 80°C and directly transferred to the glovebox. The electrolytes were prepared by adding a precise weight of Ar-flushed Milli-Q H_2O to acetonitrile (Acros organics; 99.9%, AcroSeal®, over molecular sieves) so that the final electrolyte contains the right weight percentage of H_2O. To these as-prepared solution, a precise mass of salt (anhydrous $LiClO_4$, Alfa Aesar, 99%, LiTFSI, Solvay, $NaClO_4$, Alfa Aesar, Battery Grade or $TBAClO_4$, Sigma-Aldrich for electrochemical analysis, ≥99.0%) was added to obtain the desired cation/water ratio. The electrochemical cells were rinsed in aqua-regia, boiled in Milli-Q water before to be rinsed 5 times with fresh Milli-Q and finally dried 1h at 80°C prior to be used. The density of the electrolyte was measured by weighing 2.0 ± 0.025 mL (volumetric flask) of each electrolyte. Their conductivity was measured with a SevenCompact 230 (Mettler Toledo) conductivity-meter. All their physical properties (density, concentration) are given in the **Methods Table II-1**, **Methods Table II-2** and **Methods Table II-3**.

Electrochemical measurements

Data were acquired on a Biologic VMP3 potentiostat. Prior to any measurement, platinum and gold polycrystalline electrodes (5 mm diameter, Pine research) were polished using three polishing slurries (6 µm diamond on nylon polishing disk, followed by 0.3 µm and 0.04 µm aluminum oxide on microcloth polishing disk) using a polishing machine (Le Cube, Presi). Residual traces of slurries were removed by sonicating the as-polished electrode in a 50:50 H_2O:EtOH solution two times for 2 minutes. To ensure the cleanliness of the platinum electrodes surface, the electrodes were held at + 2.0 V vs. SHE in a 0.5 M H_2SO_4 solution purged with Ar for 2 minutes followed by 10 cycles of cyclic voltammetry (from 1.350 V to 0.0 V vs. SHE) in a fresh H_2SO_4 solution. Then, freshly cleaned electrodes were rinsed with ultrapure water, air-dried and pumped in the glovebox antechamber. Inside the glovebox, the electrodes were immediately covered by a drop of acetonitrile before being mounted onto a rotating disk setup (Pine research). All electrochemical measurements were recorded using a three electrodes cell setup with an $AgNO_3$/Ag organic reference electrode (regularly calibrated against ferrocene). As for a note, this procedure does not totally guaranty the absence of potentials shifts related to changes in the

junction potentials. Nevertheless, in ACN-H_2O electrolytes with water concentrations similar to those studied in this chapter, such artefacts were previously estimated to be ~ 30-50mV,[101] and are thus "negligible" when compared to the shifts in reduction potentials discussed in this chapter (> 200 mV). Furthermore, the absence of shift of reduction potential observed for water molecules at different water concentrations in $LiClO_4$-H_2O-ACN electrolytes also suggests that junction potentials are not the cause of the shifts in reduction. During the measurements, the working electrode was rotated at 1 600 rpm or left static. A flame-annealed platinum wire was used as a counter electrode and placed in a separate compartment. A sweep rate of 50 $mV.s^{-1}$ was used during all the electrochemical experiments. The ohmic drop was measured using current-interrupt technique after every electrochemical measurement. Typical values of around ~50 to ~100 Ω were obtained. The ohmic drop compensation was performed during the data treatment (85% of correction, as suggested by the potentiostat manufacturer).

Liquid Nuclear-magnetic resonance characterization

Liquid-state NMR spectra were recorded on a Bruker 7.046 T Avance III HD NMR spectrometer mounted with a 5 mm HX(F) probe head. For electrolyte analysis, NMR tubes equipped with a D_2O (99% D, Sigma-Aldrich) filled coaxial insert were used in order to lock the magnetic field and HOD signal was used as an internal reference (4.7 ppm). Single pulses sequences were used to record the ^1H and ^7Li spectra. Values of 0.01 ppm (~ 3 Hz) for the ^1H peaks and 0.02 ppm (~ 2 Hz) for $^7Li^+$ peaks were measured for the full width at medium height, which gives a good approximation of the measurements uncertainty.

Small-angle X-Ray Scattering

Small-angle X-ray scattering data were collected at the SWING beamline (SOLEIL synchrotron, Saint-Aubin, France). The beamline was operated at 16 keV and an Eiger 4M Detector (Dectris) was used. Electrolyte samples were filled into 1 mm capillaries inside the glovebox, sealed with epoxy and the measurements were performed at room temperature. The sample-to-detector distances were set to 6.2 m and 0.5 m, which allowed to cover scattering vectors in the range from q = 0.0016 $Å^{-1}$ to 0.28 $Å^{-1}$. The data analysis (including integration, normalization and background subtraction) was carried out using the FOXTROT software.

^{1}H and ^{7}Li self-diffusion coefficient measurements by NMR

The self-diffusion coefficients were measured using 10 mm tubes in a Bruker Advance III HD 4.7 T operating at 200 MHz for ^{1}H and 77.7 MHz for ^{7}Li, using a Bruker 10 mm liquid-state probe equipped with a ^{1}H or ^{7}Li 10 mm saddle coil. The pulsed magnetic field gradients (PFG) were performed with a Bruker diff30 pulsed magnetic field gradient (up to 30 $G.cm^{-1}.A^{-1}$) coil and a Bruker GREAT60 gradient amplifier. A stimulated echo[246] was used with diffusion times of 7 to 10 ms and encoding/decoding square PFG pulses (1 to 2 ms). The PFG amplitudes were varied in 32 steps from 0 to 600 G/cm (^{7}Li) and from 0 to 300 G/cm (^{1}H). A saturation, 2 dummy scans and a repetition time of 4 s for ^{7}Li and 5 s for ^{1}H were used to ensure steady state. At least 32 transients were added for each measurement.

The Bruker Control Unit (BCU20) was used to set 5 temperatures for the water in the PFG coil (281 K to 321 K in steps of 10 K), and the temperature was calibrated using a 10 mm tube filled with glycerol in the same conditions. The sample was left to equilibrate for at least 30 minutes in the spectrometer before the measurements.

Molecular dynamic simulations for bulk electrolytes

Classical MD simulations of the bulk systems were performed using the GROMACS software package.[247] Acetonitrile solvent was described with a six-site model.[248] SPC/E model was chosen for water molecules.[249] Force field parameters for perchlorate anions and TBA cations were taken from Ref. [250] and Ref. [251], respectively. The Lennard-Jones parameters for Li^{+} and Na^{+} were taken from Åqvist.[252] Mixed Lennard-Jones parameters for all of the different atom types were obtained from the Lorentz-Berthelot combination rules. The simulations were performed in the NVT ensemble at 300 K for 100 ns, with the Nosé-Hoover thermostat[253,254] (the relaxation constant used is 0.5 ps), using a timestep of 1 fs and saving a configuration every 100 fs. The initial configuration was achieved by generating a low density cubic box by means of the PACKMOL package,[255] that was then compressed in the NPT ensemble in order to reproduce the electrolyte density at temperature and pressure conditions of 300 K and 1 atm, respectively. All the box configurations are given in **Methods Table II-1**, **Methods Table II-2** and **Methods Table II-3**. The systems were then equilibrated in the NVT ensemble at 700 K for 0.5 ns, followed by a final NVT equilibration at 300 K for 2 ns. The production simulations were finally carried out in the

NVT ensemble at 300 K for 100 ns. Long-range electrostatic interactions were computed with the particle mesh Ewald method,[256] while a cut-off distance of 9 Å was adopted for the non-bonded interactions. The LINCS algorithm was employed to constrain the stretching interactions involving hydrogen atoms.[257] The coordination numbers were obtained by the integration of the radial distribution functions (RDF), calculated every 100 fs using the GROMACS utilities.[247] The structure factors were calculated with an in-house code using the partial RDFs. The domain analysis was performed using TRAVIS,[130,258] while VMD software was used to obtain the snapshots.[259]

Water content (weight%)	1%	2.5%	5%	7.5%	10%
Density (g.cm^{-3})	0.773	0.773	0.775	0.789	0.784
[H_2O] (mol.L^{-1})	0.420	1.03	2.02	3.01	3.96
[$LiClO_4$] (mol.L^{-1})	0.096	0.095	0.092	0.092	0.091
Box Length (Å)	44.08		44.70		45.02
Number ACN	965		966		966
Number H_2O	22		110		220
Number $LiClO_4$	5		5		5

Methods Table II-1. Physical properties for the electrolytes containing 100 mM $LiClO_4$ and different water contents, as well as details for the simulation box. Similar boxes were used for $NaClO_4$ simulations, changing only the force-field for the cation.

Water content (weight%)	1%	2.5%	5%	7.5%	10%
Density (g.cm^{-3})	0.769	0.775	0.781	0.783	0.792
[H_2O] (mol.L^{-1})	0.422	1.05	2.06	3.03	3.99
[$TBAClO_4$] (mol.L^{-1})	0.097	0.096	0.094	0.092	0.091
Box Length (Å)	44.94		44.59		45.07
Number ACN	965		966		966
Number H_2O	22		110		220
Number $TBAClO_4$	5		5		5

Methods Table II-2. Physical properties for the electrolytes containing 100 mM $TBAClO_4$ and different water contents, as well as details for the simulation box.

Li/H_2O molar ratio	0.02	0.11	0.22	0.45
Density (g.cm^{-3})	0.784	0.819	0.853	0.914
[H_2O] (mol.L^{-1})	3.96	3.89	3.83	3.70
[$LiClO_4$] (mol.L^{-1})	0.091	0.445	0.878	1.69
Box Length (Å)	45.02	45.45	45.68	
Number ACN	966	966	966	
Number H_2O	220	220	220	
Number $LiClO_4$	5	25	50	

Methods Table II-3. Physical properties for the electrolytes containing 10% in mass of H_2O at different Li/H_2O molar ratio and simulation box details.

The X-Ray weighed structure factors were determined using:

$$S(q) = 1 + \frac{\sum_i \sum_j c_i c_j w_i(k) w_j^*(k) \left[S_{ij}(k) - 1\right]}{\left|\sum_i c_i w_i(k)\right|^2} \qquad (Methods\ \text{II-1})$$

where q is the scattering vector magnitude, c_i the atomic fraction of the atom i and $w_i$is the atomic form factor obtained from ref. [260], and S_{ij} the partial structure factor that is obtained by a Fourier transform of the partial distribution function:

$$S_{ij}(q) = 1 + \frac{4\pi\rho}{q} \int_0^\infty r\left[g_{ij}(r) - 1\right] \sin(qr)\, dr \qquad (Methods\ \text{II-2})$$

where ρ is the atomic number density of the electrolyte (number of atoms in the box divided by the box volume) and $g_{ij}(r)$ the partial distribution function.

Molecular dynamic simulations at constant applied voltage

Classical MD simulations of the electrolytes containing $LiClO_4$ between two planar graphite electrodes were performed at a fixed potential differences of 1 and 2 V using the Metalwalls code[261], following the approach detailed in Refs.[262,263] In short, the electrode atoms charges fluctuate in order to ensure that the fixed potential condition is matched at each timestep of the simulation. 2D periodic boundary conditions were used in the xy directions. The force field parameters were kept the same as in the bulk simulations, with the addition of the Lennard-Jones parameters for the electrode carbon atoms taken from Ref.[264] The simulations were performed in the NVT ensemble at 300 K, with the Nosé-Hoover thermostat[253,254] (the relaxation constant used is 1 ps), using a timestep of 1 fs. Long-range electrostatic interactions were computed with the Ewald summation method in 2D with a combination of point charges for the electrolyte and Gaussian charges for the electrodes,[262,265] while a cut-off distance of 12 Å was adopted for the non-bonded interactions. The SHAKE algorithm was employed to constrain the stretching interactions involving hydrogen atoms.[266,267] Further details about the box sizes are provided in **Methods Table II-4**. The electrolyte is put in between two planar graphite electrodes, each of them consisting in three layers of graphene (1440 carbon atoms per electrode).

The systems were first pre-equilibrated by fixing the electrode charges to zero (about 400 ps) and then under constant applied potential of 1 or 2 V. Regarding the simulation at 1 V, the equilibration time was 2.5 ns, 1.5 ns and 3 ns for the three systems, respectively. Once the steady state was reached, the systems were simulated for at least 3 ns. For the 2 V simulations, only the first two systems were simulated, with an equilibration time of 1.5 ns and 600 ps, respectively. The following production time was at least of 1 ns. In both cases, the simulations were stopped since no structural differences were observed with respect to the 1 V case. Similar density profiles showing water heterogeneities for the different species are observed at the different voltages, as illustrated in the **Supplementary Figure II-10** for the system containing 1% of H_2O and 100 mM $LiClO_4$.

Number $LiClO_4$	Number ACN	Number H_2O	Box Volume ($Å^3$)	Density ($g.cm^{-3}$)
20	3860	88	34.10 x 36.89 x 290.69	0.786
20	3864	880	34.10 x 36.89 x 312.13	0.794
100	1932	440	34.10 x 36.89 x 173.15	0.853

Methods Table II-4. Simulation box details for $LiClO_4$-based electrolytes between two planar graphite electrodes.

The simulation box for the 5% H_2O electrolyte contains 966 acetonitrile molecules, 110 water molecules and 25 $LiClO_4$ ion pairs with a box length of 44.32 Å (Figure II-20).

Chapter III -

Methods

Materials

All the glassware was rinsed at least 3 times with Milli-Q water prior to use. All chemicals, including lithium bis(trifluoromethanesulfonyl)amide (Solvay), potassium bis(trifluoromethanesulfonyl)amide (99.5%, Solvionic), lithium nitrate (anhydrous, 99%, Alfa Aesar), lithium chloride (anhydrous, 98+%, Alfa Aesar), o-Cresolphtahalein complexone (Alfa Aesar) LiBr (anhydrous 99+, Alfa Aesar), LiI (anhydrous, 99+ Alfa Aesar), LiBETI (TCI Chemicals) NaCl (99.0% min, Sigma-Aldrich), NaBr (99+, water < 1%, Alfa Aesar), NaI (99.5% min, Alfa), KCl (99%, Alfa Aesar), KBr (FT-IR grade, > 99%, Sigma-Aldrich) and KI (Alfa Aesar) were used without further purification. However, solutions prepared with LiFSI (TCI Chemicals) were showing some turbidity and were then centrifuged before being used in order to remove the insoluble impurities. Ultrapure water (Mili-Q) was used to prepare all the solutions.

Electrochemical measurements

Voltammetry experiments

Electrolytes were prepared by precisely weighting a mass of salt and adding the corresponding amount of ultrapure water to obtain the desired molality. Solutions were sonicated for 30 min to ensure a proper dissolution and cooled down to ambient temperature before performing any measurement. Data were acquired using either a Biologic VSP or a Biologic VMP3 potentiostat. Ohmic drop was measured using current interrupt technique after the electrochemical measurements. Prior to any measurement, mirror polished glassy carbon electrodes and platinum electrodes (Pine research) were prepared using ultrafine alumina slurries (0.05 µm on microcloth polishing disk for the GC, and three steps for the Pt starting from 5 µm on nylon polishing disk, followed by 0.3 µm and 0.05 µm on microcloth polishing disk). Residual traces of slurries were removed by sonicating the as polished electrodes in a 50:50 H_2O:EtOH solution two times for 15 minutes. To ensure the cleanliness of platinum electrodes surface, platinum electrodes were hold at + 2.0 V vs. SHE in a 0.5 M H_2SO_4 solution for 2 minutes followed by 10 cycles of cyclic voltammetry (from 1.350 V to 0.0 V vs. SHE) in the same H_2SO_4 solution. Then, freshly cleaned electrodes were rinsed by MQ-water and used within a short time (typically less than 15 minutes).

All electrochemical measurements were recorded using a three electrodes cell setup with a calomel reference electrode (0.240 mV vs. SHE), except for the electrochemical quartz microbalance for which a small Hg/$HgSO_4$ reference electrode (0.685 V vs. SHE) was used. A graphite rod was used as a counter electrode for all measurements. For static measurements, electrodes were immersed in a small volume (typically 2 mL) of solution while larger volume (typically 10 mL) of solutions were used for rotating disk electrode measurements to allow a proper laminar flow of solution on the surface of the rotating electrode. In order to prevent O_2 and CO_2 reduction, electrolytes were degassed by bubbling argon (Linde, purity 5.0) for at least 1 hour prior to the first experiment. For static cyclic voltammetry experiments, the cell was closed using septa, and argon flow was stopped during the measurement to avoid convection in the electrolyte.

Ohmic drop was measured using current-interrupt technique after every electrochemical measurement. Typical values from 15 Ω (for 1 molar electrolytes) to 150 Ω (20 m LiTFSI) were measured. The ohmic drop compensation was performed during the data treatment.

On-line electrochemical mass spectrometry

Online gas-analysis was performed using a HIDEN H1 mass spectrometer system (HIDEN Analytical, UK). A 5 necks cell described in **Methods Figure III-1** was used to perform the electrochemistry. Briefly, the top neck was filled with a plastic cap to avoid dead volume, in which a copper wire was inserted to make the electrical contact with the working electrode. Small necks were used to place a calomel reference electrode, a counter electrode compartment, a gas outlet and a gas inlet. The graphite rod counter electrode was isolated in a glass compartment to avoid O_2 evolution in the electrolyte. The cell was connected to the mass spectrometer through a flexible capillary inlet and two porous stainless steel membrane filters (~2 µm pore diameter, Valco Instruments Co. Inc.) preventing the capillary for water contamination. A small flow of argon was bubbled through the solution during the measurement to minimize the delay of detection. Electrolytes were degassed during 4 hours before performing the measurement (Ar, O_2, N_2, H_2O, CO_2 and H_2 evolutions were monitored during that time). In order to get more precise values and shorten the acquisition time, only the evolution of H_2 was monitored during the experiment. Shorter experiments (not shown here), confirmed that H_2 was the only gas evolved during the electrochemical tests, as previously observed by Suo *et al.*.[148] Typical delays were in the range of 1 to 2 minutes, as established by applying a constant negative current in a 1 M H_2SO_4 solution for 10 minutes and monitoring the H_2 evolution. The lowest current for which H_2 evolution was monitored was 1 mA.

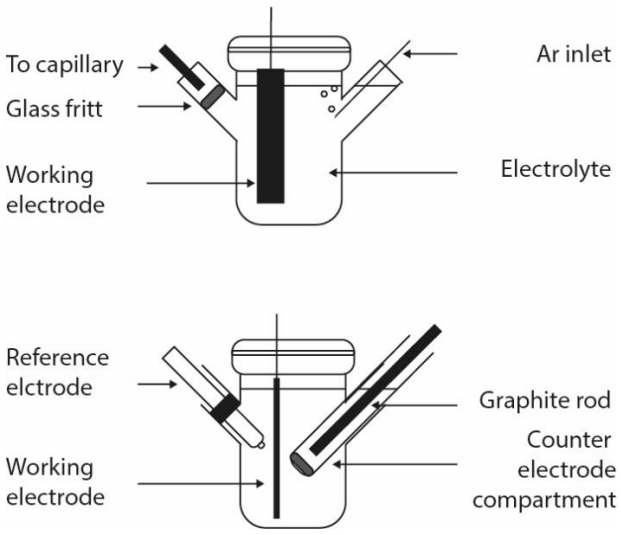

Methods Figure III-1. Cell used for the OLEMS measurements (two side views are presented).

Electrochemical Quartz Crystal Microbalance

Electrochemical quartz crystal microbalance measurements were conducted using a commercial SEIKO microbalance (SEIKO QCA 922) with AT-cut 9 MHz quartz covered with carbon on both sides. The electro-active geometric surface area was S = 0.196 cm^2. Simultaneous measurements of the quartz frequency and motional resistance were performed in order to follow both the change in weight of the electrode and the change in viscosity. Motional resistance variations were limited to around 250 Ω during the experiment.

Batteries testing

Dual-ion batteries

Dual-ion batteries using Mo_6S_8 as lithium insertion electrode and polypyrrole as chlorine insertion electrode are prepared and assembled as follows. Mo_6S_8 is obtained by leaching $Cu_2M_6S_8$ in a 6 M HCl aqueous solution under oxygen.[268] $Cu_2Mo_6S_8$ is prepared by a solid-state synthesis method (elemental precursors are introduced in a stoichiometric amount in a glass tube, that is sealed under vacuum and heated up at 1100°C for 72h). Self-standing electrodes are prepared by mixing in acetone Mo_6S_8 powder with carbon super-P, PVDF and dibutylphtalate (DBP) in the following weight ratios: 100/12.5/25/40. The as prepared slurry is spread in a petri-dish. Once the acetone is evaporated, half-inch electrodes are punched from the film. DBP is removed from the electrodes by washing them 3 times for 30 minutes in diethylether. Electrodes are dried under vacuum overnight at room temperature. Polypyrrole (PP) electrodes are obtained by electropolymerizing pyrrole (Alfa, 98+%) in 1.2 M HCl on a carbon paper, as described elsewhere.[269] Before use, PP electrodes are dechlorinated by holding them at -0.840 V vs SCE in a 1 m LiCl solution. Plastic Swagelok cells with a PTFE-disk spacer are assembled by placing the Mo_6S_8 electrode on the bottom plunger, adding first the 20 m LiTFSI and then the 18 m LiCl solution. The polypyrrole electrode – soaking only in the LiCl electrolyte - is then placed on the top of the PTFE-disk spacer and is directly in contact with the top plunger.

Intercalation-conversion batteries

The LBCG composite electrodes were prepared by hand-grinding equimolar quantities of LiBr and LiCl with KS4 (Timcal Timrex) graphite powder with a salt/graphite weight ratio of 3:2. The as obtained powder was then transferred in a zirconia planetary ball-mill (10 balls/gram of powder) and milled for 1 h. After ball-milling, PTFE (5% in mass) was added to the powder in

order to prepare self-standing electrodes, that were further dried at 80°C under vacuum overnight before being pressed on a titanium gauze. The electrodes were then mounted in a 3 electrodes Swagelok using titanium current collectors to limit the electrolyte decomposition. A AgCl/Ag electrode was used as reference electrode while a self-standing YP50 (capacitive carbon) was used as the counter electrode and Whatman glass fibers separators soaked with the degassed electrolyte were employed to prevent internal short-circuit.

Electrodes characterization

Gas diffusion layer electrodes (Freundenberg H2315/H2) were used to perform the characterization of the electrolyte degradation products as they exhibit a larger surface area than planar glassy carbon electrodes. These electrodes were rinsed and sonicated in ethanol before being used. To ensure the absence of O_2 that can generate Li_2O_2 upon reduction in WiSEs,[155] argon was bubbled during potentiostatic experiments. Finally, in order to remove residual LiTFSI salt before performing *post mortem* characterization, GDL electrodes were washed by soaking them two times for 30 minutes in dimethoxyethane (DME) and dried under vacuum for at least 30 min.

Solid-state Nuclear Magnetic Resonance (NMR) Spectroscopy

Solid-state NMR spectra were recorded on a Bruker 4.7 T Avance III spectrometer mounted with a 1.3 mm double-resonance probe head. Cycled and rinsed gas diffusion layer was packed into 1.3 mm rotors that were spun at a 50 kHz rate at the magic-angle during data acquisition. Rotor synchronized Hanh-echo sequences were used for the different experiments (^{1}H, ^{7}Li and ^{19}F). Sufficient recycle delays were used to allow a proper quantification (200, 400, and 5 s for ^{1}H, ^{7}Li and ^{19}F respectively). ^{1}H, ^{7}Li and ^{19}F were externally referenced respectively to H_2O in 1 M LiCl (4.70 ppm), 1 M LiCl (0.00 ppm) and fluoroacetophenone at – 107 ppm. Resulting spectra were fitted using DMFIT[270].

X-ray Diffraction (XRD)

All the diffractograms were acquired on a Bruker D8 advanced diffractometer using a Cu K_α radiation source in a Bragg-Brentano geometry.

Electrolytes Characterization

Fourier-Transform Infrared Spectroscopy

FTIR spectra are recorded on a Nicolet iS5 FTIR spectrometer, mounted with a diamond Attenuated Total Reflectance accessory (iD1 ATR). One drop of solution was analyzed using 16 scans with a 4 cm^{-1} resolution from 4 000 to 500 cm^{-1}. The background correction is performed by measuring the ambient atmosphere under the same conditions as for the solutions measured in this work**.**

Liquid-state Nuclear Magnetic Resonance

Liquid-state NMR spectra were recorded on a Bruker 7.046 T Avance III HD NMR spectrometer mounted with a 5 mm HX(F) probe head. For electrolyte analysis, NMR tubes equipped with a D_2O (99% D, Sigma-Aldrich) filled coaxial insert were used in order to lock the magnetic field. Single pulses sequences were used to record ^{1}H, ^{7}Li and ^{19}F spectra for the electrolytes. 90° pulses were optimized for the 1 m LiTFSI solution. As the salinity of the samples may affect the pulses length required for a 90° impulsion, the intensity of the measured signal is not a relevant parameter, therefore intensities were normalized. For the NMR data shown **Figure III-6,** a proton decoupled ^{19}F experiment was used with 4 dummy scans, 128 scans, 2 seconds acquisition and 1 second for recycle delay.

Liquid-state Nuclear Magnetic Resonance Imaging

Liquid-sate NMR spectra are recorded on a Bruker 4.7 T Avance HD spectrometer mounted with a Diff-30 Z-gradient probe head. ^{1}H and ^{7}Li mapping of the tubes are recorded using a 1D Chemical Shift Imaging (CSI) sequence with 4 transients and 128 gradient increments. The gradient pulse was 1 ms long, with a maximum gradient strength of 20.2 G/cm for ^{7}Li and 7.9 G/cm for ^{1}H, corresponding to an overall field of view of 3 cm. The RF pulse strength was set to 6 kHz for ^{1}H and 15.6 kHz for ^{7}Li, and the recycle delays were set to 1s in both cases. The concentration profiles for ^{1}H, ^{7}Li and ^{19}F are obtained using a direct acquisition under a small constant gradient. The full echo signal is recorded with an echo sequence (“improf” in Bruker spectrometers), with a 90° pulse followed by a short gradient pulse during the first echo delay, and after a refocusing 180° pulse, the gradient is switched on and the full echo FID is recorded. The parameters used are shown in the table below for each nucleus:

Nucleus	Transients number	Recovery delay	RF strength	Gradient strength
^{1}H	32	3 s	6 kHz	12 G/cm
^{19}F	128	1 s	7.4 kHz	12 G/cm
^{7}Li	16	10 s	15.6 kHz	12 G/cm

Methods Table III-1. NMR parameters used for the concentration profiles.

The excited zone corresponds to the liquid inside the NMR coil, which is roughly 2.5-3 cm high. The longitudinal relaxation times (T_1) of each species have been measured to ensure quantitative measurements.

Phase	^{1}H	^{19}F	^{7}Li
LiTFSI.H_2O	667 ms	631 ms	366 ms
LiCl.H_2O	510 ms	859 ms	1.943 s

Methods Table III-2. Longitudinal relaxation times (T_1) measured for the different species in the 12m LiCl – 5 m LiTFSI system

It must be noted that a small amount of TFSI was detected in the LiCl phase in the 1D spectrum, and its peak is weaker by a factor of around 760. A similar ratio (1/740) is observed in the 1D concentration profile (detail not shown).

Viscosity measurements

Viscosity measurements are carried out on a Discovery HR-2 (TA instruments) rheometer using a Peltier concentric cylinders geometry at 25°C (controlled temperature, +/- 0.2°C). Kinematic viscosity is measured for shear rates between 1.0 $s^{-1}$and 30.0 s^{-1}. Retained values for the viscosity resulted from the average of 5 measurements recorded with shear rates comprised between 12.6 s^{-1} and 30 s^{-1}. Error bars are calculated from the standard deviation of the 5 measurements with the average value.

c_{ion} vs. c_{H2O} plot construction

The densities d of solution containing a precisely know amount of a salt (m_{salt}) and water (m_{H_2O}) were measured with an electronic densitometer (Anton Paar, DMA 35 Basic). The c_{salt} and c_{H_2O} were then extracted following the equations: $c_{salt} = \frac{d}{M_{salt}\left[\frac{m_{H_2O}}{m_{salt}}+1\right]}$ and $c_{H_2O} = \frac{d}{M_{H_2O}\left[\frac{m_{salt}}{m_{H_2O}}+1\right]}$ and were further converted to the nm^{-3} scale.

Phase Diagram Construction

The phase diagrams were constructed using the cloud point titration method as described in the main text and inspired from elswhere.[204] Briefly, to a solution with a known amount of a salt and water, a perfectly known mass of the other salt aqueous solution is added until a cloudy solution is obtained after being vortexed. Then, water is added dropwise till the solution becomes clear again. After weighing the water added, the first step is reproduced. Generally, the diagrams were constructed in two times: first, the solution containing the inorganic salt is added to the one containing the organic salt and after, the reverse operation is conducted.

Molecular simulations

Simulations of the LiCl/LiTFSI ABS

All-atom molecular dynamics simulations are carried out with the GROMACS 5.1 simulation package.[271] Initially, two independent simulation boxes for LiCl+water and LiTFSI+water are prepared with the PACKMOL package[272] according to the concentrations of interest. The sizes of the simulation box and numbers of species are summarized in Methods Table III-3 . The initial configurations in the simulation boxes are first relaxed by minimizing the potential energy using steepest descent and then the two independent simulation boxes are merged into a single simulation box. For the equilibration and production runs, the simulation boxes are maintained at an isotropic pressure of 1 bar with the Parrinello-Rahman barostat[273] and the temperature at 298 K with a velocity rescaling thermostat.[274] We monitor the density profiles for ions and water molecules until the profiles are converged (see **Methods Table III-3** for the duration of the equilibration and production runs). The density profiles reported in the figures correspond only to the production runs. Periodic boundary conditions are applied in all three spatial directions. Non-bonded interatomic interactions are described by a 6–12 Lennard-Jones potential with a cut-off at 1.2 nm. The Particle-Mesh-Ewald (PME) method[275] with a Fourier spacing of 0.12 nm and a 1.2 nm real-space cut-off is used to calculate electrostatic interactions. The LINCS algorithm[276] is employed for all bond constraints. The OPLS-AA force field[277] is used for Li^+, Cl^- and the CL & P force field[278] is employed for $TFSI^-$. The SPC/E model is used for the water molecules.[279]

System	Equilibrium box lengths (nm) X x Y x Z	Equilibration & Production run (ns)	Number of ions/molecules			
			Li^+	Cl^-	$TFSI^-$	Water
1 M+1 M	4.2 x 4.2 x 21.0	100 & 400	400	200	200	10746
4m+4m	4.2 x 4.2 x 30.2	500 & 230	1600	800	800	10746
6m+6m	4.2 x 4.2 x 35.9	500 & 180	2340	1170	1170	10746
12m+5m	9.1 x 9.0 x 26.2	200 & 160	11137	7937	3200	35988

Methods Table III-3. Simulation box sizes, duration of the production run and numbers of ions/molecules in MD simulations for the LiCl/LiTFSI ABS.

Condensed phase *ab initio* molecular dynamics calculations

Initial configurations composed of one anion and 111 water molecules were generated using a Monte Carlo procedure implemented in the packmol[255] program, with densities set to the experimental value at the corresponding LiX ($X=Br^-$, I^-, NO_3^-, ClO_4^-) concentrations. All subsequent calculations were performed using DFT within the Generalized Gradient Approximation (GGA) in the form of the rev-PBE exchange-correlation functional.[280] A correction to dispersion interactions in the form of the D3 method[281] was applied. We adopted a representation in the form of a dual basis of atom-centered Gaussian orbitals and plane waves (GPW), as implemented in the QUICKSTEP package of the CP2K program.[282] A grid cutoff of 500 Ry with an associated relative cutoff of 50 Ry were found enough to converge the total energy, using molecule-optimized short-range double-zeta valence plus polarization basis sets, and GTH pseudopotentials (DZVP-MOLOPT-SR-GTH). The Kohn-Sham equations were solved self-consistently using the Orbital Transformation (OT) method, with a convergence criterion set to 10^{-5}. For each system, we performed a 72 ps – long Born-Oppenheimer molecular dynamics simulation. We used the deuterium mass for hydrogen, in order to guarantee a satisfying energy conservation using a time step of 0.5 fs. Systems were propagated in the canonical ensemble, using a Nosé-Hoover chain of three thermostats with a time constant set to 50 fs. The first 12 ps were discarded as equilibration, according to the time evolution of the total energy of the systems; the subsequent 60 ps were used to calculate radial distribution functions associated to the anion hydration. Voronoi tessellation was performed using the TRAVIS program[258] on the sampled dynamics.

Gas phase quantum chemistry calculations

All gas phase calculations were performed using the all-electron ORCA program.[283,284] We have used the PBE0 hybrid functional[285] with D3 correction, along with minimally-augmented triple-zeta valence plus polarization basis sets (ma-def2-TZVP). All anion geometries were optimized, with tight convergence criteria, which also applies to the SCF convergence ("TightSCF" keyword). The converged wavefunctions were further post-processed using the Multiwfn program[286] to compute the molecular polarity indexs (MPI), defined as:

$$MPI = \frac{1}{A}\iint_{S} |V(\boldsymbol{r})|\, dS,$$

where A is the area of the 0.001 e/Å^3 isosurface of the electron density (S), and $V(\boldsymbol{r})$ is the electrostatic potential. The electrostatic potential maps were rendered using the VESTA program.[287]

Chapter IV -

Supplementary Data

VI_3		$R\bar{3}$	R_{Bragg} = 3.78 %	χ^2 = 18.5		
a = 6.9269(2) Å		*c* = 19.9418(2) Å			Vol = 683.05(3) Å^3	
Atom	***Wyckoff Position***	***x/a***	***y/b***	***z/c***	***B_{iso} (Å^2)***	***Occupancy***
I	18*f*	0.0013(3)	0.3343(4)	0.0796 (2)	2.06(2)	1
V	6*c*	0	0	0.3327(4)	2.24(12)	1

Supplementary Table IV-1. Crystallographic data and atomic positions of VI3 determined from Rietveld refinement of its synchrotron X-ray pattern.

VBr_3		$R\bar{3}$	R_{Bragg} = 3.63 %	χ^2 = 19.7		
a = 6.3962(2) Å		*c* = 18.5027(2) Å			Vol = 655.551(7) Å^3	
Atom	***Wyckoff Position***	***x/a***	***y/b***	***z/c***	***B_{iso} (Å^2)***	***Occupancy***
Br	18*f*	0.0010(3)	0.3448(3)	0.0800(2)	2.258(16)	1
V1	6*c*	0	0	0.3376(6)	1.000(2)	0.71(16)
V2	3*a*	0	0	0	1.000(2)	0.58(16)

Supplementary Table IV-2. Crystallographic data and atomic positions of VBr3 determined from Rietveld refinement of its synchrotron X-ray pattern.

$Li_{0.5}VBr_3$		$R\bar{3}$	R_{Bragg} = 15.76 %	χ^2 = 2.54		
a = 6.5177(2) Å		*c* = 18.5664(7) Å			Vol = 683.05(3) Å^3	
Atom	***Wyckoff Position***	***x/a***	***y/b***	***z/c***	***B_{iso} (Å^2)***	***Occupancy***
Br	18*f*	0.0155(9)	0.3447(10)	0.0776(4)	1.04(4)	1
V1	6*c*	0	0	0.337(6)	3.7(3)	0.74(16)
V2	3*a*	0	0	0	3.7(3)	0.52(16)
Li1	3*b*	0	0	0.5	1*	1/3*
Li2	6*c*	0	0	0.16667*	1*	1/3*

Supplementary Table IV-3. Crystallographic data and atomic positions for $Li_{0.5}VBr_3$ determined from Rietveld refinement of its synchrotron X-ray pattern. The "*" symbol indicates that these parameters have not been refined. For the Vanadium atoms the Biso parameters have been constrained in the refinement to be the same.

$Li_{0.5}VI_3$		$R\bar{3}$	R_{Bragg} = 6.84 %	χ^2 = 8.17		
a = 7.0351(2) Å		*c* = 20.1469(3) Å			Vol = 863.525(16) Å^3	
Atom	***Wyckoff Position***	***x/a***	***y/b***	***z/c***	B_{iso} (Å^2)	***Occupancy***
I	18*f*	0.0008(9)	0.329(8)	0.07905(13)	1.665(19)	1
V	6*c*	0	0	0.3241(11)	3.1(3)	1
Li1	3*b*	0	0	0.5	1*	1/3*
Li2	6*c*	0	0	0.16667*	1*	1/3*

Supplementary Table IV-4 Crystallographic data and atomic positions of $Li_{0.5}VI_3$ determined from Rietveld refinement of its synchrotron X-ray pattern. The "*" symbol indicates that these parameters have not been refined.

$LiVCl_3$		$R\bar{3}m$	R_{Bragg} = 4.07 %	χ^2 = 24.7		
a = 3.6273(2) Å		*c* = 17.9394(5) Å			Vol = 204.415(6) Å^3	
Atom	***Wyckoff Position***	***x/a***	***y/b***	***z/c***	B_{iso} (Å^2)	***Occupancy***
Cl	6*c*	0	0	0.2570(6)	0.94(3)	1
V	3*a*	0	0	0	0.83(4)	2/3
Li	3*b*	0	0	0.5	3.3(3)	2/3

Supplementary Table IV-5. Crystallographic data and atomic positions for $LiVCl_3$ determined from Rietveld refinement of both its synchrotron X-ray and neutron patterns.

$LiVBr_3$		$R\bar{3}m$	R_{Bragg} = 3.17 %	χ^2 = 28.3		
a = 3.8225(2) Å		*c* = 19.0100(3) Å			Vol = 240.510(10) Å^3	
Atom	***Wyckoff Position***	***x/a***	***y/b***	***z/c***	B_{iso} (Å^2)	***Occupancy***
Br	6*c*	0	0	0.2545(4)	1.805(11)	1
V	3*a*	0	0	0	1.89(5)	2/3
Li	3*b*	0	0	0.5	1.27(9)	2/3

Supplementary Table IV-6. Crystallographic data and atomic positions for $LiVBr_3$ determined from Rietveld refinement of both its synchrotron X-ray and neutron patterns.

$LiVI_3$		$R\bar{3}$	R_{Bragg} = 1.91 %	χ^2 = 83.2		
a **= 7.1439(2) Å**		***c*** **= 20.6642(2) Å**				**Vol = 913.306(12) Å^3**
Atom	***Wyckoff Position***	***x/a***	***y/b***	***z/c***	B_{iso} ***(Å^2)***	***Occupancy***
I	18*f*	0.0022(2)	0.3337(3)	0.0788(5)	1.964(13)	1
V	6*c*	0	0	0.3326(4)	2.61(11)	1
Li1	3*b*	0	0	0.5	1.1(3)	2/3
Li2	6*c*	0	0	0.1511(11)	1.1(3)	2/3

Supplementary Table IV-7. Crystallographic data and atomic positions of$LiVI_3$ determined from Rietveld refinement of both its synchrotron X-ray and neutron patterns

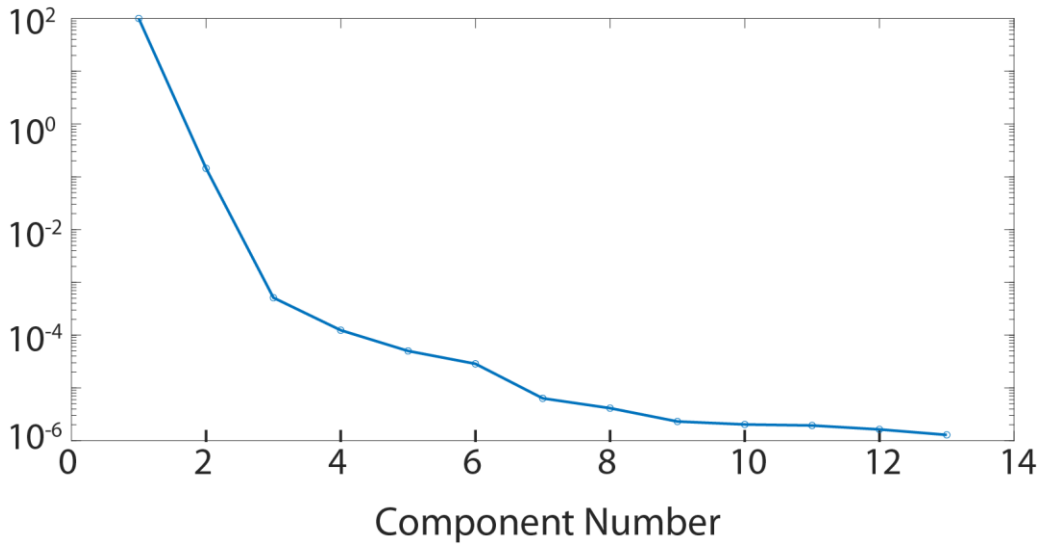

Supplementary Figure IV-1. Logarithm-scale representation of the scores obtained by the PCA analysis on the *operando* XAS spectra at V K-edge during the lithiation of VCl_3. Only three scores (components) were considered statistically relevant to describe the whole process.

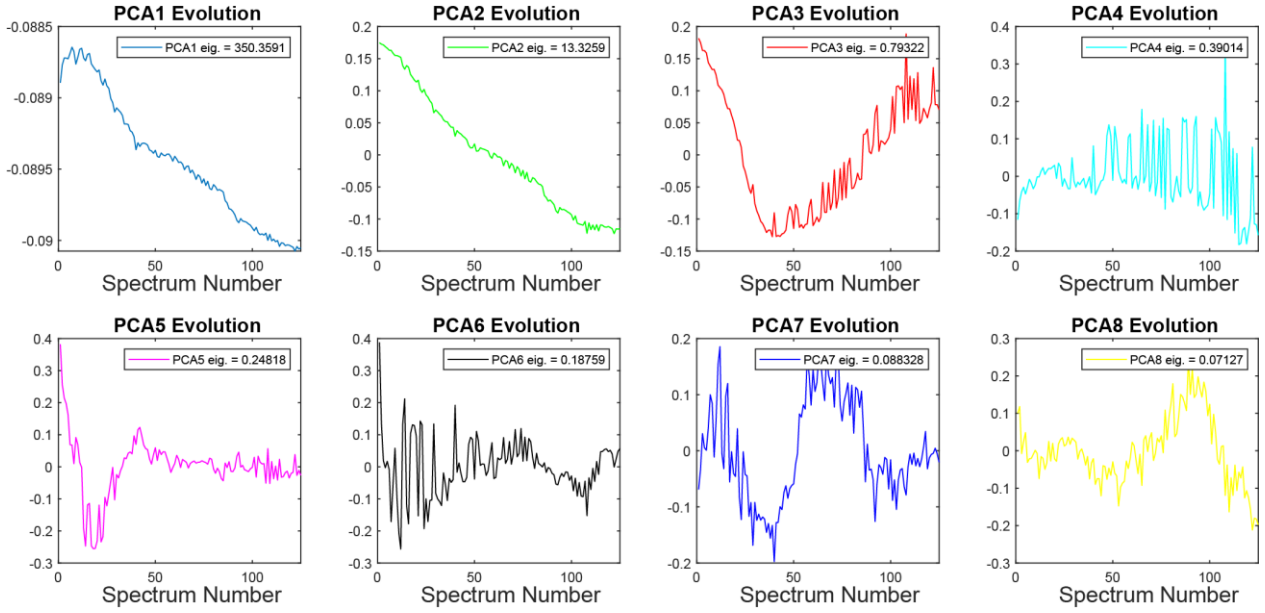

Supplementary Figure IV-2. Evolution of the first 8 scores obtained by the PCA analysis on the *operando* XAS spectra at V K-edge during the lithiation of VCl_3. The first three components exhibit a clear evolution during the whole process.

Methods

Synthesis

VBr_3 and VI_3 were grown in evacuated quartz sealed tubes by reacting elementary vanadium (vanadium powder, -325 mesh 99.5% - Alfa Aesar), iodine (99+%, Alfa Aesar) and purified bromine (Sigma-Aldrich) with a slight excess of halide. Because bromine is a liquid, the tube was place in a liquid nitrogen bath to freeze bromine before being evacuated and quickly flame-sealed. The tubes were placed in a tubular oven, the extremity containing the reactants being heated at 400°C for VBr_3 and 450°C for VI_3 while the other extremity was placed at almost room temperature, as reported elsewhere.[218,219] After a 72 h synthesis, large crystals were collected at the cold extremity of the tube, placed in a Schlenk tube and further heated at 200°C for few hours under vacuum (10^{-2} mbar) to eliminate the excess bromine or iodine traces. VCl_3 (97%, Sigma-Aldrich) was used as received. Lithiated phases were obtained by adding the VX_3 phases in a 3 times excess of n-butyllithium solution (2.5 M in hexane, Sigma Aldrich) and stirring the suspension for at least 1 hour. The solution was further centrifuged and the collected powder was washed 3 times with hexane before drying under vacuum in the glovebox antechamber.

The β–Li_3PS_4 solid electrolyte was obtained in our laboratory via a THF-mediated route proposed by Liu et al.[288] and with a room temperature ionic conductivity of σ_{RT}= 0.21 mS/cm. On the other hand, commercial Li_6PS_5Cl electrolyte was used (NEI), having an ionic conductivity of σ_{RT}= 3.8 mS/cm.

Electrochemical measurements

Liquid electrolytes

All the electrochemical experiments were carried out in an Ar-filled glovebox. All the materials tested were mixed with conductive carbon super-P in an active-material/carbon ratio of 7/3. For all the experiments using a liquid electrolyte (LP30 1 M LiPF6 dissolved in 1:1 v/v ethylene carbonate/dimethyl carbonate, Solvionic or LiFSI 5M in dimethyl carbonate, Solvionic) the as prepared composite were tested in a coin-cell configuration versus a Li metal negative electrode separated by one Whatman glass fiber separator, soaked with ~ 100 µL of electrolyte. The mass of composite loaded in the coin cells was comprised between 3 and 5 mg. The cells were

cycled on VMP or MPG potentiostats (BioLogic) at room temperature, except for the GITT for which the cells were placed in a 25°C oven.

Solid-state batteries

Both anode and cathode composites were prepared by hand grinding the components in the proportions mentioned below with mortar and pestle in an Ar-filled glovebox. The electrochemical testing of the VX_3 compounds (X = Cl, Br, I) in all-solid state configuration was conducted in a three-pieced homemade cell consisting in two stainless steel pistons which are inserted into a PEI body. The cell is closed by means of six axial screws which also provide the pressure required for correct operation. Additionally, a ferrule-cone pair is also integrated in each piston making the setup airtight.

For the battery assembling 35 mg of Li_6PS_5Cl electrolyte were firstly loaded into the cell and cold pressed at 200 kg/cm^2 for 1 minute. Next, 10 to 12 mg/cm^2 of catholyte (VX_3:β–Li_3PS_4:VGCF, 65:30:5 wt.%) were evenly spread onto one side of the compressed solid electrolyte and a pressure of 1000 kg/cm^2 was applied during 1 minute. Lastly, 35 mg of anode composite ($Li_{0.8}In$: Li_6PS_5Cl, 60:40 w%) were added onto the opposite side and the whole stack densified at 4000 kg/cm^2 for 15 min. The fully assembled cell was then closed with a torque key applying 2.3 Nm torque in each screw, which yields an internal pressure of ~1000 kg/cm^2. Galvanostatic cycling were carried out at room temperature, at C/10 using a VMP3 potentiostat (BioLogic).

Materials characterization

Diffraction experiments

Ex Situ synchrotron X-ray diffraction patterns were collected on the BL04-MSPD beamline of the ALBA synchrotron (Barcelona area, Spain) at a wavelength λ = 0.41378 Å using the Position Sensitive Detector MYTHEN. Powder samples were filled in 0.6 mm diameter borosilicate capillaries inside an Ar-atmosphere glovebox and subsequently flame-sealed. *Operando* measurements were carried out in transmission mode using dedicated coin cells[289] assembled under argon filled glovebox and mounted on an ALBA designed 4 samples changer. Constant wavelength (λ = 1.622 Å) neutron powder diffraction (NPD) data were collected for $LiVX_3$ (X= Cl, Br, I) at room temperature using the ECHIDNA high angular resolution powder diffractometer installed at

the OPAL research reactor (Lucas Heights, Australia).[290] To prevent reaction of the samples with ambient atmosphere, the samples were loaded into 9 mm diameter cylindrical vanadium cans in Ar-filled glove box and sealed with In seals. All diffraction patterns were refined using the FullProf program.

Microscopy experiments

The scanning electron microscopy images were measured on a FEI Magellan scanning electron microscope equipped with an Energy dispersive X-ray spectroscopy (EDX) Oxford Instrument detector. EDX measurements were carried out using an acceleration voltage of 10 kV. The Li metal anode samples were collected from cycled cells, washed with dimethyl carbonate and sealed in an air tight container. The transfer from the container to the microscope vacuum chamber was realized rapidly (~ 10 s) to minimize air exposure.

X-Ray Absorption Spectroscopy

Synchrotron X-ray absorption spectroscopy was performed at the vanadium K-edge at the ROCK beamline of the SOLEIL synchrotron facility (Saint-Aubin, France).[291] The Si(111) quick-XAS monochromator with an oscillation frequency of 2 Hz was employed to select the incident photons energy. The spectra were collected in transmission using three gas ionization chambers in series as detectors. A vanadium metal foil was placed between the second and the third ionization chambers to ensure the energy calibration. An average of 900 scans per spectrum (corresponding to 15 minutes of acquisition time for one merged XAS spectrum) was recorded to ensure the reproducibility and to increase the signal-to-noise ratio. The VCl_2 and VCl_3 reference samples were prepared by mixing uniformly the active material with carbon, then pressed into pellets of 10 mm in diameter. For the *operando* measurements, a self-standing electrode was prepared by mixing VCl_3 active material with carbon black and polytetrafluoroethylene (PTFE) in the ratio of 20:70:10 (by wt.%). The electrode was placed in the *in situ* electrochemical cell[292] and cycled against metallic Li using a Celgard membrane as separator and ~100 µL of 5 M LiFSI in DMC as electrolyte. Then, the *in situ* cell was discharged from the OCV (3.025 V) to 2.5 V vs Li^+/Li at a C-rate of C/20 and a XAS spectrum was recorded every 15 minutes.

Solubility measurements

To ensure that the concentrations of vanadium measured in the electrolytes match the thermodynamic limit of solubility for VX_3 materials, a large excess of powder (~100-500 mg, depending on the material) was added in 1 mL of organic electrolyte and stirred for 3 days at room temperature in a Ar-filled glovebox. The as prepared solutions were centrifuged (6 000 rpm, 1 hour), and the supernatant was collected and further filtered on 0.2 μm pore size PTFE syringe filter in an Ar-filled glovebox. Outside of the glovebox, the as prepared solutions were diluted 1 000 or 10 000 times in a 2w% HNO_3 (prepared from HNO_3 99.999% metal basis, Alfa Aesar, and Mili-Q ultrapure water) to reach final vanadium concentrations below 1 ppm. The vanadium concentration in the as prepared aqueous solutions were measured by ICP-MS (Nexion 2000 Perkin Elmer) using a calibration curve obtained by diluting a vanadium standard solution for ICP-MS (TraceCERT, 1 mg/L V in nitric acid, Sigma Aldrich).

UV-vis characterization

The organic solutions were placed in a 0.1 mm optical pathway cuvette (Helma) and their UV-vis spectra was measured with a UV5 Bio Mettler Toledo spectrophotometer using a 1 M LiFSI in dimethyl carbonate blank solution.

References

(1) IEA. *World Energy Outlook 2020, IEA, Paris*; 2020.
(2) CO2 emissions statistics – Data services https://www.iea.org/subscribe-to-data-services/co2-emissions-statistics (accessed 2021 -02 -22).
(3) IEA. The Future of Hydrogen. **2019**.
(4) Timeline of Hydrogen Technologies. *Wikipedia*; 2021.
(5) Paets van Troostwijk, A.; Deiman, J. R. Sur Une Manière de Décomposer l'Eau En Air Inflammable et En Air Vital. *Obs Phys* **1789**, 369–384.
(6) Electrolysis of Water. *Wikipedia*; 2021.
(7) Bockris, J. O.; Potter, E. C. The Mechanism of the Cathodic Hydrogen Evolution Reaction. *J. Electrochem. Soc.* **1952**, *99* (4), 169. https://doi.org/10.1149/1.2779692.
(8) Gileadi, E. *Physical Electrochemistry*; Wiley-VCH Verlag GmbH & Co. KGaA, 2011.
(9) Vesborg, P. C. K.; Seger, B.; Chorkendorff, I. Recent Development in Hydrogen Evolution Reaction Catalysts and Their Practical Implementation. *J. Phys. Chem. Lett.* **2015**, *6* (6), 951–957. https://doi.org/10.1021/acs.jpclett.5b00306.
(10) Lagadec, M. F.; Grimaud, A. Water Electrolysers with Closed and Open Electrochemical Systems. *Nat. Mater.* **2020**, *19* (11), 1140–1150. https://doi.org/10.1038/s41563-020-0788-3.
(11) Pearce, P. E.; Yang, C.; Iadecola, A.; Rodriguez-Carvajal, J.; Rousse, G.; Dedryvère, R.; Abakumov, A. M.; Giaume, D.; Deschamps, M.; Tarascon, J.-M.; Grimaud, A. Revealing the Reactivity of the Iridium Trioxide Intermediate for the Oxygen Evolution Reaction in Acidic Media. *Chem. Mater.* **2019**, *31* (15), 5845–5855. https://doi.org/10.1021/acs.chemmater.9b01976.
(12) Yang, C.; Rousse, G.; Louise Svane, K.; Pearce, P. E.; Abakumov, A. M.; Deschamps, M.; Cibin, G.; Chadwick, A. V.; Dalla Corte, D. A.; Anton Hansen, H.; Vegge, T.; Tarascon, J.-M.; Grimaud, A. Cation Insertion to Break the Activity/Stability Relationship for Highly Active Oxygen Evolution Reaction Catalyst. *Nat. Commun.* **2020**, *11* (1), 1378. https://doi.org/10.1038/s41467-020-15231-x.
(13) Lin, Y.; Tian, Z.; Zhang, L.; Ma, J.; Jiang, Z.; Deibert, B. J.; Ge, R.; Chen, L. Chromium-Ruthenium Oxide Solid Solution Electrocatalyst for Highly Efficient Oxygen Evolution Reaction in Acidic Media. *Nat. Commun.* **2019**, *10* (1), 162. https://doi.org/10.1038/s41467-018-08144-3.
(14) Seitz, L. C.; Dickens, C. F.; Nishio, K.; Hikita, Y.; Montoya, J.; Doyle, A.; Kirk, C.; Vojvodic, A.; Hwang, H. Y.; Norskov, J. K.; Jaramillo, T. F. A Highly Active and Stable IrOx/SrIrO3 Catalyst for the Oxygen Evolution Reaction. *Science* **2016**, *353* (6303), 1011–1014. https://doi.org/10.1126/science.aaf5050.
(15) Colli, A. N.; Girault, H. H.; Battistel, A. Non-Precious Electrodes for Practical Alkaline Water Electrolysis. *Materials* **2019**, *12* (8), 1336. https://doi.org/10.3390/ma12081336.
(16) Oener, S. Z.; Foster, M. J.; Boettcher, S. W. Accelerating Water Dissociation in Bipolar Membranes and for Electrocatalysis. *Science* **2020**, *369* (6507), 1099–1103. https://doi.org/10.1126/science.aaz1487.
(17) Eftekhari, A. Electrocatalysts for Hydrogen Evolution Reaction. *Int. J. Hydrog. Energy* **2017**, *42* (16), 11053–11077. https://doi.org/10.1016/j.ijhydene.2017.02.125.
(18) Chao, D.; Zhou, W.; Xie, F.; Ye, C.; Li, H.; Jaroniec, M.; Qiao, S.-Z. Roadmap for Advanced Aqueous Batteries: From Design of Materials to Applications. *Sci. Adv.* **2020**, *6* (21), eaba4098. https://doi.org/10.1126/sciadv.aba4098.
(19) Kim, H.; Hong, J.; Park, K.-Y.; Kim, H.; Kim, S.-W.; Kang, K. Aqueous Rechargeable Li and Na Ion Batteries. *Chem Rev* **2014**, 40.
(20) Li, W.; Dahn, J. R.; Wainwright, D. S. Rechargeable Lithium Batteries with Aqueous Electrolytes. *Science* **1994**, *264* (5162), 1115–1118. https://doi.org/10.1126/science.264.5162.1115.

(21) Li, W.; McKinnon, W. R.; Dahn, J. R. Lithium Intercalation from Aqueous Solutions. *J. Electrochem. Soc.* **1994**, *141* (9), 2310–2316. https://doi.org/10.1149/1.2055118.
(22) Imanishi, N.; Toyoda, M.; Takeda, Y.; Yamamoto, O. Study on Lithium Intercalation into MoS2. *Solid State Ion.* **1992**, *58* (3), 333–338. https://doi.org/10.1016/0167-2738(92)90137-E.
(23) Voiry, D.; Yamaguchi, H.; Li, J.; Silva, R.; Alves, D. C. B.; Fujita, T.; Chen, M.; Asefa, T.; Shenoy, V. B.; Eda, G.; Chhowalla, M. Enhanced Catalytic Activity in Strained Chemically Exfoliated WS2 Nanosheets for Hydrogen Evolution. *Nat. Mater.* **2013**, *12* (9), 850–855. https://doi.org/10.1038/nmat3700.
(24) Shinagawa, T.; Garcia-Esparza, A. T.; Takanabe, K. Insight on Tafel Slopes from a Microkinetic Analysis of Aqueous Electrocatalysis for Energy Conversion. *Sci. Rep.* **2015**, *5*, 13801. https://doi.org/10.1038/srep13801.
(25) Platinum mine production by country 2019 https://www.statista.com/statistics/273645/global-mine-production-of-platinum/ (accessed 2021 -02 -02).
(26) Chen, X.; McCrum, I. T.; Schwarz, K. A.; Janik, M. J.; Koper, M. T. M. Co-Adsorption of Cations as the Cause of the Apparent PH Dependence of Hydrogen Adsorption on a Stepped Platinum Single-Crystal Electrode. *Angew. Chem. Int. Ed.* **2017**, *56* (47), 15025–15029. https://doi.org/10.1002/anie.201709455.
(27) Janik, M. J.; McCrum, I. T.; Koper, M. T. M. On the Presence of Surface Bound Hydroxyl Species on Polycrystalline Pt Electrodes in the "Hydrogen Potential Region" (0–0.4 V-RHE). *J. Catal.* **2018**, *367*, 332–337. https://doi.org/10.1016/j.jcat.2018.09.031.
(28) McCrum, I. T.; Chen, X.; Schwarz, K. A.; Janik, M. J.; Koper, M. T. M. Effect of Step Density and Orientation on the Apparent PH Dependence of Hydrogen and Hydroxide Adsorption on Stepped Platinum Surfaces. *J. Phys. Chem. C* **2018**, *122* (29), 16756–16764. https://doi.org/10.1021/acs.jpcc.8b03660.
(29) Becker, M.; Breiter, M. Untersuchung der Sauerstoffbelegung an Edelmetallelektroden mit Hilfe von Impedanzmessungen und kathodischen Ladekurven I. Glatte Platinelektroden. *Z. Für Elektrochem. Berichte Bunsenges. Für Phys. Chem.* **1956**, *60* (9–10), 1080–1089. https://doi.org/10.1002/bbpc.19560600926.
(30) Breiter, M. W. Electrochemical Study of Hydrogen Adsorption on Clean Platinum Metal Surfaces. *Ann. N. Y. Acad. Sci.* **1963**, *101* (3), 709–721. https://doi.org/10.1111/j.1749-6632.1963.tb54927.x.
(31) Will, F. G. Hydrogen Adsorption on Platinum Single Crystal Electrodes I . Isotherms and Heats of Adsorption. *J. Electrochem. Soc.* **1965**, *112* (4), 451–455. https://doi.org/10.1149/1.2423567.
(32) Clavilier, J.; Faure, R.; Guinet, G.; Durand, R. PREPARATION OF MONOCRYSTALLINE Pt MICROELECTRODES AND ELECTROCHEMICAL STUDY OF THE PLANE SURFACES CUT IN THE DIRECTION OF THE (111) AND (110) PLANES. 5.
(33) Zolfaghari, A.; Chayer, M.; Jerkiewicz, G. Energetics of the Underpotential Deposition of Hydrogen on Platinum Electrodes I. Absence of Coadsorbed Species. *J. Electrochem. Soc.* **1997**, *144* (9), 3034–3041. https://doi.org/10.1149/1.1837955.
(34) Marković, N. M.; Grgur, B. N.; Ross, P. N. Temperature-Dependent Hydrogen Electrochemistry on Platinum Low-Index Single-Crystal Surfaces in Acid Solutions. *J. Phys. Chem. B* **1997**, *101* (27), 5405–5413. https://doi.org/10.1021/jp970930d.
(35) Durst, J.; Simon, C.; Hasché, F.; Gasteiger, H. A. Hydrogen Oxidation and Evolution Reaction Kinetics on Carbon Supported Pt, Ir, Rh, and Pd Electrocatalysts in Acidic Media. *J. Electrochem. Soc.* **2015**, *162* (1), F190–F203. https://doi.org/10.1149/2.0981501jes.
(36) Ishikawa, Y.; Mateo, J. J.; Tryk, D. A.; Cabrera, C. R. Direct Molecular Dynamics and Density-Functional Theoretical Study of the Electrochemical Hydrogen Oxidation Reaction and

Underpotential Deposition of H on Pt(111). *J. Electroanal. Chem.* **2007**, *607* (1), 37–46. https://doi.org/10.1016/j.jelechem.2006.10.011.

(37) Zwaschka, G.; Tong, Y.; Wolf, M.; Campen, R. K. Probing the Hydrogen Evolution Reaction and Charge Transfer on Platinum Electrodes on Femtosecond Timescales. *ChemElectroChem* **2019**, celc.201900336. https://doi.org/10.1002/celc.201900336.

(38) Clavilier, J.; Faure, R.; Guinet, G.; Durand, R. Preparation of Monocrystalline Pt Microelectrodes and Electrochemical Study of the Plane Surfaces Cut in the Direction of the {111} and {110} Planes. *J. Electroanal. Chem. Interfacial Electrochem.* **1980**, *107* (1), 205–209. https://doi.org/10.1016/S0022-0728(79)80022-4.

(39) Conway, B. E.; Bockris, J. O. Electrolytic Hydrogen Evolution Kinetics and Its Relation to the Electronic and Adsorptive Properties of the Metal. *J. Chem. Phys.* **1957**, *26* (3), 532–541. https://doi.org/10.1063/1.1743339.

(40) Trasatti, S. Work Function, Electronegativity, and Electrochemical Behaviour of Metals. *J. Electroanal. Chem. Interfacial Electrochem.* **1972**, *39* (1), 163–184. https://doi.org/10.1016/S0022-0728(72)80485-6.

(41) Nørskov, J. K.; Bligaard, T.; Logadottir, A.; Kitchin, J. R.; Chen, J. G.; Pandelov, S.; Stimming, U. Trends in the Exchange Current for Hydrogen Evolution. *J. Electrochem. Soc.* **2005**, *152* (3), J23. https://doi.org/10.1149/1.1856988.

(42) Zeradjanin, A. R.; Vimalanandan, A.; Polymeros, G.; Topalov, A. A.; Mayrhofer, K. J. J.; Rohwerder, M. Balanced Work Function as a Driver for Facile Hydrogen Evolution Reaction – Comprehension and Experimental Assessment of Interfacial Catalytic Descriptor. *Phys. Chem. Chem. Phys.* **2017**, *19* (26), 17019–17027. https://doi.org/10.1039/C7CP03081A.

(43) Hinnemann, B.; Moses, P. G.; Bonde, J.; Jørgensen, K. P.; Nielsen, J. H.; Horch, S.; Chorkendorff, I.; Nørskov, J. K. Biomimetic Hydrogen Evolution: MoS2 Nanoparticles as Catalyst for Hydrogen Evolution. *J. Am. Chem. Soc.* **2005**, *127* (15), 5308–5309. https://doi.org/10.1021/ja0504690.

(44) Jaramillo, T. F.; Jørgensen, K. P.; Bonde, J.; Nielsen, J. H.; Horch, S.; Chorkendorff, I. Identification of Active Edge Sites for Electrochemical H2 Evolution from MoS2 Nanocatalysts. *Science* **2007**, *317* (5834), 100–102. https://doi.org/10.1126/science.1141483.

(45) Sheng, W.; Gasteiger, H. A.; Shao-Horn, Y. Hydrogen Oxidation and Evolution Reaction Kinetics on Platinum: Acid vs Alkaline Electrolytes. *J. Electrochem. Soc.* **2010**, *157* (11), B1529. https://doi.org/10.1149/1.3483106.

(46) Subbaraman, R.; Tripkovic, D.; Strmcnik, D.; Chang, K.-C.; Uchimura, M.; Paulikas, A. P.; Stamenkovic, V.; Markovic, N. M. Enhancing Hydrogen Evolution Activity in Water Splitting by Tailoring Li+-Ni(OH)2-Pt Interfaces. *Science* **2011**, *334* (6060), 1256–1260. https://doi.org/10.1126/science.1211934.

(47) Sheng, W.; Myint, M.; Chen, J. G.; Yan, Y. Correlating the Hydrogen Evolution Reaction Activity in Alkaline Electrolytes with the Hydrogen Binding Energy on Monometallic Surfaces. *Energy Environ. Sci.* **2013**, *6* (5), 1509–1512. https://doi.org/10.1039/C3EE00045A.

(48) Sheng, W.; Zhuang, Z.; Gao, M.; Zheng, J.; Chen, J. G.; Yan, Y. Correlating Hydrogen Oxidation and Evolution Activity on Platinum at Different PH with Measured Hydrogen Binding Energy. *Nat. Commun.* **2015**, *6*, 5848. https://doi.org/10.1038/ncomms6848.

(49) Zheng, J.; Sheng, W.; Zhuang, Z.; Xu, B.; Yan, Y. Universal Dependence of Hydrogen Oxidation and Evolution Reaction Activity of Platinum-Group Metals on PH and Hydrogen Binding Energy. *Sci. Adv.* **2016**, *2* (3), e1501602. https://doi.org/10.1126/sciadv.1501602.

(50) Dubouis, N.; Yang, C.; Beer, R.; Ries, L.; Voiry, D.; Grimaud, A. Interfacial Interactions as an Electrochemical Tool To Understand Mo-Based Catalysts for the Hydrogen Evolution Reaction. *ACS Catal.* **2018**, *8* (2), 828–836. https://doi.org/10.1021/acscatal.7b03684.

(51) Jackson, M. N.; Jung, O.; Lamotte, H. C.; Surendranath, Y. Donor-Dependent Promotion of Interfacial Proton-Coupled Electron Transfer in Aqueous Electrocatalysis. *ACS Catal.* **2019**, 3737–3743. https://doi.org/10.1021/acscatal.9b00056.
(52) Zheng, Y.; Jiao, Y.; Vasileff, A.; Qiao, S.-Z. The Hydrogen Evolution Reaction in Alkaline Solution: From Theory, Single Crystal Models, to Practical Electrocatalysts. *Angew. Chem. Int. Ed.* **2018**, *57* (26), 7568–7579. https://doi.org/10.1002/anie.201710556.
(53) Subbaraman, R.; Tripkovic, D.; Chang, K.-C.; Strmcnik, D.; Paulikas, A. P.; Hirunsit, P.; Chan, M.; Greeley, J.; Stamenkovic, V.; Markovic, N. M. Trends in Activity for the Water Electrolyser Reactions on 3d M(Ni,Co,Fe,Mn) Hydr(Oxy)Oxide Catalysts. *Nat. Mater.* **2012**, *11* (6), 550–557. https://doi.org/10.1038/nmat3313.
(54) McCrum, I. T.; Koper, M. T. M. The Role of Adsorbed Hydroxide in Hydrogen Evolution Reaction Kinetics on Modified Platinum. *Nat. Energy* **2020**. https://doi.org/10.1038/s41560-020-00710-8.
(55) Martins, P. F. B. D.; Lopes, P. P.; Ticianelli, E. A.; Stamenkovic, V. R.; Markovic, N. M.; Strmcnik, D. Hydrogen Evolution Reaction on Copper: Promoting Water Dissociation by Tuning the Surface Oxophilicity. *Electrochem. Commun.* **2019**. https://doi.org/10.1016/j.elecom.2019.01.006.
(56) Strmcnik, D.; Uchimura, M.; Wang, C.; Subbaraman, R.; Danilovic, N.; van der Vliet, D.; Paulikas, A. P.; Stamenkovic, V. R.; Markovic, N. M. Improving the Hydrogen Oxidation Reaction Rate by Promotion of Hydroxyl Adsorption. *Nat. Chem.* **2013**, *5* (4), 300–306. https://doi.org/10.1038/nchem.1574.
(57) Grozovski, V.; Vesztergom, S.; Láng, G. G.; Broekmann, P. Electrochemical Hydrogen Evolution: H+ or H2O Reduction? A Rotating Disk Electrode Study. *J. Electrochem. Soc.* **2017**, *164* (11), E3171–E3178. https://doi.org/10.1149/2.0191711jes.
(58) You, B.; Zhang, Y.; Jiao, Y.; Davey, kenneth; Qiao, S. Negative Charging of Transition-Metal Phosphides via Strong Electronic Coupling for Destabilization of Alkaline Water. *Angew. Chem. Int. Ed.* **2019**. https://doi.org/10.1002/anie.201906683.
(59) Muñoz-Santiburcio, D.; Marx, D. Nanoconfinement in Slit Pores Enhances Water Self-Dissociation. *Phys. Rev. Lett.* **2017**, *119* (5), 056002. https://doi.org/10.1103/PhysRevLett.119.056002.
(60) Lamoureux, P. S.; Singh, A. R.; Chan, K. PH Effects on Hydrogen Evolution and Oxidation over Pt(111): Insights from First-Principles. *ACS Catal.* **2019**, 6194–6201. https://doi.org/10.1021/acscatal.9b00268.
(61) Lu, S.; Zhuang, Z. Investigating the Influences of the Adsorbed Species on Catalytic Activity for Hydrogen Oxidation Reaction in Alkaline Electrolyte. *J. Am. Chem. Soc.* **2017**, *139* (14), 5156–5163. https://doi.org/10.1021/jacs.7b00765.
(62) Intikhab, S.; Snyder, J. D.; Tang, M. H. Adsorbed Hydroxide Does Not Participate in the Volmer Step of Alkaline Hydrogen Electrocatalysis https://pubs.acs.org/doi/abs/10.1021/acscatal.7b02787 (accessed 2019 -04 -08). https://doi.org/10.1021/acscatal.7b02787.
(63) Auinger, M.; Katsounaros, I.; Meier, J. C.; Klemm, S. O.; Biedermann, P. U.; Topalov, A. A.; Rohwerder, M.; Mayrhofer, K. J. J. Near-Surface Ion Distribution and Buffer Effects during Electrochemical Reactions. *Phys. Chem. Chem. Phys.* **2011**, *13* (36), 16384. https://doi.org/10.1039/c1cp21717h.
(64) Santos, E.; Lundin, A.; Pötting, K.; Quaino, P.; Schmickler, W. Model for the Electrocatalysis of Hydrogen Evolution. *Phys. Rev. B* **2009**, *79* (23), 235436. https://doi.org/10.1103/PhysRevB.79.235436.
(65) van der Niet, M. J. T. C.; Garcia-Araez, N.; Hernández, J.; Feliu, J. M.; Koper, M. T. M. Water Dissociation on Well-Defined Platinum Surfaces: The Electrochemical Perspective. *Catal. Today* **2013**, *202*, 105–113. https://doi.org/10.1016/j.cattod.2012.04.059.

(66) McCrum, I. T.; Janik, M. J. PH and Alkali Cation Effects on the Pt Cyclic Voltammogram Explained Using Density Functional Theory. *J. Phys. Chem. C* **2016**, *120* (1), 457–471. https://doi.org/10.1021/acs.jpcc.5b10979.
(67) Garcia-Araez, N.; Climent, V.; Feliu, J. Potential-Dependent Water Orientation on Pt(111), Pt(100), and Pt(110), As Inferred from Laser-Pulsed Experiments. Electrostatic and Chemical Effects. *J. Phys. Chem. C* **2009**, *113* (21), 9290–9304. https://doi.org/10.1021/jp900792q.
(68) Velasco-Velez, J.-J.; Wu, C. H.; Pascal, T. A.; Wan, L. F.; Guo, J.; Prendergast, D.; Salmeron, M. The Structure of Interfacial Water on Gold Electrodes Studied by X-Ray Absorption Spectroscopy. *Science* **2014**, *346* (6211), 831–834. https://doi.org/10.1126/science.1259437.
(69) Ledezma-Yanez, I.; Wallace, W. D. Z.; Sebastián-Pascual, P.; Climent, V.; Feliu, J. M.; Koper, M. T. M. Interfacial Water Reorganization as a PH-Dependent Descriptor of the Hydrogen Evolution Rate on Platinum Electrodes. *Nat. Energy* **2017**, *2* (4), 17031. https://doi.org/10.1038/nenergy.2017.31.
(70) Sarabia, F. J.; Sebastián-Pascual, P.; Koper, M. T. M.; Climent, V.; Feliu, J. M. Effect of the Interfacial Water Structure on the Hydrogen Evolution Reaction on Pt(111) Modified with Different Nickel Hydroxide Coverages in Alkaline Media. *ACS Appl. Mater. Interfaces* **2019**, *11* (1), 613–623. https://doi.org/10.1021/acsami.8b15003.
(71) Feliu, J. M.; Sarabia, F. J.; Climent, V. Interfacial Study of Nickel Modified Pt(111) Surfaces in Phosphate Containing Solutions. Effect on the Hydrogen Evolution Reaction. *ChemPhysChem* **2019**, cphc.201900543. https://doi.org/10.1002/cphc.201900543.
(72) Pecina, O.; Schmickler, W. A Model for Electrochemical Proton-Transfer Reactions. *Chem. Phys.* **1998**, *228* (1), 265–277. https://doi.org/10.1016/S0301-0104(97)00299-1.
(73) Trasatti, S. Work Function, Electronegativity, and Electrochemical Behaviour of Metals. *J. Electroanal. Chem. Interfacial Electrochem.* **1971**, *33* (2), 351–378. https://doi.org/10.1016/S0022-0728(71)80123-7.
(74) Rossmeisl, J.; Chan, K.; Skúlason, E.; Björketun, M. E.; Tripkovic, V. On the PH Dependence of Electrochemical Proton Transfer Barriers. *Catal. Today* **2016**, *262*, 36–40. https://doi.org/10.1016/j.cattod.2015.08.016.
(75) Filhol, J.-S.; Neurock, M. Elucidation of the Electrochemical Activation of Water over Pd by First Principles. *Angew. Chem. Int. Ed.* **2006**, *45* (3), 402–406. https://doi.org/10.1002/anie.200502540.
(76) Markovic, N. M. Electrocatalysis: Interfacing Electrochemistry. *Nat. Mater.* **2013**, *12* (2), 101–102.
(77) Stamenkovic, V. R.; Strmcnik, D.; Lopes, P. P.; Markovic, N. M. Energy and Fuels from Electrochemical Interfaces. *Nat. Mater.* **2016**, *16* (1), 57–69. https://doi.org/10.1038/nmat4738.
(78) Favaro, M.; Jeong, B.; Ross, P. N.; Yano, J.; Hussain, Z.; Liu, Z.; Crumlin, E. J. Unravelling the Electrochemical Double Layer by Direct Probing of the Solid/Liquid Interface. *Nat. Commun.* **2016**, *7* (1). https://doi.org/10.1038/ncomms12695.
(79) Toney, M. F.; Howard, J. N.; Richer, J.; Borges, G. L.; Gordon, J. G.; Melroy, O. R.; Wiesler, D. G.; Yee, D.; Sorensen, L. B. Voltage-Dependent Ordering of Water Molecules at an Electrode–Electrolyte Interface. *Nature* **1994**, *368* (6470), 444–446. https://doi.org/10.1038/368444a0.
(80) Li, C.-Y.; Le, J.-B.; Wang, Y.-H.; Chen, S.; Yang, Z.-L.; Li, J.-F.; Cheng, J.; Tian, Z.-Q. In Situ Probing Electrified Interfacial Water Structures at Atomically Flat Surfaces. *Nat. Mater.* **2019**, *18* (7), 697–701. https://doi.org/10.1038/s41563-019-0356-x.
(81) Limmer, D. T.; Willard, A. P.; Madden, P.; Chandler, D. Hydration of Metal Surfaces Can Be Dynamically Heterogeneous and Hydrophobic. *Proc. Natl. Acad. Sci.* **2013**, *110* (11), 4200–4205. https://doi.org/10.1073/pnas.1301596110.
(82) Limmer, D. T.; Willard, A. P.; Madden, P. A.; Chandler, D. Water Exchange at a Hydrated Platinum Electrode Is Rare and Collective. *J. Phys. Chem. C* **2015**, *119* (42), 24016–24024. https://doi.org/10.1021/acs.jpcc.5b08137.

(83) Kattirtzi, J. A.; Limmer, D. T.; Willard, A. P. Microscopic Dynamics of Charge Separation at the Aqueous Electrochemical Interface. *Proc. Natl. Acad. Sci.* **2017**, *114* (51), 13374–13379. https://doi.org/10.1073/pnas.1700093114.
(84) Frumkin Effect. In *IUPAC Compendium of Chemical Terminology*; Nič, M., Jirát, J., Košata, B., Jenkins, A., McNaught, A., Eds.; IUPAC: Research Triagle Park, NC, 2009. https://doi.org/10.1351/goldbook.F02538.
(85) Auinger, M.; Katsounaros, I.; Meier, J. C.; Klemm, S. O.; Biedermann, P. U.; Topalov, A. A.; Rohwerder, M.; Mayrhofer, K. J. J. Near-Surface Ion Distribution and Buffer Effects during Electrochemical Reactions. *Phys. Chem. Chem. Phys.* **2011**, *13* (36), 16384. https://doi.org/10.1039/c1cp21717h.
(86) Feliu, J. M. Future Tasks in Interfacial Electrochemistry and Surface Reactivity. *J. Solid State Electrochem.* **2020**. https://doi.org/10.1007/s10008-020-04690-3.
(87) O'Mahony, A. M.; Silvester, D. S.; Aldous, L.; Hardacre, C.; Compton, R. G. Effect of Water on the Electrochemical Window and Potential Limits of Room-Temperature Ionic Liquids. *J. Chem. Eng. Data* **2008**, *53* (12), 2884–2891. https://doi.org/10.1021/je800678e.
(88) Feng, G.; Jiang, X.; Qiao, R.; Kornyshev, A. A. Water in Ionic Liquids at Electrified Interfaces: The Anatomy of Electrosorption. *ACS Nano* **2014**, *8* (11), 11685–11694. https://doi.org/10.1021/nn505017c.
(89) Bi, S.; Wang, R.; Liu, S.; Yan, J.; Mao, B.; Kornyshev, A. A.; Feng, G. Minimizing the Electrosorption of Water from Humid Ionic Liquids on Electrodes. *Nat. Commun.* **2018**, *9* (1), 5222. https://doi.org/10.1038/s41467-018-07674-0.
(90) de Souza, R. F.; Padilha, J. C.; Gonçalves, R. S.; Rault-Berthelot, J. Dialkylimidazolium Ionic Liquids as Electrolytes for Hydrogen Production from Water Electrolysis. *Electrochem. Commun.* **2006**, *8* (2), 211–216. https://doi.org/10.1016/j.elecom.2005.10.036.
(91) de Souza, R. F.; Padilha, J. C.; Gonçalves, R. S.; de Souza, M. O.; Rault-Berthelot, J. Electrochemical Hydrogen Production from Water Electrolysis Using Ionic Liquid as Electrolytes: Towards the Best Device. *J. Power Sources* **2007**, *164* (2), 792–798. https://doi.org/10.1016/j.jpowsour.2006.11.049.
(92) Meng, Y.; Aldous, L.; Belding, S. R.; Compton, R. G. The Hydrogen Evolution Reaction in a Room Temperature Ionic Liquid: Mechanism and Electrocatalyst Trends. *Phys. Chem. Chem. Phys.* **2012**, *14* (15), 5222–5228. https://doi.org/10.1039/C2CP23801B.
(93) Aurbach, D. The Electrochemical Behavior of Lithium Salt Solutions of Γ-Butyrolactone with Noble Metal Electrodes. *J. Electrochem. Soc.* **1989**, *136* (4), 906–913. https://doi.org/10.1149/1.2096876.
(94) Aurbach, D.; Daroux, M.; Faguy, P.; Yeager, E. The Electrochemistry of Noble Metal Electrodes in Aprotic Organic Solvents Containing Lithium Salts. *J. Electroanal. Chem. Interfacial Electrochem.* **1991**, *297* (1), 225–244.
(95) Aurbach, D. The Correlation Between the Surface Chemistry and the Performance of Li-Carbon Intercalation Anodes for Rechargeable 'Rocking-Chair' Type Batteries. *J. Electrochem. Soc.* **1994**, *141* (3), 603. https://doi.org/10.1149/1.2054777.
(96) Aurbach, D.; Weissman, I.; Schechter, A.; Cohen, H. X-Ray Photoelectron Spectroscopy Studies of Lithium Surfaces Prepared in Several Important Electrolyte Solutions. A Comparison with Previous Studies by Fourier Transform Infrared Spectroscopy. *Langmuir* **1996**, *12* (16), 3991–4007.
(97) Xu, K. Electrolytes and Interphases in Li-Ion Batteries and Beyond. *Chem. Rev.* **2014**, *114* (23), 11503–11618. https://doi.org/10.1021/cr500003w.
(98) Kitz, P. G.; Novák, P.; Berg, E. J. Influence of Water Contamination on the SEI Formation in Li-Ion Cells: An Operando EQCM-D Study. *ACS Appl. Mater. Interfaces* **2020**, *12* (13), 15934–15942. https://doi.org/10.1021/acsami.0c01642.

(99) Xiong, D. J.; Petibon, R.; Madec, L.; Hall, D. S.; Dahn, J. R. Some Effects of Intentionally Added Water on LiCoO $_2$ /Graphite Pouch Cells. *J. Electrochem. Soc.* **2016**, *163* (8), A1678–A1685. https://doi.org/10.1149/2.0901608jes.
(100) Wang, R.; Boyd, S.; Bonnesen, P. V.; Augustyn, V. Effect of Water in a Non-Aqueous Electrolyte on Electrochemical Mg2+ Insertion into WO3. *J. Power Sources* **2020**, *477*, 229015. https://doi.org/10.1016/j.jpowsour.2020.229015.
(101) Lanning, J. A.; Chambers, J. Q. Voltammetric Study of the Hydrogen Ion/Hydrogen Couple in Acetonitrile/Water Mixtures. 7.
(102) Ledezma-Yanez, I.; Díaz-Morales, O.; Figueiredo, M. C.; Koper, M. T. M. Hydrogen Oxidation and Hydrogen Evolution on a Platinum Electrode in Acetonitrile. *ChemElectroChem* **2015**, *2* (10), 1612–1622. https://doi.org/10.1002/celc.201500341.
(103) Ledezma-Yanez, I.; Koper, M. T. M. Influence of Water on the Hydrogen Evolution Reaction on a Gold Electrode in Acetonitrile Solution. *J. Electroanal. Chem.* **2017**, *793*, 18–24. https://doi.org/10.1016/j.jelechem.2016.08.018.
(104) Suárez-Herrera, M. F.; Costa-Figueiredo, M.; Feliu, J. M. Voltammetry of Basal Plane Platinum Electrodes in Acetonitrile Electrolytes: Effect of the Presence of Water. *Langmuir* **2012**, *28* (11), 5286–5294. https://doi.org/10.1021/la205097p.
(105) Strmcnik, D.; Uchimura, M.; Wang, C.; Subbaraman, R.; Danilovic, N.; van der Vliet, D.; Paulikas, A. P.; Stamenkovic, V. R.; Markovic, N. M. Improving the Hydrogen Oxidation Reaction Rate by Promotion of Hydroxyl Adsorption. *Nat. Chem.* **2013**, *5* (4), 300–306. https://doi.org/10.1038/nchem.1574.
(106) Irr, L. G. Voltammetric Studies of Lithium Salt-Acetonitrile Solutions Containing Traces of Water. *Electrochimica Acta* **1984**, *29* (1), 1–5. https://doi.org/10.1016/0013-4686(84)80028-6.
(107) Dubouis, N.; Lemaire, P.; Mirvaux, B.; Salager, E.; Deschamps, M.; Grimaud, A. The Role of the Hydrogen Evolution Reaction in the Solid–Electrolyte Interphase Formation Mechanism for "Water-in-Salt" Electrolytes. *Energy Environ. Sci.* **2018**. https://doi.org/10.1039/C8EE02456A.
(108) Lutz, L.; Alves Dalla Corte, D.; Tang, M.; Salager, E.; Deschamps, M.; Grimaud, A.; Johnson, L.; Bruce, P. G.; Tarascon, J.-M. Role of Electrolyte Anions in the Na–O2 Battery: Implications for NaO2 Solvation and the Stability of the Sodium Solid Electrolyte Interphase in Glyme Ethers. *Chem. Mater.* **2017**, *29* (14), 6066–6075. https://doi.org/10.1021/acs.chemmater.7b01953.
(109) Smith, D. W. Ionic Hydration Enthalpies. *J. Chem. Educ.* **1977**, *54* (9), 540. https://doi.org/10.1021/ed054p540.
(110) Nagano, Y.; Mizuno, H.; Sakiyama, M.; Fujiwara, T.; Kondo, Y. Hydration Enthalpy of Tetra-n-Butylammonium Ion. *J. Phys. Chem.* **1991**, *95* (6), 2536–2540. https://doi.org/10.1021/j100159a079.
(111) Newsome, J. R.; Neilson, G. W.; Enderby, J. E. Lithium Ions in Aqueous Solution. *J. Phys. C Solid State Phys.* **1980**, *13* (32), L923. https://doi.org/10.1088/0022-3719/13/32/001.
(112) Cartailler, T.; Kunz, W.; Turq, P.; Bellisent-Funel, M.-C. Lithium Bromide in Acetonitrile and Water: A Neutron Scattering Study. *J. Phys. Condens. Matter* **1991**, *3* (47), 9511. https://doi.org/10.1088/0953-8984/3/47/023.
(113) Mähler, J.; Persson, I. A Study of the Hydration of the Alkali Metal Ions in Aqueous Solution. *Inorg. Chem.* **2012**, *51* (1), 425–438. https://doi.org/10.1021/ic2018693.
(114) Spångberg, D.; Hermansson, K. The Solvation of Li+ and Na+ in Acetonitrile from Ab Initio-Derived Many-Body Ion–Solvent Potentials. *Chem. Phys.* **2004**, *300* (1), 165–176. https://doi.org/10.1016/j.chemphys.2004.01.011.

(115) Suárez-Herrera, M. F.; Costa-Figueiredo, M.; Feliu, J. M. Voltammetry of Basal Plane Platinum Electrodes in Acetonitrile Electrolytes: Effect of the Presence of Water. *Langmuir* **2012**, *28* (11), 5286–5294. https://doi.org/10.1021/la205097p.

(116) Deng, H.; Peljo, P.; Stockmann, T. J.; Qiao, L.; Vainikka, T.; Kontturi, K.; Opallo, M.; Girault, H. H. Surprising Acidity of Hydrated Lithium Cations in Organic Solvents. *Chem Commun* **2014**, *50* (42), 5554–5557. https://doi.org/10.1039/C4CC01892C.

(117) Cassone, G.; Creazzo, F.; Giaquinta, P. V.; Sponer, J.; Saija, F. Ionic Diffusion and Proton Transfer in Aqueous Solutions of Alkali Metal Salts. *Phys. Chem. Chem. Phys.* **2017**, *19* (31), 20420–20429. https://doi.org/10.1039/C7CP03663A.

(118) Masiker, M. C.; Mayne, C. L.; Boone, B. J.; Orendt, A. M.; Eyring, E. M. 7Li NMR Chemical Shift Titration and Theoretical DFT Calculation Studies: Solvent and Anion Effects on Second-Order Complexation of 12-Crown-4 and 1-Aza-12-Crown-4 with Lithium Cation in Several Aprotic Solvents. *Magn. Reson. Chem. MRC* **2010**, *48* (2), 94–100. https://doi.org/10.1002/mrc.2542.

(119) Thordarson, P. Determining Association Constants from Titration Experiments in Supramolecular Chemistry. *Chem Soc Rev* **2011**, *40* (3), 1305–1323. https://doi.org/10.1039/C0CS00062K.

(120) Dubouis, N.; Serva, A.; Salager, E.; Deschamps, M.; Salanne, M.; Grimaud, A. The Fate of Water at the Electrochemical Interfaces: Electrochemical Behavior of Free Water Versus Coordinating Water. *J. Phys. Chem. Lett.* **2018**, *9* (23), 6683–6688. https://doi.org/10.1021/acs.jpclett.8b03066.

(121) Marx, D.; Tuckerman, M. E.; Hutter, J.; Parrinello, M. The Nature of the Hydrated Excess Proton in Water. *Nature* **1999**, *397* (6720), 601–604. https://doi.org/10.1038/17579.

(122) Tuckerman, M. E.; Marx, D.; Parrinello, M. The Nature and Transport Mechanism of Hydrated Hydroxide Ions in Aqueous Solution. *Nature* **2002**, *417* (6892), 925–929. https://doi.org/10.1038/nature00797.

(123) Geissler, P. L. Autoionization in Liquid Water. *Science* **2001**, *291* (5511), 2121–2124. https://doi.org/10.1126/science.1056991.

(124) Lange, K. M.; Hodeck, K. F.; Schade, U.; Aziz, E. F. Nature of the Hydrogen Bond of Water in Solvents of Different Polarities. *J. Phys. Chem. B* **2010**, *114* (50), 16997–17001. https://doi.org/10.1021/jp109790z.

(125) Lange, K. M.; Könnecke, R.; Soldatov, M.; Golnak, R.; Rubensson, J.-E.; Soldatov, A.; Aziz, E. F. On the Origin of the Hydrogen-Bond-Network Nature of Water: X-Ray Absorption and Emission Spectra of Water-Acetonitrile Mixtures. *Angew. Chem. Int. Ed.* **2011**, *50* (45), 10621–10625. https://doi.org/10.1002/anie.201104161.

(126) Huang, Y.; Nielsen, R. J.; Goddard, W. A.; Soriaga, M. P. The Reaction Mechanism with Free Energy Barriers for Electrochemical Dihydrogen Evolution on MoS_2. *J. Am. Chem. Soc.* **2015**, *137* (20), 6692–6698. https://doi.org/10.1021/jacs.5b03329.

(127) Nishikawa, K.; Kasahara, Y.; Ichioka, T. Inhomogeneity of Mixing in Acetonitrile Aqueous Solution Studied by Small-Angle X-Ray Scattering. *J. Phys. Chem. B* **2002**, *106* (3), 693–700. https://doi.org/10.1021/jp011964v.

(128) Takamuku, T.; Yamaguchi, A.; Matsuo, D.; Tabata, M.; Kumamoto, M.; Nishimoto, J.; Yoshida, K.; Yamaguchi, T.; Nagao, M.; Otomo, T.; Adachi, T. Large-Angle X-Ray Scattering and Small-Angle Neutron Scattering Study on Phase Separation of Acetonitrile−Water Mixtures by Addition of NaCl. *J. Phys. Chem. B* **2001**, *105* (26), 6236–6245. https://doi.org/10.1021/jp003011n.

(129) Huang, N.; Nordlund, D.; Huang, C.; Bergmann, U.; Weiss, T. M.; Pettersson, L. G. M.; Nilsson, A. X-Ray Raman Scattering Provides Evidence for Interfacial Acetonitrile-Water Dipole Interactions in Aqueous Solutions. *J. Chem. Phys.* **2011**, *135* (16), 164509. https://doi.org/10.1063/1.3655468.

(130) Brehm, M.; Weber, H.; Thomas, M.; Hollóczki, O.; Kirchner, B. Domain Analysis in Nanostructured Liquids: A Post-Molecular Dynamics Study at the Example of Ionic Liquids. *ChemPhysChem* **2015**, *16* (15), 3271–3277. https://doi.org/10.1002/cphc.201500471.

(131) Liu, E.; Li, J.; Jiao, L.; Doan, H. T. T.; Liu, Z.; Zhao, Z.; Huang, Y.; Abraham, K. M.; Mukerjee, S.; Jia, Q. Unifying the Hydrogen Evolution and Oxidation Reactions Kinetics in Base by Identifying the Catalytic Roles of Hydroxyl-Water-Cation Adducts. *J. Am. Chem. Soc.* **2019**, *141* (7), 3232–3239. https://doi.org/10.1021/jacs.8b13228.

(132) Chen, M.; Zheng, L.; Santra, B.; Ko, H.-Y.; DiStasio Jr, R. A.; Klein, M. L.; Car, R.; Wu, X. Hydroxide Diffuses Slower than Hydronium in Water Because Its Solvated Structure Inhibits Correlated Proton Transfer. *Nat. Chem.* **2018**, *10* (4), 413–419. https://doi.org/10.1038/s41557-018-0010-2.

(133) Hollóczki, O.; Macchieraldo, R.; Gleede, B.; Waldvogel, S. R.; Kirchner, B. Interfacial Domain Formation Enhances Electrochemical Synthesis. *J. Phys. Chem. Lett.* **2019**, *10* (6), 1192–1197. https://doi.org/10.1021/acs.jpclett.9b00112.

(134) Suo, L.; Borodin, O.; Gao, T.; Olguin, M.; Ho, J.; Fan, X.; Luo, C.; Wang, C.; Xu, K. "Water-in-Salt" Electrolyte Enables High-Voltage Aqueous Lithium-Ion Chemistries. *Science* **2015**, *350* (6263), 938–943. https://doi.org/10.1126/science.aab1595.

(135) Yamada, Y.; Usui, K.; Sodeyama, K.; Ko, S.; Tateyama, Y.; Yamada, A. Hydrate-Melt Electrolytes for High-Energy-Density Aqueous Batteries. *Nat. Energy* **2016**, *1* (10), 16129. https://doi.org/10.1038/nenergy.2016.129.

(136) Borodin, O.; Suo, L.; Gobet, M.; Ren, X.; Wang, F.; Faraone, A.; Peng, J.; Olguin, M.; Schroeder, M.; Ding, M. S.; Gobrogge, E.; von Wald Cresce, A.; Munoz, S.; Dura, J. A.; Greenbaum, S.; Wang, C.; Xu, K. Liquid Structure with Nano-Heterogeneity Promotes Cationic Transport in Concentrated Electrolytes. *ACS Nano* **2017**, *11* (10), 10462–10471. https://doi.org/10.1021/acsnano.7b05664.

(137) Dubouis, N.; Lemaire, P.; Mirvaux, B.; Salager, E.; Deschamps, M.; Grimaud, A. The Role of the Hydrogen Evolution Reaction in the Solid–Electrolyte Interphase Formation Mechanism for " *Water-in-Salt* " Electrolytes. *Energy Environ. Sci.* **2018**, *11* (12), 3491–3499. https://doi.org/10.1039/C8EE02456A.

(138) McEldrew, M.; Goodwin, Z. A. H.; Kornyshev, A. A.; Bazant, M. Z. Theory of the Double Layer in Water-in-Salt Electrolytes. *J. Phys. Chem. Lett.* **2018**, *9* (19), 5840–5846. https://doi.org/10.1021/acs.jpclett.8b02543.

(139) Birdja, Y. Y.; Pérez-Gallent, E.; Figueiredo, M. C.; Göttle, A. J.; Calle-Vallejo, F.; Koper, M. T. M. Advances and Challenges in Understanding the Electrocatalytic Conversion of Carbon Dioxide to Fuels. *Nat. Energy* **2019**, *4* (9), 732–745. https://doi.org/10.1038/s41560-019-0450-y.

(140) Andersen, S. Z.; Čolić, V.; Yang, S.; Schwalbe, J. A.; Nielander, A. C.; McEnaney, J. M.; Enemark-Rasmussen, K.; Baker, J. G.; Singh, A. R.; Rohr, B. A.; Statt, M. J.; Blair, S. J.; Mezzavilla, S.; Kibsgaard, J.; Vesborg, P. C. K.; Cargnello, M.; Bent, S. F.; Jaramillo, T. F.; Stephens, I. E. L.; Nørskov, J. K.; Chorkendorff, I. A Rigorous Electrochemical Ammonia Synthesis Protocol with Quantitative Isotope Measurements. *Nature* **2019**, *570* (7762), 504–508. https://doi.org/10.1038/s41586-019-1260-x.

(141) Armand, M.; Tarascon, J.-M. Building Better Batteries. *nature* **2008**, *451* (7179), 652.

(142) Verma, P.; Maire, P.; Novák, P. A Review of the Features and Analyses of the Solid Electrolyte Interphase in Li-Ion Batteries. *Electrochimica Acta* **2010**, *55* (22), 6332–6341. https://doi.org/10.1016/j.electacta.2010.05.072.

(143) Wang, A.; Kadam, S.; Li, H.; Shi, S.; Qi, Y. Review on Modeling of the Anode Solid Electrolyte Interphase (SEI) for Lithium-Ion Batteries. *Npj Comput. Mater.* **2018**, *4* (1), 15. https://doi.org/10.1038/s41524-018-0064-0.

(144) Larcher, D.; Tarascon, J.-M. Towards Greener and More Sustainable Batteries for Electrical Energy Storage. *Nat. Chem.* **2015**, *7* (1), 19–29. https://doi.org/10.1038/nchem.2085.

(145) Yamada, Y.; Furukawa, K.; Sodeyama, K.; Kikuchi, K.; Yaegashi, M.; Tateyama, Y.; Yamada, A. Unusual Stability of Acetonitrile-Based Superconcentrated Electrolytes for Fast-Charging Lithium-Ion Batteries. *J. Am. Chem. Soc.* **2014**, *136* (13), 5039–5046. https://doi.org/10.1021/ja412807w.

(146) Wang, J.; Yamada, Y.; Sodeyama, K.; Chiang, C. H.; Tateyama, Y.; Yamada, A. Superconcentrated Electrolytes for a High-Voltage Lithium-Ion Battery. *Nat. Commun.* **2016**, *7*, 12032. https://doi.org/10.1038/ncomms12032.

(147) Suo, L.; Borodin, O.; Gao, T.; Olguin, M.; Ho, J.; Fan, X.; Luo, C.; Wang, C.; Xu, K. "Water-in-Salt" Electrolyte Enables High-Voltage Aqueous Lithium-Ion Chemistries. *Science* **2015**, *350* (6263), 938–943. https://doi.org/10.1126/science.aab1595.

(148) Suo, L.; Oh, D.; Lin, Y.; Zhuo, Z.; Borodin, O.; Gao, T.; Wang, F.; Kushima, A.; Wang, Z.; Kim, H.-C.; Qi, Y.; Yang, W.; Pan, F.; Li, J.; Xu, K.; Wang, C. How Solid-Electrolyte Interphase Forms in Aqueous Electrolytes. *J. Am. Chem. Soc.* **2017**, *139* (51), 18670–18680. https://doi.org/10.1021/jacs.7b10688.

(149) Suo, L.; Borodin, O.; Sun, W.; Fan, X.; Yang, C.; Wang, F.; Gao, T.; Ma, Z.; Schroeder, M.; von Cresce, A.; Russell, S. M.; Armand, M.; Angell, A.; Xu, K.; Wang, C. Advanced High-Voltage Aqueous Lithium-Ion Battery Enabled by "Water-in-Bisalt" Electrolyte. *Angew. Chem. Int. Ed.* **2016**, *55* (25), 7136–7141. https://doi.org/10.1002/anie.201602397.

(150) Wang, F.; Suo, L.; Liang, Y.; Yang, C.; Han, F.; Gao, T.; Sun, W.; Wang, C. Spinel LiNi0.5Mn1.5O4 Cathode for High-Energy Aqueous Lithium-Ion Batteries. *Adv. Energy Mater.* **2017**, *7* (8), 1600922. https://doi.org/10.1002/aenm.201600922.

(151) Yang, C.; Chen, J.; Qing, T.; Fan, X.; Sun, W.; Cresce, A. von; Ding, M. S.; Borodin, O.; Vatamanu, J.; Schroeder, M. A.; Eidson, N.; Wang, C.; Xu, K. 4.0 V Aqueous Li-Ion Batteries. *Joule* **2017**, *1* (1), 122–132. https://doi.org/10.1016/j.joule.2017.08.009.

(152) Yang, C.; Ji, X.; Fan, X.; Gao, T.; Suo, L.; Wang, F.; Sun, W.; Chen, J.; Chen, L.; Han, F.; Miao, L.; Xu, K.; Gerasopoulos, K.; Wang, C. Flexible Aqueous Li-Ion Battery with High Energy and Power Densities. *Adv. Mater.* **2017**, *29* (44), 1701972. https://doi.org/10.1002/adma.201701972.

(153) Suo, L.; Borodin, O.; Wang, Y.; Rong, X.; Sun, W.; Fan, X.; Xu, S.; Schroeder, M. A.; Cresce, A. V.; Wang, F.; Yang, C.; Hu, Y.-S.; Xu, K.; Wang, C. "Water-in-Salt" Electrolyte Makes Aqueous Sodium-Ion Battery Safe, Green, and Long-Lasting. *Adv. Energy Mater.* **2017**, *7* (21). https://doi.org/10.1002/aenm.201701189.

(154) Leonard, D. P.; Wei, Z.; Chen, G.; Du, F.; Ji, X. Water-in-Salt Electrolyte for Potassium-Ion Batteries. *ACS Energy Lett.* **2018**, *3* (2), 373–374. https://doi.org/10.1021/acsenergylett.8b00009.

(155) Dong, Q.; Yao, X.; Zhao, Y.; Qi, M.; Zhang, X.; Sun, H.; He, Y.; Wang, D. Cathodically Stable Li-O2 Battery Operations Using Water-in-Salt Electrolyte. *Chem* **2018**. https://doi.org/10.1016/j.chempr.2018.02.015.

(156) Lannelongue, P.; Bouchal, R.; Mourad, E.; Bodin, C.; Olarte, M.; Vot, S. le; Favier, F.; Fontaine, O. "Water-in-Salt" for Supercapacitors: A Compromise between Voltage, Power Density, Energy Density and Stability. *J. Electrochem. Soc.* **2018**, *165* (3), A657–A663. https://doi.org/10.1149/2.0951803jes.

(157) Coustan, L.; Shul, G.; Bélanger, D. Electrochemical Behavior of Platinum, Gold and Glassy Carbon Electrodes in Water-in-Salt Electrolyte. *Electrochem. Commun.* **2017**, *77* (Supplement C), 89–92. https://doi.org/10.1016/j.elecom.2017.03.001.

(158) Vatamanu, J.; Borodin, O. *Ramifications of Water-in-Salt Interfacial Structure at Charged Electrodes for Electrolyte Electrochemical Stability*; 2017; Vol. 8. https://doi.org/10.1021/acs.jpclett.7b01879.

(159) Bouchal, R.; Li, Z.; Bongu, C.; Vot, S. L.; Berthelot, R.; Rotenberg, B.; Favier, F.; Freunberger, S. A.; Salanne, M.; Fontaine, O. Competitive Salt Precipitation/Dissolution During Free-Water Reduction

in Water-in-Salt Electrolyte. *Angew. Chem.* **2020**, *132* (37), 16047–16051. https://doi.org/10.1002/ange.202005378.

(160) Takenaka, N.; Inagaki, T.; Shimada, T.; Yamada, Y.; Nagaoka, M.; Yamada, A. Theoretical Analysis of Electrode-Dependent Interfacial Structures on Hydrate-Melt Electrolytes. *J. Chem. Phys.* **2020**, *152* (12), 124706. https://doi.org/10.1063/5.0003196.

(161) Ko, S.; Yamada, Y.; Yamada, A. Formation of a Solid Electrolyte Interphase in Hydrate-Melt Electrolytes. *ACS Appl. Mater. Interfaces* **2019**, *11* (49), 45554–45560. https://doi.org/10.1021/acsami.9b13662.

(162) Miyazaki, K.; Takenaka, N.; Watanabe, E.; Iizuka, S.; Yamada, Y.; Tateyama, Y.; Yamada, A. First-Principles Study on the Peculiar Water Environment in a Hydrate-Melt Electrolyte. *J. Phys. Chem. Lett.* **2019**, *10* (20), 6301–6305. https://doi.org/10.1021/acs.jpclett.9b02207.

(163) Miyazaki, K.; Takenaka, N.; Watanabe, E.; Yamada, Y.; Tateyama, Y.; Yamada, A. First-Principles Study on the Cation-Dependent Electrochemical Stabilities in Li/Na/K Hydrate-Melt Electrolytes. *ACS Appl. Mater. Interfaces* **2020**, *12* (38), 42734–42738. https://doi.org/10.1021/acsami.0c10472.

(164) Peljo, P.; Girault, H. H. Electrochemical Potential Window of Battery Electrolytes: The HOMO–LUMO Misconception. *Energy Environ. Sci.* **2018**, *11* (9), 2306–2309. https://doi.org/10.1039/C8EE01286E.

(165) Zheng, J.; Tan, G.; Shan, P.; Liu, T.; Hu, J.; Feng, Y.; Yang, L.; Zhang, M.; Chen, Z.; Lin, Y.; Lu, J.; Neuefeind, J. C.; Ren, Y.; Amine, K.; Wang, L.-W.; Xu, K.; Pan, F. Understanding Thermodynamic and Kinetic Contributions in Expanding the Stability Window of Aqueous Electrolytes. *Chem* **2018**, *4* (12), 2872–2882. https://doi.org/10.1016/j.chempr.2018.09.004.

(166) Li, Z.; Jeanmairet, G.; Méndez-Morales, T.; Rotenberg, B.; Salanne, M. Capacitive Performance of Water-in-Salt Electrolytes in Supercapacitors: A Simulation Study. *J. Phys. Chem. C* **2018**, *122* (42), 23917–23924. https://doi.org/10.1021/acs.jpcc.8b07557.

(167) Serva, A.; Dubouis, N.; Grimaud, A.; Salanne, M. Confining Water in Ionic and Organic Solvents to Tune Its Adsorption and Reactivity at Electrified Interfaces. *Acc. Chem. Res.* **2021**. https://doi.org/10.1021/acs.accounts.0c00795.

(168) Borodin, O.; Ren, X.; Vatamanu, J.; von Wald Cresce, A.; Knap, J.; Xu, K. Modeling Insight into Battery Electrolyte Electrochemical Stability and Interfacial Structure. *Acc. Chem. Res.* **2017**, *50* (12), 2886–2894. https://doi.org/10.1021/acs.accounts.7b00486.

(169) Dubouis, N.; Lemaire, P.; Mirvaux, B.; Salager, E.; Deschamps, M.; Grimaud, A. The Role of the Hydrogen Evolution Reaction in the Solid–Electrolyte Interphase Formation Mechanism for "Water-in-Salt" Electrolytes. *Energy Environ. Sci.* **2018**, *11* (12), 3491–3499. https://doi.org/10.1039/C8EE02456A.

(170) Visser, A. E.; Swatloski, R. P.; Rogers, R. D. PH-Dependent Partitioning in Room Temperature Ionic Liquids Provides a Link to Traditional Solvent Extraction Behavior. *Green Chem.* **2000**, *2* (1), 1–4. https://doi.org/10.1039/A908888A.

(171) G. Huddleston, J.; D. Willauer, H.; P. Swatloski, R.; E. Visser, A.; D. Rogers, R. Room Temperature Ionic Liquids as Novel Media for 'Clean' Liquid–Liquid Extraction. *Chem. Commun.* **1998**, *0* (16), 1765–1766. https://doi.org/10.1039/A803999B.

(172) Gras, M.; Papaiconomou, N.; Schaeffer, N.; Chainet, E.; Tedjar, F.; Coutinho, J. A. P.; Billard, I. Ionic-Liquid-Based Acidic Aqueous Biphasic Systems for Simultaneous Leaching and Extraction of Metallic Ions. *Angew. Chem. Int. Ed.* **2018**, *57* (6), 1563–1566. https://doi.org/10.1002/anie.201711068.

(173) Beijerinck, M. Über Eine Eigentümlichkeit Der Löslichen Stärke. *Zentralblatt Bakteriol. Parasiten Infekt.* **1896**, *2*, 679–699.

(174) Gutowski, K. E.; Broker, G. A.; Willauer, H. D.; Huddleston, J. G.; Swatloski, R. P.; Holbrey, J. D.; Rogers, R. D. Controlling the Aqueous Miscibility of Ionic Liquids: Aqueous Biphasic Systems of Water-Miscible Ionic Liquids and Water-Structuring Salts for Recycle, Metathesis, and Separations. *J. Am. Chem. Soc.* **2003**, *125* (22), 6632–6633. https://doi.org/10.1021/ja0351802.

(175) Bridges, N. J.; Gutowski, K. E.; Rogers, R. D. Investigation of Aqueous Biphasic Systems Formed from Solutions of Chaotropic Salts with Kosmotropic Salts (Salt–Salt ABS). *Green Chem.* **2007**, *9* (2), 177–183. https://doi.org/10.1039/B611628K.

(176) Freire, M. G.; Cláudio, A. F. M.; Araújo, J. M. M.; Coutinho, J. A. P.; Marrucho, I. M.; Lopes, J. N. C.; Rebelo, L. P. N. Aqueous Biphasic Systems: A Boost Brought about by Using Ionic Liquids. *Chem. Soc. Rev.* **2012**, *41* (14), 4966. https://doi.org/10.1039/c2cs35151j.

(177) Sides, W. D.; Huang, Q. Electrodeposition of Manganese Thin Films on a Rotating Disk Electrode from Choline Chloride/Urea Based Ionic Liquids. *Electrochimica Acta* **2018**, *266*, 185–192. https://doi.org/10.1016/j.electacta.2018.01.120.

(178) Tsionsky, V.; Daikhin, L.; Gileadi, E. Response of the Electrochemical Quartz Crystal Microbalance for Gold Electrodes in the Double-Layer Region. *J. Electrochem. Soc.* **1996**, *143* (7), 2240–2245.

(179) Levi, M. D.; Salitra, G.; Levy, N.; Aurbach, D.; Maier, J. Application of a Quartz-Crystal Microbalance to Measure Ionic Fluxes in Microporous Carbons for Energy Storage. *Nat. Mater.* **2009**, *8* (11), 872–875. https://doi.org/10.1038/nmat2559.

(180) Tsai, W.-Y.; Taberna, P.-L.; Simon, P. Electrochemical Quartz Crystal Microbalance (EQCM) Study of Ion Dynamics in Nanoporous Carbons. *J. Am. Chem. Soc.* **2014**, *136* (24), 8722–8728. https://doi.org/10.1021/ja503449w.

(181) Griffin, J. M.; Forse, A. C.; Tsai, W.-Y.; Taberna, P.-L.; Simon, P.; Grey, C. P. In Situ NMR and Electrochemical Quartz Crystal Microbalance Techniques Reveal the Structure of the Electrical Double Layer in Supercapacitors. *Nat. Mater.* **2015**, *14* (8), 812–819. https://doi.org/10.1038/nmat4318.

(182) Li, Z.; Jeanmairet, G.; Mendez-Morales, T.; Rotenberg, B.; Salanne, M. Capacitive Performance of Water-in-Salt Electrolyte in Supercapacitors: A Simulation Study. *figshare* **2018**. https://doi.org/10.26434/chemrxiv.6933110.v1.

(183) Meyer, B. M.; Leifer, N.; Sakamoto, S.; Greenbaum, S. G.; Grey, C. P. High Field Multinuclear NMR Investigation of the SEI Layer in Lithium Rechargeable Batteries. *Electrochem. Solid-State Lett.* **2005**, *8* (3), A145. https://doi.org/10.1149/1.1854117.

(184) Hall, D. S.; Werner-Zwanziger, U.; Dahn, J. R. 19F and 31P Solid-State NMR Characterization of a Pyridine Pentafluorophosphate-Derived Solid-Electrolyte Interphase. *J. Electrochem. Soc.* **2017**, *164* (9), A2171–A2175. https://doi.org/10.1149/2.1631709jes.

(185) McEldrew, M.; Goodwin, Z. A. H.; Bi, S.; Bazant, M. Z.; Kornyshev, A. A. Theory of Ion Aggregation and Gelation in Super-Concentrated Electrolytes. *J. Chem. Phys.* **2020**, *152* (23), 234506. https://doi.org/10.1063/5.0006197.

(186) Lux, S. F.; Terborg, L.; Hachmöller, O.; Placke, T.; Meyer, H.-W.; Passerini, S.; Winter, M.; Nowak, S. LiTFSI Stability in Water and Its Possible Use in Aqueous Lithium-Ion Batteries: PH Dependency, Electrochemical Window and Temperature Stability. *J. Electrochem. Soc.* **2013**, *160* (10), A1694–A1700. https://doi.org/10.1149/2.039310jes.

(187) Hartnig, C.; Koper, M. T. M. Solvent Reorganization in Electron and Ion Transfer Reactions near a Smooth Electrified Surface: A Molecular Dynamics Study. *J. Am. Chem. Soc.* **2003**, *125* (32), 9840–9845. https://doi.org/10.1021/ja035498u.

(188) Santos, E.; Koper, M. T. M.; Schmickler, W. Bond-Breaking Electron Transfer of Diatomic Reactants at Metal Electrodes. *Chem. Phys.* **2008**, *344* (1–2), 195–201. https://doi.org/10.1016/j.chemphys.2008.01.016.

(189) Howlett, P. C.; Izgorodina, E. I.; Forsyth, M.; MacFarlane, D. R. Electrochemistry at Negative Potentials in Bis(Trifluoromethanesulfonyl)Amide Ionic Liquids. *Z. Für Phys. Chem.* **2006**, *220* (10), 1483–1498. https://doi.org/10.1524/zpch.2006.220.10.1483.

(190) Yang, C.; Fontaine, O.; Tarascon, J.-M.; Grimaud, A. Chemical Recognition of Active Oxygen Species on the Surface of Oxygen Evolution Reaction Electrocatalysts. *Angew. Chem. Int. Ed.* **2017**, *56* (30), 8652–8656. https://doi.org/10.1002/anie.201701984.

(191) Benrabah, D.; Arnaud, R.; Sanchez, J. Y. Comparative Ab Initio Calculations on Several Salts. *Electrochimica Acta* **1995**, *40* (13–14), 2437–2443.

(192) Rey, I.; Johansson, P.; Lindgren, J.; Lassègues, J. C.; Grondin, J.; Servant, L. Spectroscopic and Theoretical Study of (CF3SO2)2N- (TFSI-) and (CF3SO2)2NH (HTFSI). *J. Phys. Chem. A* **1998**, *102* (19), 3249–3258. https://doi.org/10.1021/jp980375v.

(193) Jenkins, H. D. B.; Marcus, Y. Viscosity B-Coefficients of Ions in Solution. *Chem. Rev.* **1995**, *95* (8), 2695–2724.

(194) Marcus, Y. Effect of Ions on the Structure of Water: Structure Making and Breaking. *Chem. Rev.* **2009**, *109* (3), 1346–1370. https://doi.org/10.1021/cr8003828.

(195) Su, H.-L.; Lan, M.-T.; Lin, K.-W.; Hsieh, Y.-Z. Chaotropic Salts: Novel Modifiers for the Capillary Electrophoretic Analysis of Benzodiazepines. *ELECTROPHORESIS* **2008**, *29* (16), 3384–3390. https://doi.org/10.1002/elps.200800073.

(196) Levy, A.; McEldrew, M.; Bazant, M. Z. Spin-Glass Charge Ordering in Ionic Liquids. *ArXiv180806156 Cond-Mat Physicsphysics* **2018**.

(197) Lo Celso, F.; Triolo, A.; Triolo, R. Phase Separation in Multi-Component Mixtures: The Four-Component Case. *Phys. Stat. Mech. Its Appl.* **2002**, *304* (1), 299–307. https://doi.org/10.1016/S0378-4371(01)00511-8.

(198) Kuzmina, O.; Bordes, E.; Schmauck, J.; Hunt, P. A.; Hallett, J. P.; Welton, T. Solubility of Alkali Metal Halides in the Ionic Liquid [C4C1im][OTf]. *Phys. Chem. Chem. Phys.* **2016**, *18* (24), 16161–16168. https://doi.org/10.1039/C6CP02286C.

(199) Lo Celso, F.; Triolo, A.; Triolo, R. Phase Separation in Multi-Component Mixtures: The Four-Component Case. *Phys. Stat. Mech. Its Appl.* **2002**, *304* (1), 299–307. https://doi.org/10.1016/S0378-4371(01)00511-8.

(200) Marcus, Y. Ionic Radii in Aqueous Solutions. 24.

(201) Smith, A. M.; Lee, A. A.; Perkin, S. The Electrostatic Screening Length in Concentrated Electrolytes Increases with Concentration. *J. Phys. Chem. Lett.* **2016**, *7* (12), 2157–2163. https://doi.org/10.1021/acs.jpclett.6b00867.

(202) Coles, S. W.; Park, C.; Nikam, R.; Kanduč, M.; Dzubiella, J.; Rotenberg, B. Correlation Length in Concentrated Electrolytes: Insights from All-Atom Molecular Dynamics Simulations. *J. Phys. Chem. B* **2020**, *124* (9), 1778–1786. https://doi.org/10.1021/acs.jpcb.9b10542.

(203) Shannon, R. D. Revised Effective Ionic Radii and Systematic Studies of Interatomic Distances in Halides and Chalcogenides. *Acta Crystallogr. A* **1976**, *32* (5), 751–767. https://doi.org/10.1107/S0567739476001551.

(204) Dubouis, N.; Park, C.; Deschamps, M.; Abdelghani-Idrissi, S.; Kanduč, M.; Colin, A.; Salanne, M.; Dzubiella, J.; Grimaud, A.; Rotenberg, B. Chasing Aqueous Biphasic Systems from Simple Salts by Exploring the LiTFSI/LiCl/H2O Phase Diagram. *ACS Cent. Sci.* **2019**, *5* (4), 640–643. https://doi.org/10.1021/acscentsci.8b00955.

(205) Lamoureux, G.; Roux, B. Absolute Hydration Free Energy Scale for Alkali and Halide Ions Established from Simulations with a Polarizable Force Field. *J. Phys. Chem. B* **2006**, *110* (7), 3308–3322. https://doi.org/10.1021/jp056043p.

(206) Ambrosone, L.; Andini, S.; Castronuovo, G.; Elia, V.; Guarino, G. Empirical Correlations between Thermodynamic and Spectroscopic Properties of Aqueous Solutions of Alkan-m,n-Diols. Excess Enthalpies and Spin–Lattice Relaxation Times at 298.15 K. *J. Chem. Soc. Faraday Trans.* **1991**, *87* (18), 2989–2993. https://doi.org/10.1039/FT9918702989.

(207) Sun, W.; Wang, F.; Zhang, B.; Zhang, M.; Küpers, V.; Ji, X.; Theile, C.; Bieker, P.; Xu, K.; Wang, C.; Winter, M. A Rechargeable Zinc-Air Battery Based on Zinc Peroxide Chemistry. *Science* **2021**, *371* (6524), 46–51. https://doi.org/10.1126/science.abb9554.

(208) Navalpotro, P.; Palma, J.; Anderson, M.; Marcilla, R. A Membrane-Free Redox Flow Battery with Two Immiscible Redox Electrolytes. *Angew. Chem. Int. Ed.* **2017**, *56* (41), 12460–12465. https://doi.org/10.1002/anie.201704318.

(209) Missoni, L. L.; Marchini, F.; Pozo, M. del; Calvo, E. J. A LiMn2O4-Polypyrrole System for the Extraction of LiCl from Natural Brine. *J. Electrochem. Soc.* **2016**, *163* (9), A1898. https://doi.org/10.1149/2.0591609jes.

(210) Yang, C.; Chen, J.; Ji, X.; Pollard, T. P.; Lü, X.; Sun, C.-J.; Hou, S.; Liu, Q.; Liu, C.; Qing, T.; Wang, Y.; Borodin, O.; Ren, Y.; Xu, K.; Wang, C. Aqueous Li-Ion Battery Enabled by Halogen Conversion–Intercalation Chemistry in Graphite. *Nature* **2019**, *569* (7755), 245–250. https://doi.org/10.1038/s41586-019-1175-6.

(211) Droguet, L.; Grimaud, A.; Fontaine, O.; Tarascon, J.-M. Water-in-Salt Electrolyte (WiSE) for Aqueous Batteries: A Long Way to Practicality. *Adv. Energy Mater.* **2020**, *10* (43), 2002440. https://doi.org/10.1002/aenm.202002440.

(212) Chen, L.; Zhang, J.; Li, Q.; Vatamanu, J.; Ji, X.; Pollard, T. P.; Cui, C.; Hou, S.; Chen, J.; Yang, C.; Ma, L.; Ding, M. S.; Garaga, M.; Greenbaum, S.; Lee, H.-S.; Borodin, O.; Xu, K.; Wang, C. A 63 m Superconcentrated Aqueous Electrolyte for High-Energy Li-Ion Batteries. *ACS Energy Lett.* **2020**, *5* (3), 968–974. https://doi.org/10.1021/acsenergylett.0c00348.

(213) Ko, S.; Yamada, Y.; Yamada, A. A 62 m K-Ion Aqueous Electrolyte. *Electrochem. Commun.* **2020**, *116*, 106764. https://doi.org/10.1016/j.elecom.2020.106764.

(214) Reber, D.; Takenaka, N.; Kühnel, R.-S.; Yamada, A.; Battaglia, C. Impact of Anion Asymmetry on Local Structure and Supercooling Behavior of Water-in-Salt Electrolytes. *J. Phys. Chem. Lett.* **2020**, *11* (12), 4720–4725. https://doi.org/10.1021/acs.jpclett.0c00806.

(215) Ko, S.; Yamada, Y.; Miyazaki, K.; Shimada, T.; Watanabe, E.; Tateyama, Y.; Kamiya, T.; Honda, T.; Akikusa, J.; Yamada, A. Lithium-Salt Monohydrate Melt: A Stable Electrolyte for Aqueous Lithium-Ion Batteries. *Electrochem. Commun.* **2019**, 106488. https://doi.org/10.1016/j.elecom.2019.106488.

(216) Gschwend, G. C.; Girault, H. H. Discrete Helmholtz Charge Distribution at Liquid-Liquid Interfaces: Electrocapillarity, Capacitance and Non-Linear Spectroscopy Studies. *J. Electroanal. Chem.* **2020**, *872*, 114240. https://doi.org/10.1016/j.jelechem.2020.114240.

(217) Morita, A.; Koizumi, A.; Hirano, T. Recent Progress in Simulating Microscopic Ion Transport Mechanisms at Liquid–Liquid Interfaces. *J. Chem. Phys.* **2021**, *154* (8), 080901. https://doi.org/10.1063/5.0039172.

(218) Kong, T.; Guo, S.; Ni, D.; Cava, R. J. Crystal Structure and Magnetic Properties of the Layered van Der Waals Compound VB r 3. *Phys. Rev. Mater.* **2019**, *3* (8), 084419. https://doi.org/10.1103/PhysRevMaterials.3.084419.

(219) Kong, T.; Stolze, K.; Timmons, E. I.; Tao, J.; Ni, D.; Guo, S.; Yang, Z.; Prozorov, R.; Cava, R. J. VI3—a New Layered Ferromagnetic Semiconductor. *Adv. Mater.* **2019**, *31* (17), 1808074. https://doi.org/10.1002/adma.201808074.

(220) Song, T.; Fei, Z.; Yankowitz, M.; Lin, Z.; Jiang, Q.; Hwangbo, K.; Zhang, Q.; Sun, B.; Taniguchi, T.; Watanabe, K.; McGuire, M. A.; Graf, D.; Cao, T.; Chu, J.-H.; Cobden, D. H.; Dean, C. R.; Xiao, D.; Xu,

X. Switching 2D Magnetic States via Pressure Tuning of Layer Stacking. *Nat. Mater.* **2019**, *18* (12), 1298–1302. https://doi.org/10.1038/s41563-019-0505-2.

(221) Berthelot, R.; Carlier, D.; Delmas, C. Electrochemical Investigation of the P2–NaxCoO2 Phase Diagram. *Nat. Mater.* **2011**, *10* (1), 74–80. https://doi.org/10.1038/nmat2920.

(222) Skyllas-Kazacos, M.; Cao, L.; Kazacos, M.; Kausar, N.; Mousa, A. Vanadium Electrolyte Studies for the Vanadium Redox Battery-A Review. *ChemSusChem* **2016**, *9* (13), 1521–1543. https://doi.org/10.1002/cssc.201600102.

(223) Dey, A. N.; Sullivan, B. P. The Electrochemical Decomposition of Propylene Carbonate on Graphite. *J. Electrochem. Soc.* **1970**, *117* (2), 222. https://doi.org/10.1149/1.2407470.

(224) Fong, R. Studies of Lithium Intercalation into Carbons Using Nonaqueous Electrochemical Cells. *J Electrochem Soc* **1990**, *137* (7), 5.

(225) Jeong, S.-K.; Inaba, M.; Iriyama, Y.; Abe, T.; Ogumi, Z. Electrochemical Intercalation of Lithium Ion within Graphite from Propylene Carbonate Solutions. *Electrochem. Solid-State Lett.* **2002**, *6* (1), A13. https://doi.org/10.1149/1.1526781.

(226) Yamada, Y.; Takazawa, Y.; Miyazaki, K.; Abe, T. Electrochemical Lithium Intercalation into Graphite in Dimethyl Sulfoxide-Based Electrolytes: Effect of Solvation Structure of Lithium Ion. *J. Phys. Chem. C* **2010**, *114* (26), 11680–11685. https://doi.org/10.1021/jp1037427.

(227) Yamada, Y.; Usui, K.; Chiang, C. H.; Kikuchi, K.; Furukawa, K.; Yamada, A. General Observation of Lithium Intercalation into Graphite in Ethylene-Carbonate-Free Superconcentrated Electrolytes. *ACS Appl. Mater. Interfaces* **2014**, *6* (14), 10892–10899. https://doi.org/10.1021/am5001163.

(228) Wang, J.; Yamada, Y.; Sodeyama, K.; Watanabe, E.; Takada, K.; Tateyama, Y.; Yamada, A. Fire-Extinguishing Organic Electrolytes for Safe Batteries. *Nat. Energy* **2018**, *3* (1), 22–29. https://doi.org/10.1038/s41560-017-0033-8.

(229) Yamada, Y.; Wang, J.; Ko, S.; Watanabe, E.; Yamada, A. Advances and Issues in Developing Salt-Concentrated Battery Electrolytes. *Nat. Energy* **2019**. https://doi.org/10.1038/s41560-019-0336-z.

(230) Yue, J.; Lin, L.; Jiang, L.; Zhang, Q.; Tong, Y.; Suo, L.; Hu, Y.; Li, H.; Huang, X.; Chen, L. Interface Concentrated-Confinement Suppressing Cathode Dissolution in Water-in-Salt Electrolyte. *Adv. Energy Mater.* **2020**, 2000665. https://doi.org/10.1002/aenm.202000665.

(231) Sun, D.; Okubo, M.; Yamada, A. Optimal Water Concentration for Aqueous Li^+ Intercalation in Vanadyl Phosphate. *Chem. Sci.* **2021**, 10.1039.D0SC04647G. https://doi.org/10.1039/D0SC04647G.

(232) Mendiboure, A.; Delmas, C.; Hagenmuller, P. Electrochemical Intercalation and Deintercalation of NaxMnO2 Bronzes. *J. Solid State Chem.* **1985**, *57* (3), 323–331. https://doi.org/10.1016/0022-4596(85)90194-X.

(233) Dubouis, N.; Park, C.; Deschamps, M.; Abdelghani-Idrissi, S.; Kanduč, M.; Colin, A.; Salanne, M.; Dzubiella, J.; Grimaud, A.; Rotenberg, B. Chasing Aqueous Biphasic Systems from Simple Salts by Exploring the LiTFSI/LiCl/H2O Phase Diagram. *ACS Cent. Sci.* **2019**, *5* (4), 640–643. https://doi.org/10.1021/acscentsci.8b00955.

(234) Soubeyroux, J. L.; Cros, C.; Gang, W.; Kanno, R.; Pouchard, M. Neutron Diffraction Investigation of the Cationic Distribution in the Structure of the Spinel-Type Solid Solutions Li2−2xM1+xCl4 (M = Mg, V): Correlation with the Ionic Conductivity and NMR Data. *Solid State Ion.* **1985**, *15* (4), 293–300. https://doi.org/10.1016/0167-2738(85)90132-8.

(235) de Juan, A.; Tauler, R. Chemometrics Applied to Unravel Multicomponent Processes and Mixtures. *Anal. Chim. Acta* **2003**, *500* (1–2), 195–210. https://doi.org/10.1016/S0003-2670(03)00724-4.

(236) Xin, N.; Sun, Y.; He, M.; Radke, C. J.; Prausnitz, J. M. Solubilities of Six Lithium Salts in Five Non-Aqueous Solvents and in a Few of Their Binary Mixtures. *Fluid Phase Equilibria* **2018**, *461*, 1–7. https://doi.org/10.1016/j.fluid.2017.12.034.

(237) Díaz-Duque, Á.; Sandoval-Rojas, A. P.; Molina-Osorio, A. F.; Feliu, J. M.; Suárez-Herrera, M. F. Electrochemical Reduction of CO2 in Water-Acetonitrile Mixtures on Nanostructured Cu Electrode. *Electrochem. Commun.* **2015**, *61*, 74–77. https://doi.org/10.1016/j.elecom.2015.10.003.

(238) Figueiredo, M. C.; Ledezma-Yanez, I.; Koper, M. T. M. In Situ Spectroscopic Study of CO2 Electroreduction at Copper Electrodes in Acetonitrile. *ACS Catal.* **2016**, *6* (4), 2382–2392. https://doi.org/10.1021/acscatal.5b02543.

(239) Aurbach, D.; Daroux, M.; Faguy, P.; Yeager, E. The Electrochemistry of Noble Metal Electrodes in Aprotic Organic Solvents Containing Lithium Salts. *J. Electroanal. Chem. Interfacial Electrochem.* **1991**, *297* (1), 225–244. https://doi.org/10.1016/0022-0728(91)85370-5.

(240) Castelli, I. E.; Zorko, M.; Østergaard, T. M.; Martins, P. F. B. D.; Lopes, P. P.; Antonopoulos, B. K.; Maglia, F.; Markovic, N. M.; Strmcnik, D.; Rossmeisl, J. The Role of an Interface in Stabilizing Reaction Intermediates for Hydrogen Evolution in Aprotic Electrolytes. *Chem. Sci.* **2020**, *11* (15), 3914–3922. https://doi.org/10.1039/C9SC05768D.

(241) Marken, F.; Wadhawan, J. D. Multiphase Methods in Organic Electrosynthesis. *Acc. Chem. Res.* **2019**, *52* (12), 3325–3338. https://doi.org/10.1021/acs.accounts.9b00480.

(242) Gras, M.; Papaiconomou, N.; Schaeffer, N.; Chainet, E.; Tedjar, F.; Coutinho, J. A. P.; Billard, I. Ionic-Liquid-Based Acidic Aqueous Biphasic Systems for Simultaneous Leaching and Extraction of Metallic Ions. *Angew. Chem. Int. Ed.* **2018**, *57* (6), 1563–1566. https://doi.org/10.1002/anie.201711068.

(243) Gambou-Bosca, A.; Bélanger, D. Electrochemical Characterization of MnO2-Based Composite in the Presence of Salt-in-Water and Water-in-Salt Electrolytes as Electrode for Electrochemical Capacitors. *J. Power Sources* **2016**, *326*, 595–603. https://doi.org/10.1016/j.jpowsour.2016.04.088.

(244) Han, K. S.; Yu, Z.; Wang, H.; Redfern, P. C.; Ma, L.; Cheng, L.; Chen, Y.; Hu, J. Z.; Curtiss, L. A.; Xu, K.; Murugesan, V.; Mueller, K. T. Origin of Unusual Acidity and Li^+ Diffusivity in a Series of Water-in-Salt Electrolytes. *J. Phys. Chem. B* **2020**, *124* (25), 5284–5291. https://doi.org/10.1021/acs.jpcb.0c02483.

(245) Yi, J.; Lee, W. H.; Choi, C. H.; Lee, Y.; Park, K. S.; Min, B. K.; Hwang, Y. J.; Oh, H.-S. Effect of Pt Introduced on Ru-Based Electrocatalyst for Oxygen Evolution Activity and Stability. *Electrochem. Commun.* **2019**, *104*, 106469. https://doi.org/10.1016/j.elecom.2019.05.018.

(246) Tanner, J. E. Use of the Stimulated Echo in NMR Diffusion Studies. *J. Chem. Phys.* **1970**, *52* (5), 2523–2526. https://doi.org/10.1063/1.1673336.

(247) Abraham, M. J.; Murtola, T.; Schulz, R.; Páll, S.; Smith, J. C.; Hess, B.; Lindahl, E. GROMACS: High Performance Molecular Simulations through Multi-Level Parallelism from Laptops to Supercomputers. *SoftwareX* **2015**, *1–2*, 19–25. https://doi.org/10.1016/j.softx.2015.06.001.

(248) Grabuleda, X.; Jaime, C.; Kollman, P. A. Molecular dynamics simulation studies of liquid acetonitrile: New six-site model. *J. Comput. Chem.* **2000**, *21* (10), 901–908. https://doi.org/10.1002/1096-987X(20000730)21:10<901::AID-JCC7>3.0.CO;2-F.

(249) Berendsen, H. J. C.; Grigera, J. R.; Straatsma, T. P. The Missing Term in Effective Pair Potentials. *J. Phys. Chem.* **1987**, *91* (24), 6269–6271. https://doi.org/10.1021/j100308a038.

(250) Liu, X.; Zhang, S.; Zhou, G.; Wu, G.; Yuan, X.; Yao, X. New Force Field for Molecular Simulation of Guanidinium-Based Ionic Liquids. *J. Phys. Chem. B* **2006**, *110* (24), 12062–12071. https://doi.org/10.1021/jp060834p.

(251) Bhowmik, D.; Malikova, N.; Mériguet, G.; Bernard, O.; Teixeira, J.; Turq, P. Aqueous Solutions of Tetraalkylammonium Halides: Ion Hydration, Dynamics and Ion–Ion Interactions in Light of Steric Effects. *Phys. Chem. Chem. Phys.* **2014**, *16* (26), 13447–13457. https://doi.org/10.1039/C4CP01164C.

(252) Åqvist, J. Ion-Water Interaction Potentials Derived from Free Energy Perturbation Simulations. *J. Phys. Chem.* **1990**, *94* (21), 8021–8024. https://doi.org/10.1021/j100384a009.
(253) Nosé, S. A Unified Formulation of the Constant Temperature Molecular Dynamics Methods. *J. Chem. Phys.* **1984**, *81* (1), 511–519. https://doi.org/10.1063/1.447334.
(254) Evans, D. J.; Holian, B. L. The Nose–Hoover Thermostat. *J. Chem. Phys.* **1985**, *83* (8), 4069–4074. https://doi.org/10.1063/1.449071.
(255) Martínez, L.; Andrade, R.; Birgin, E. G.; Martínez, J. M. PACKMOL: A package for building initial configurations for molecular dynamics simulations. *J. Comput. Chem.* **2009**, *30* (13), 2157–2164. https://doi.org/10.1002/jcc.21224.
(256) Essmann, U.; Perera, L.; Berkowitz, M. L.; Darden, T.; Lee, H.; Pedersen, L. G. A Smooth Particle Mesh Ewald Method. *J. Chem. Phys.* **1995**, *103* (19), 8577–8593. https://doi.org/10.1063/1.470117.
(257) Hess, B.; Bekker, H.; Berendsen, H. J. C.; Fraaije, J. G. E. M. LINCS: A Linear Constraint Solver for Molecular Simulations. *J. Comput. Chem.* **1997**, *18* (12), 1463–1472. https://doi.org/10.1002/(SICI)1096-987X(199709)18:12<1463::AID-JCC4>3.0.CO;2-H.
(258) Brehm, M.; Kirchner, B. TRAVIS - A Free Analyzer and Visualizer for Monte Carlo and Molecular Dynamics Trajectories. *J. Chem. Inf. Model.* **2011**, *51* (8), 2007–2023. https://doi.org/10.1021/ci200217w.
(259) Humphrey, W.; Dalke, A.; Schulten, K. VMD: Visual Molecular Dynamics. *J. Mol. Graph.* **1996**, *14* (1), 33–38. https://doi.org/10.1016/0263-7855(96)00018-5.
(260) Atomic form factors http://lampx.tugraz.at/~hadley/ss1/crystaldiffraction/atomicformfactors/formfactors.php (accessed 2019 -11 -06).
(261) Marin-Laflèche, A.; Haefele, M.; Scalfi, L.; Coretti, A.; Dufils, T.; Jeanmairet, G.; Reed, S.; Serva, A.; Berthin, R.; Bacon, C.; Bonella, S.; Rotenberg, B.; Madden, P. A.; Salanne, M. MetalWalls: A Classical Molecular Dynamics Software Dedicated to the Simulation of Electrochemical Systems. **2020**. https://doi.org/10.26434/chemrxiv.12389777.v1.
(262) Reed, S. K.; Lanning, O. J.; Madden, P. A. Electrochemical Interface between an Ionic Liquid and a Model Metallic Electrode. *J. Chem. Phys.* **2007**, *126* (8), 084704. https://doi.org/10.1063/1.2464084.
(263) Siepmann, J. I.; Sprik, M. Influence of Surface Topology and Electrostatic Potential on Water/Electrode Systems. *J. Chem. Phys.* **1995**, *102* (1), 511–524. https://doi.org/10.1063/1.469429.
(264) Werder, T.; Walther, J. H.; Jaffe, R. L.; Halicioglu, T.; Koumoutsakos, P. On the Water−Carbon Interaction for Use in Molecular Dynamics Simulations of Graphite and Carbon Nanotubes. *J. Phys. Chem. B* **2003**, *107* (6), 1345–1352. https://doi.org/10.1021/jp0268112.
(265) Gingrich, T. R.; Wilson, M. On the Ewald Summation of Gaussian Charges for the Simulation of Metallic Surfaces. *Chem. Phys. Lett.* **2010**, *500* (1), 178–183. https://doi.org/10.1016/j.cplett.2010.10.010.
(266) Ryckaert, J.-P.; Ciccotti, G.; Berendsen, H. J. C. Numerical Integration of the Cartesian Equations of Motion of a System with Constraints: Molecular Dynamics of n-Alkanes. *J. Comput. Phys.* **1977**, *23* (3), 327–341. https://doi.org/10.1016/0021-9991(77)90098-5.
(267) Ciccotti, G.; Ferrario, M.; Ryckaert, J.-P. Molecular Dynamics of Rigid Systems in Cartesian Coordinates A General Formulation. *Mol. Phys.* **1982**, *47* (6), 1253–1264. https://doi.org/10.1080/00268978200100942.
(268) Lancry, E.; Levi, E.; Gofer, Y.; Levi, M.; Salitra, G.; Aurbach, D. Leaching Chemistry and the Performance of the Mo6S8 Cathodes in Rechargeable Mg Batteries. *Chem. Mater.* **2004**, *16* (14), 2832–2838. https://doi.org/10.1021/cm034944+.

(269) Missoni, L. L.; Marchini, F.; Pozo, M. del; Calvo, E. J. A LiMn2O4-Polypyrrole System for the Extraction of LiCl from Natural Brine. *J. Electrochem. Soc.* **2016**, *163* (9), A1898–A1902. https://doi.org/10.1149/2.0591609jes.
(270) Massiot, D.; Fayon, F.; Capron, M.; King, I.; Calvé, S. L.; Alonso, B.; Durand, J.-O.; Bujoli, B.; Gan, Z.; Hoatson, G. Modelling One- and Two-Dimensional Solid-State NMR Spectra. *Magn. Reson. Chem. 40* (1), 70–76. https://doi.org/10.1002/mrc.984.
(271) Spoel, D. V. D.; Lindahl, E.; Hess, B.; Groenhof, G.; Mark, A. E.; Berendsen, H. J. C. GROMACS: Fast, Flexible, and Free. *J. Comput. Chem.* **2005**, *26* (16), 1701–1718. https://doi.org/10.1002/jcc.20291.
(272) Martínez, L.; Andrade, R.; Birgin, E. G.; Martínez, J. M. PACKMOL: A package for building initial configurations for molecular dynamics simulations. *J. Comput. Chem.* **2009**, *30* (13), 2157–2164. https://doi.org/10.1002/jcc.21224.
(273) Parrinello, M.; Rahman, A. Polymorphic Transitions in Single Crystals: A New Molecular Dynamics Method. *J. Appl. Phys.* **1981**, *52* (12), 7182–7190. https://doi.org/10.1063/1.328693.
(274) Bussi, G.; Donadio, D.; Parrinello, M. Canonical Sampling through Velocity Rescaling. *J. Chem. Phys.* **2007**, *126* (1), 014101. https://doi.org/10.1063/1.2408420.
(275) Darden, T.; York, D.; Pedersen, L. Particle Mesh Ewald: An N·log(N) Method for Ewald Sums in Large Systems. *J. Chem. Phys.* **1993**, *98* (12), 10089–10092. https://doi.org/10.1063/1.464397.
(276) Hess, B. P-LINCS: A Parallel Linear Constraint Solver for Molecular Simulation. *J. Chem. Theory Comput.* **2008**, *4* (1), 116–122. https://doi.org/10.1021/ct700200b.
(277) Jorgensen, W. L.; Maxwell, D. S.; Tirado-Rives, J. Development and Testing of the OPLS All-Atom Force Field on Conformational Energetics and Properties of Organic Liquids. *J. Am. Chem. Soc.* **1996**, *118* (45), 11225–11236. https://doi.org/10.1021/ja9621760.
(278) Canongia Lopes, J. N.; Pádua, A. A. H. Molecular Force Field for Ionic Liquids Composed of Triflate or Bistriflylimide Anions. *J. Phys. Chem. B* **2004**, *108* (43), 16893–16898. https://doi.org/10.1021/jp0476545.
(279) Berendsen, H. J. C.; Grigera, J. R.; Straatsma, T. P. The Missing Term in Effective Pair Potentials. *J. Phys. Chem.* **1987**, *91* (24), 6269–6271. https://doi.org/10.1021/j100308a038.
(280) Zhang, Y.; Yang, W. Comment on ``Generalized Gradient Approximation Made Simple''. *Phys. Rev. Lett.* **1998**, *80* (4), 890–890. https://doi.org/10.1103/PhysRevLett.80.890.
(281) Grimme, S.; Antony, J.; Ehrlich, S.; Krieg, H. A Consistent and Accurate Ab Initio Parametrization of Density Functional Dispersion Correction (DFT-D) for the 94 Elements H-Pu. *J. Chem. Phys.* **2010**, *132* (15), 154104. https://doi.org/10.1063/1.3382344.
(282) Kühne, T. D.; Iannuzzi, M.; Del Ben, M.; Rybkin, V. V.; Seewald, P.; Stein, F.; Laino, T.; Khaliullin, R. Z.; Schütt, O.; Schiffmann, F.; Golze, D.; Wilhelm, J.; Chulkov, S.; Bani-Hashemian, M. H.; Weber, V.; Borštnik, U.; Taillefumier, M.; Jakobovits, A. S.; Lazzaro, A.; Pabst, H.; Müller, T.; Schade, R.; Guidon, M.; Andermatt, S.; Holmberg, N.; Schenter, G. K.; Hehn, A.; Bussy, A.; Belleflamme, F.; Tabacchi, G.; Glöß, A.; Lass, M.; Bethune, I.; Mundy, C. J.; Plessl, C.; Watkins, M.; VandeVondele, J.; Krack, M.; Hutter, J. CP2K: An Electronic Structure and Molecular Dynamics Software Package - Quickstep: Efficient and Accurate Electronic Structure Calculations. *J. Chem. Phys.* **2020**, *152* (19), 194103. https://doi.org/10.1063/5.0007045.
(283) Neese, F. The ORCA Program System. *WIREs Comput. Mol. Sci.* **2012**, *2* (1), 73–78. https://doi.org/10.1002/wcms.81.
(284) Neese, F. Software Update: The ORCA Program System, Version 4.0. *WIREs Comput. Mol. Sci.* **2018**, *8* (1), e1327. https://doi.org/10.1002/wcms.1327.

(285) Adamo, C.; Barone, V. Toward Reliable Density Functional Methods without Adjustable Parameters: The PBE0 Model. *J. Chem. Phys.* **1999**, *110* (13), 6158–6170. https://doi.org/10.1063/1.478522.

(286) Lu, T.; Chen, F. Multiwfn: A Multifunctional Wavefunction Analyzer. *J. Comput. Chem.* **2012**, *33* (5), 580–592. https://doi.org/10.1002/jcc.22885.

(287) Momma, K.; Izumi, F. VESTA 3 for Three-Dimensional Visualization of Crystal, Volumetric and Morphology Data. *J. Appl. Crystallogr.* **2011**, *44* (6), 1272–1276. https://doi.org/10.1107/S0021889811038970.

(288) Liu, Z.; Fu, W.; Payzant, E. A.; Yu, X.; Wu, Z.; Dudney, N. J.; Kiggans, J.; Hong, K.; Rondinone, A. J.; Liang, C. Anomalous High Ionic Conductivity of Nanoporous β - Li 3 PS 4. **2013**, 20–23. https://doi.org/10.1021/ja3110895.

(289) Herklotz, M.; Weiß, J.; Ahrens, E.; Yavuz, M.; Mereacre, L.; Kiziltas-Yavuz, N.; Dräger, C.; Ehrenberg, H.; Eckert, J.; Fauth, F.; Giebeler, L.; Knapp, M. A Novel High-Throughput Setup for *in Situ* Powder Diffraction on Coin Cell Batteries. *J. Appl. Crystallogr.* **2016**, *49* (1), 340–345. https://doi.org/10.1107/S1600576715022165.

(290) Avdeev, M.; Hester, J. R. ECHIDNA: A Decade of High-Resolution Neutron Powder Diffraction at OPAL. *J. Appl. Crystallogr.* **2018**, *51* (6), 1597–1604. https://doi.org/10.1107/S1600576718014048.

(291) Briois, V.; La Fontaine, C.; Belin, S.; Barthe, L.; Moreno, T.; Pinty, V.; Carcy, A.; Girardot, R.; Fonda, E. ROCK: The New Quick-EXAFS Beamline at SOLEIL. *J. Phys. Conf. Ser.* **2016**, *712*, 012149. https://doi.org/10.1088/1742-6596/712/1/012149.

(292) Leriche, J. B.; Hamelet, S.; Shu, J.; Morcrette, M.; Masquelier, C.; Ouvrard, G.; Zerrouki, M.; Soudan, P.; Belin, S.; Elkaïm, E.; Baudelet, F. An Electrochemical Cell for Operando Study of Lithium Batteries Using Synchrotron Radiation. *J. Electrochem. Soc.* **2010**, *157* (5), A606. https://doi.org/10.1149/1.3355977.

Résumé en Français de la Thèse

La demande mondiale en énergie a continuellement augmenté depuis le 19ème siècle et le début de l'ère industrielle. La plus grande part de l'énergie a été fournie par combustion de carburants fossiles et a inéluctablement donné lieu à l'émission de gaz à effets de serre, responsables du changement climatique. Afin de fournir une énergie plus responsable à une population toujours grandissante, il devient crucial de réduire l'intensité carbone de nos sources primaires d'énergies. C'est dans cette optique que le monde a connu un déploiement exponentiel de solutions de productions d'énergies dites renouvelables, *i.e.* convertissant des phénomènes naturels en électricité. Un des enjeux majeurs associé à la production d'électricité renouvelable est de palier à l'intermittence des phénomènes physiques ainsi exploités (solaires, vents, marées, etc.) afin de proposer une énergie « à la demande ». Ainsi, la transition vers un monde 100% renouvelable ne peut s'envisager sans le déploiement massif de moyens de stockage de l'énergie électrique.

Dans le cadre de cette thèse, nous nous sommes intéressés au stockage électrochimique de l'énergie, et en particulier à la compréhension fondamentale des réactions convertissant l'énergie électrique en énergie chimie au sein d'électrolyseurs ou de batteries. Ces dispositifs partagent une même architecture : ils sont composés d'électrodes auxquelles les réactions électrochimiques ont lieu, et d'un électrolyte composé de solvants et de sels afin d'assurer la neutralité électrique en tout point de ces dispositifs. Le choix de matériaux adaptés afin de concevoir les électrodes est l'un des facteurs les plus déterminants quant à la performance de ces dispositifs. Après des années de recherche frénétique ayant débouché sur des matériaux d'électrodes très performants (avec une grande densité énergétique pour les batteries, et une grande activité catalytique pour les électrolyseurs), il apparaît que les performances de ces derniers peuvent être limités par la nature des interfaces formées avec l'électrolyte. En vue d'obtenir des dispositifs du stockage électrochimique de l'énergie moins coûteux, plus efficaces et plus résilients, il semble crucial de mieux appréhender et maîtriser la nature de ces interfaces electrodes/electrolytes.

Dans cette thèse, nous avons tenté d'affiner notre compréhension sur l'impact des structures de solvatations des différentes espèces de l'électrolyte sur les performances de divers dispositifs de stockage électrochimique de l'énergie. C'est dans cette optique que nous avons étudié la

structure de différents électrolytes en combinant des techniques de simulations moléculaires avec des caractérisation physico-chimiques de ces liquides. Armés de cette compréhension de l'environnement des différents constituants de ces électrolytes, nous avons étudié leurs propriétés électrochimiques et avons abouti à des corrélations entre la structure de ces électrolytes, et leur réactivité.

Dans un premier temps, nous avons jeté notre dévolu sur la production d'hydrogène par électrolyse de l'eau. Nous rappelons quelles ont été les étapes clés dans la compréhension du rôle de la structure des matériaux d'électrodes sur les performances des électrolyseurs. En particulier, nous discutons des limites de descripteurs physiques, comme l'énergie d'adsorption de l'hydrogène sur l'électrode, permettant de prédire les cinétiques de la réduction électrochimique de l'eau. Bien que ces descripteurs permettent de classer les différents matériaux d'électrodes selon leurs performances électrochimiques, ils échouent à expliquer pourquoi la réaction de réduction de l'eau est impactée lorsque l'électrolyte est modifié. En particulier, un examen détaillé de la littérature démontre que l'atténuation des performances du platine pour la réduction de l'eau en milieu alcalin comparée à celle effectuée dans un électrolyte acide ne peut être simplement rationnalisée par ces descripteurs qui ne considèrent que l'électrode. Nous discutons ensuite des récents développements de méthodes expérimentales et computationnelles qui ont permis de démontrer que l'environnement des molécules d'eau au sein de la double couche électrochimique est à-même de modifier drastiquement la cinétique de production d'hydrogène par électrolyse de l'eau.

Afin d'améliorer la compréhension du rôle de la molécule d'eau dans la réaction de réduction de l'eau, nous avons développé une méthodologie, dite de confinement, afin de contrôler de manière fine la structure de l'eau au sein d'électrolytes et d'en étudier sa réactivité sur des électrodes modèles (platine, or). Pour ce faire, nous avons sélectionné un solvant organique (l'acétonitrile) stable à des potentiels assez négatifs pour réduire les molécules d'eau. Au sein de ce solvant, nous avons ajouté des molécules d'eau en présence de différents sels supports ($LiClO_4$, $NaClO_4$ et $TBAClO_4$). Nous avons remarqué que les molécules d'eau étaient plus faciles à réduire en présence des cations les plus acides au sens de Lewis. A l'aide de simulations de dynamique moléculaire classique et de spectroscopie de résonance magnétique nucléaire nous avons pu conclure que la réactivité des molécules d'eau présentes dans la sphère de solvatation d'un cation « acide » était exacerbée du fait d'un affaiblissement de la liaison O-H. En augmentant la

concentration en molécule d'eau dans ces électrolytes, nous avons observé que les molécules d'eau interagissaient les unes avec les autres par liaisons hydrogène. En présence d'un sel avec un cation hydrophobe, la réduction de l'eau est observée à des potentiels moins négatifs, ce qui confirme que l'affaiblissement des liaisons O-H des molécules d'eau (ici par liaison hydrogène avec d'autres molécules d'eau) facilite leur réduction. En revanche, en présence d'un cation « acide », la réduction de l'eau n'est pas impactée par sa concentration. En comparant l'énergie d'interaction entre une molécule d'eau et un tel cation avec celle par liaison hydrogène entre deux cations, nous avons trouvé que l'affaiblissement de la liaison O-H de la molécule d'eau était bien plus prononcé en présence d'un cation acide du fait de la très forte interaction non-covalente entre la molécule d'eau et ce cation. En revanche, en additionnant des quantités de sel support $LiClO_4$ plus importantes dans les électrolytes, nous avons observé que la réduction de l'eau était poussée à des potentiels plus élevés. Une analyse effectuée par dynamique moléculaire et diffusion de rayons X aux petits angles (SAXS) de la structure à l'échelle nanoscopique des électrolytes a montré qu'en présence d'une grande quantité de sel support, des nano-hétérogénéités étaient formées dans l'électrolyte. Des simulations de dynamique moléculaire nous ont permis d'affirmer que ces structures particulières étaient aussi présentes à l'interface électrode-électrolyte et facilitaient le transfert d'espèces chargées produites lors de la réduction de l'eau depuis l'interface de l'électrode vers le reste de l'électrolyte, facilitant donc la réaction électrochimique. Ces différentes études confirment que la réduction de la molécule d'eau est particulièrement sensible à la structure de la double couche et au transport des espèces chargées en son sein.

Nous avons ensuite étudié la réactivité des molécules d'eau au sein d'électrolytes aqueux employés dans les batteries Li-ion. Dans ce cas, il est intéressant repousser la réduction de l'eau à des potentiels plus négatifs afin d'accroître la plage de fonctionnement en potentiel des batteries. Il a récemment été proposé d'utiliser des électrolytes aqueux superconcentrés, dits *water-in-salt*, lesquels sont fabriqués par l'ajout d'une très grande quantité d'un sel de lithium organique (LiTFSI) dans un faible volume d'eau. En mesurant la stabilité de ces électrolytes en réduction sur des électrodes modèles, nous avons montré que la réduction de l'eau n'est initialement pas perturbée par l'ajout de ces grandes quantités de sels. En revanche, nous avons dévoilé que les anions OH^- générés lors de la réduction de l'eau pouvaient réagir avec les anions organiques, et donner lieu à la précipitation d'une couche passivante riche en fluor sur l'électrode qui permet *in fine* d'utiliser

ces électrolytes à des potentiels plus négatifs qu'un électrolyte dilué. Ayant en tête de réduire la quantité d'anion organique utilisés afin de minimiser les coûts et dangers de production de ces électrolytes organiques, nous avons tenté d'en substituer une partie par des sels de lithium inorganiques bien plus accessibles comme les halogénures de lithium. Ce faisant, nous avons observé que des solutions aqueuses très concentrées en halogénures de lithium ne se mélangeaient pas avec des solutions très concentrées en sels organiques de lithium (*e.g.* LiTFSI) et qu'un système aqueux biphasique se formait. En analysant les propriétés physico-chimiques de ces diverses solutions de manière expérimentale et computationnelle, nous avons pu dégager des critères permettant de prédire la formation de systèmes aqueux biphasiques en présence de deux sels de lithium. Tout d'abord, nous avons démontré qu'une différence de taille notable entre les deux anions était requise. Cependant, en comparant des anions avec un diamètre ionique similaire par des mesures de densité, nous avons montré que le critère de taille n'est pas suffisant. Des modélisations *ab initio* de ces anions en solution nous ont permis de conclure que la géométrie des deux ions doit être aussi différente pour donner lieu à la naissance d'un système aqueux biphasique. Finalement, nous avons tenté d'utiliser ces systèmes aqueux biphasiques afin de créer une preuve de concept d'une batterie avec un anolyte et un catholyte ne nécessitant pas de membrane pour empêcher le mélange des deux électrolytes mais reposant sur leur non-miscibilité intrinsèque.

Enfin, dans le dernier chapitre nous nous sommes intéressés à des électrolytes organiques. Comme mentionné dans l'introduction de ce résumé, un des défis pour la création de nouveaux matériaux de batteries est la compatibilité de ceux-ci avec l'électrolyte. Nous avons donc étudié une famille de matériaux VX_3 (X = Cl, Br, I) présentant une structure lamellaire similaire à celles des matériaux habituellement utilisés en tant que cathodes pour les batteries Li-ion, mais n'ayant jamais été employée pour effectuer de l'intercalation électrochimique car trop soluble dans les électrolytes polaires type carbonates habituellement utilisés dans les batteries Li-ion. Après avoir synthétisé VBr_3 et VI_3 en tubes scellés, nous avons montré qu'il n'était en effet pas possible de cycler ces matériaux dans des électrolytes type carbonates ou liquides ioniques dopés aux ions Li^+. Ayant préalablement démontré la très faible solubilité des halogénures (de lithium) avec les électrolytes superconcentrés contenant des sels organiques, nous avons testé de cycler les matériaux VX_3 dans des électrolytes organiques superconcentrés et obtenu une trace électrochimique réversible, suggérant que cette approche permet de drastiquement diminuer la

dissolution de ces matériaux. Des analyses structurales *operando* (diffraction des rayons-X) et *e*avons rappelé *x-situ* (diffraction des neutrons) nous ont permis de démontrer qu'une évolution structurale de ces phases avec insertion de lithium accompagne leur réduction électrochimique. Des analyses électrochimiques (GITT) et de spectroscopie d'absorption des rayons-X nous ont permis de démontrer que l'insertion de ce cation de lithium est associée à la réduction de V(III) en V(II). Nous avons ensuite proposé un modèle permettant de rationaliser l'absence de solubilité de ces composés dans des électrolytes superconcentrés. Pour cela, nous avons analysé par spectrométrie de masse couplée à un plasma inductif et par spectroscopie UV-visible différents électrolytes saturés en VX_3. Ces expériences nous ont permis de confirmer que la solubilité de ces composés était très basse dans les électrolytes superconcentrés et bien plus importante à des concentrations d'électrolyte support traditionnellement employées dans les batteries du fait de la formation de complexes entre les anions du sel et le vanadium. A plus haute concentration en sel, nous avons pu démontrer que la suppression de la solubilité des VX_3 relevait de la modification des coefficients d'activité et non pas d'empêchements cinétiques. Au global, cette étude suggère que des nouvelles familles de matériaux jusqu'alors jugées incompatibles avec les électrolytes traditionnellement employés dans les batteries Li-ion pourraient être explorées en utilisant des électrolytes superconcentrés.

Au global, cette thèse nous a permis d'avoir une compréhension aux échelles moléculaires, nanoscopiques et mesoscopiques de l'influence de la structure des électrolytes pour d'éventuelles applications électrochimiques liées au stockage de l'énergie.